Università degli Studi di Modena e Reggio Emilia

PhD Course in Models and Methods for Material and Environmental Sciences

XXXIII Cycle

Bioapatite in fossil and living organisms

PhD Student: Martina Savioli

Tutor: Prof. Annalisa Ferretti

Co-tutor: Dr. Daniele Malferrari

Director of the PhD Course: Prof. Alfonso Pedone

Contents

Chapter V

INTRODUCTION

Architecture and development of the PhD project

Bioapatite is a calcium phosphate mineral that has triggered the evolution of living organisms for over five hundred million years. Bioapatite diffusion involved vertebrates and invertebrates in the sea, on the lands and in the sky acting as a shelter of soft organs, a support of the body, an offense with weapons and a way to process food. In contrast to this importance of bioapatite in evolution of life and survival strategies, studies on the corresponding variation of its *mineralogical structur*e over geological time are limited. Hence, one the main purpose of this PhD project has been to collect and interpret data on bioapatite changes in time also in relation to diagenesis and fossilization. Article below cited, if not differently specified are annexes at the end of Chapters III and IV.

Define and calibrate the analytical method. We fixed an approach (*Malferrari et al., 2019*) to measure major element concentration through home-made matrix matched external calibration standards for laser ablation inductively coupled plasma mass spectrometry (LA-ICP-MS). We tested the method on living and fossil shark teeth; after we critically compared these results with their analogue obtained using other analytical techniques and certified external standards. A similar approach was applied also in *Righi et al., 2020* on completely different samples: chaetae from living invertebrates (fireworms *Hermodice carunculata*) that were characterized from a crystal-chemical point of view.

Fossils characterization. First (*Medici et al., 2020*) we focused our multi-analytical approach on conodonts, the first vertebrates to experiment in the sea with skeletal biomineralization of tooth-like elements in their feeding apparatus. Conodonts are extinct animals that lived for a time record of over 300 million years, offering a unique tool to test possible variation of bioapatite structure from the very primitive mineralization to a more evolved pattern. The unit cell parameters of bioapatite of about one hundred conodont elements from the late Cambrian to the Late Triassic were correlated with age, taxonomy, CAI (Color Alteration Index) and geographic provenance. We later considered more chemical information from conodonts apatite (*Medici et al., 2021*) zooming the uptake of trace elements in conodonts from a single stratigraphic horizon in the Upper Ordovician of Normandy (France). Assuming that all the specimens have undergone an identical diagenetic history, we have assessed whether conodont taxonomy and morphology impacts trace element uptake and crystallinity index.

Later, we considered also other phosphatic and "enigmatic" elements such as "conodont pearls" (*Ferretti et al., 2020*). Conodont pearls are phosphatic sub-spherical structure usually associated (i.e., in the same residue) with conodonts. We compared their crystal-chemical characteristics of pearls and conodonts from the same stratigraphic horizon to finally provide a possible response about their relation. Our conclusion was that, in spite of their name, "conodont pearls" do not belong to conodonts and could be more easily associated to brachiopods.

Finally (*Ferretti et al., submitted*) we collected data from fossil, dead and living bioapatite remains from major phyla that share the use of this mineralogy in order to finally understand how fossilization and diagenesis modified bioapatite over time.
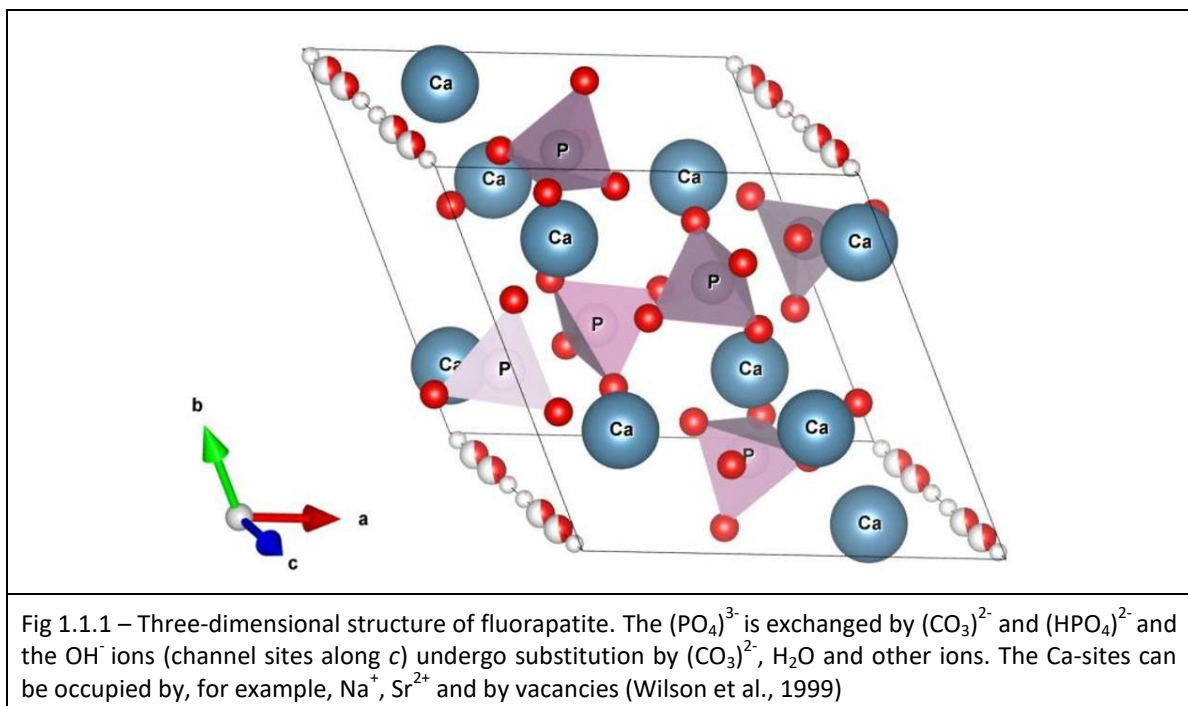
CHAPTER I

# State of the art

1.1 - Apatite and Bioapatite

Bioapatite, a bio-mediated calcium phosphate, is the mineralogical component of bones, teeth and other mineralized hard tissues. As will be better detailed later, even during life bioapatite can be easily affected by iso- and hetero-valent substitutions that change its crystal structure and properties imparting specific features (e.g. greater resistance to mechanical rather than chemical stress) to the hard tissues. For these reasons, the "use" of bioapatite by living organisms has been known since Precambrian times and, today, its crystal-chemistry and properties are studied in several fields of life-science research such as, for example, medicine and biology.

A short look to abiotic apatite

The apatite group encompasses mineral with the generic formula $Ca_5(PO_4)_3$(F, Cl, OH) and, based on the prevailing anion, it is possible to distinguish between fluorapatite, hydroxyapatite and chlorapatite. Two of the monovalent anions OH^-, Cl^- and/or F^- per unit cell can occupy the so called "channel site" inside the apatite structure. Other sites, or crystallographic positions, in the apatite unit cell are (Fig. 1.1.1):

Fig 1.1.1 – Three-dimensional structure of fluorapatite. The $(PO_4)^{3-}$ is exchanged by $(CO_3)^{2-}$ and $(HPO_4)^{2-}$ and the OH^- ions (channel sites along *c*) undergo substitution by $(CO_3)^{2-}$, H_2O and other ions. The Ca-sites can be occupied by, for example, Na^+, Sr^{2+} and by vacancies (Wilson et al., 1999)

- Tetrahedral sites for six ions P^{5+}, each in tetrahedral coordination with oxygen;
- Ca sites for four ions Ca^{2+};
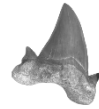
- Ca sites for six ions Ca^{2+} arranged in the so called "anion-channel", a channel along the *c*-axis (*Wopenka & Pasteris, 2005*).

Iso- and hetero-valent atomic substitutions may occur within apatite structure in several crystallographic positions accommodating different elements with a wide range of ionic radius and charge (*Pan & Fleet, 2002; Piccoli & Candela, 2002*). Actually, for abiotic (inorganic) apatites in a sedimentary environment, the local geochemistry can provide a wide range of elements and, moreover, heating occurring during burial and diagenesis may favour and accelerate substitution rate. For example, at high temperature, OH^-, Cl^- and F^- can substitute for each other in any proportion and PO_4^{3-} can be replaced by AsO_4^{3-}, SO_4^{2-}, CO_3^{2-} or SiO_4^{4-}. Moreover, a large number of metal cations, such as K^+, Na^+, Mn^{2+}, Ni^{2+}, Cu^{2+}, Co^{2+}, Zn^{2+}, Sr^{2+}, Ba^{2+}, Pb^{2+}, Cd^{2+}, Y^{3+} and trivalent ions of rare earth elements can be substitute for Ca^{2+}, usually in trace concentrations.

Similarly, apatite characterized by a wide range of chemical substitution may be found also in magmatic (mostly ortho-magmatic and pegmatitic) and metamorphic environments forming euhedral crystals also with important dimensions. Generalizing, it is possible to conclude that apatite inside its atomic structure can incorporate half of the elements of the periodic chart (*Pan & Fleet, 2002; Piccoli & Candela, 2002; Hughes & Rakovan, 2002*). These chemical substitutions may be detected and analysed using different analytical methods and instruments (see chapter 2).
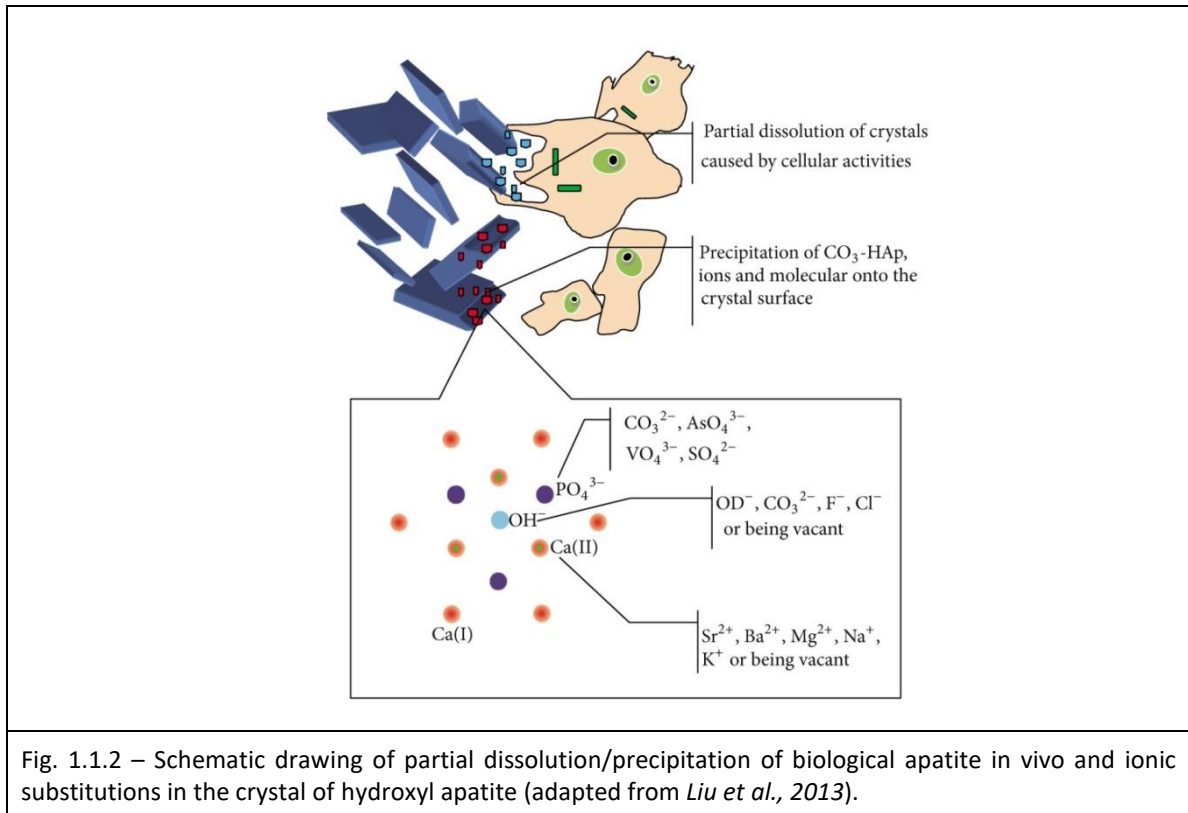
A short look to bioapatite

As reported above, bioapatites are biosynthesized calcium phosphates. Usually bioapatites are hydroxylapatites and fluorapatite, characterized by the variable presence of the ion CO_3^{2-}. In literature these minerals are extensively named carbonate-hydroxylapatites and carbonate-fluorapatites, although these names are not officially accepted by IMA-CNMNC (*Burke, 2008; Pasero et al., 2010*). Numerous investigations (e.g., *Trueman & Tuross, 2002; Nemliher et al., 2004; Wopenka & Pasteris, 2005; Trotter & Eggins, 2006; Keenan, 2016*) demonstrated that ionic substitutions can occur in bioapatite although, during the life of the organism, they are more limited than in the *post mortem* phase or for abiotic apatites. During life, major substitutions concern K^+, Na^+, Fe^{2+}, Mg^{2+} (more rarely Zn^{2+} and Sr^{2+}) for Ca^{2+} and carbonate for phosphate even if little amount of carbonate may be accommodated also in the channel site (*Skinner et al., 1987; LeGeros, 1991; Gross & Berndt, 2002; McConnell, 2012*). Chlorine, for example, which is abundant in blood, having a large ionic size is difficultly incorporated in bioapatite (on the other hand, it is commonly present in geological apatite which crystallize at non-ambient temperature, *Piccoli & Candela, 2002*). In contrast, the presence of F^- is frequent as it occurs at room (body) temperature. As a further detail, it should be emphasized that fluorine in tooth enamel imparts teeth a greater resistance being fluorapatite less soluble in acid environment than hydroxylapatite (*Hughes & Rakovan, 2002*).

Another important substitution, that it is not yet clear how it occurs during the life of the organism, regards the carbonate substitution. Two possible sites can be involved: the anion site, called *A-type* substitution, or the PO_4 site, called *B-type* substitution. It is nowadays generally accepted that biological apatite is a mix of both the forms where the major substitutions of

CO_3^{2-} occur in the PO_4 site (*LeGeros, 1999; Elliot, 2002; Kolmas et al., 2012*). In physiological environment, cellular activities can cause an acidification of the microenvironment, inducing a partial dissolution of bioapatite, leading to increase the supersaturation of the fluids (Fig. 1.1.2).

Fig. 1.1.2 – Schematic drawing of partial dissolution/precipitation of biological apatite in vivo and ionic substitutions in the crystal of hydroxyl apatite (adapted from *Liu et al., 2013*).

Further, precipitation of new bioapatite, together with other ions and organic molecules, occurs, with the incorporation of CO_3^{2-} and OH^- (*LeGeros, 2008*).
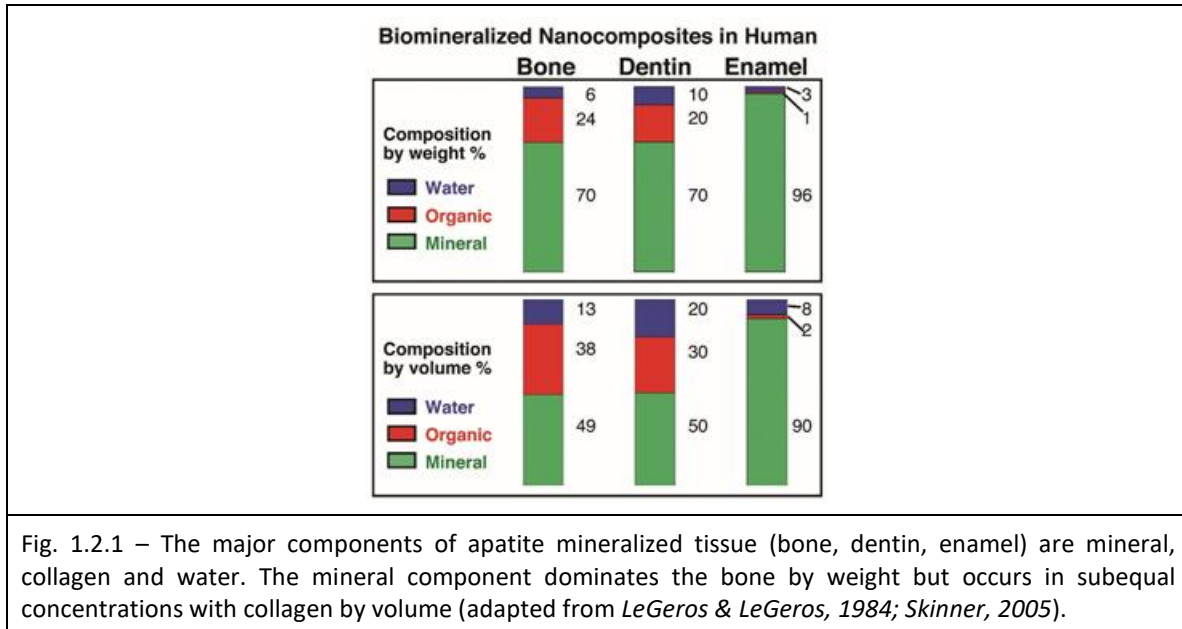
Two different crystal forms are recognizable in bioapatites, showing a hexagonal symmetry (*a = b*, γ = 120°; *Posner et al., 1958*) and a monoclinic symmetry (*b = 2a*, γ = 120°; *Elliott et al., 1973*). The two forms have the same elements, but with orientational ordering of (OH)⁻ anions within [00z] anionic columns. Generally, the stoichiometric Ca/P ratio is 1.67 or little lower (*Elliott, 1994; Kuhn et al., 2008*), but were also reported higher values (*Joschek, 2000; Barakat, 2008; Janus, 2008*) depending not only by the intrinsic characteristics of the materials, but also on detections methods and errors (*Joschek, 2000; Kim et al., 2004*). Additionally, the incorporation of carbonate may increase with the age of crystals in dead organism regardless of whether a fossilization process has started (*Liu et al., 2013*).

1.2 – Bones and teeth

Different organisms, both living and fossil, share the use of bioapatite for building their mineralized tissues. Bioapatite in fact, more than other minerals, has the physical and chemical properties which are required for structural support (bones), mechanical grinding (teeth) or protections (shells). Considering that the amount and the composition of bioapatite in the mineralized tissues change depending on their function, it is possible to affirm that, over time, the various living organisms "have learned to modulate" bioapatite synthesis and distribution.

Moreover, bioapatite is a reservoir of phosphorus that represents a fundamental nourishing for the body as it is present in biomolecules like DNA, RNA, ATP, collagen and a lot of other proteins; actually, bioapatite stores in bones about the 50, 80, 99 wt% of the human body magnesium, phosphorus and calcium, respectively (Fig. 1.2.1, *Skinner, 2005; Glimcher, 2006; Pasteris et al., 2008*).

Fig. 1.2.1 – The major components of apatite mineralized tissue (bone, dentin, enamel) are mineral, collagen and water. The mineral component dominates the bone by weight but occurs in subequal concentrations with collagen by volume (adapted from *LeGeros & LeGeros, 1984; Skinner, 2005*).

Bones

Mineralized tissues are formed by intercalation of organic and inorganic material, organised in a hierarchical way with different structural units at different size scales (Fig. 1.2.2; *Weiner & Traub, 1992*). These units work in concert and play different roles imparting specific mechanical properties to the bones (*Rho et al., 1998; Currey, 2002*). The organic part of bones is largely represented by collagen and other proteins (about 30 wt%), whereas the inorganic fraction is composed in various amount by "fresh bones" and "dry bones" which are non-stoichiometric, impure and poorly crystalline form of hydroxyapatite with the latter, however, better crystallized (*Wang et al., 2010*). The mineral/collagen ratio is not constant among animals and within the same species and it plays a close control on various physical properties of bones such as toughness, stiffness and strength. For example, higher mineral/collagen ratios typically correspond to stronger but brittle bones (*Rogers & Zioupos, 1999; Currey, 2004; Currey et al., 2004*) characterized by nanosized plate and/or elongated bioapatite crystals (usually with length varying from 50 to 60 Å, more rarely up to 180 Å) embedded in an organic matrix (*Piga et al., 2009, 2013*) where the crystals are clustered to form fibrous structures of varying sizes (*Weiner & Wagner, 1998; Glimcher, 2006*). Due to the high mineral/collagen ratio, bioapatite crystallinity in living organisms is quite low, in particular if compared with abiotic apatite (*Hench, 1993*).
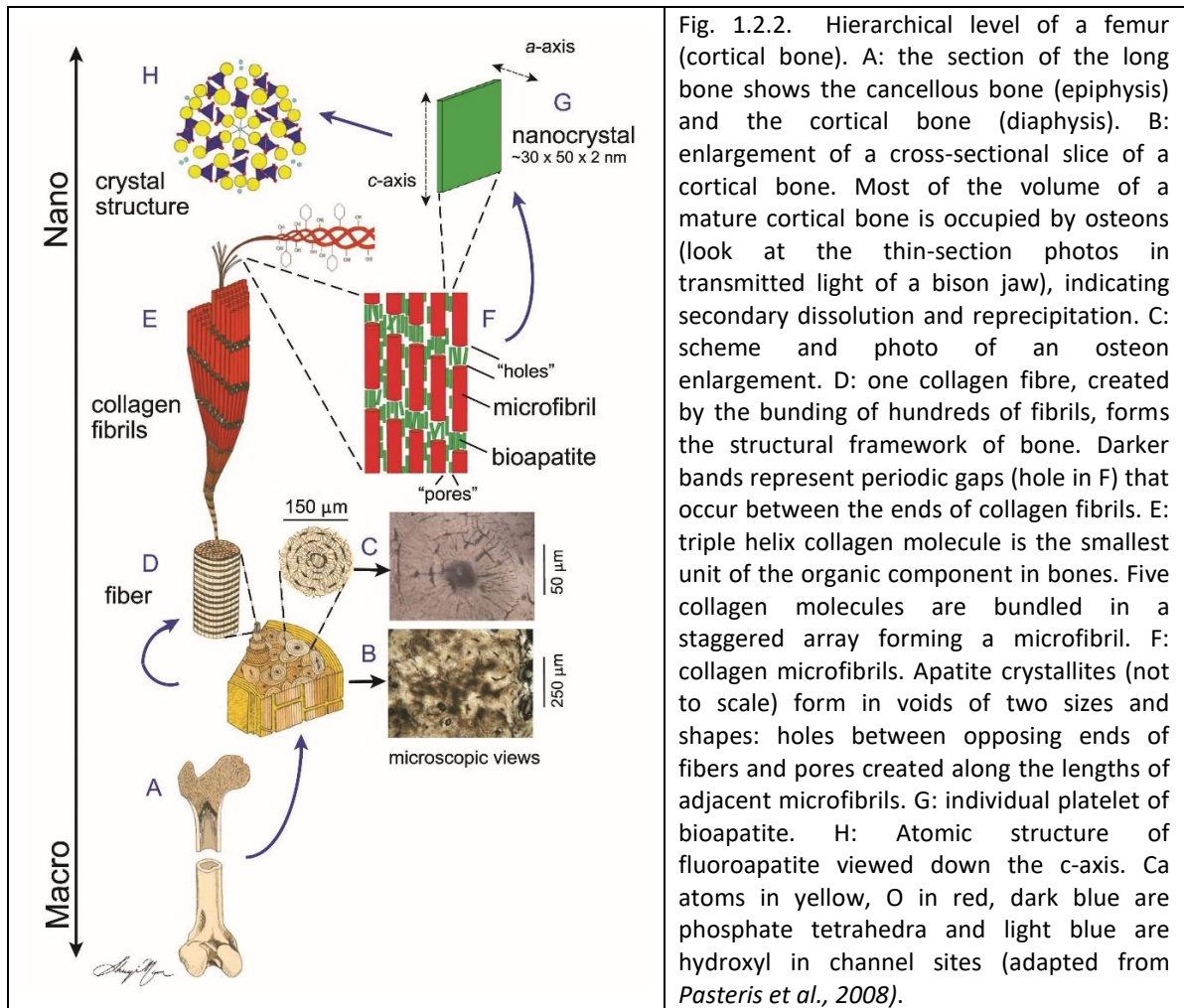
Fig. 1.2.2. Hierarchical level of a femur (cortical bone). A: the section of the long bone shows the cancellous bone (epiphysis) and the cortical bone (diaphysis). B: enlargement of a cross-sectional slice of a cortical bone. Most of the volume of a mature cortical bone is occupied by osteons (look at the thin-section photos in transmitted light of a bison jaw), indicating secondary dissolution and reprecipitation. C: scheme and photo of an osteon enlargement. D: one collagen fibre, created by the bunding of hundreds of fibrils, forms the structural framework of bone. Darker bands represent periodic gaps (hole in F) that occur between the ends of collagen fibrils. E: triple helix collagen molecule is the smallest unit of the organic component in bones. Five collagen molecules are bundled in a staggered array forming a microfibril. F: collagen microfibrils. Apatite crystallites (not to scale) form in voids of two sizes and shapes: holes between opposing ends of fibers and pores created along the lengths of adjacent microfibrils. G: individual platelet of bioapatite. H: Atomic structure of fluoroapatite viewed down the c-axis. Ca atoms in yellow, O in red, dark blue are phosphate tetrahedra and light blue are hydroxyl in channel sites (adapted from *Pasteris et al., 2008).*

Another important constituent of fresh bones is water. Mechanical behaviour of fresh bones is heavily dependent on the reciprocal interactions between water, mineral and collagen (*Nyman et al., 2006*). There are many types of water in bones (*Nomura et al., 1977; Peters et al., 2000*): free water, structural water forming hydrogen bonds within the triple helix of collagen molecules and crystal water bonding to apatite surface or in the crystal lattice.

In bone formation, during both primary growth and repair, deposition of collagen occurs before the apatite mineralization. Anyway, bone mineralization is a dynamic process. Every 5-10 years (depending on age, diet and health), bones undergo a complete biological renewal that replaces the entire skeleton; likewise, the collagen-mineral composite, initially produced by osteoblast cells, is completely reworked. The cells of the osteoclasts cause them to dissolve and, subsequently, the osteoblast can deposit new bone material. Osteoblasts and osteoclasts are involved in a feedback mechanism to increase the diameter of bones that bare weight. Osteoclasts can also be deployed to release necessary calcium or phosphate to the body fluid for use elsewhere (*Glimcher, 2006; Boskey, 2007*).

Bioapatite precipitation in regular pattern and with fixed crystallite size on the collagen fibrils of bone is driven by a mechanism that is not yet fully understood. It seems that the precipitation

starts from the biochemical removal of a ubiquitous nucleation inhibitor with the consequent increase in the concentration of apatite components, especially phosphorus. First, it is necessary the formation of a biological-biochemical environment favourable to mineralization according to the "classic" principles of inorganic chemistry. In other words, the concentration of the elements necessary for the formation of the crystals must be equal to or greater than the saturation value and only at that point bioapatite nucleation starts (*Mann, 2001*). Apatite crystallites nucleate and grow within the collagen network in two ways: i) in larger "holes" between the termination of end-to-end-aligned collagen microfibrils and, ii) in smaller "pores" between side-by-side collagen microfibrils. Bone bioapatite usually crystallizes with the *c*-axes oriented parallel to the long axis of the microfibril. The nature of the binding between apatite and collagen is not clear, but the affinity is strong, as demonstrated by the remarkable flexibility and strength of bones and the difficulty in physical and chemical separation of the two components (*LeGeros & LeGeros, 1984; Elliott, 2002; Currey, 2004; Currey et al., 2004; Glimcher, 2006; Boskey, 2007*).

At a macroscopic level, two osseous tissue types are present: cortical and trabecular bone. The difference is visible at a microstructural level. Cortical bones are composed of osteons or Haversian systems; trabecular rods and plates form the trabecular or cancellous bones. Both cortical and trabecular bones are formed by lamellae composed by the fibres and fibrils mentioned above. It is also possible to distinguish between cellular (Fig. 1.2.3) and acellular bone tissues.
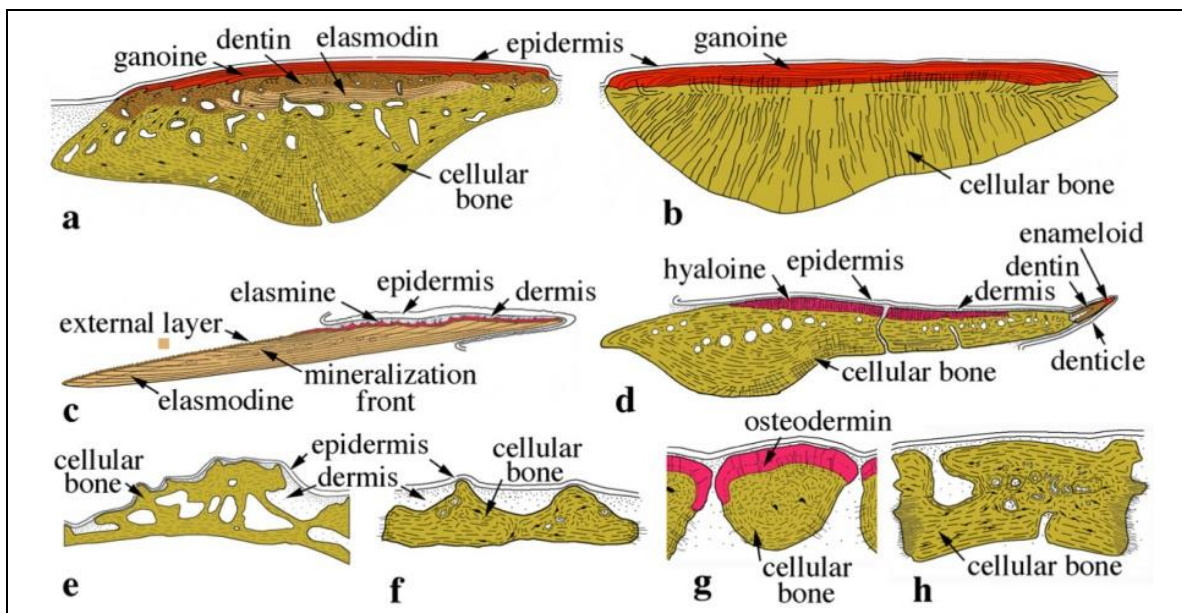
Fig. 1.2.3 - Drawings of various types of integumentary skeletal elements illustrating the diversity of bone and dentin in living vertebrates. a: Ganoid scale of *Polypterus senegalus*; b: ganoid scale of *Lepisosteus oculatus*; c: elasmoid scale of the teleost fish *Danio rerio*; d: dermal scute of the teleost fish *Corydoras aeneus*; e: dermal plate of the teleost fish *Gasterosteus*; f: osteoderm of the amphibian *Phyllomedusa*; g: osteoderm of the lizard *Tarentola mauritanica*; h: osteoderm of the armadillo *Dasypus novemcinctus* (*Sire & Kawasaky, 2012*).

Cellular bone is any osseous tissue containing cells (osteocytes) that are enclosed in bone lacunae, called periosteocytic lacunae, having numerous, fine cytoplasmic extension hosted in

canaliculi. The number, shape and size of lacunae vary between bone tissues and these variations reflect, in general, the deposition rate of the matrix (*Francillon-Vieillot et al., 1990; Zyelberberg et al., 1992*). Acellular bone is defined as any osseous tissues totally devoid of enclosed osteocytes (*Moss, 1961; Moss, 1963; Moss, 1965*). This type of bone is found in derived teleost fishes in dermal and endoskeletal bones. Acellular bone can survive without osteocytes as the matrix houses canaliculi that contain cytoplasmic extensions from the osteoblasts that remain inside the periosteum, on the bone surface. Indeed, acellular bone matrix is not thick enough to house cells (*Huysseune & Sire, 1998; Sire & Huysseune, 2003*). As acellular bone is present only in derived teleost fishes, it is considered as specialized and cellular bone as generalized (*Meunier, 1987*).

Chondroid bone is a skeletal tissue, which exhibits histological characteristics occurring both in bone, like collagen rich matrix, and cartilage, like embedded, large, closely packed cells resembling chondrocytes. The presence of chondroid bone suggests a continuum of mineralized tissues composing the skeletal elements and also the existence of a common embryological and evolutionary origin (*Beresford, 1981; Cole & Hall, 2004*).

Teeth

Teeth are fundamental elements in most vertebrates used not only for feeding. Teeth, in fact, may be also used for fight and defence, or have an aesthetic role or even participate to phonetics. Teeth are parts of the skeleton and are formed by different tissues each with well-defined properties and structure.

Cementum (Fig. 1.2.4) is a tissue with a structure close to that of bone, but showing some differences in mineralization. In addition, it may or may not contain cells and vascular canal, probably depending on the thickness of the tissue. With the exception of crocodiles, cementum occurs only in mammals. In tooth, cementum is localized in the root area and includes periodontal ligaments (*Poole, 1967; Shimada et al., 1992*).
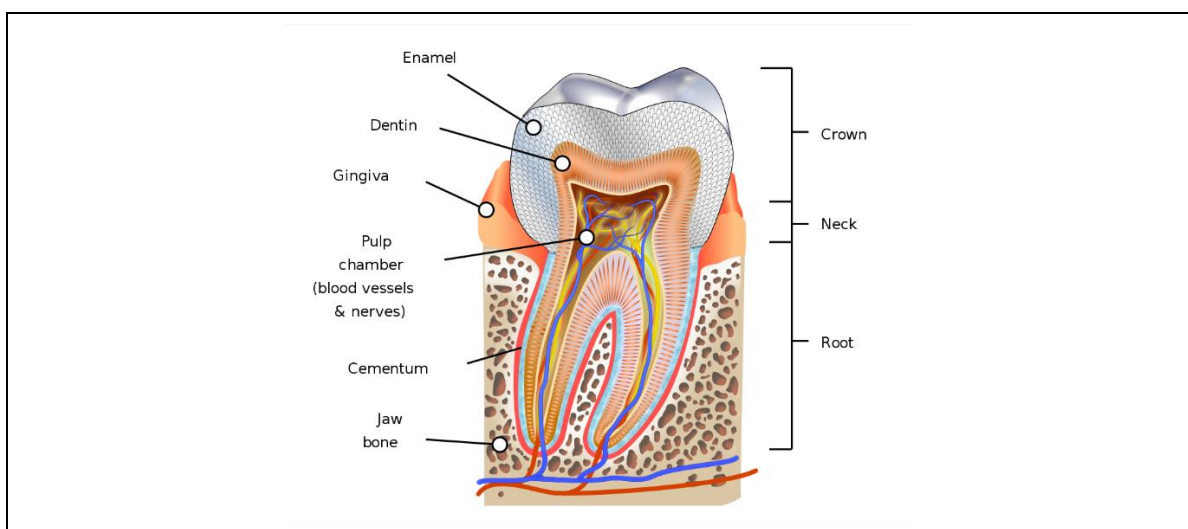

Fig. 1.2.4 - Schematic section of a human tooth. Enamel is the outermost layer of the crown and covers the dentin. The pulp contains nerves and blood vessels, while the cementum is the outermost layer of the mineralized tissues of the root (adapted from *Sander, 2000*).

Dentin (Fig. 1.2.4) is a collagen rich, well mineralized (70-75 wt% in mammals) tissue and is deposited by specialized cells, the odontoblasts. Dentin is always formed in two steps: the first is the deposition of a non-mineralized matrix, called *predentin*, that is rich in both collagen and proteoglycans, followed by the mineralization of the matrix. In fossil and living vertebrates, several dentin types (i.e., orthodentin, osteodentin and vasodentin, Fig. 1.2.5) have been described and they are distinguished by the arrangement and orientation of the tubules that host cytoplasmic processes of the odontoblasts, by the occurrence or absence of embedded odontoblasts, and by the lamellar organization of the matrix (*Ørvig, 1977; Sander, 2000*).
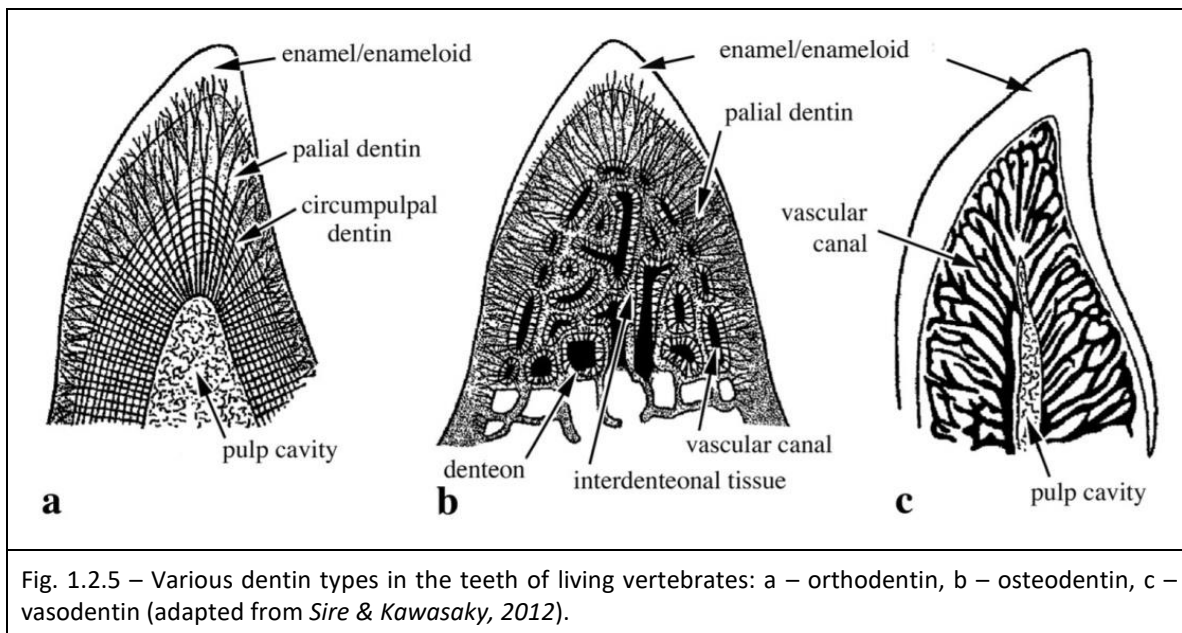

Fig. 1.2.5 – Various dentin types in the teeth of living vertebrates: a – orthodentin, b – osteodentin, c – vasodentin (adapted from *Sire & Kawasaky, 2012*).

Enamel (Fig 1.2.4) is the hardest material formed by vertebrates and represents the most mineralized skeletal tissue present in the body with 95-97 wt% of bioapatite and less than 1 wt% of organic material, mostly represented by the protein amelogenin, the main secretory product of ameloblast (*Pasteris et al., 2008*). Enamel is distinct from bones in terms of architecture, pathology and the biological mechanism mediating its formation. Mature enamel is acellular and does not resorb or remodel (*Robinson et al., 2003*). In mammal tooth, enamel forms the uppermost 1-2 mm of the crown. This tissue consists of organized interweaving bundles of crystallites called rods or prisms. The organization of the crystallites is essential for enamel function (*White et al., 2001*). Because of the high mineral content and the minimal organic presence, enamel is brittle but the architecture of crystallites can deflect a propagating crack, preventing it from reaching the junction between dentin and enamel which, anyway, is resistant to delamination of the tissues despite their differences in composition (*Lin et al., 1993; Imbeni et al., 2005*). At a nanoscale structure, crystallites grow preferentially along the *c*-axis and their size varies depending on the age and stage of mineralization (*Kirkham et al., 2000; Wen et al., 2005*). It is possible to distinguish between three different structural components inside the enamel: the *rod*, the *interrod* and the a*prismatic enamel*. Rods are the main components, constituted by bundles of aligned crystallites that are woven into intricate architectures approximately 3-5 µm

in diameter (*Daculsi & Kerebel, 1978*). The lengths of the rods and crystallites vary among species, but crystallites are generally about ten times wider and 1000 times longer than bone and dentin ones (*LeGeros & LeGeros, 1984; Mann, 2001; Skinner, 2005; Glimcher, 2006; Robinson et al., 2017*). Interrod (or interprismatic) enamel, which surrounds and packs between the rods is the second component and can be distinguished from the rod for the orientation of the apatite crystallites that are aligned in the rod and less ordered in the interred. Aprismatic enamel refers to the structures containing apatite that does not show any type of alignment (*Garant, 2003; Robinson et al., 2017*).

Enameloid (Fig. 1.2.4) is an ipermineralized tissue that was documented also in early vertebrates capping the odontodes of osteostracans and heterostracans, the dermal denticles of teleodonts, dermal denticles and teeth of extinct chondrichthyans. In living vertebrates, it is possible to find enameloid cover the tip of teeth and dermal denticles of chondrichthyans, called *adameloid* in this case, the teeth and dermal denticles of teleosts and the teeth of larval caudate amphibians (*Davit-Béal et al., 2007*). In the latter, during ontogeny, enameloid is secondarily covered with *enamel* and is no longer present in post-metamorphosed individuals. Enameloid and enamel are similar in structure, topology and function, but formation of enameloid requires the co-participation of ameloblasts and odontoblasts and the matrix is composed of a loose network of fibrillary collagen. During the mineralization process, the organic matrix is degraded by proteases and a marked mineralogical transformation takes place (*Poole, 1967; Moss, 1970; Schaeffer, 1977; Herold et al., 1980*). For example, in adult tetrapods, enameloid does not form a distinct tissue in the upper region of the teeth, but the enamel-dentin junction in which dentine and enamel matrices are mixed, could be considered as a remnant of enameloid (*Sire & Kawasaki, 2012*).

1.3 - Shells and other phosphatic mineralization in invertebrates

The majority of skeletal structures of invertebrates is composed of calcium carbonate. A few invertebrates, mostly inarticulate brachiopods, are unique as they possess calcium phosphate shells instead of carbonate shells. In spite of the rare occurrence of this mineralogy, only few studies have been published on the structure and formation of these shells. This PhD thesis will focus both on living and fossil vertebrates and invertebrates, with the additional aim of zooming on differences between living and dead organisms (i.e., before the beginning of fossilization but accounting of eventual *post-mortem* transformation).

Invertebrates and protozoans share two types of calcium phosphate structures: loose granules and rigid and well-organized skeletal forms. The grains forming these parts can be crystalline or amorphous, being the latter more frequent. Mineralized spherules are present within a variety of cell of invertebrates. They reach a diameter of approximately 200 μm, with spherical or oval shapes and frequently exhibiting concentric layers; chemical compositions is variable with Ca^{2+} and Mg^{2+} and CO_3^{2-} and PO_4^{3-} as main cations and anions, respectively (*Simkiss, 1976; Watabe et al., 1976*). Amorphous calcium phosphate granules are found in calcium cells of the foot, connective tissues, head, digestive glands and gills and in kidney epithelial cells of various molluscs (*Simkiss & Mason, 1983; Silverman et al., 1983; Foumie & Chetail, 1984*). Minor elements were also found in granules and their chemical composition (major and trace

elements) varies significantly depending on the species. Likewise, the organic content, mostly comprehensive of proteins, carbohydrate and proteins, varies in different species, ranging from about 5 to 30 wt% of the dry weight (*Rosenberg, 1966; Howard et al., 1981; Simkiss & Mason, 1983*).

Amorphous, hydrous, ferric phosphatic granules, including also calcium, are present in the connective tissue of the dermis of holothurians, the echinoderms commonly called "sea cucumbers". These granules are 10-350 μm in diameter, spherical, ovoidal or ellipsoidal, composed by layers alternately separated by organic material (*Lowenstam & Rossman, 1975*).

Crystalline granules of calcium phosphate have been reported in cytoplasmic vacuoles of the ciliate protist *Spirostomum ambiguum* (*Müller, 1786*). They have diameters of about 0.5-3 μm and a single mature cell can contain thousands of granules. Every granule is composed of radially arranged filaments fully calcified or calcified only at the periphery. The formation of mineralized granules begins by the coalescence of vesicles in the cytoplasm, forming large vacuoles, within which embryos of granules are formed. Later, filaments within the embryos appear and get calcified starting from the periphery. The granules can move inside the cell, but they are not excreted (*Pautard, 1981*).

Serpulid polychaete worms form calcareous tubes in which the animal dwells. The tubes are composed by calcium carbonate and organic matrix and are secreted by specific ventral glands. Cells near those tissues contain concretions composed of an admixture of hydroxyapatite and calcium magnesium phosphate (*Watabe, 1989*).

An amorphous calcium phosphate skeleton studied in detail is that of nemertean stylet. Phylum Nemertea includes the so called "ribbon or proboscis worms". The stylet is present in a member of the taxa and it is formed by a pointed and mineralized bump with which the animal hits the prey by injecting paralyzing toxins and digestive acids (*Stricker & Cloney, 1981*). Several reserve stylets are also present into a special sac, used to replace the lost or damage central stylet. The stylet, which is usually calcareous, can be also made by calcium phosphate with minor Ba and Sr substitutions (*Stricker & Weiner, 1985*). The stylet apparatus is supported by a mineralized phosphatic plate which increases the rigidity and helps keeping the central stylet during prey attack (*Stricker & Cloney, 1981*).

Nematocist batteries of some siphonophore, belonging to the Phylum Cnidaria, have amorphous calcium phosphate spicules. Depending on the district of the siphinophore body in which they are located, spicules can be of about 15 μm long and rod shaped, or about 35 μm longed and with prominent barbs. The role of the spicules is to avoid losing prey once grabbed (*Mackie & Marx, 1988*).

Crystalline apatite was reported in radular teeth of polyplacophorans, marine molluscs also called chiton with a particular shell composed of eight separate valves. They are able to precipitate four different minerals: aragonite in shells, spines and girdle scales, two iron compounds and calcium phosphate in radular teeth. Additionally, a transformation of the apatite mineral occurs during the teeth maturation. From the mineralogical point of view, the mineralized fraction of the mature radular teeth of chitons is composed by 63-65 wt% of apatite,

33 wt% of magnetite and 2 wt% of lepidocrocite (*Lewenstam, 1967*). Studies on the apatite component revealed that, initially, bioapatite is amorphous and only after some weeks gets crystallized and with a preferred orientation, having the *c*-axis aligned perpendicular to the tooth surface suggesting a mediation by the accretion with organic matrix (*Lowenstam & Weiner, 1985*).

The periostracum of a few species of mytilid bivalve contains crystalline calcium phosphate. It can be organized in irregular masses or granules or hexagonal cylinders. Dimensions of crystals are about 1-10 μm with composition close to that of fluorapatite and variable amount of CO_2 content depending on the provenance area (*Waller, 1983; Carter & Clark, 1985*).

Brachiopods are benthic marine animals that mostly secrete their valves of low-Mg calcite or calcium phosphate apatite (*Brand et al., 2003; Cusack & Williams, 2007*). Shells of linguliform brachiopods are deposited as mineralized laminae alternating with organic rich laminae (*Cusack et al., 1999; Williams & Cusack, 1999, 2007*). These shells have various microstructural complexity (called *baculate shell structure*), characterized by alternating compact and baculate laminae (*Cusack et al., 1999*). Compact laminae are composed of tightly packed apatite crystals. Baculate laminae are formed of trellised phosphatic rods, called *bacula*, which are supposed to have been enmeshed into organic matrix at the lifetime of the brachiopod (*Williams & Cusack, 1999*).

Functions of calcium phosphate in invertebrate animals are diverse. Gill granules of unionid mussels serve as a calcium reservoir during periods of hypoxia (*Silverman et al., 1983*) and are mobilized during reproduction (*Silverman et al., 1985*). The amorphous granules in crab hepatopancreas are storage for calcium and phosphate during intermolt stage (*Becker et al., 1974*). The cestode granules are able to neutralize metabolic products (*von Brand, 2013*). Molluscan hepatopancreas granules can accumulate heavy metals and probably serve as a metal-detoxification system (*Howard et al. 1981; Simkiss &Mason, 1983; Simkiss, 1984; Fournie & Chetail, 1984*). The granules of some ciliates appear to increase the ability to withstand hydrostatic pressure of the animal and to serve as mobile endoskeleton which prevent crushing of the cell during silt movement, or allow great tension in the myonomes without damage to the cell (*Arnott & Pautard, 1970*). They can also be used as a metabolic storage during reproduction (*Pautard, 1959*).

1.4 - Apatite structures in vertebrates

The evolution of skeletal tissues (cartilage, bone, dentin, enamel) of vertebrates, documented over times through fossils, has always attracted scientists of various research areas (e.g., evolution, adaptive strategies, biomaterial engineering, etc). Several hypotheses about the origin of the skeleton have been reported in literature (*Stensiö, 1927; Romer, 1933, 1942, 1963, 1964, 1967; Forey & Janvier, 1994; Forey, 1995; Shu et al., 1999; Donoghue et al., 2000; Donoghue & Smith, 2001*). A detailed description of each taxon is beyond the aims of this thesis. However, the main features of the first skeletal architectures will be briefly summarized in the present chapter in order to provide basic information related to their organization and appearance.

Phylum Chordata includes all vertebrates and other two groups: tunicates (sea squirts) and cephalochordates (amphioxus). These two taxa show no evidence of skeletonization, except for some tunicates that are able to secrete mineralized tissues of various composition that are used to create microscopic spicules embedded in the tunic wall (*Lambert et al., 1990*). Cephalochordates exhibit limited evidence of unmineralized skeletonization in the form of small imbricating cartilaginous rods that support the buccal cirri and the external openings of the pharynx (*DeBeer, 1937*).

Myxiniformes (hagfishes) and lampreys are basal vertebrates that are distinguished from more derived living groups by the absence of jaws (Fig. 1.4.1). It is not clear if their characteristics are representative or not of Paleozoic ancestors (*Langille & Hall, 1993; Marinelli & Stranger, 1956*).
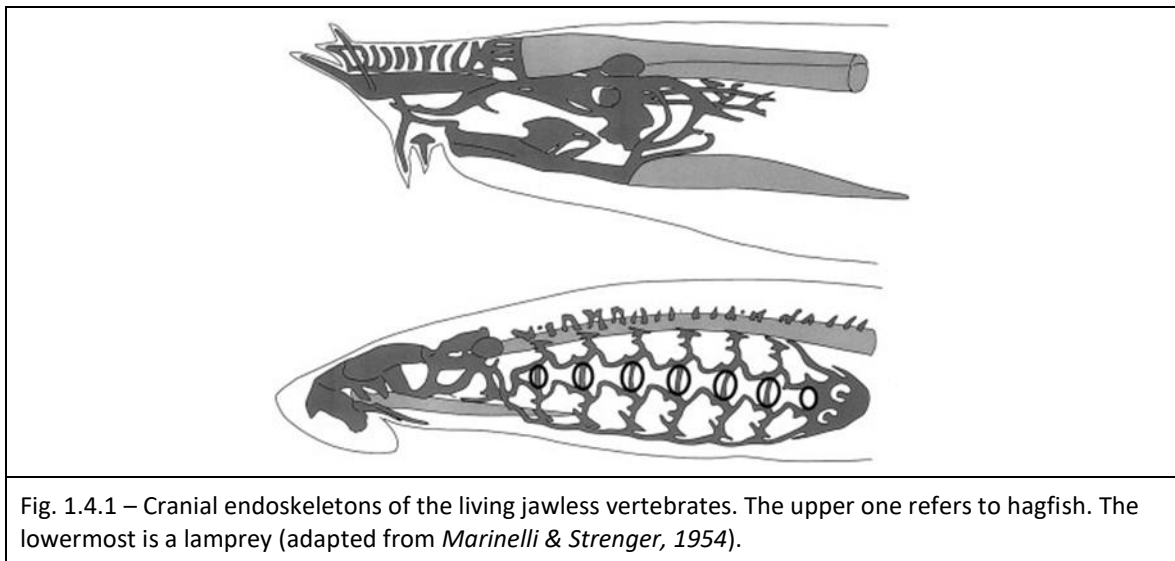
Fig. 1.4.1 – Cranial endoskeletons of the living jawless vertebrates. The upper one refers to hagfish. The lowermost is a lamprey (adapted from *Marinelli & Strenger, 1954*).

Chordate are now dominated by vertebrates and, in particular, by jawed vertebrates. However, until the late Paleozoic, jawed vertebrates did not attain their numeric dominance over jawless vertebrates. The fossil record revealed that, in contrast to living basal vertebrates that are "naked", the vast majority of jawless vertebrates were extensively skeletonized. So, living representatives are entirely unrepresentative of their extinct relatives (*Donoghue & Sansom, 2002*).

Fossil jawless vertebrates are dominated by the ostracoderms that were characterized by an extensively developed mineralized dermal skeleton. In some groups, the dermal skeleton is composed of individual scales, in a manner comparable to living sharks, in others only the trunk and the tail are covered by discrete scales, while the head and portion of the trunk immediately adjacent are encased in large plates, sometimes fused to form a head capsule (*Ritchie, 1968; Ørvig, 1980*).

Anaspids are a group that share many anatomical similarities to lampreys, such as morphology of the caudal fin and apparent single nostril. Anaspids differ from lampreys in the possession of paired ventro-lateral fins, a mineralized dermal skeleton composed of hundreds of scales, and a

mandibular plate that acted in dorsoventral orientation rather than the bilaterally acting rasping tongues proper of lampreys and hagfishes (*Stensiö, 1939; Arsenault & Janvier, 1991*).

Conodonts represent an extinct group of jawless vertebrates that lived in the oceans from the Cambrian to the Triassic. They were the first which experimented skeletal biomineralization with tooth-like elements in their feeding apparatus. The gross anatomy of conodonts is common to hagfishes and lampreys, but the difference is the presence of a complex array of "dental" elements. These elements, ranging in average size from 0.1 to 5 mm, mainly consist in carbonate apatite and were arranged in a bilaterally-symmetrical apparatus within the cephalic part of the animal. It is possible to distinguish between the more ancient paraconodonts and the more recent euconodonts, according to the difference in the organization of the phosphatic lamellae that form the elements (*Murdock et al., 2013*). The earliest stage of growth in paraconodonts is the protoelement, which is the more distal part of the element, around which the formations of the element occurs which apposition of lamella layers to the proximal surface only.

Fig. 1.4.2 – Element growth of the late Cambrian euconodont *Procondontus posterocostatus*. In the first left picture a longitudinal section shows that the lement is composed by a crown and a basal body. Following pictures consist of a SRXTM renderings of the initial two growth layers of basal body and the relationship between the crown (red) and the basal body (blue, purple, green). The growth of the basal body continues as in elements of the paraconodont *Furnishina*, but with addition of crown tissue (adapted from *Murdock et al., 2013*).

It is possible to distinguish between three grades of paraconodont elements on the base of the degree of tissue differentiation. The simplest grade consists on a single tissue type that exhibits punctuated incremental growth lines which define hollow conical laminae extending around the entire proximal margin and partly around the antapical margins. Lamellae are oblique to the outer surface of the element and they do not extend over the distal tip, the protoelement, that is not enveloped by successive laminae. The second grade of organization is characterized by two type of tissue. The distal part of the element is formed of conical laminae and the proximal

part is formed of subsequent laminae extending across the entire proximal surface, forming a series of sub-parallel laminae-extension of the laminae comprise the rest of the element. The third grade is characterized by three principal tissue layers. The outermost consist of tapering rings that do not extend fully over the outer surface nor are they continuous over the proximal surface. These outer layers are bordered on the inside of the proximal surface by subparallel lamellae and it is unclear if they converge to the apex. The basal cavity is filled with spheritic mineralization (*Murdock et al., 2013*).

Euconodont elements (Fig. 1.4.2) exhibit a clear distinction between the ialine tissue, transparent, the albid tissue, matt and white, both components of the crown, and the basal body tissue, rarely preserved and less mineralized. These tissues, in living animals, probably contained different amount of organic matter and are characterized by different dimensions of apatite crystals, that are bigger in the ialine tissue of the crown (from less than 1 μm to more than 30 μm). Following initial mineralization of the primordial element, subsequent laminae are added to the proximal margins. The basal body is differentiated into two tissue layers, distal hollow conical laminae and subparallel laminae across the proximal surface. The crown tissue forms a cap over the entire surface of the basal body (Fig. 1.4.3), thickening towards an enlarged cusp (*Pietzner et al., 1968; Murdock et al., 2013*).
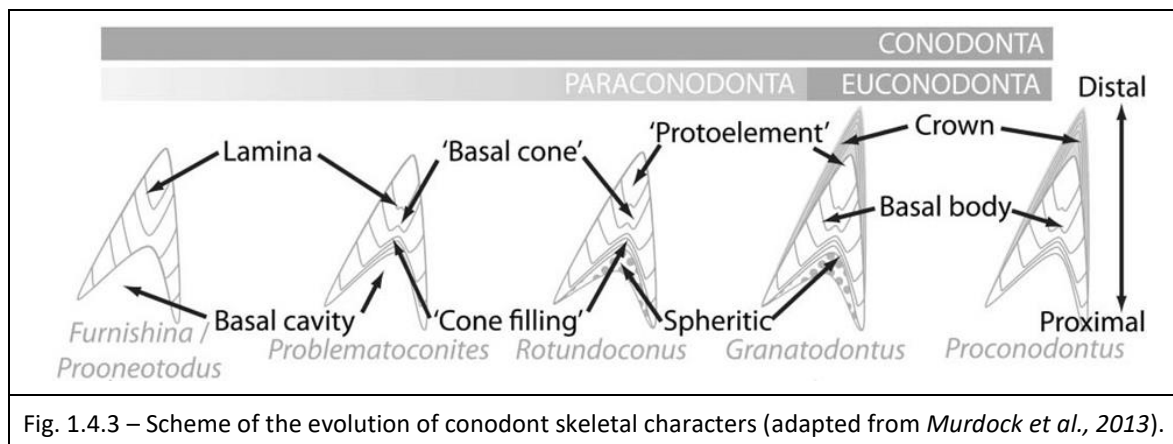
Fig. 1.4.3 – Scheme of the evolution of conodont skeletal characters (adapted from *Murdock et al., 2013*).

Galeaspids are a group that exhibits an anatomy that is superficially similar to the osteostracans. Galeaspids appear to primitively lack paired fins and easily discriminated from osteostracans by the presence of a large rostral olfactory opening in the cranial dermoskeleton. It is possible to distinguish between a cranial and a postcranial dermoskeleton. The first one is composed of two or more large plates that are probably fused together in the branchial area of the animal. The skeleton is composed of acellular bone and is also present an internal unmineralized cartilaginous endoskeleton, lined with perichondrally ossified acellular bone (*Janvier, 1990; Min & Janvier, 1998*).

The heterostracomorphs are dominated by the heterostracans, which are characterised by a cephalotoracic dermal skeleton composed of two or more large plates that enclose the body. Some of the plates are fused together but, more frequently, they grow one in front to the other. Dermoskeleton of trunk and tail is composed of diamond or lath-shaped overlapping scales. All elements of the dermoskeleton are composed of a superficial layer of dentine, acellular bone,

and in some taxa, enameloid, arranged in discrete tubercles or ridges. This overlies a middle stratus of acellular bone that exhibits a spongy texture organized into discrete osteons onto which the pulp cavities of the superficial layer open. Also the basal layer is composed of acellular bone arranged in sheets that join the osteons (*Donoghue & Sansom, 2002*).

Osteostracans include a wide range of anatomical designs, including forms with and without paired pectoral fins. They are characterized by a completely fused head capsule composed of dentine and cellular bone. Osteostracans are one of the few groups of jawless vertebrates with a mineralized endoskeleton which is limited to head and shoulder girdle and is composed of unmineralized and mineralized cartilage lined with cellular perichondral bone (*Stensiö, 1927*).

Thelodonts possess a dermoskeleton of numerous minute scales, similar to those of sharks. Individual scales are composed of dentine and acellular bone. Some thelodonts also exhibit a skeleton composed of minute scales lining the buccopharynx and associated with the gills (*Van der Brugghen & Janvier, 1993; Donoghue & Smith, 2001*). Theleodonts possess paired pectoral appendages.

Chondrichthyans (sharks and rays), actinopterygians (ray-finned fishes) and sarcopterygians (lungfishes, coelacanths and tetrapods) are the basal living groups of jawed vertebrates an all of the animals included within these groups possess an axial and appendicular endoskeleton.

Chondrichthyans possessed a dermal skeleton composed of microscopic scales (Fig. 1.4.4) growing from single dental papillae as in teeth. Endoskeleton is cartilaginous, although some living groups exhibit perichondral bone lining the cartilage. Fossils remains suggest that among the oldest known chondrichthyans, there were specimens without teeth (*Sansom et al., 1996, 2001*).
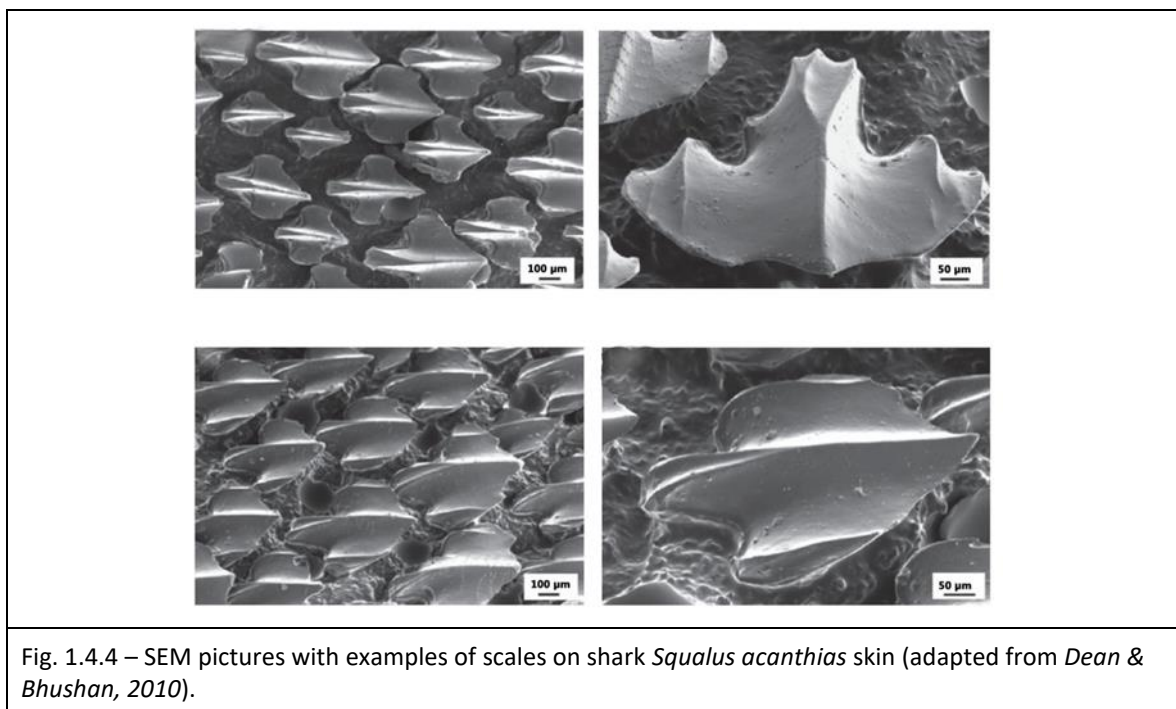

Fig. 1.4.4 – SEM pictures with examples of scales on shark *Squalus acanthias* skin (adapted from *Dean & Bhushan, 2010*).

Primitive osteichthyans, such as *Polypterus* and *Latimeria*, possess a dermal skeleton including growing scales that are composed of numerous dental units that are added in succession and teeth that are replaced from below (like in humans). The primitive endoskeleton is heavily skeletonized, but more derived members of the clade, particularly among actinopterygians, exhibit evidence of secondary reduction in calcification of the skeleton (*Donoghue & Sansom, 2002*).

There are two principal extinct groups of jawed vertebrates: acanthodians and placoderms. The jawed dermoskeleton of acanthodians consists of a trunk and a tail composed by diamond-shaped scales whereas the cranial dermoskeleton is formed by mineralized plates. Dermoskeleton also includes fin spines. Teeth are present only in ischnacanthids, a subgroup of acanthodians. Ischnacanthids had two types of teeth: symphyseal tooth whorls and marginal jaw-borne teeth (*Ørvig, 1973; Denison, 1978*). All the elements of the dermoskeleton and all the teeth are composed of dentin and cellular bone; enamel-like tissues were never found (*Richter & Smith, 1995*). Endoskeleton is composed of cartilage, lined with perichondral bone and permeated by endochondral bone.

Placoderms possess a dermal skeleton that has two divisions. The trunk and the tail skeletons are composed of diamond-shaped scales, while cranial and immediately postcranial skeleton is fused in a head capsule composed of a number of large plates united by scarf joints. The dermoskeleton is composed by dentine and cellular bone. Teeth or tooth like tissues are not evident, except for small dentine tubercles present on the lingual margin of the jaw bone in some taxa (*Ørvig, 1980*). The jaw bone provides a self-sharpening biting surface. Endoskeleton includes an ossified perichondrally brain case, often having distinct sensory capsules (*Denison, 1978*).

In general, bone and dentin were always found together in most dermal skeletal elements and their histological characteristics were similar to those of modern vertebrates. This means that specialized cells, osteoblast/osteocytes and odontoblasts, the regulatory gene networks, the specific proteins of their organic matrix and the mineral (hydroxyapatite) appeared early in vertebrates and did not change drastically for more than 460 Ma. In addition, bone and dentin are often associated with an hyper-mineralized, covering tissue (enamel or enameloid) (*Sire & Kawasaki, 2012*).

1.5 - Fossilization and diagenesis

Bioapatite persists over long time in fossilized form recording information about paleoenvironment and past life. Changes occurring to biological remains (not only those phosphatic) after death and burial are commonly referred as *diagenetic transformation* (*Lee-Thorp, 2002*). These processes are not yet fully understood for phosphatic material, but several data suggest that the original properties of bioapatites strongly influence the way in which they are preserved. Anyway, the vast majority of mineralized tissues is destroyed relatively quickly, especially if exposed to acid environments, strong solar radiation, alternate wet and dry conditions or invasion by micro-organisms (*Sillen, 1989*).

It is possible to distinguish between an *early* and a *late phase of diagenesis* (Fig. 1.5.1). For bones, early diagenesis usually refers to the initial alteration of bone once introduced into the diagenetic environment, although there is some ambiguity regarding the timing of this period (*Trueman et al., 2008a, 2008b*). Early diagenetic processes include removal of soft tissues like muscles and skin, the degradation of collagen and the first chemical and structural changes to the mineralized component, ultimately resulting in decomposition or eventually in preservation (*Greenlee, 1996; Sponheimer & Lee-Thorp, 1999*). The removal of organic compounds and in particular of collagen represents a crucial stage for the beginning of the interactions between fluids circulating in sediment and phosphatic remains (and thus bioapatite lattice) as increases the area of the exposed phosphatic surface. Migration of fluids from the surrounding environment facilitates the substitution of ions in bioapatite leading to a more stable phase (*Hinz & Kohn, 2010*). Late diagenetic alteration includes further structural and chemical changes with the complete transformation of the original bone.

Fig. 1.5.1 – Schematic view of diagenesis of a skeletal remain. a-b: Following the death, bones may be deposited with the same system occupied in life. c: The activity of scavengers, microorganisms and physical processes may remove some of the bones leading to an incomplete fossil record. Burial and diagenesis enhance preservation potential transforming bones in fossils. d: Erosion of sediments may bring the fossil bone back to the surface (adapted from *Keenan, 2014*).

After the death of the organism, the "lattice flexibility" of bioapatite may accommodate several types of iso- and hetero-valent substitutions at all ionic sites (*Trueman, 1999; Nielsen-Marsh & Hedges, 2000*). There are two distinct Ca sites (or types) within the apatite lattice, differentiated based on shared bonds with neighbouring oxygen atoms. In modern bone, Ca type I is in nine-fold coordination with oxygens from PO_4^{3-} and Ca type II is in seven-fold coordination with oxygens and anionic sites OH^-. In particular, during diagenesis, CO_3^{2-} ions are incorporated into the lattice and form a carbonate-enriched apatite phase largely at the expense of PO_4^{3-}. This forms type B carbonate associated with the type I Ca sites. Type A carbonate associated with the type II Ca sites forms from OH^- substitutions (*Sponheimer & Lee-Thorp, 1999; Trueman et al., 2008a*). Alteration of type A to type B carbonate usually increases the crystallinity (*Hassan et al.,*

1977; Tuross et al., 1989; Weiner et al., 1993; Person et al., 1995; Sponheimer & Lee-Thorp, 1999a) affecting bone dissolution rates (*Trueman et al., 2008*). The increase can apparently occur very quickly and in the absence of environmental promoters; it is a spontaneous process which produce a well crystallized material starting from a poorly one conferring high stability in time. In addition to the crystal growth, recrystallization and dissolution may provide a route for the introduction of "external" ions from surrounding environment.

Because of the initial reactivity, bone apatite is most vulnerable during the early phase of diagenesis, when dissolution and recrystallization are most probable. With the increase of crystallinity, the mineral becomes more resistant, although subsequent cycles of dissolution may occur. An exception is the enamel as it is more crystalline and stable than bone, so possibilities for recrystallization and crystal growth are greatly reduced. Ionic and isotopic exchange, however, may continue in both tissues over long timescales (*Lee-Thorp, 2002; Hassan et al., 1977*). Diagenesis frequently results in an extreme variability of chemical composition of fossilized bones (*Trueman, 1999; Goodwin et al., 2007*) although the vast majority of fossil bioapatite is represented by fluorine- and/or carbonate-enriched (*Sponheimer & Lee-Thorp, 1999; Trueman, 1999; Berna et al., 2004*). More in detail, major and trace elements composition is highly site specific, and varies even within a single bone or between bones preserved at the same site (*Trueman & Benton, 1997; Suarez et al., 2010*).

Diagenesis can also drive the addition of other phosphatic and/or non-phosphatic minerals, such as pyrites, silicates and carbonates, in pores and in spaces freed up by the decomposition of the organic matrix. Like for substitutions, the formation of "extra-apatitic" minerals is more likely to occur in porous bones and dentin than in highly mineralized enamel (*Suarez et al., 2010*).

Collagen, as mentioned before, is a very important component of bone and plays a critical role in the transformation of mineralized tissue after death. Collagen is removed through autolytic or biologic activity (*Grupe, 1995; Balzer et al., 1997; Collins et al, 2002; Leikina et al., 2002; Jans et al., 2004*), causing pores spaces opening in bone, where fluids, dissolved ions and microorganisms can move, facilitating the alteration of bioapatite crystallites. *In vitro* studies on collagen demonstrates that the molecule can begin to alter if exposed to varying temperatures (*Leikina et al., 2002*). Relaxation of the triple helix structure of the type I collagen may drive to further decomposition reactions. Moreover, collagen tends to swell in aqueous solutions, that can explain fracturing observed in bones deposited in aqueous environments (*Pfretzschner, 2004*). The consequence is a significant difference in the conservation of the fossil remains when the burial site and climatic conditions change.

Microorganisms, like bacteria and fungi, have been implicated in bone breakdown in the fields of archaeology and palaeontology, because they actively scavenge the carbon and nitrogen-rich constituent amino acids forming the complex collagen molecule (*Child, 1995; Jans et al., 2004; Jans, 2008*). It has been hypothesized that the first line of attack of collagen can be constituted by microbial communities specialized in the production of a collagenolytic proteases (*Watanabe, 2004*). Bones do not increase in the severity or frequency of microbial attack with duration of burial at least in a time scale of 4000 years or more but an accurate measure is impossible as there is a great variability also within a single bone and within different bones in the same site

(*Hedges, 2002*). However, some evidences suggested that the microbial alteration is probably established in considerably less than 500 years, so in the early phase of diagenesis, although evidence for recently buried bones suggest that it may not be immediate (i.e, it does not occur in the first three or four decades after burial, *Nielsen-Marsh, 1997*). Abnormal low temperatures environments, permanently waterlogged sites, that are anoxic, show very little microbial alteration (*Bocherens et al., 1997*) and also stained areas (from humic acid, perhaps) or very dry environments are more immune (*Hedges, 2002*).

Dissolution can dramatically affect bones, in particular in sites where water circulation is more active. The overall rate of dissolution depends on the concentration gradient around the bone, which, in turn, is dependent on the soil water composition (*Pike et al., 2001*). Neutral pH soils usually have calcium and phosphate concentrations close to the saturation with respect to the hydroxyapatite. In consideration of the possible variation over time in the geochemical composition of the soil, sediments and of the interstitial and pore waters (as well as of other chemical parameters such as, for example, Eh, pH), the dissolving processes can be extremely variable and non-constant in time (*Kenaan, 2014*).
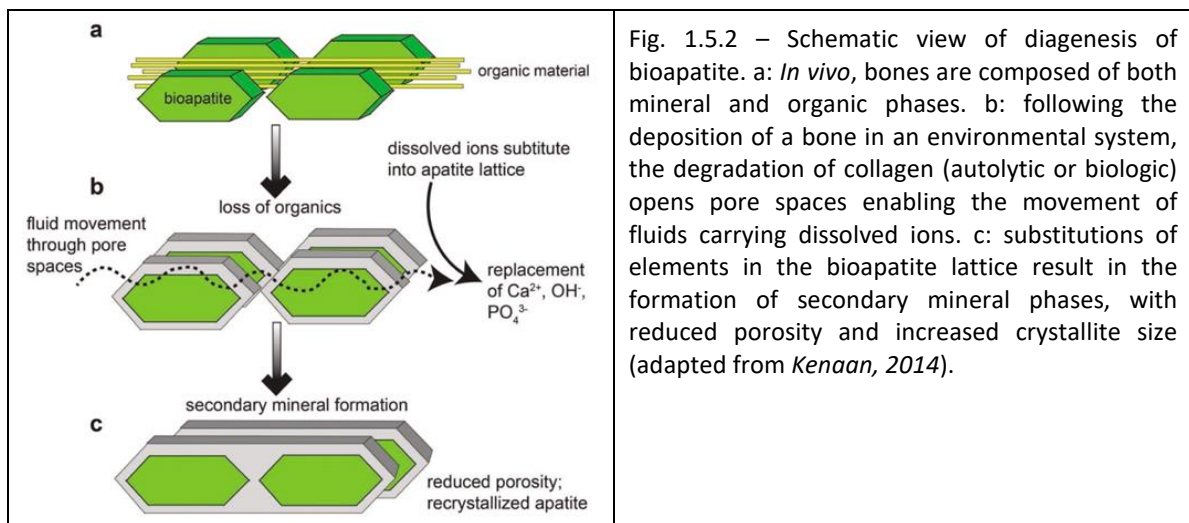
Fig. 1.5.2 – Schematic view of diagenesis of bioapatite. a: *In vivo*, bones are composed of both mineral and organic phases. b: following the deposition of a bone in an environmental system, the degradation of collagen (autolytic or biologic) opens pore spaces enabling the movement of fluids carrying dissolved ions. c: substitutions of elements in the bioapatite lattice result in the formation of secondary mineral phases, with reduced porosity and increased crystallite size (adapted from *Kenaan, 2014*).

CHAPTER II

Materials and methods

2.1 - Samples

This Ph.D. study has analysed fossils, alive and dead remains of apatite biomineralizing organisms, both vertebrates and invertebrates, ranging from the Cambrian to the Recent, a time-lapse spanning over 500 million years. We detected the bioapatite crystal chemistry of the major phosphatic phyla (brachiopods, arthropods, bryozoans, and chordates: the latter including conodonts, cartilaginous and bony fishes, amphibians, reptiles, sauropods, birds and mammals). The main taxonomic groups were investigated using either fossil or recent material (dead and alive, the latter referring to material extracted from living organisms). Moreover, other phosphatic "enigmatic organisms" such as conodont pearls or enigmatic rings were considered as well.

The samples collected for this thesis are reported in Tabs. 1-2 (end of this chapter) and Tab. 1 SOM (annex-6 to Chapter V). Tab. 1 reports samples classified but not yet analysed, Tab. 2 samples analysed, but not yet discussed, Tab. 1 SOM samples fully characterized and discussed. Basic information about each sample are reported in each table, whereas the method of collection and preparation of groups with common characteristics are synthetically described below (paragraph 2.2). A photographic atlas of just a part of the collection is reported in Plates 1, 2, 3, 4 and 5 at the end of the thesis. A creation of such a large and varied collection of phosphatic remains was possible only thanks to the collaboration of other researchers and friends.

Below will be reported some general information relating to the samples belonging to the taxa perhaps less known at a general level (for example conodonts, bryozoans, etc.). Regarding the most common ones (for example mammals, reptiles, etc.), please refer to the numerous literatures also available in open access mode.

Conodont elements

Among samples considered in this research, 98 belong to conodonts, an extinct group of jawless vertebrates. Tooth-like elements from the feeding apparatus of this organisms are the remains that were collected and studied from these organisms. The entire stratigraphic range of conodonts (late Cambrian to Late Triassic) is covered by this study.

Conodonts under investigation are comprehensive of both paraconodonts, more ancient and with a simpler structure, and euconodonts, having a more complex architecture (see chapter 1, paragraph 1.4). Different species, age, provenience, location in the apparatus and different CAI was considered when selecting samples.

Bryozoans

Are aquatic invertebrates, usually diffused in tropical marine waters (with some exceptions). They are filter feeders, commonly colonial. Mineralized skeletons of bryozoans first appear in

rocks from the Early Ordovician. Among our samples, we have collected 6 phosphatized undetermined specimen of bryozoans.

Brachiopods

We have considered 19 brachiopods for this work. They are animals with two valves, shells that protect the upper and the lower part of their body. Brachiopod valves are hinged at the rear end, while the front can be opened for feeding or closed for protection. The Phylum appears in the Early Cambrian and is still well represented by living species.

2.2 – Sample preparation

Samples processed in this study are extremely different in dimension (from less than a mm to various centimetres long) and physical properties, like hardness or fragility. As a consequence, a wide range of analytical techniques has been necessarily applied. Preparation methods that have been adopted are sometimes "unusual"; even if they have been detailed in the published papers, the most common are described below.

Selective acid dissolution

This is a quite standardized procedure of micropaleontology used when phosphatic or siliceous microfossils are incorporated in calcareous rocks. Weak acids are used to dissolve the rock matrix and "to free" the phosphatic residue. Acetic acid (CH_3COOH) is commonly in use for the procedure. It is diluted and buffered with calcium carbonate in order to prevent damages to the fossils. Another possibility is to use formic acid (HCOOH) even if it is more aggressive than the first one. The advantage is that less time is required to process the rocks, the disadvantage is the risk of damages on fossils.

The first step of the procedure is the removal of the altered surface of the rocks. Then, sample must be weighed, fragmented and put inside sieves with large holes. The sieves are placed inside buckets that are filled with a solution of water and acid at 10%. Every rock fragment must be totally covered by the solution. Bucket are put under a fume hood for 2 days, a time usually adequate to gain a first dissolution of the carbonate matrix. When the reaction is complete, fresh acid solution must be added again up to total dissolution (i.e., when the residue stops reacting with the acid). The residue is washed with water in a sieve to further remove the finest fraction (clay), reposed on a filter paper and dried. When the residue is dry, it can be observed or, if it is too abundant, it can be added to a solution of sodium polytungstate (density of 2,8 g/cm^3). As "conodont density" is about 3 g/cm^3 they may be separated from the lighter materials. This is a way to differentiate a heavier fraction, with conodont elements, and a lighter fraction with, for example, siliceous remains.

As you can guess, it is not uncommon to lose or damage the material during this procedure, which is why large quantities (several kg) of rock are usually dissolved. The so-called "conodont pearls" were obtained in the same way.

Picking

Picking is a classical technique of micropaleontology that consists in a manual separation under the microscope of the microfossils from the rest of the residue obtained through the acid digestion. For this procedure the use of a little metal container with different areas drawn inside, a thin brush, a series of proper sample-holders called "slides", water-soluble glue, a little amount of water and, most important, a stereo microscope with magnification usually of 1,6x and 4x is requested. A little amount of residue is put in the metal container and the recovered microfossil (conodont, brachiopod, pearl, etc.) is transferred into a slide using a fine paintbrush. Selected fossils are then moved into a second clean slide where a thin layer of glue was preliminarily placed. Fossils must be placed in an ordered way (such as position in the apparatus for conodonts). The glue is necessary to keep the fossils in place but it is possible to move away the elements very easily using a drop of water that dissolves the water-soluble glue.

Sample "slice" preparation

Sometimes it is necessary to cut samples in order to analyse the internal portion. To do that, it is a best practice to incorporate and thus block sample into epoxy resin before cutting the slice with a circular or a wire saw. For this work, two types of saws were used depending on the dimensions and the shape of the samples. a circular table saw (model Isomet 11-1180 low speed saw, from Buehler LTD) and a wire saw with a diamond coated wire (model AGB9001, from Agar Scientific). Samples were cut in order to expose the part that are interesting to analyse. Both these saws can make precise cuts, avoiding the removal of big portion of the sample, and are instruments easy to use. The circular table saw was generally use for sample from less than 1 cm until about 4-5 cm. The wire saw was used for sample bigger than 5 cm. Saws can be use also to remove useless portions of resin normally present around the sample to reduce its dimensions.

Depending on the measurement to carry out the cut surfaces may be polished or not with a lapping machine with different sizes of grinders. After polishing the micro-residues of abrasive can be removed in a ultrasonic bath.

"Fresh" sample preparation

Some of the samples we collected, such as bones and teeth from living organisms, still had high amounts of organic matter. Therefore, these samples were prepared following a non-standard procedure, but trying to find the best way to remove all the organic matter without damaging chemically or physically the phosphatic structures. This was quite simple for teeth, but not so easy for bones which may contain remains of marrow, blood and bone cells. Since there is no known standard procedure to remove these organic parts, we have experimented a double approach. More in detail on a fragment of femur (sample B17, Tab. 1 SOM) used as a test we have:

i) treated with H_2O_2 until the reaction with the organic matter was exhausted. After that, it has been dried in stove, incorporated in resin, sectioned and polished (sample B17-A).

ii) boiled in Millipore water until the organic remains are detached. Therefore, the residue was dried in stove and processed like described above (sample B17-B).

Samples from B56.1 to B56.21 (Tab. 2) were acquired as frozen shark heads; the focus was to extract from them the jaws in order to obtain and analyse some teeth for every sample. Data

about dimension, gender and sexual maturity have been provided by the donor. Heads have been previously unfrozen in hot water, that has also the function of making the tissues very fragile and easy to separate from the bones. Jaws has been extracted using a scalpel and organic tissues residues were eliminated washing the jaws in hot water and after air dried. The same was done for samples from B55.1 to B55.9, but with the aim to analyse teeth and scales. Every sample was measured, gender and sexual maturity were determined following the indication of *Carbonara & Fellosa, 2019* (Tab. 2)

Three teeth were separated in both sets of samples using a stereo microscope and mounted on a stub with a carbon tab for microscopic and X-ray diffractometric measurements.

2.3 - Instruments

One of the strengths of this thesis is the multi-analytical and multidisciplinary approach applied for the characterization of the various phosphatic organisms. This method allowed to describe diagenetic crystals in term of size, morphology, composition, geometry and spatial arrangement. The instruments used will be briefly described below, while for details about experimental condition please see the articles attached to chapters 3, 4 and 5. With the exception of X-ray micro-diffractometer, all the instruments are available at the Centro Interdipartimentale Grandi Strumenti (CIGS) or at the Dipartimento di Scienze Chimiche e Geologiche (DSCG), both at the University of Modena and Reggio Emilia, Italy.

Optical stereo-microscope

Stereo-microscope was used both to separate and collect samples (picking, see paragraph 2.2) and to characterize samples morphology.

(Environmental) Scanning Electron Microscope (ESEM/SEM)

Most samples, especially the smaller ones, were characterize under optical and electron microscopy. Specimens were mounted on aluminium stubs previously covered with carbon-conductive adhesive tape. Au-coated (SEM) and non-coated (ESEM) samples were observed using an Environmental Scanning Electron Microscope (ESEM) FEI ESEM-Quanta 200, equipped with an Oxford EDX INCA 300 X-ray energy dispersive spectrometer and by a Scanning Electron Microscope (SEM) Nova NanoSEM FEI 450 equipped with a XEDS Bruker QUANTAX-200 detector. ESEM observations were performed in high and low vacuum (low vacuum brackets 1 and 0.5 Torr) with an accelerating voltage usually ranging between 5 and 25 keV for imaging and between 5 and 15 keV for elemental analyses. SEM observations were in high vacuum with an accelerating voltage between 15 and 25 keV for imaging and between 15 and 25 keV for elemental analyses.

X-ray diffractometer (XRDP)

The X-ray diffraction powder (XRPD) patterns were collected from randomly oriented grain mounts at ambient and non-ambient temperature conditions using a Philips X'Pert PRO diffractometer (PANalytical B.V., Almelo, The Netherlands) equipped with an X'Celerator

detector and HTK16 Anton Paar in situ heating apparatus (Anton Paar Korea Ltd., Seoul, Republic of Korea). Typical experimental conditions were: Cu $K\alpha$ radiation at 40 kV and 40 mA, with a Ni filter, 0.04 rad Soller slits, a 20 mm anti-scatter mask, a ¼° anti-scatter slit, and a ¼° divergence slit. The diffracted beam conditions were as follows: X'Celerator X-ray detector with a position sensitive detector (PSD), a 5.0 mm anti-scatter mask, 0.04 rad Soller slits, and a 30 s integration time in a continuous scan with a PSD length of 2.12 °(2θ).

X-ray micro-diffractometer (µ-XRD)

The model that has been used was D-max Rapid from Rigaku. The instrument is equipped with Cu$K\alpha$ source operating at 40 kV and 30 mA, curved-image-plate detector, flat graphite monochromator, variety of beam collimators, motorised stage, that allows rotation Φ and revolution ω angular movements, and microscope for accurate positioning of the sample. Analyses with this instrument have been performed at the Institute of Methodologies for Environmental Analysis of the National Research Council of Italy (CNR-IMAA), at Tito Scalo, Potenza, Italy. In *Ferretti et al., 2017* (not part of this thesis) our research group applied X-ray microdiffraction on a group of conodonts from Late Ordovician for the first time. The fossils were characterised by the occurrence of diagenetic crystals and overgrowth on the surfaces.

Laser ablation inductively coupled plasma mass spectrometer (LA-ICP-MS)

The laser ablation (LA) model that have been used was UP 213 from New-wave. It has a motorised variable zoom from 5.6X to 36X optical magnification, a motorised stage with 52 mm of movement in X and Y directions, spot sized from a minimum of 4 µm to a maximum of 110 µm and the possibility to lightening the sample with reflect or transmitted light. It is coupled with the inductively coupled plasma mass spectrometer (ICP-MS) XSeries[II] ICP-MS from Thermo Electron Corporation.

Chemical analyses

Perkin Elmer ICP-OES DA 4500 (Perkin Elmer Optima 4200 DV), after calibrating with certified standard solutions, was employed to measure major elements on acid digested samples. Major elements measurements also were carried out on powder pressed pellets through a wavelength dispersive Philips PW 1480 X-ray fluorescence (XRF) spectrometer; concentrations were corrected considering matrix effect and loss on ignition (obtained from thermogravimetric measurements – see below).

Termogravimetry coupled with evolved gas mass spectrometry

Thermal analyses measurements were carried out with a Seiko SSC 5200 thermal analyser coupled with a quadrupole mass spectrometer (ESS, GeneSys Quadstar 422), which allowed the analyses of gasses evolved during thermal reactions. Gas sampling by the spectrometer was via an inert, fused silicon capillary system, heated to prevent gas condensing. Typical experimental conditions were: heating rate: 20 °C/min; heating range: 25-1250 °C; data measurement: every 0.5 s; purging gas: ultrapure helium, flow rate: 100 µL/min.

Tab. 1: samples collected but not yet analysed. D (dead), F (fossil), A (alive), see Chapter V for further details.

CODE	PHYLUM (Subphylum)/Class/Order	TAXONOMIC ASSIGNMENT	BONE (B), TEETH (T), SHELL (S), OTHER (O)	AGE	D / F / A
B12	BRYOZOA	undetermined	O	(unknown)	F
B18	CHORDATA/Chondrichthyes	undetermined	T	(unknown)	F
B20	CHORDATA/Chondrichthyes/Lamniformes	undetermined	T	(unknown)	F
B22	CHORDATA/Mammalia/Primates	*Homo sapiens* (Linnaeus, 1758)	T	Recent (2018)	A
B26	CHORDATA/Chondrichthyes/Lamniformes	*Otodus* sp.	T	Eocene	F
B27	CHORDATA/Chondrichthyes/Lamniformes	*Otodus* sp.	T	Eocene	F
B28	CHORDATA/Chondrichthyes/Lamniformes	*Squalicorax* sp.	T	Late Cretaceous	F
B29	CHORDATA/Chondrichthyes/Lamniformes	*Otodus* sp.	T	Eocene	F
B30	CHORDATA/Chondrichthyes/Lamniformes	*Otodus* sp.	T	Eocene	F
B31	CHORDATA/Chondrichthyes/Lamniformes	*Otodus* sp.	T	Eocene	F
B33	CHORDATA/Chondrichthyes/Lamniformes	*Otodus* sp.	T	Eocene	F
B38.2	CHORDATA/Mammalia/Artiodactyla	*Sus scrofa domesticus* Linnaeus, 1753	T, B	Recent (2018)	D
B38.3	CHORDATA/Mammalia/Artiodactyla	*Sus scrofa domesticus* Linnaeus, 1754	T, B	Recent (2018)	D
B38.4	CHORDATA/Mammalia/Artiodactyla	*Sus scrofa domesticus* Linnaeus, 1755	T, B	Recent (2018)	D
B38.5	CHORDATA/Mammalia/Artiodactyla	*Sus scrofa domesticus* Linnaeus, 1756	T, B	Recent (2018)	D
B38.6	CHORDATA/Mammalia/Artiodactyla	*Sus scrofa domesticus* Linnaeus, 1757	T, B	Recent (2018)	D
B38.7	CHORDATA/Mammalia/Artiodactyla	*Sus scrofa domesticus* Linnaeus, 1758	T, B	Recent (2018)	D
B38.8	CHORDATA/Mammalia/Rodentia	undetermined	B	Recent (2018)	D
B38.9	CHORDATA/Mammalia/Artiodactyla	*Sus scrofa domesticus* Linnaeus, 1758	T, B	Recent (2018)	D
B48	CHORDATA/Mammalia/Artiodactyla	*Sus scrofa* Linnaeus, 1758	B	Pleistocene	F
B49	CHORDATA/Mammalia/Artiodactyla	undetermined (Bovidae)	B	Pleistocene	F
B50	CHORDATA/Mammalia/Proboscidea	*Elephas maximus* Linnaeus, 1758	B	Recent	D
B51	CHORDATA/Chondrichthyes/Carcharhiniformes	*Galeocerdo cuvier* (Péron & Lesueur, 1822)	T	Recent	D
B52	CHORDATA/Mammalia/Carnivora	*Ursus spelaeus* Rosenmüller, 1794	T	Pleistocene	F
B53	CHORDATA/Mammalia/Carnivora	*Martes foina* (Erxleben, 1777)	B	Recent (2014)	D
B55.1	CHORDATA/Chondrichthyes/Carcharhiniformes	*Scyliorhinus canicula* (Linnaeus, 1758)	T, O	Recent (2019)	D
B55.2	CHORDATA/Chondrichthyes/Carcharhiniformes	*Scyliorhinus canicula* (Linnaeus, 1758)	T, O	Recent (2019)	D
B55.3	CHORDATA/Chondrichthyes/Carcharhiniformes	*Scyliorhinus canicula* (Linnaeus, 1758)	T, O	Recent (2019)	D
B55.4	CHORDATA/Chondrichthyes/Carcharhiniformes	*Scyliorhinus canicula* (Linnaeus, 1758)	T, O	Recent (2019)	D
B55.5	CHORDATA/Chondrichthyes/Carcharhiniformes	*Scyliorhinus canicula* (Linnaeus, 1758)	T, O	Recent (2019)	D
B55.6	CHORDATA/Chondrichthyes/Carcharhiniformes	*Scyliorhinus canicula* (Linnaeus, 1758)	T, O	Recent (2019)	D
B55.7	CHORDATA/Chondrichthyes/Carcharhiniformes	*Scyliorhinus canicula* (Linnaeus, 1758)	T, O	Recent (2019)	D
B55.8	CHORDATA/Chondrichthyes/Carcharhiniformes	*Scyliorhinus canicula* (Linnaeus, 1758)	T, O	Recent (2019)	D
B55.9	CHORDATA/Chondrichthyes/Carcharhiniformes	*Scyliorhinus canicula* (Linnaeus, 1758)	T, O	Recent (2019)	D
B56.1	CHORDATA/Chondrichthyes/Carcharhiniformes	*Galeus melastomus* (Rafinesque, 1810)	T	Recent (2019)	D
B56.2	CHORDATA/Chondrichthyes/Carcharhiniformes	*Galeus melastomus* (Rafinesque, 1810)	T	Recent (2019)	D
B56.3	CHORDATA/Chondrichthyes/Carcharhiniformes	*Galeus melastomus* (Rafinesque, 1810)	T	Recent (2019)	D
B56.4	CHORDATA/Chondrichthyes/Carcharhiniformes	*Galeus melastomus* (Rafinesque, 1810)	T	Recent (2019)	D
B56.5	CHORDATA/Chondrichthyes/Carcharhiniformes	*Galeus melastomus* (Rafinesque, 1810)	T	Recent (2019)	D
B56.6	CHORDATA/Chondrichthyes/Carcharhiniformes	*Galeus melastomus* (Rafinesque, 1810)	T	Recent (2019)	D
B56.7	CHORDATA/Chondrichthyes/Carcharhiniformes	*Galeus melastomus* (Rafinesque, 1810)	T	Recent (2019)	D
B56.8	CHORDATA/Chondrichthyes/Carcharhiniformes	*Galeus melastomus* (Rafinesque, 1810)	T	Recent (2019)	D
B56.9	CHORDATA/Chondrichthyes/Carcharhiniformes	*Galeus melastomus* (Rafinesque, 1810)	T	Recent (2019)	D
B56.10	CHORDATA/Chondrichthyes/Carcharhiniformes	*Galeus melastomus* (Rafinesque, 1810)	T	Recent (2019)	D
B56.11	CHORDATA/Chondrichthyes/Carcharhiniformes	*Galeus melastomus* (Rafinesque, 1810)	T	Recent (2019)	D
B56.12	CHORDATA/Chondrichthyes/Carcharhiniformes	*Galeus melastomus* (Rafinesque, 1810)	T	Recent (2019)	D
B56.13	CHORDATA/Chondrichthyes/Carcharhiniformes	*Galeus melastomus* (Rafinesque, 1810)	T	Recent (2019)	D
B56.14	CHORDATA/Chondrichthyes/Carcharhiniformes	*Galeus melastomus* (Rafinesque, 1810)	T	Recent (2019)	D
B56.15	CHORDATA/Chondrichthyes/Carcharhiniformes	*Galeus melastomus* (Rafinesque, 1810)	T	Recent (2019)	D

B56.16	CHORDATA/Chondrichthyes/Carcharhiniformes	*Galeus melastomus* (Rafinesque, 1810)	T	Recent (2019)	D
B56.17	CHORDATA/Chondrichthyes/Carcharhiniformes	*Galeus melastomus* (Rafinesque, 1810)	T	Recent (2019)	D
B56.18	CHORDATA/Chondrichthyes/Carcharhiniformes	*Galeus melastomus* (Rafinesque, 1810)	T	Recent (2019)	D
B56.19	CHORDATA/Chondrichthyes/Carcharhiniformes	*Galeus melastomus* (Rafinesque, 1810)	T	Recent (2019)	D
B56.20	CHORDATA/Chondrichthyes/Carcharhiniformes	*Galeus melastomus* (Rafinesque, 1810)	T	Recent (2019)	D
B56.21	CHORDATA/Chondrichthyes/Carcharhiniformes	*Galeus melastomus* (Rafinesque, 1810)	T	Recent (2019)	D
B57	ANNELIDA/Polichaeta/Aciculata	*Hermodice carunculata* (Pallas, 1766)	O	Recent (2018)	A
B58	CHORDATA/Chondrichthyes/Hybodontiformes	*Ptychodus whipplei* Marcou, 1858	T	Late Cretaceous (Turonian)	F
B59	CHORDATA/Reptilia/Testudines	*Caretta caretta* Linnaeus, 1758	B	Recent	D
B60	CHORDATA/Amphibia/Anura	*Hoplobatrachus rugulosus* (Wiegmann, 1834)	B	Recent (2019)	D
B61	CHORDATA/Reptilia/Crocodylia	*Crocodylus niloticus* Laurenti, 1768	T	Recent	D
B62	CHORDATA/Aves/Galliformes	*Gallus gallus domesticus* (Linnaeus, 1758)	B	Recent (2019)	D
51	CHORDATA/Conodonta/Prioniodontida	*Amorphognathus* sp. (Pb)	O	Late Ordovician (Katian)	F
102	CHORDATA/Conodonta/Protopanderodontida	*Scabbardella altipes* (Henningsmoen, 1948)	O	Late Ordovician (Katian)	F
P01	?	? Conodont pearl	O	Silurian (Ludlow, latest Gorstian-early Ludfordian)	F
P03	?	?Conodont pearl	O	Silurian (Ludlow, latest Gorstian-early Ludfordian)	F
P05	?	?Conodont pearl	O	Silurian (Ludlow, latest Gorstian-early Ludfordian)	F
P09	?	undetermined skeletal element		Silurian (Ludlow, latest Gorstian-early Ludfordian)	F
P11	?	?Conodont pearl	O	Silurian (Ludlow, latest Gorstian-early Ludfordian)	F
P13	?	undetermined skeletal element		Silurian (Ludlow, latest Gorstian-early Ludfordian)	F
P17	/	Inorganic material		Silurian (Ludlow, latest Gorstian-early Ludfordian)	F
P18	/	Inorganic material		Silurian (Ludlow, latest Gorstian-early Ludfordian)	F

Tab. 2: sample of *Scyliorhinus canicula* (Linnaeus, 1758) and *Galeus melastomus* (Rafinesque, 1810). Lenght, gender and sexual maturity determined following the indication of *Carbonara & Fellosa, 2019*

Code	Animal	Lenght (cm)	Gender	Maturity
B55.1	CHORDATA/Chondrichthyes/Carcharhiniformes	42,0	male	3B
B55.2	CHORDATA/Chondrichthyes/Carcharhiniformes	41,0	female	2
B55.3	CHORDATA/Chondrichthyes/Carcharhiniformes	33,0	female	2
B55.4	CHORDATA/Chondrichthyes/Carcharhiniformes	32,0	female	2
B55.5	CHORDATA/Chondrichthyes/Carcharhiniformes	50,0	female	3B
B55.6	CHORDATA/Chondrichthyes/Carcharhiniformes	32,0	female	3B
B55.7	CHORDATA/Chondrichthyes/Carcharhiniformes	38,0	female	3A
B55.8	CHORDATA/Chondrichthyes/Carcharhiniformes	36,0	female	3A
B55.9	CHORDATA/Chondrichthyes/Carcharhiniformes	32,0	female	2
B56.1	CHORDATA/Chondrichthyes/Carcharhiniformes	45,0	female	4A
B56.2	CHORDATA/Chondrichthyes/Carcharhiniformes	42,5	female	2
B56.3	CHORDATA/Chondrichthyes/Carcharhiniformes	28,5	female	1
B56.4	CHORDATA/Chondrichthyes/Carcharhiniformes	50,0	female	3B
B56.5	CHORDATA/Chondrichthyes/Carcharhiniformes	45,0	female	2
B56.6	CHORDATA/Chondrichthyes/Carcharhiniformes	24,0	male	1
B56.7	CHORDATA/Chondrichthyes/Carcharhiniformes	24,0	female	1
B56.8	CHORDATA/Chondrichthyes/Carcharhiniformes	45,5	female	3B
B56.9	CHORDATA/Chondrichthyes/Carcharhiniformes	44,0	male	3A
B56.10	CHORDATA/Chondrichthyes/Carcharhiniformes	40,0	female	1
B56.11	CHORDATA/Chondrichthyes/Carcharhiniformes	38,5	male	1
B56.12	CHORDATA/Chondrichthyes/Carcharhiniformes	42,0	male	2
B56.13	CHORDATA/Chondrichthyes/Carcharhiniformes	30,5	male	1
B56.14	CHORDATA/Chondrichthyes/Carcharhiniformes	24,0	female	1
B56.15	CHORDATA/Chondrichthyes/Carcharhiniformes	44,0	male	3A
B56.16	CHORDATA/Chondrichthyes/Carcharhiniformes	38,0	male	1
B56.17	CHORDATA/Chondrichthyes/Carcharhiniformes	25,0	male	1
B56.18	CHORDATA/Chondrichthyes/Carcharhiniformes	26,0	female	1
B56.19	CHORDATA/Chondrichthyes/Carcharhiniformes	28,0	male	1
B56.20	CHORDATA/Chondrichthyes/Carcharhiniformes	26,5	female	1
B56.21	CHORDATA/Chondrichthyes/Carcharhiniformes	26,0	male	1

CHAPTER III

Refinement and application of the multi-analytical and multi-methodical approach

As previously stated, one of the innovative aspects of this thesis project is the application of the multi-analytical approach typical of mineralogy to the study of the biomineralized structures of fossils. The first step of this work was the refinement of a method for a correct chemical analysis of major elements; subsequently this routine, as well as the multi-analytical approach itself, was tested on recent organisms. The main results of these two steps are summarized below and the resulting published papers are attached at the end of the chapter (ANNEXES 1 and 2).

Annex-1: *How Much Can We Trust Major Element Quantification in Bioapatite Investigation?*

In this research (*Malferrari et al., 2019*) the attention is focused on laser ablation inductively coupled plasma mass spectrometry (LA-ICP-MS), that is considered among the best tools to obtain chemical information on small samples or on small areas of a sample. Some issues are preliminarily fixed. The absolute amount of material removed by laser can vary due to differences in physical-chemical features of the sample matrix and to the related absorption behaviour of the used laser wavelength that affects accuracy and precision of the resulting data. An internal standard is usually required to correct and validate the result. However, it is not easy to identify a unique standard for bioapatite whose lattice can accommodate iso- and hetero-valent substitutions during life or after death of the organism.

In the paper we propose a method to measure major element concentration, with special attention on the main substituents of bioapatite, using home-made external calibration standards. The method was tested on both living and fossil shark teeth. Following an approach similar to that used by *Guillong et al., 2005* and *Liu et al., 2008*, we compared the obtained results using diverse external standards. Moreover, we tested different calibration strategies for quantifying major elements, comparing the results from LA-ICP-MS, X-ray fluorescence (XRF) and inductively coupled plasma optical emission spectrometry (ICP-OES) on acid digested samples.

In general, the ultimate goal in LA-ICP-MS detection is to create an aerosol, that will be transformed into a mass spectrum fully representative of the composition of the ablated material. However, we demonstrate that this cannot be fulfilled in diverse practical applications as a consequence of various chemical-physical effects that can occur during aerosol formations. Moreover, we can check that, when matrix matched calibration standards are available, with the same analytical conditions, the major limiting factors are removed through calibration if the physical properties of the sample are homogenously distributed.

Annex-2: *Unravelling the ultrastructure and mineralogical composition of fireworm stinging bristles*

In *Righi et al., 2020* (Annex-2a) samples are represented by living invertebrates, the so-called fireworms *Hermodice carunculata*. The goal of the research is to characterize from a structural and a crystal-chemical points of view the fireworm chaetae in order to understand if the irritation caused by the contact between them and skin (or, more in general, a prey) is mechanical or due to transport of toxin through a phosphatized apparatus. For the first time, chemical and mineralogical compositions have been examined, as well as the ultrastructure and the external structures of chaetae from fireworms. For these purposes, results from diverse techniques were matched.

Major element concentrations were measured through ICP-OES and also checked via XRF, the latter performed in light of the results obtained in *Malferrari et al., 2019*. Also, to assess the amount of carbon and nitrogen, an Elemental Analysis (EA) was carried out. In order to analyse the gas produced during thermal reactions, TGA measurements were carried out. Moreover, XRPD measurements evidenced that the phosphatic part of the apparatus is amorphous, but crystallized into apatite when heated. Structural and ultrastructural observations were carried out with SEM and ESEM equipped with X-EDS.

This research stimulated a debate within the reference scientific community, essentially arising from different opinions on the interpretation of the experimental results. In this regard, see Annex-2b.
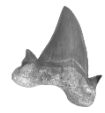
ANNEX-1

How Much Can We Trust Major Element Quantification in Bioapatite Investigation?

Luca Medici, Martina Savioli, Annalisa Ferretti & Daniele Malferrari

How Much Can We Trust Major Element Quantification in Bioapatite Investigation?

Daniele Malferrari,*,[†] Annalisa Ferretti,[†] Maria Teresa Mascia,[‡] Martina Savioli,[†] and Luca Medici[§]

[†]Department of Chemical and Geological Sciences, University of Modena and Reggio Emilia, Via Campi 103, I-41125 Modena, Italy

[‡]Department of Diagnostics, Clinical and Public Health Medicine, University of Modena and Reggio Emilia, Via Campi 213/b, I-41125 Modena, Italy

[§]National Research Council of Italy, Institute of Methodologies for Environmental Analysis, C. da S. Loja, Zona Industriale, I-85050 Tito Scalo, Potenza, Italy

Ⓢ *Supporting Information*

ABSTRACT: Bioapatite is probably the key factor in the unreplicated success of vertebrates. Chemical data on bioapatite composition can be achieved on a solid sample by using different analytical tools such as spectroscopic and spectrometric methods. As analytical outputs can be affected by the physical−chemical characteristics of the sample matrix, an internal standard is usually required to correct and validate the results. Bioapatite lattice can accommodate iso- and heterovalent substitutions during life or diagenesis varying its chemical composition through (geological) time. If on the one hand, this makes bioapatite a unique archive of physical and chemical information for both the living cycle and the events occurring after death, on the other, it excludes the identification of a sole internal standard. Here, we propose a method to measure major element concentration with specific care for P, Ca, Mg, Na, K, Si, Al, and Fe, which are the main substituent atoms in bioapatite, through homemade matrix-matched external calibration standards for laser ablation inductively coupled plasma mass spectrometry (LA-ICPMS). We tested the method on living and fossil shark teeth, critically comparing the results obtained using other analytical techniques and certified external standards. We demonstrated that matrix-matched calibration in LA-ICPMS is mandatory for obtaining a reliable chemical characterization even if factors such as matrix aggregation variability, diverse presence of volatile compounds, the fossilization footprint, and the instrumental variability can represent further variability parameters.
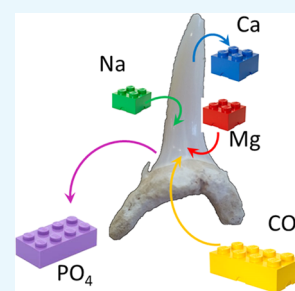
INTRODUCTION

Bioapatite played a fundamental role in the evolution of life as it has triggered the unreplicated success of living and fossil vertebrates. In addition, bioapatite represents in fossil organisms a unique archive of physical and chemical environmental information. Chemical data are in this case achieved with a wide range of analytical tools targeted to evaluate not only elemental composition itself but also highlight crystal-chemical evidence. Such techniques include scanning electron microscopy (SEM), mass spectrometry, X-ray (micro)diffraction, Fourier-transform infrared spectroscopy, electron microprobe (EMP) analysis, and Raman analysis.[1−4] Among them, electron microprobe (EMP) and laser ablation inductively coupled plasma mass spectrometry (LA-ICPMS) represent powerful analytical tools that are also potentially able to provide the spatial distribution of major (EMP) and trace (LA-ICPMS) elements in several types of solid matrices. However, as for LA-ICPMS, the absolute amount of materials removed by laser can vary due to differences in the physical−chemical features of the sample matrix and to the related absorption behavior of the used laser wavelength, thus, strongly affecting the accuracy and precision of the resulting data.[5,6] Therefore, an internal standard is generally in use to adjust variations in the quantity of material ablated during each run. Likewise, the chemical composition

determined by comparing the characteristic X-ray intensities obtained from the sample and standard in EMP measurements must be corrected for the matrix effect. Although EMP is generally considered the more appropriate method to gain major element concentration, it is also strictly dependent on the calibrating standards (usually minerals). Moreover, EMP is, undoubtedly, more expensive and less diffused than other instruments.

In fossil and living organisms with calcium carbonate matrix, calcium is unequivocally adopted as internal standard according to the nearly constant stoichiometry of $CaCO_3$ (i.e., lack of relevant iso- and heterovalent substitutions of Ca^{2+}). On the other hand, when dealing with organisms with a phosphate matrix (i.e., bioapatite), it is not a trivial matter to adopt a unique internal standard. In fact, hydroxyapatite (HA), which is the main form of bioapatite in living and fossil organisms, may accommodate chemical substitutions (typically with carbonate ions) both in the phosphatic (A-type substitutions) and hydroxylic (B-type substitutions) sites of its structure.[7−11] During life, substitutions are limited but once isolated from living tissues, the HA lattice can potentially

accommodate iso- and heterovalent substitutions at all sites during or after burial by diagenesis in consequence of the combination of physical and chemical alteration processes. In this way, the chemical composition of HA can vary over geological time.[12−17] Moreover, long-term preservation of bioapatite can involve recrystallization and alteration processes and drive to enrichment in other elements [e.g., rare-earth element (REE), Si, Fe, Mg, and Mn].[16,18,19]

For biological matrices, such as invertebrate shells or vertebrate teeth and bones, either living or fossil, several approaches to major element quantification have been proposed,[20] and a large number among them appeals to National Institute of Standards and Technology (NIST) Standard Reference Materials (SRM) as single and/or multiple point calibrators. More specifically, NIST SRM 610 (and/or NIST SRM 612) trace elements in glass, NIST SRM 1400 bone ash, and NIST SRM 1486 bone meal (below labeled as NIST 610, NIST 612, SRM 1400, and SRM 1486, respectively) are the most used certified standards in measurements of phosphate matrix.[21,22] However, when an exclusive (i.e., not affected by isomorphic substitutions) internal standard is missing, the matrix-matching constrain remains dramatically unsolved. In fact, while SRM 1400 and SRM 1486 are both bone-based materials, they differ in their organic content [0.87 and 31.5 wt % by mass loss on ignition (LOI), respectively],[21,22] which can affect ablation rates. Likewise, the drawback of NIST glasses is that the matrix of NIST 610 and NIST 612 is mainly SiO_2, so fundamentally different from the HA matrix, resulting in significant analytical biases.

In the literature, possible solutions that do not require the use of the internal standard are mentioned. Guillong et al. proposed to normalize the concentration of all elements as oxides to 100 wt % after external calibration against reference glasses.[23] Following a similar approach, Liu et al. described an internal standard-independent calibration strategy for LA-ICPMS analysis of anhydrous minerals and glasses based not only on the normalization of the sum of all metal oxides to 100 wt % but also introducing a matrix correction factor that considers the concentration and the net count rates of an analyte measured in the sample and in the reference material for calibration.[24]

Our research is aimed to explore similar paths, by comparing results obtained using different calibration standards as external calibrators in a multianalytical approach. We tested diverse calibration strategies for quantifying major elements in fossil and living bioapatite shark teeth using X-ray fluorescence (XRF), LA-ICPMS, and inductively coupled plasma optical emission spectroscopy (ICP-OES), the latter on acid-digested samples. We prepared a series of in-home HA matrix-matched standards (HMMS) and used them as external calibrating curve for LA-ICPMS and XRF to measure concentration of major elements (P, Ca, Mg, Na, K, Si, Ti, Al, Fe, and Mn) reported as oxides wt % in bioapatite. Later, SRM 1400 and SRM 1486 were used as single-point calibrator to calculate the concentration of the same elements. Results were thus critically compared. Our definitive goal is to develop a reliable method or find conclusions for chemical characterization by LA-ICPMS of small-sized samples (i.e., 50−500 μm, not measurable by XRF and ICP-OES) avoiding the use of EMP, which also deserves some constrains.

As reported above, two structural Ca sites allow various type of cationic substitutions into the lattice, while anionic substitutions occur at the OH (F, Cl, CO_3) and PO_4 (CO_3) sites. Bioapatites are commonly represented by HA (i.e., dahllite structure); however, carbonate- and fluoro-substituted hydroxyapatites (i.e., francolite structure) are quite common, thanks to carbonate- and fluoride-enriched mechanisms (up to 1% in weight) occurring during in vivo mineralization.[7,25−27] Herein, we will focus on cationic substitutions, and therefore fluorine, carbonate, and other possible substitutions with volatile elements are not dealt in the discussion but only considered as contributing to the loss on ignition (LOI), which will be measured through thermal methods.

MATERIALS AND METHODS

Samples. Teeth of the widespread Paleogene mega toothed shark *Otodus* sp. and living *Charcharias taurus* Rafinesque, 1810 (Figure 1) were selected for our study. Even if shark
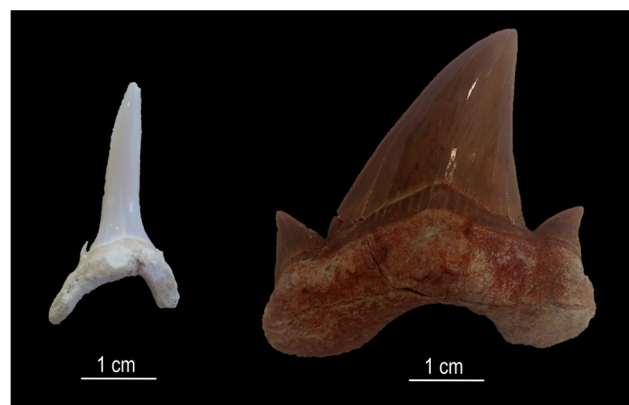

Figure 1. Shark teeth analyzed in this paper: living *C. taurus* (left) and Paleogene *Otodus* sp. (right).

teeth, like those of other cartilaginous fish, are mostly composed of fluorapatite rather than hydroxyapatite, we selected such samples as they are widespread in time and space and, therefore, largely investigated. Moreover, as mentioned above, the composition of the anionic site is not relevant to the aims of our investigations.

Teeth were longitudinally cut using a high-precision wire saw (model AGB9001, from Agar Scientific) equipped with a diamond-coated cutting wire. Two separate portions were produced from each tooth. After drying at 30 °C for 24 h, one piece was incorporated in resin (Figure S1, Supporting Information) and later used for LA-ICPMS measurements. The remaining half was further transversally cut to isolate the dentin and enameloid fractions of the teeth, which, after drying, were separately ground to a fine powder. Resulting materials were finally processed for XRF and ICP-OES analyses, the latter after acid digestion.

Intruments. ICP-MS X series II from Thermo Fisher Scientific equipped with the 213 nm laser ablation device UP-213 from New Wave Research was employed for the sample and standard characterization. Prior to optimizing laser ablation for the bioapatite matrix, the instrument was tuned using the NIST 610 and NIST 612 glasses measuring at instrument-optimized working conditions the intensity of the signals from U and Th (U/Th vs U). We fixed to measure abundance ratios between two glasses to gain a double check on bulk measurement accuracy. The laser ablation device employs a single long-working distance lens to focus the beam

on the sample surface with the possibility to modulate the geometry of the ablation (from a single spot to lines with size varying from 4 to 100 μm). Standards and samples were mounted to expose their surface to the focal plane of the laser.

Before sample- and matrix-matched standard measurements, the following experimental parameters need to be optimized: (i) laser intensity (%), i.e., the percentage of the laser beam that reaches the sample surface, can be modulated by changing the geometry of the reflective ends where initial beam is directed; (ii) laser frequency (Hz), i.e., the time when the laser output pulse power remains continuously above half its maximum value; (iii) laser fluence (J/cm^2), i.e., the energy delivered per unit area; it depends not only on laser features but also on sample chemical and physical properties, therefore this parameter could not be preset, but is measured during ablation; (iv) ablation line width (μm), i.e., the width of the ablation line that can be set varying the slits opening; (v) duration(s) and scan-speed, i.e., the time of persistence of the laser ablation on the ablating surface; (vi) purging gas flow (argon, mL/min), i.e., the volume of gas used to transport the ablated sample to plasma (we kept this parameter constant at 500 mL/min). A preablation, that is an ablation at mild conditions producing a fluency about approximately equal to 1/10 compared to the operating conditions, was always applied to clean up the surface. The approach to reach the optimized ablation conditions on standards and samples will be further discussed.

XRF data were collected using a wavelength dispersive Philips PW 1480 X-ray fluorescence (XRF) spectrometer (Philips, Almelo, The Netherlands) using the methods of Franzini et al. for determination of elemental concentration.[28] With this method, the fluorescence intensity I_j of the element j in a sample containing N elements is related to the mass absorption coefficients of the sample by the formula

$$I_j = \frac{C_j}{\sum_{i=1}^{N} K_{j,i} C_i}$$

where C_j and N are the concentrations of the elements and the number of elements in the sample, respectively, and $K_{j,i}$ is absorption coefficient. Loss on ignition (LOI) values for samples were obtained from thermogravimetric measurements (see below).

Inductively coupled plasma optical emission spectroscopy (ICP-OES, PerkinElmer Optima 4200 DV) was employed to check element concentration in acid-digested samples after calibration with certified standard solutions.

Thermogravimetry coupled with evolved gas mass spectrometry was employed to find the weight percentage of volatile compounds. Measurements were carried out with a Seiko SSC 5200 thermal analyzer equipped with a quadrupole mass spectrometer (ESS, GeneSys Quadstar 422), which allowed the analysis of gas produced during thermal reactions. Gas sampling by the spectrometer was via an inert, fused silicon capillary system, heated to prevent gas condensing. Gas analyses were carried out to determine the nature of the released chemical species with temperature. Background subtraction was used to obtain the point zero conditions before starting the evolved gas analysis. Experimental conditions were: heating rate 20 °C/min; heating range 25–1100 °C; purging gas ultrapure helium at a flow rate of 100 μL/min. Mass analyses were carried out in multiple ion detection modes measuring the m/z ratios 18 for H_2O, 30 for

NO, and 44 for CO_2, where m/z is the dimensionless ratio between the mass number and the charge of an ion (these gasses were selected to better define the real contribution to the LOI of organic matter rather than the substituting volatile compounds); SEM detector at 900 V was employed with 0.5 s of integration time on each measured mass.

HMMS Preparation. The concentrations of each element in the highest and lowest standard were chosen to bracket as better as possible ranges reported in selected literature papers.[15,29] Operatively, a stock solution with defined Na and K concentration was prepared using pure grade analytical reagents ($NaNO_3$ and KNO_3, respectively) and Millipore water. Later, appropriate aliquots of the stock solution were separately added to four mixtures formed by proper amounts of ultrapure micronized HA (Sigma-Aldrich) and the oxides MgO, SiO_2, TiO_2, Al_2O_3, Fe_2O_3, and MnO_2 (analytical grade reagents, Sigma-Aldrich). To prevent apatite dissolution, immediately after the addition of the solution, the pH of each aliquot was adjusted to 7.5 ± 0.1 using few drops of ammonia diluted solution. Each suspension was mixed and homogenized in an agate mortar and then dried at 30 °C for 12 h; the resulting powders were then rehomogenized in the agate mortar. Afterward, 750 mg of each powder was pressed for 1 min under 6 t pressure into 12 mm diameter tablets.[30] These "standard tablets", each at a different elemental concentration (Table 1), were used to calibrate the LA-ICPMS following the

Table 1. Element Concentrations (Oxide wt %) in HMMS Calibration Curve

	HMMS 1	HMMS 2	HMMS 3	HMMS 4
SiO_2	1.76	0.99	0.39	0.01
Al_2O_3	1.01	0.60	0.29	0.01
Fe_2O_3	1.30	0.86	0.38	0.05
TiO_2	0.04	0.02	0.01	0.00
P_2O_5	24.81	29.92	33.36	34.84
MnO	0.04	0.02	0.01	0.00
MgO	1.64	0.98	0.44	0.11
CaO	32.67	39.39	43.91	45.87
Na_2O	1.73	0.76	0.26	0.11
K_2O	0.71	0.47	0.26	0.08
LOI	34.30	25.98	20.70	18.91

analytical procedure discussed in Nardelli et al. and better detailed in the following.[31] Likewise, 300 mg of each powder was employed to calibrate XRF following an approach like those reported in Castellini et al.[32]

LA-ICPMS Calibration. Our first goal was to optimize the ablation conditions, as the amount of material removed by the laser beam in standards and samples strongly reflects their physical–chemical properties (hardness, massiveness, density, etc.). We initially applied mild ablation conditions setting laser intensity at 40%, with a frequency of 5 Hz and tracing 55 μm width ablation lines for a duration of 240 s. Such laser setting was applied to HMMS and produced fluence values close to those reported by Willmes et al. for bioapatite matrix samples.[13] We have chosen applying ablation lines instead of single spot ablations as the latter can be affected by laser-induced elemental fractioning. This side effect may occur when a large number of shots is carried out in close sequence as a consequence of the thermal effects taking place in the vicinity of the ablation crater and of the increasing degree of elemental

fractioning occurring when ablating for a long time and, therefore, from ever deeper cavities.

The mass spectrometer was then preliminarily calibrated with HMMS at the above-reported ablation conditions and, later, tablet prepared with SRM 1400, SRM 1486, and with pure HA (12 mm diameter, 750 mg weight, 6 t pressed) were analyzed as unknown samples. Ablation conditions were then modulated and optimized (Table S1, Supporting Information) as long as the concentrations measured for Ca and P in SRM standards and HA returned values close to those certified or stoichiometric (Figure 2). These ablation conditions were then
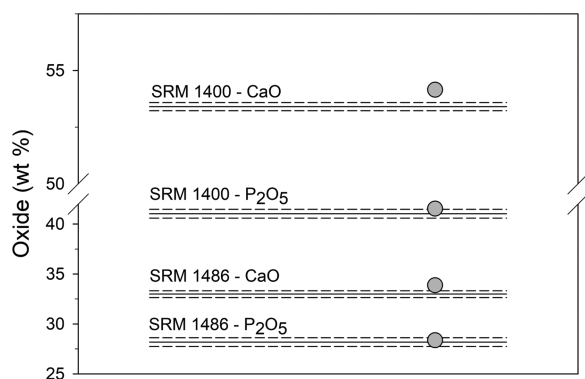

Figure 2. Feedback on the selected calibration parameters as highlighted by the measured concentration of Ca and P (filled circles, reported as oxide weight %) in SRM 1400 and SRM 1486. Assigned values (SRM data sheets) are indicated by solid lines along with the associated expanded uncertainty (dashed lines).

applied to HMMS, SRM standards, and shark teeth. Precision and accuracy were within ±1%. Ti and Mn detected by LA-ICPMS were always below 0.01 wt % and this result was also confirmed by XRF and ICP-OES. As regards Mn in SRM standards, this limit also agrees with the concentrations (not certified) reported in the data sheets (17 and 1 μg/g for SRM 1400 and 1486, respectively), whereas Ti concentrations are not reported. However, as Ti and Mn do not play a relevant role in isomorphic substitutions in bioapatite, we did not experiment with other methods to better refine their concentrations that will be not reported and further commented in the Results and Discussion section.

■ RESULTS AND DISCUSSION

Table 2 reports the measurements on teeth obtained with the different analytical methods. The chemical formulae were calculated assuming ideal stoichiometry and normalized on the basis of 16 (A + T)-site cations,[33] according to the general apatite formula $A_{10}(TO_4)_6X_2$, where A stands for Ca^{2+}, Mg^{2+}, Na^+, K^+, Fe^{3+}, and Al^{3+}, whereas the tetrahedral T-site is occupied by P^{5+}, Si^{4+}, Al^{3+}. The normalization must satisfy the equation

$$\frac{moles \ (Ca + Mg + Na + K + Fe + Al + P + Si)}{k} = 16$$

where k is a numerical constant. The anionic X site is occupied by OH^-, F^-, Cl^-, CO_3^{2-}, O^{2-}, but it is not necessary to know its chemistry for our aims as it does not influence the normalization of the cationic sites. Likewise, REE, C, and S were not determined and are not considered in the chemical formulae as their absence does not affect the significance of the

comparisons among the different techniques. The same normalization procedure applies also to Table 3, which will be discussed later.

The numerical results are in good agreement with those described in literature for living and/or fossil organisms.[14,15,29] In general, and without considering differences arising from each analytical method, Table 2 shows that the P_2O_5 content ranges from 26.01 to 35.01 wt %. The minimal and maximal P_2O_5 concentrations were recorded in porous dentin and enameloid of living shark, respectively. Similar considerations also apply to CaO (35.27 wt % in living shark dentin and 49.49 wt % in fossil shark enameloid). In fossil teeth, SiO_2 can be primarily ascribed to fossilization (i.e., isomorphic substitutions and, more likely, to inclusions of terrigenous materials, as evidenced by the simultaneous increase of Al_2O_3 well evident in enameloid and dentin of *Otodus* sp., but absent in *C. taurus*, Figure 3). On the other hand, Na and Mg may have been incorporated into the bioapatite lattice also during living cycle. As already evidenced by Nemliher et al.,[14] it is not possible to discriminate which cations are, actually, of biogenic origin or which have been integrated during ageing/fossilization, although it is reasonable that Al and Si are incorporated only in very small quantities (a few parts per million) during life-cycle, as evidenced by measurements obtained on *C. taurus*.

It is crucial to highlight that percentage data obtained with LA-ICPMS (Table 2a) strongly differ from those obtained with XRF (Table 2b) and ICP-OES (Table 2c); in particular, sums of percentage concentrations measured through LA-ICPMS on all of the samples are clearly lower than those measured through XRF and ICP-OES. Likewise, atoms per formula unit obtained by applying the method above detailed, do not show a unique trend. Before commenting on these differences, it is opportune to check how concentration values change after calibrating with SRM 1400 and SRM 1486 (single-point calibration). More in detail, SRM 1400 (bone ash) and SRM 1486 (bone meal) were used to measure major element concentrations in fossil and recent teeth, respectively. This procedure did not require the ablation of new areas on the sample surface, as the intensity signals produced by previous ablations and used for quantification with HMMS standards were reelaborated using the signals from SRM standards. In this way, differences in concentration can neither be ascribed to instrumental biases as all of the signals are taken in the same working session, nor to compositional variations of samples. Moreover, it should be stressed that ablation conditions applied to SRM have been optimized through HMMS and, therefore, it would not be possible to set such values a priori using exclusively the one-point calibration method.

Results are reported in Table 3 and, basically, parallel to those illustrated in Table 2 even if with minor discrimination between enameloid and dentin values. Significantly, major elements Ca and P analyzed in living shark teeth (Table 3a) show close percentage concentrations for dentin and enameloid, and are in general lower than those detected for dentin and enameloid in fossil teeth (Table 3b).

Data reported in Table 2a (XRF) and Table 2b (ICP-OES) are in good agreement. In fact, using acid digestion and dilution both for sample and standards (ICP-OES) and matrix-matched solid standards (XRF), the matrix constrain is nearly irrelevant. In fact, at these conditions, ICP-OES and XRF are almost exclusively affected by interelement interference issues (i.e., the effects related to radiation interferences, optical or X-rays, respectively), but not by the overall matrix and the

Table 2. Chemical Composition (Oxide wt %) and Atoms per Formula Unit (See Text for Details) for Living C. *taurus* and Fossil *Otodus* sp. Shark Teeth Measured with LA-ICPMS after Calibrating with HMMS (a), XRF (b), and ICP-OES (c)[a]

(a) LA-ICPMS results	P_2O_5	CaO	MgO	Na_2O	K_2O	SiO_2	Al_2O_3	Fe_2O_3	sum
C. *taurus* E.—AL-1	29.05	42.10	0.67	0.95	0.10	0.01	0.01	0.08	72.97
C. *taurus* E.—AL-2	28.22	40.05	0.65	0.84	0.10	0.01	0.01	0.07	69.94
C. *taurus* E.—AL-3	29.04	41.65	0.73	0.87	0.10	0.01	0.01	0.08	72.47
C. *taurus* E.—average	28.77	41.26	0.68	0.89	0.10	0.01	0.01	0.08	71.79
C. *taurus* D.—AL-1	26.83	35.70	0.57	0.98	0.27	0.01	0.00	0.07	64.44
C. *taurus* D.—AL-2	27.47	34.89	0.42	1.08	0.21	0.01	0.00	0.08	64.16
C. *taurus* D.—AL-3	26.31	35.21	0.53	1.09	0.20	0.01	0.00	0.07	63.42
C. *taurus* D.—average	26.87	35.27	0.50	1.05	0.23	0.01	0.00	0.07	64.01
Otodus sp. E.—AL-1	28.08	42.41	0.62	0.95	0.19	1.02	0.21	0.32	73.81
Otodus sp. E.—AL-2	28.63	42.34	0.62	0.86	0.18	1.02	0.22	0.31	74.19
Otodus sp. E.—AL-3	27.72	41.38	0.65	0.85	0.17	1.01	0.22	0.31	72.32
Otodus sp. E.—average	28.14	42.04	0.63	0.89	0.18	1.02	0.22	0.31	73.44
Otodus sp. D.—AL-1	28.59	45.05	0.74	1.08	0.20	1.08	0.29	0.37	77.41
Otodus sp. D.—AL-2	27.73	44.11	0.73	1.06	0.20	1.06	0.29	0.36	75.53
Otodus sp. D.—AL-3	28.19	44.47	0.74	1.07	0.20	1.07	0.29	0.36	76.39
Otodus sp. D.—average	28.17	44.55	0.74	1.07	0.20	1.07	0.29	0.36	76.45

				chemical formulae calculated on the basis of 16 cations					
	P	Ca	Mg	Na	K	Si	Al	Fe	Ca/P
C. *taurus* E.—AL-1	5.409	9.919	0.219	0.407	0.029	0.001	0.002	0.013	1.834
C. *taurus* E.—AL-2	5.493	9.865	0.222	0.374	0.030	0.001	0.002	0.013	1.796
C. taurus E.—AL-3	5.450	9.892	0.240	0.372	0.030	0.001	0.002	0.013	1.815
C. taurus E.—average	5.450	9.893	0.227	0.384	0.030	0.001	0.002	0.013	1.815
C. *taurus* D.—AL-1	5.668	9.544	0.212	0.474	0.085	0.002	0.001	0.013	1.684
C. *taurus* D.—AL-2	5.841	9.389	0.157	0.527	0.068	0.002	0.001	0.015	1.607
C. *taurus* D.—AL-3	5.636	9.548	0.198	0.536	0.064	0.002	0.001	0.014	1.694
C. *taurus* D.—average	5.715	9.493	0.189	0.512	0.073	0.002	0.001	0.014	1.661
Otodus sp. E.—AL-1	5.158	9.859	0.202	0.400	0.054	0.222	0.053	0.052	1.912
Otodus sp. E.—AL-2	5.244	9.815	0.201	0.362	0.050	0.222	0.056	0.050	1.872
Otodus sp. E.—AL-3	5.204	9.832	0.216	0.365	0.049	0.225	0.058	0.051	1.889
Otodus sp. E.—average	5.202	9.835	0.206	0.376	0.051	0.223	0.056	0.051	1.891
Otodus sp. D.—AL-1	4.987	9.948	0.228	0.433	0.053	0.223	0.071	0.057	1.995
Otodus sp. D.—AL-2	4.956	9.977	0.229	0.433	0.053	0.223	0.071	0.057	2.013
Otodus sp. D.—AL-3	4.982	9.949	0.229	0.434	0.053	0.223	0.071	0.057	1.997
Otodus sp. D.—average	4.975	9.958	0.229	0.433	0.053	0.223	0.071	0.057	2.002

(b) XRF results	LOI	P_2O_5	CaO	MgO	Na_2O	K_2O	SiO_2	Al_2O_3	Fe_2O_3	sum
C. *taurus* E.	15.8	34.86	46.75	0.37	1.54	0.28	<0.1	<0.1	<0.1	99.60
C. *taurus* D.	34.6	26.01	36.83	0.27	1.36	0.18	<0.1	<0.1	<0.1	99.25
Otodus sp. E.	6.80	31.68	49.49	0.79	1.02	0.26	1.25	0.23	0.38	91.91
Otodus sp. D.	7.57	29.88	47.45	0.88	1.09	0.23	1.29	0.28	0.36	89.04

			chemical formulae calculated on the basis of 16 cations						
	P	Ca	Mg	Na	K	Si	Al	Fe	Ca/P
C. *taurus* E.	5.655	9.598	0.106	0.572	0.068	n.c.	n.c.	n.c.	1.697
C. *taurus* D.	5.441	9.751	0.099	0.652	0.057	n.c.	n.c.	n.c.	1.792
Otodus sp. E.	5.040	9.964	0.221	0.371	0.062	0.236	0.052	0.054	1.977
Otodus sp. D.	4.951	9.949	0.257	0.415	0.056	0.253	0.066	0.053	2.010

(c) ICP-OES results	LOI	P_2O_5	CaO	MgO	Na_2O	K_2O	SiO_2	Al_2O_3	Fe_2O_3	sum
C. *taurus* E.	15.8	35.01	46.64	0.77	1.25	0.12	0.01	0.00	0.10	99.70
C. *taurus* D.	34.6	26.33	36.62	0.65	1.19	0.12	0.01	0.01	0.08	99.60
Otodus sp. E.	6.80	32.46	49.03	0.72	1.10	0.22	1.18	0.24	0.75	92.13
Otodus sp. D.	7.57	30.41	47.92	0.79	1.15	0.21	1.15	0.31	0.39	89.92

			chemical formulae calculated on the basis of 16 cations						
	P	Ca	Mg	Na	K	Si	Al	Fe	Ca/P
C. *taurus* E.	5.685	9.584	0.219	0.466	0.030	0.001	0.000	0.014	1.686
C. *taurus* D.	5.485	9.654	0.237	0.568	0.037	0.002	0.002	0.016	1.760
Otodus sp. E.	5.158	9.860	0.202	0.400	0.054	0.222	0.053	0.052	1.912
Otodus sp. D.	4.988	9.947	0.228	0.433	0.053	0.223	0.071	0.057	1.994

[a]Symbol < denotes concentration below the detection limit (value after the symbol); n.c., not calculable; loss on ignition (LOI) is from thermogravimetric measurement and is included in the sum; AL: ablation line; D.: dentin; E.: enameloid.

Table 3. Chemical Composition (Oxide wt %) and Atoms per Formula Unit (See Text for Detail) for Living (a) and Fossil (b) Shark Teeth Obtained with LA-ICPMS after Calibrating with SRM 1486 and SRM 1400, Respectively[a]

(a) LA-ICPMS SRM 1486	P_2O_5	CaO	MgO	Na_2O	K_2O	SiO_2	Al_2O_3	Fe_2O_3	sum
C. taurus E.—AL-1	25.15	38.32	0.59	0.79	0.10	0.00	0.01	0.07	65.02
C. taurus E.—AL-2	25.00	36.25	0.57	0.73	0.10	0.00	0.01	0.07	62.73
C. taurus E.—AL-3	24.90	36.99	0.51	0.73	0.09	0.001	0.01	0.07	63.30
C. taurus E.—average	25.02	37.18	0.56	0.75	0.10	0.00	0.01	0.07	63.69
C. taurus D.—AL-1	23.93	36.69	0.58	1.01	0.29	0.01	0.00	0.06	62.57
C. taurus D.—AL-2	25.60	37.01	0.55	1.03	0.27	0.01	0.00	0.07	64.54
C. taurus D.—AL-3	25.01	35.99	0.52	1.00	0.26	0.01	0.00	0.07	62.86
C. taurus D.—average	24.85	36.56	0.55	1.01	0.27	0.01	0.00	0.07	63.32
			chemical formulae calculated on the basis of 16 cations						
	P	Ca	Mg	Na	K	Si	Al	Fe	Ca/P
C. taurus E.—AL-1	5.245	10.114	0.215	0.378	0.031	0.001	0.002	0.013	1.928
C. taurus E.—AL-2	5.422	9.947	0.219	0.362	0.033	0.001	0.002	0.013	1.835
C. taurus E.—AL-3	5.348	10.054	0.195	0.357	0.031	0.001	0.002	0.013	1.880
C. taurus E.—average	5.337	10.039	0.210	0.366	0.031	0.001	0.002	0.013	1.881
C. taurus D.—AL-1	5.160	10.011	0.222	0.499	0.093	0.002	0.001	0.011	1.940
C. taurus D.—AL-2	5.371	9.829	0.203	0.496	0.085	0.002	0.001	0.013	1.830
C. taurus D.—AL-3	5.391	9.817	0.199	0.493	0.084	0.002	0.001	0.013	1.821
C. taurus D.—average	5.308	9.885	0.208	0.496	0.087	0.002	0.001	0.012	1.862
(b) LA-ICPMS SRM 1400	P_2O_5	CaO	MgO	Na_2O	K_2O	SiO_2	Al_2O_3	Fe_2O_3	sum
Otodus sp. E.—AL-1	26.44	40.80	0.60	0.90	0.15	1.00	0.19	0.29	70.37
Otodus sp. E.—AL-2	26.54	40.69	0.60	0.88	0.15	1.00	0.19	0.30	70.35
Otodus sp. E.—AL-3	26.12	41.12	0.61	0.82	0.15	0.97	0.20	0.29	70.27
Otodus sp. E.—average	26.37	40.87	0.60	0.87	0.15	0.99	0.19	0.29	70.33
Otodus sp. D.—AL-1	28.11	44.85	0.74	1.00	0.20	1.01	0.31	0.32	76.55
Otodus sp. D.—AL-2	27.73	44.11	0.73	1.06	0.20	1.06	0.29	0.35	75.52
Otodus sp. D.—AL-3	28.01	44.21	0.70	1.04	0.20	1.03	0.32	0.33	75.86
Otodus sp. D.—average	27.95	44.39	0.72	1.03	0.20	1.03	0.31	0.34	75.97
			chemical formulae calculated on the basis of 16 cations						
	P	Ca	Mg	Na	K	Si	Al	Fe	Ca/P
Otodus sp. E.—AL-1	5.090	9.939	0.204	0.396	0.044	0.228	0.050	0.049	1.953
Otodus sp. E.—AL-2	5.114	9.921	0.204	0.388	0.044	0.227	0.051	0.051	1.940
Otodus sp. E.—AL-3	5.035	10.029	0.205	0.363	0.044	0.220	0.054	0.050	1.992
Otodus sp. E.—average	5.079	9.963	0.204	0.382	0.044	0.225	0.052	0.050	1.962
Otodus sp. D.—AL-1	4.960	10.015	0.230	0.404	0.053	0.210	0.077	0.050	2.019
Otodus sp. D.—AL-2	4.956	9.978	0.229	0.433	0.053	0.223	0.071	0.056	2.013
Otodus sp. D.—AL-3	4.988	9.964	0.219	0.425	0.054	0.217	0.080	0.053	1.998
Otodus sp. D.—average	4.968	9.986	0.226	0.420	0.053	0.217	0.076	0.053	2.010

[a]The integrated signals from samples are the same from Table 2 (same ablation lines). AL: ablation line; D.: dentin; E.: enameloid.

physical properties of the sample. Likewise, variation in intensity signals and, therefore, in concentration values arising from the different abundance of volatile compounds in the sample in ICP-OES and XRF are solved as well. In fact, volatile molecules are removed during acid digestion (ICP-OES); otherwise, their contribution, when the total amount is known, can be easily accounted during data elaboration (XRF).

On the other hand, volatile compounds can play a predominant role in affecting concentration values when they are dispersed in the aerosol produced by laser ablation. Actually, as clearly shown by the thermogravimetric curves and mass spectrometry of the gases evolved during heating (Figures S2–S5, Supporting Information), the difference in concentration in both enameloid and dentin of living shark teeth is high (overall weight loss 15.8 and 34.6 wt %, Figures S2a and S3a, respectively), whereas it is significantly lower in fossil samples (6.80 and 7.57 wt %, Figures S4a and S5a). In dentin and enameloid of living shark, the major thermal events occurred between 200 and 500 °C and are mainly related to

the thermal decomposition of the organic fraction as evidenced by the intense exothermic reactions (differential thermal analysis curves, Figures S2a and S3a) and by the release of H_2O, NO, and CO_2 (Figures S2b and S3b). In contrast, in fossil teeth, in the same thermal range, the weight loss is strongly limited and a clear signal related to the release of CO_2 was observed only in dentin (Figure S5b). Furthermore, in fossil enameloid and dentin, two reactions occurring between 700 and 800 °C producing the release of CO_2 are well evident (Figures S4b and S5b). First, forming a shoulder between 720 and 750 °C in enameloid and a peak with maximum at about 730 °C in dentin, is from the decarbonatation of B-type substitutions in bioapatite frames;[34] second, higher temperature (maxima at 805 and 792 °C in enameloid and dentin, respectively) can be related to decarbonation of calcium carbonate present in terrigenous materials as mentioned when discussing chemical data. These reactions, which are less evident in C. taurus, further prove that the complexity of the matrix sometimes depends also on the coexistence of elements
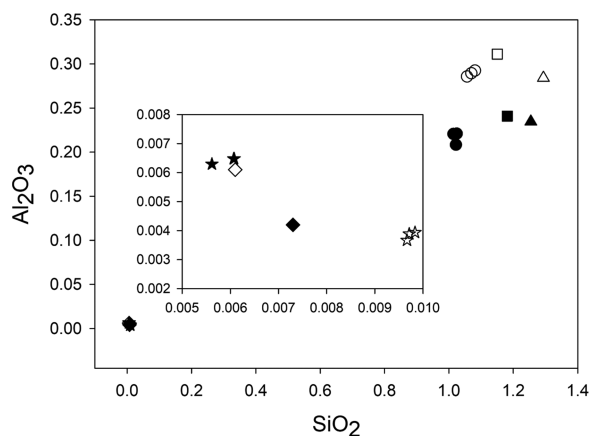
Figure 3. Correlation between SiO_2 and Al_2O_3 concentrations (oxide weight percent, Table 2) in enameloid (filled symbols) and dentin (open symbols) for fossil *Otodus* sp. obtained through LA-ICPMS (circles; average values), XRF (triangles), and ICP-OES (squares) and, as better evident in the magnification, for living *C. taurus* measured with LA-ICPMS (stars; average values) and ICP-OES (diamonds).
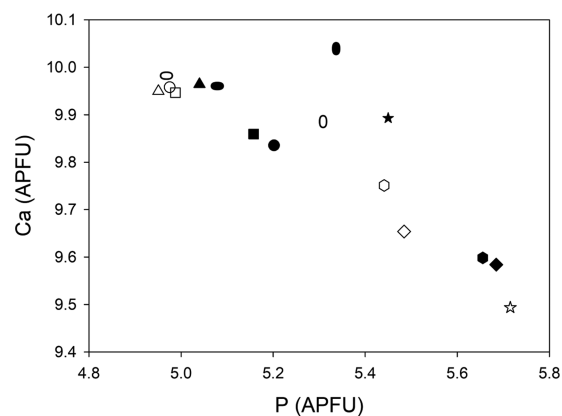

Figure 4. Correlation between P and Ca atoms per formula unit in enameloid (filled symbols) and dentin (open symbols) for fossil *Otodus* sp. obtained through LA-ICPMS (circles; average values; after calibrating with HMMS), XRF (triangles), ICP-OES (squares), and LA-ICPMS (horizontal ellipses; average values; after calibrating with SRM standards) and for living *C. taurus* obtained through LA-ICPMS (stars; average values; after calibrating with HMMS), XRF (hexagons), ICP-OES (diamonds), and LA-ICPMS (vertical ellipses; average values; after calibrating with SRM standards).

with different chemical speciation (i.e., Ca in bioapatite and in carbonate). Moreover, differences in the temperature values at which a thermal event occurs indicate that energy bond varies. This behavior can be related not only to fossilization (fossilized tooth is fully mineralized, i.e., the organic matrix had nearly decomposed over time) but also to anionic substitutions in the bioapatite frame. The discussion of the other reactions related to thermal decomposition of apatite is beyond the aim of this work; nevertheless, they well match with those reported in literature.[34,35]

The presence of volatile compounds in the ablated aerosol and differences in matrix physical properties can result in mass response variations. However, the specific pattern of apparent enrichment and depletion of the various elements that characterize the matrix effect signature probably mirrors a composite interplay between composition and size distribution of ablated particles and their decomposition and ionization mechanisms in the plasma. In fact, it is demonstrated that the LA-ICPMS may also cause elemental fractionation due to the dependence of vaporization, ionization, and ion transmission on the composition and size distribution of the particles in the laser-generated aerosol.[36] Larger particles or particles that consist of a highly refractory matrix need longer residence time within the ICP or higher gas temperatures for complete vaporization.[37] Of course, such constrains do not apply to other techniques.

Proper comparisons among the different analytical techniques were required to better evaluate the significances of the obtained results and the analytical goodness of the proposed method. Measurements carried out on dentin of *Otodus* sp. showed a clear agreement among the three analytical techniques; this portion of the tooth should contain a higher amount of C in the tetrahedral site as highlighted by the lowest presence of P, fully confirmed by the three methodologies. On the other hand, Ca and P atoms per formula unit from enameloid are in good agreement when calculated through LA-ICPMS and ICP-OES measurements, but are slightly different with respect to those from XRF (Figure 4 and Table S2, Supporting Information). However, according to Lübke et al.,[29] Ca/P molar ratio of teeth of fossil sharks should be higher

in dentin than that in enameloid, and this behavior was confirmed by all our results (Figure 5).
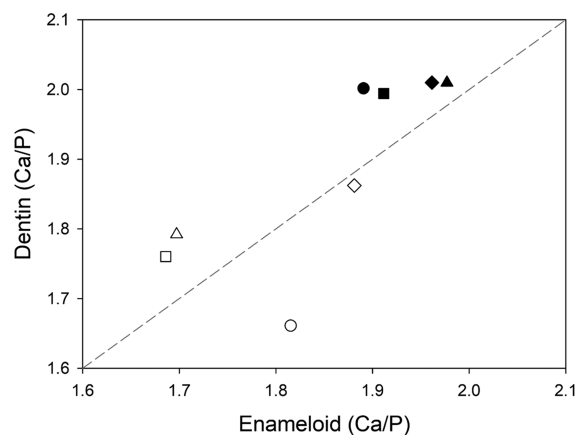

Figure 5. Correlation between Ca/P ratios in dentin and enameloid in *Otodus* sp. (filled symbols) and *C. taurus* (open symbols) obtained through LA-ICPMS (circles; average values; after calibrating with HMMS), XRF (triangles), ICP-OES (squares), and LA-ICPMS (diamonds; average values; after calibrating with SRM standards).

Measurements performed on living *C. taurus* teeth are more variable. The most significant differences arise, both for enameloid and dentin, from LA-ICPMS that revealed Ca and P atoms per formula unit significantly different with respect to those calculated through XRF and ICP-OES measurements (Table S2); the dissimilarity was confirmed by Ca/P molar ratio as well. According to Lübke et al.,[29] Ca/P molar ratio of teeth from recent sharks should be higher in enameloid than that in dentin, contrary to fossil sharks. LA-ICPMS results showed (Figure 5) a Ca/P molar ratio in good agreement with the cited literature, both by average values and by single measurements, confirming the effectiveness of the proposed methodology. Average values of Ca/P molar ratios obtained by SRM 1400 and SRM 1486 international standards also agree with literature,[29] although differences between enameloid and

dentin resulted less sharp (Table S2); nevertheless, single measurements on teeth of living shark are sometimes significantly different from the average values, highlighting possible constrain in their chemical characterization.

CONCLUSIONS

This study has demonstrated that matrix-matched calibration in LA-ICPMS is a significant and effective condition, mandatory for obtaining a reliable chemical analysis of bioapatite. Uncertainties still concern some aspects: (i) matrix aggregation variability in different parts of the same sample; (ii) greater or lesser presence of volatile compounds (not only organic but also anions such as fluorine, chlorine, and hydroxyls that form possible isomorphic substitutions); (iii) fossilization footprint; (iv) instrumental variability.

The ultimate goal in LA-ICPMS detection is to create an aerosol to be transformed into a mass spectrum fully representing the composition of the ablated material. This cannot be fulfilled in many practical applications because of the variability of the different processes that occur during the generation of the aerosol. Elemental fractionation due to preferential vaporization during the ablation can change the composition in the aerosol formed during ablation and also before the next laser shot occurs.[37] Likewise, vaporization and ionization of aerosols showing different particle size distributions inside the ICP ion source may further change the relative response of the elements when different materials are sampled.

When matrix-matched calibration standards are available, the processes occurring during LA mainly affect the sensitivity of the method in general. As changes in the ablation rates, particle size distributions, and composition of the aerosol should be identical for the calibration standards and the unknown samples, the major limiting factors should be removed through calibration but only if the physical properties of the sample are homogeneously distributed. It is, of course, mandatory that quantitative data acquisition is carried out at identical ablation conditions, i.e., during the same ablation session.

ASSOCIATED CONTENT

ⓢ Supporting Information

The Supporting Information is available free of charge on the ACS Publications website at DOI: 10.1021/acsomega.9b02426.

Pictures of shark teeth after cutting and incorporation in resin, optimized laser parameters, thermal analyses of enameloid and denting, and atoms per formula unit grouped for sample type (PDF)

AUTHOR INFORMATION

Corresponding Author

*E-mail: daniele.malferrari@unimore.it. Web: http://personale.unimore.it/rubrica/dettaglio/dmalf.

ORCID

Daniele Malferrari: 0000-0002-0879-1703

Author Contributions

All authors contributed equally. The manuscript was written through the contributions of all authors. All authors have given approval to the final version of the manuscript.

Notes

The authors declare no competing financial interest.

REFERENCES

(1) Piga, G.; Santos-Cubedo, A.; Solá, S. M.; Brunetti, A.; Malgosa, A.; Enzo, S. An X-ray Diffraction (XRD) and X-ray Fluorescence (XRF) investigation in human and animal fossil bones from Holocene to Middle Triassic. *J. Archaeol. Sci.* **2009**, *36*, 1857−1868.

(2) Li, Z.; Pasteris, J. D. Tracing the pathway of compositional changes in bone mineral with age: preliminary study of bioapatite aging in hypermineralized dolphin's bulla. *Biochim. Biophys. Acta, Gen. Subj.* **2014**, *1840*, 2331−2339.

(3) Ferretti, A.; Medici, L.; Malferrari, D.; Savioli, M. Diagenesis does not invent anything new: Precise replication of conodont structures by secondary apatite. *Sci. Rep.* **2017**, *7*, No. 1624.

(4) Medici, L.; Malferrari, D.; Savioli, M.; Ferretti, A. Mineralogy and crystallization patterns in conodont bioapatite from first occurrence (Cambrian) to extinction (end-Triassic). *Palaeogeogr. Palaeoclimatol. Palaeoecol.* **2019**, DOI: 10.1016/j.palaeo.2019.02.024.

(5) Longerich, H. P.; Jackson, S. E.; Günther, D. Laser ablation inductively coupled plasma mass spectrometry transient signal data acquisition and analyte concentration calculation. *J. Anal. At. Spectrom.* **1996**, *11*, 899−904.

(6) Horn, I.; Guillong, M.; Gunther, D. Wavelength dependent ablation rates for metals and silicate glasses using homogenized laser beam profiles - implications for LA-ICP-MS. *Appl. Surf. Sci.* **2001**, *182*, 91−102.

(7) LeGeros, R. Z. Apatites in biological systems. *Prog. Cryst. Growth Charact.* **1981**, *4*, 1−45.

(8) Whitenack, L. B.; Simkins, D. C.; Motta, P. J. Biology meets engineering: the structural mechanics of fossil and extant shark teeth. *J. Morphol.* **2011**, *272*, 169−179.

(9) Enax, J.; Prymak, O.; Raabe, D.; Epple, M. Structure, composition, and mechanical properties of shark teeth. *J. Struct. Biol.* **2012**, *178*, 290−299.

(10) Enax, J.; Janus, A. M.; Raabe, D.; Epple, M.; Fabritius, H. O. Ultrastructural organization and micromechanical properties of shark tooth enameloid. *Acta Biomater.* **2014**, *10*, 3959−3968.

(11) Elliott, J. C. Calcium Phosphate Biominerals. In *Phosphates: Reviews in Mineralogy and Geochemistry*; Kohn, M. J., Rakovan, J., Hughes, J. M., Eds.; Mineralogical Society of America: Washington, DC, 2002; Vol. *48*, pp 427−453.

(12) Margariti, E.; Stathopoulou, E. T.; Sanakis, Y.; Kotopoulou, E.; Pavlakis, P.; Godelitsas, A. A geochemical approach to fossilization processes in Miocene vertebrate bones from Sahabi, NE. *J. Afr. Earth Sci.* **2019**, *149*, 1−18.

(13) Willmes, M.; Kinsley, L.; Moncel, M. H.; Armstrong, R. A.; Aubert, M.; Eggins, S.; Grün, R. Improvement of laser ablation in situ micro-analysis to identify diagenetic alteration and measure strontium isotope ratios in fossil human teeth. *J. Archaeol. Sci.* **2016**, *70*, 102−116.

(14) Nemliher, J. G.; Baturin, G. N.; Kallaste, T. E.; Murdmaa, I. O. Transformation of hydroxyapatite of bone phosphate from the ocean bottom during fossilization. *Lithol. Miner. Resour.* **2004**, *39*, 468−479.

(15) Keenan, S. W.; Engel, A. S.; Roy, A.; Bovenkamp-Langlois, G. L. Evaluating the consequences of diagenesis and fossilization on bioapatite lattice structure and composition. *Chem. Geol.* **2015**, *413*, 18−27.

(16) Keenan, S. W. From bone to fossil: A review of the diagenesis of bioapatite. *Am. Mineral.* **2016**, *101*, 1943−1951.

(17) Hedges, R. E. M. Bone diagenesis: an overview of processes. *Archaeometry* **2002**, *44*, 319−328.

(18) Nielsen-Marsh, C. M.; Hedges, R. E. M. Patterns of diagenesis in bone I: the effects of site environments. *J. Archaeol. Sci.* **2000**, *27*, 1139−1150.

(19) Penel, G.; Leroy, G.; Rey, C.; Bres, E. MicroRaman spectral study of the PO_4 and CO_3 vibrational modes in synthetic and biological apatites. *Calcif. Tissue Int.* **1998**, *63*, 475−481.

(20) Jochum, K. P.; Willbold, M. Reference materials in geo-analytical research − review for 2004 and 2005. *Geostand. Geoanal. Res.* **2006**, *30*, 143−156.

(21) *NIST SRM 1400 Bone Ash Certificate of Analysis*; NIST: Gaithersburg, 1992; http://www.nist.gov/srm (accessed Jan 29, 2019).

(22) *NIST SRM 1486 Bone Meal Certificate of Analysis*; NIST: Gaithersburg, 1992; http://www.nist.gov/srm (accessed Jan 29, 2019).

(23) Guillong, M.; Hametner, K.; Reusser, E.; Wilson, S. A.; Günther, D. Preliminary characterisation of new glass reference materials (GSA-1G, GSC-1G, GSD-1G and GSE-1G) by laser ablation-inductively coupled plasma-mass spectrometry using 193 nm, 213 nm and 266 nm wavelengths. *Geostand. Geoanal. Res.* **2005**, *29*, 315−333.

(24) Liu, Y.; Hu, Z.; Gao, S.; Günther, D.; Xu, J.; Gao, C.; Chen, H. In situ analysis of major and trace elements of anhydrous minerals by LA-ICP-MS without applying an internal standard. *Chem. Geol.* **2008**, *257*, 34−43.

(25) LeGeros, R. Z.; Suga, S. Crystallographic nature of fluoride in enameloids of fish. *Calcif. Tissue Int.* **1980**, *32*, 169−174.

(26) LeGeros, R. Z.; Go, P.; Suga, S. Fluoride in fish enameloids: X-ray diffraction and spectroscopic studies. *J. Dent. Res.* **1978**, *57A*, 280.

(27) McConnell, D. *Apatite: Its Crystal Chemistry, Mineralogy, Utilization, and Geologic and Biologic Occurrences*; Springer Verlag: Wien, 1973; 111 p.

(28) Franzini, M.; Leoni, L.; Saitta, M. Revisione di una metodologia analitica per fluorescenza-X, basata sulla correzione completa degli effetti di matrice. *Rend. Soc. Ital. Mineral. Petrol.* **1975**, *31*, 365−378.

(29) Lübke, A.; Enax, J.; Loza, K.; Prymak, O.; Gaengler, P.; Fabritius, H.-O.; Raabe, D.; Epple, M. Dental lessons from past to present: ultrastructure and composition of teeth from plesiosaurs, dinosaurs, extinct and recent sharks. *RSC Adv.* **2015**, *76*, 61612−61622.

(30) Praamsma, M. L.; Parsons, P. J. Characterization of calcified reference materials for assessing the reliability of manganese determinations in teeth and bone. *J. Anal. At. Spectrom.* **2014**, *29*, 1243−1251.

(31) Nardelli, M. P.; Malferrari, D.; Ferretti, A.; Bartolini, A.; Sabbatini, A.; Negri, A. Zinc incorporation in the miliolid foraminifer *Pseudotriloculina rotunda* under laboratory conditions. *Mar. Micropaleontol.* **2016**, *126*, 42−49.

(32) Castellini, E.; Malferrari, D.; Bernini, F.; Brigatti, M. F.; Castro, G. R.; Medici, L.; Mucci, A.; Borsari, M. Baseline studies of The Clay Minerals Society Source Clay montmorillonite STx-1b. *Clays Clay Miner.* **2017**, *65*, 220−233.

(33) Brigatti, M. R.; Malferrari, D.; Medici, L.; Ottolini, L.; Poppi, L. Crystal chemistry of apatites from the Tapira carbonatite complex, Brazil. *Eur. J. Mineral.* **2004**, *16*, 677−685.

(34) Lafon, J. P.; Champion, E.; Bernache-Assollant, C. D.; Gibert, R.; Danna, A. M. Thermal decomposition of carbonated calcium phosphate apatites. *J. Therm. Anal. Calorim.* **2003**, *72*, 1127−1134.

(35) Tõnsuaadu, K.; Peld, M.; Bender, V. Thermal analysis of apatite structure. *J. Therm. Anal. Calorim.* **2003**, *72*, 363−371.

(36) Figg, D. J.; Cross, J. B.; Brink, C. More investigations into elemental fractionation resulting from laser ablation inductively coupled plasma mass spectrometry on glass samples. *Appl. Surf. Sci.* **1998**, *127−129*, 287−291.

(37) Hattendorf, B.; Günther, D. Laser Ablation Inductively Coupled Plasma Mass Spectrometry (LA-ICPMS). *Handbook of Spectroscopy*, 2nd enlarged ed.; Gauglitz, G., Moore, D. S., Eds.; Wiley-VCH Verlag GmbH & Co. KGaA, 2014; pp 647−698.

SUPPORTING INFORMATION

How much can we trust major element quantification in bioapatite investigation?

Daniele Malferrari [a, *], Annalisa Ferretti [a], Maria Teresa Mascia [b],

Martina Savioli [a], Luca Medici [c]

(a) Department of Chemical and Geological Sciences, University of Modena and Reggio Emilia, Via Campi 103, I–41125 Modena, Italy

(b) Department of Diagnostics, Clinical and Public Health Medicine, University of Modena and Reggio Emilia, Via Campi 213/b, I–41125 Modena, Italy

(c) National Research Council of Italy, Institute of Methodologies for Environmental Analysis, C.da S. Loja–Zona Industriale, I–85050 Tito Scalo (Potenza), Italy

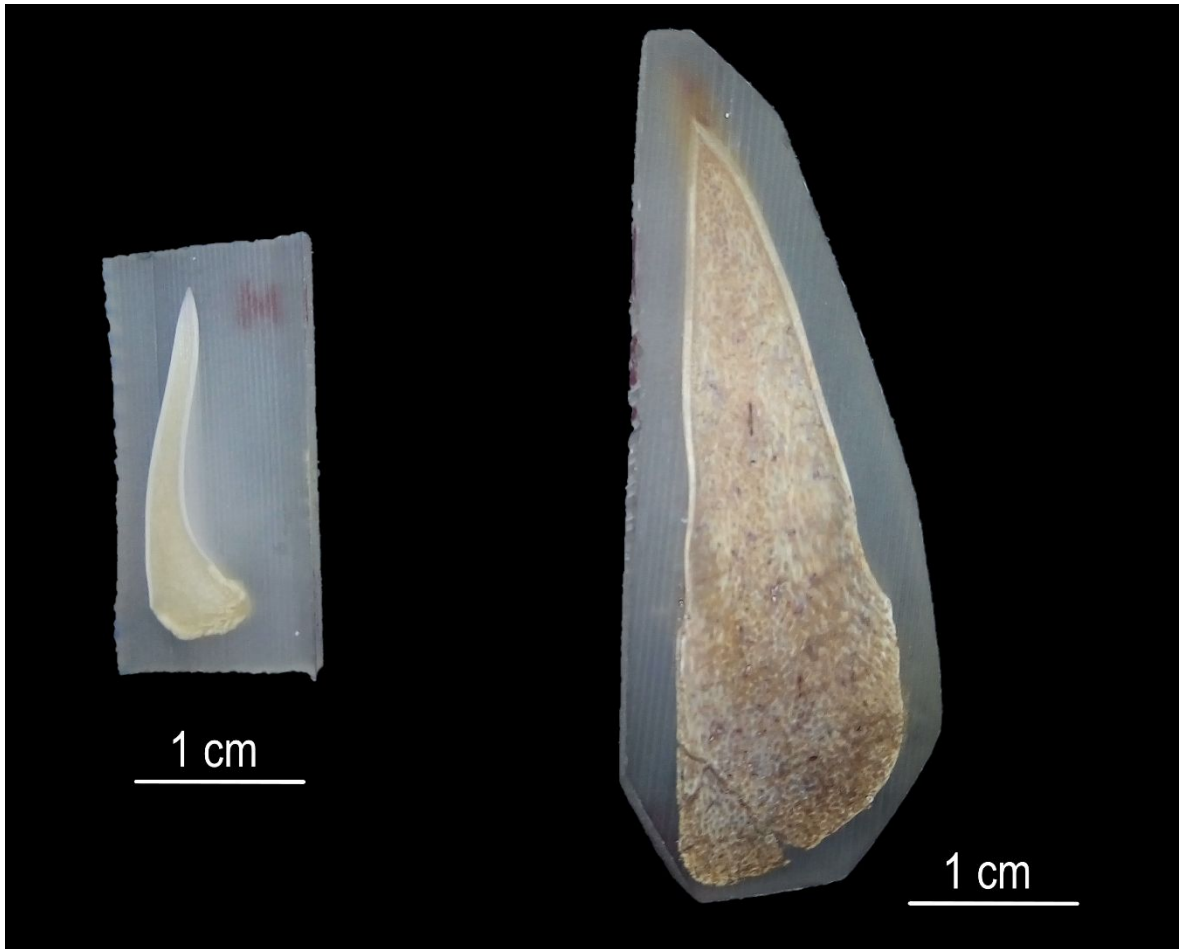(*) Corresponding author – daniele.malferrari@unimore.it

Figure S1. Shark teeth analysed in this paper after cutting and incorporation in resin. Living *Charcharias taurus* (left) and Paleogene *Otodus* sp. (right).

Table S1. Optimized laser parameters. A pre-ablation was applied both to standards and samples applying a laser intensity of 10%.

	Laser intensity (%)	Frequency (Hz)	Ablation line width (μm)	Duration (s)	Laser fluence J/cm^2 (*)
HMMS	50	10	55	240	7.6.
SRM 1400	50	10	55	240	7.4
SRM 1486	50	10	55	240	7.7

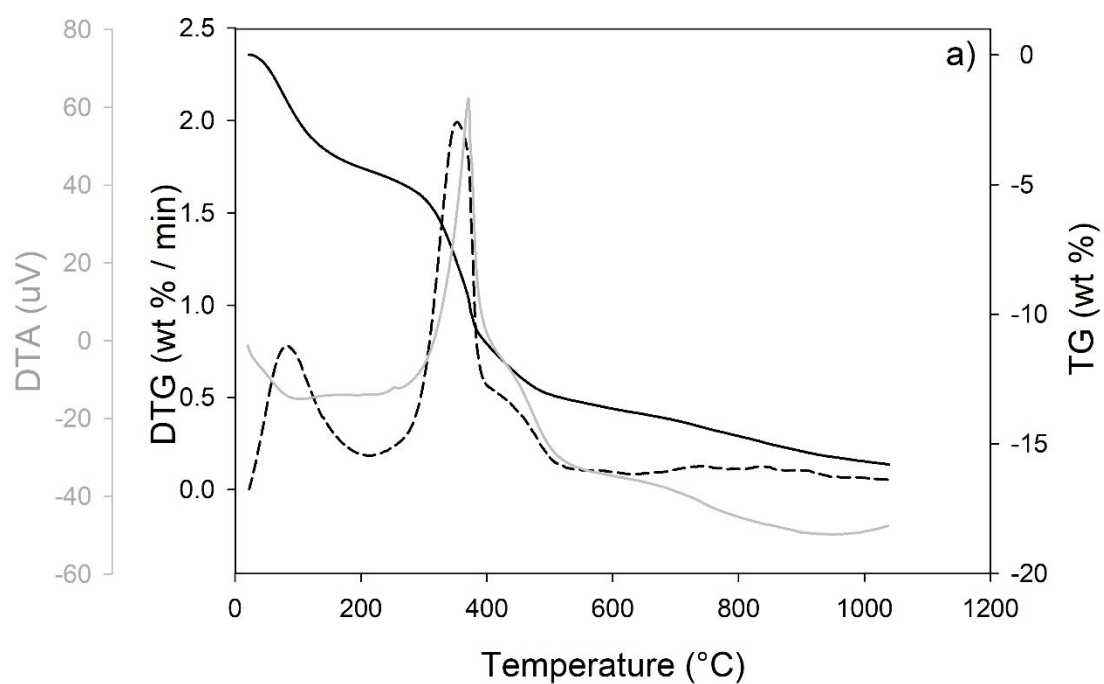(*) Average value measured for the four points of the calibration curve.
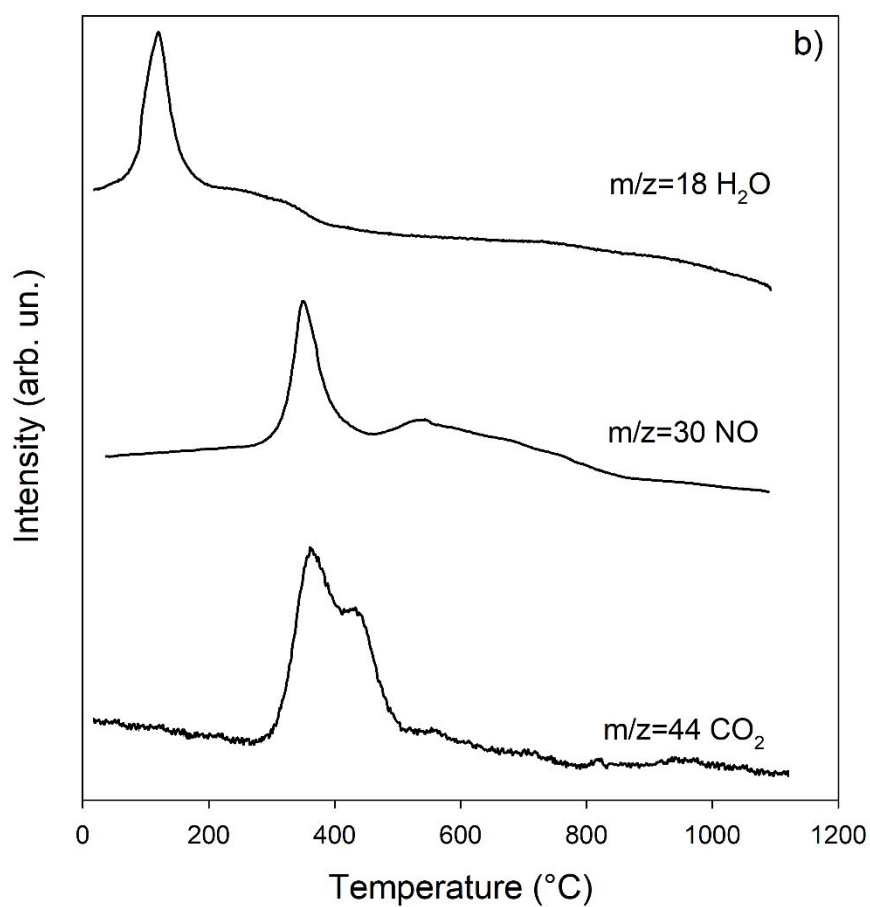
Figure S2. (a) TG (solid black line), DTG (dashed black line), and DTA (solid grey line) and (b) MSEGA curves for enameloid from the living shark *Charcharias taurus*.
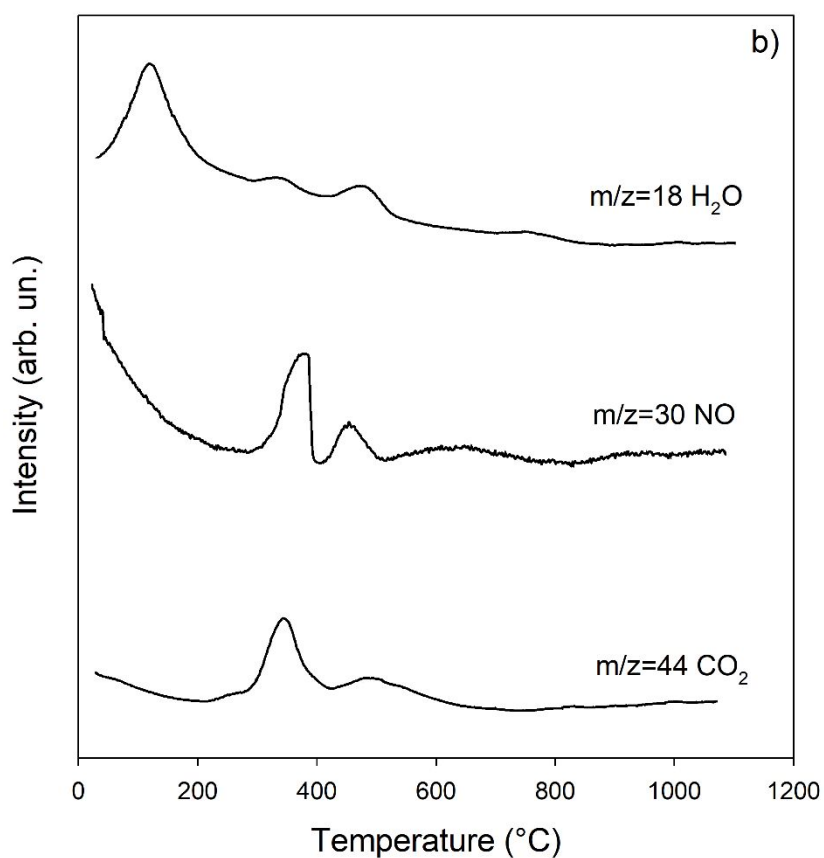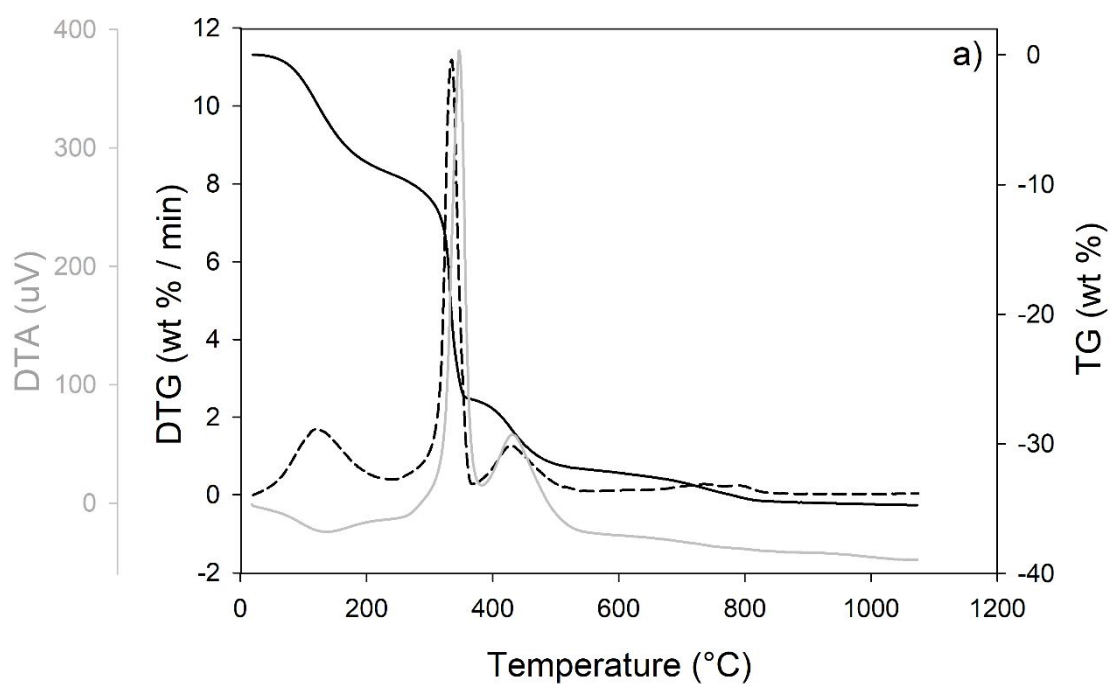
Figure S3. (a) TG (solid black line), DTG (dashed black line), and DTA (solid grey line) and (b) MSEGA curves for dentin from the living shark *Charcharias taurus*.
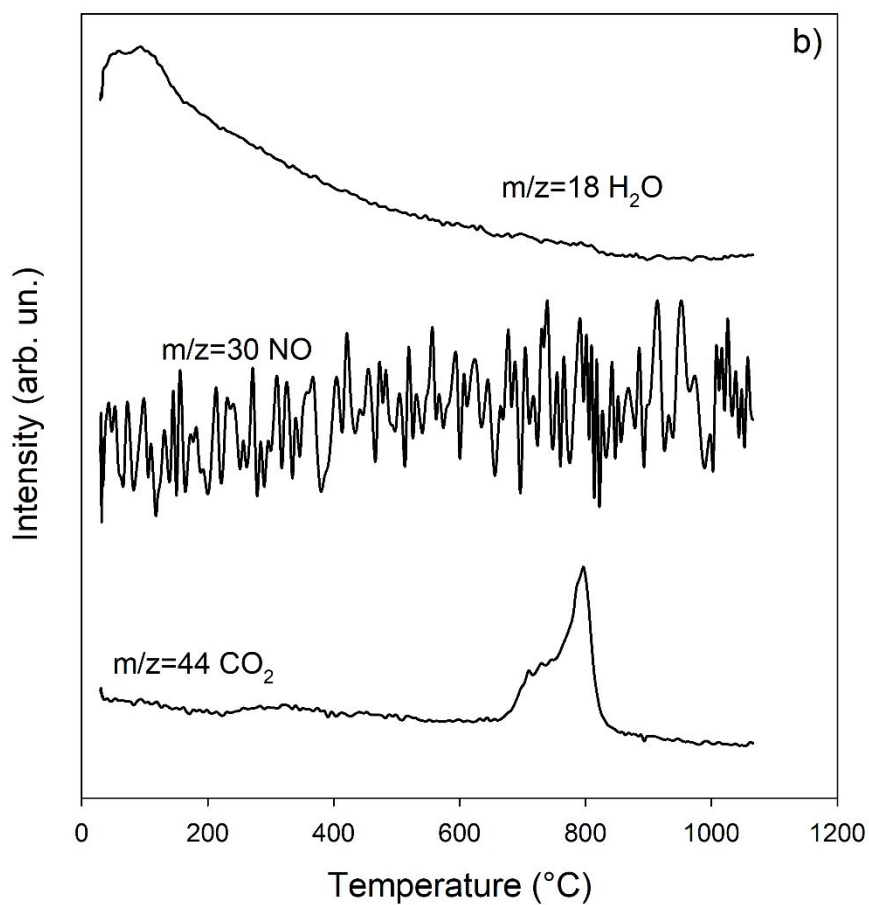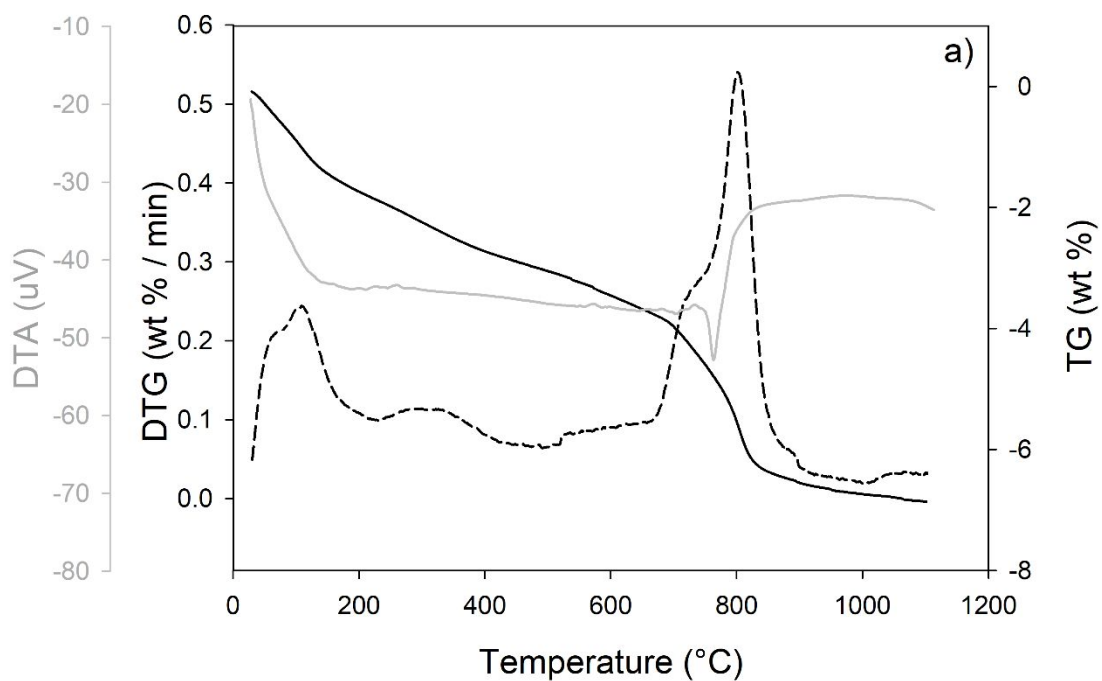
Figure S4. (a) TG (solid black line), DTG (dashed black line), and DTA (solid grey line) and (b) MSEGA curves for enameloid from the fossil shark *Otodus* sp.
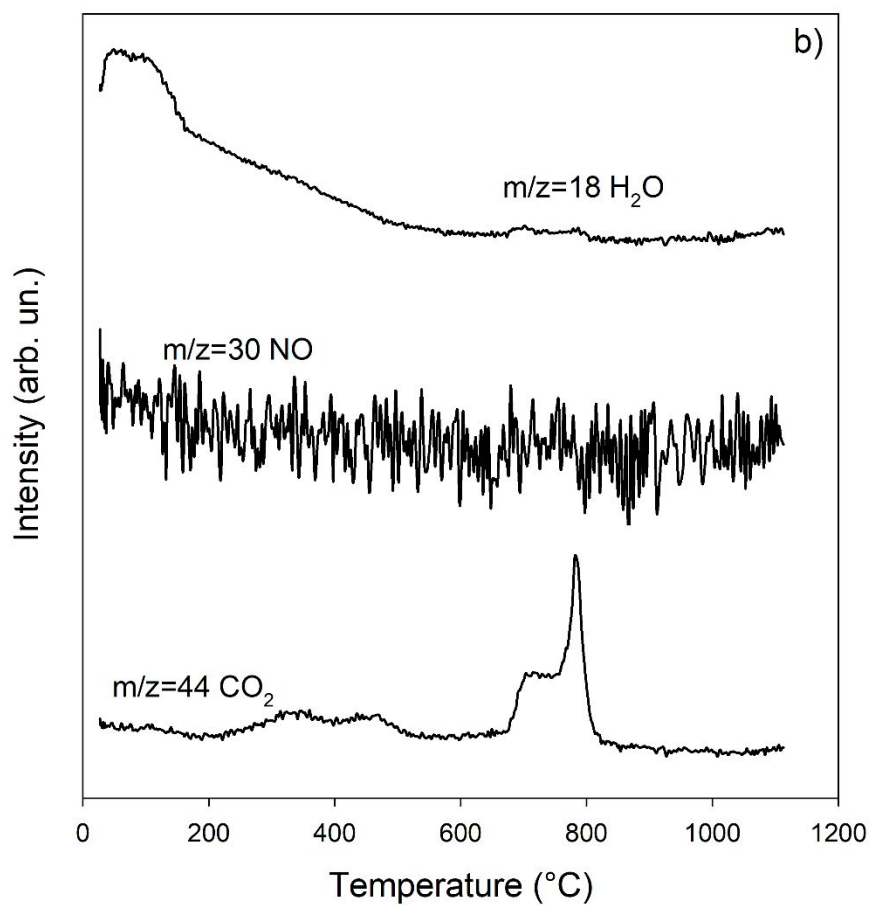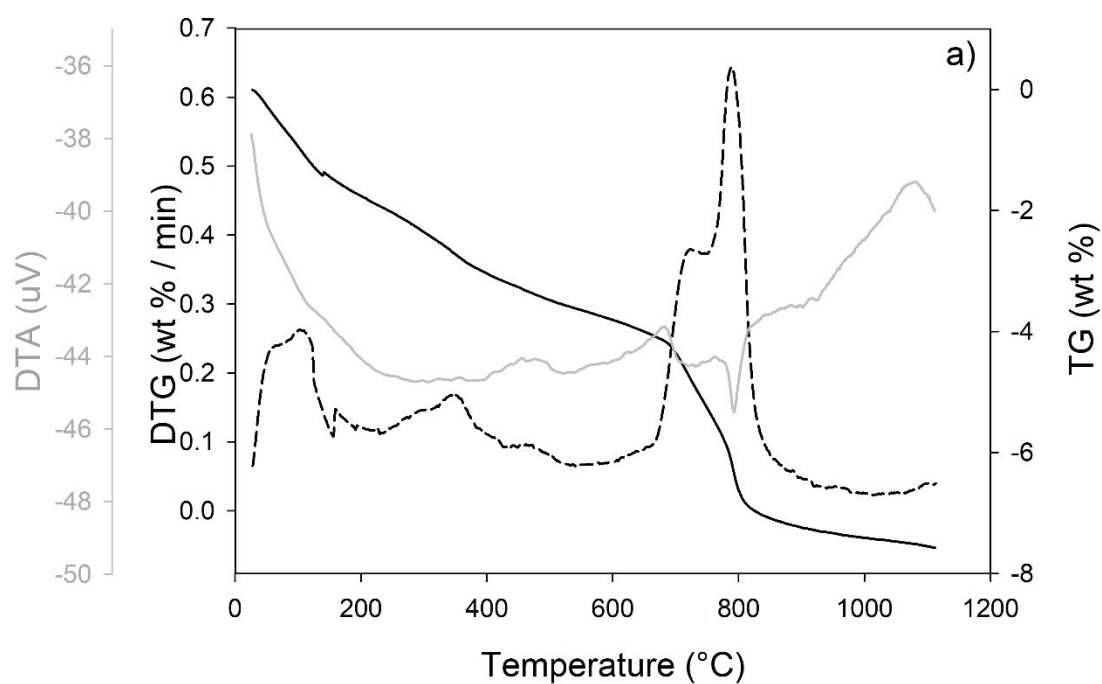
Figure S5. (a) TG (solid black line), DTG (dashed black line), and DTA (solid grey line) and (b) MSEGA curves for dentin from the fossil shark *Otodus* sp.

Table S2. Atoms per formula unit for living and fossil shark teeth measured with LA-ICPMS, XRF, and ICP-OES. Here are reported the same values as in Tables 2 and 3, but grouped for sample rather than methodology to simplify the reading of the discussion. Labels and abbreviations as in Tables 2 and 3.

		P	Ca	Mg	Na	K	Si	Al	Fe	Ca/P
LA-ICPMS	*C. taurus* D. - average	5.715	9.493	0.189	0.512	0.073	0.002	0.001	0.014	1.661
XRF	*C. taurus* D.	5.441	9.751	0.099	0.652	0.057	n.c.	n.c.	n.c.	1.792
ICP-OES	*C. taurus* D.	5.485	9.654	0.237	0.568	0.037	0.002	0.002	0.016	1.760
LA-ICPMS SRM 1486	*C. taurus* D. - average	5.308	9.885	0.208	0.496	0.087	0.002	0.001	0.012	1.862
	ST.DEV.	*0.170*	*0.165*	*0.059*	*0.070*	*0.022*	*0.000*	*0.000*	*0.002*	*0.084*
LA-ICPMS	*C. taurus* E. - average	5.450	9.893	0.227	0.384	0.030	0.001	0.002	0.013	1.815
XRF	*C. taurus* E.	5.655	9.598	0.106	0.572	0.068	n.c.	n.c.	n.c.	1.697
ICP-OES	*C. taurus* E.	5.685	9.584	0.219	0.466	0.030	0.001	0.001	0.014	1.686
LA-ICPMS SRM 1486	*C. taurus* E. - average	5.337	10.039	0.210	0.366	0.031	0.001	0.002	0.013	1.881
	ST.DEV.	*0.167*	*0.225*	*0.057*	*0.094*	*0.019*	*0.000*	*0.000*	*0.001*	*0.094*
LA-ICPMS	*Otodus* sp. D. - average	4.975	9.958	0.229	0.433	0.053	0.223	0.071	0.057	2.002
XRF	*Otodus* sp. D.	4.951	9.949	0.257	0.415	0.056	0.253	0.066	0.053	2.010
ICP-OES	*Otodus* sp. D.	4.988	9.947	0.228	0.433	0.053	0.223	0.071	0.057	1.994
LA-ICPMS SRM 1400	*Otodus* sp. D. - average	4.968	9.986	0.226	0.420	0.053	0.217	0.076	0.053	2.010
	ST.DEV.	*0.015*	*0.018*	*0.015*	*0.009*	*0.002*	*0.016*	*0.004*	*0.002*	*0.008*
LA-ICPMS	*Otodus* sp. E. - average	5.202	9.835	0.206	0.376	0.051	0.223	0.056	0.051	1.891
XRF	*Otodus* sp. E.	5.040	9.964	0.221	0.371	0.062	0.236	0.052	0.054	1.977
ICP-OES	*Otodus* sp. E.	5.158	9.860	0.202	0.400	0.054	0.222	0.053	0.052	1.912
LA-ICPMS SRM 1400	*Otodus* sp. E. - average	5.079	9.963	0.204	0.382	0.044	0.225	0.052	0.050	1.961
	ST.DEV.	*0.073*	*0.068*	*0.009*	*0.013*	*0.008*	*0.006*	*0.002*	*0.002*	*0.041*

ANNEX-2

<u>Annex-2a</u>: *Unravelling the ultrastructure and mineralogical composition of fireworm stinging bristles*

Sara Righi, Martina Savioli, Daniela Prevedelli, Roberto Simonini & Daniele Malferrari

Zoology (2021)

<u>Annex-2b</u>: *Commentary on: "Unravelling the ultrastructure and mineralogical composition of fireworm stinging bristles" by Righi et al., 2020*
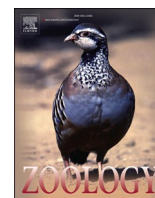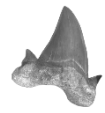
Ekin Tilic & Thomas Bartolomaeus

Zoology (2021)

Response to Tilic and Bartolomaeus's Commentary on the original Research Paper: "Unravelling the ultrastructure and mineralogical composition of fireworm stinging bristles" (Zoology, 144)

Sara Righi, Martina Savioli, Daniela Prevedelli, Roberto Simonini & Daniele Malferrari

Zoology (2021)

Unravelling the ultrastructure and mineralogical composition of fireworm stinging bristles

Sara Righi [a,b,*], Martina Savioli [b], Daniela Prevedelli [a], Roberto Simonini [a], Daniele Malferrari [b]

[a] *Department of Life Sciences, University of Modena and Reggio Emilia, Via Campi 213/D, 41125 Modena, Italy*
[b] *Department of Chemical and Geological Sciences, University of Modena and Reggio Emilia, Via Campi 103, 41125 Modena, Italy*

ARTICLE INFO

ABSTRACT

Amphinomid fireworms are notorious for their stinging dorsal bristles (notochaetae), but it is still unclear whether the irritation they cause is merely mechanical or if the notochaetae contain toxins. Furthermore, although fireworm chaetae have always been described as calcareous, their composition has never been investigated to date and strong debates are ongoing on their internal structure. Unravelling the native ultrastructure and composition of fireworm chaetae is the first crucial step to assess whether the hypothesis of toxin vehiculation could be fully considered.

We examined for the first time the chemical and mineralogical composition, the ultrastructure and the external structure of the dorsal and ventral chaetae of the large species *Hermodice carunculata*. All the measurements were carried out on samples prepared without the use of chemical reagents, except for those targeted to investigate if decalcification altered the ultrastructure of the chaetae. A crystal-chemical strategy, combining chemical, diffraction and thermal analyses clearly showed the occurrence of crystalline calcium carbonate and clusters of phosphatic amorphous material. Scanning electron micrographs and energy dispersive X-ray measurements showed that the dorsal chaetae have an extremely shallow insertion point in the body respect to the ventral chaetae, that could facilitate the release of the notochaetae in the environment. Their proximal part is characterized by canals with a hexagonal pattern rich in Ca and P, followed by a large cavity upwards. The harpoon-shaped ends and the central canals of the notochaetae completely disappeared after exposure to EDTA. The notochaetae are hollow and may be able to vehicle toxins. The absence of the honeycomb pattern in the distal part of the notochaetae and their slenderness probably contribute to their brittleness and high sensitivity to breakage on contact. These observations constitute keystone understandings to shed light on fireworm defensive and offensive capacities and their ecological success.

1. Introduction

Annelid chaetae are chitinous structures showing a broad array of forms (e.g. uncini, pectinate chaetae, composite spiningers and falcigers; Day, 1967; Fauchald, 1977). They are largely composed by an organic phase of β-chitin (a linear polysaccharid) bounds with tanned proteins and the degree of sclerotization determines their hardness and rigidity (Rouse and Pleijel, 2001). Some chaetae may also contain a mineral phase, like calcium carbonate, which makes them harder (Rouse and Pleijel, 2001).

In general, chaetae are symmetrically arranged in pair on dorsal and ventral ramous of parapodia, appendages of the body wall for each segment (Schroeder, 1984; Beesley et al., 2000; Rouse and Pleijel, 2001). Dorsal and ventral chaetae (notochaetae and neurochaetae, respectively) may resemble each other, or they may have different structures. Indeed, although chaetal ultrastructure is frequently similar, a considerable diversity of external forms occurs (Fauchald, 1977). The typical chaeta is more or less elongated and composed by many longitudinal hollow canals, which are tightly packed in a honeycomb hexagonal pattern (Schroeder, 1984; Hausen, 2005). Ultrastructural studies evidenced that each chaeta origins from a chaetal follicle, which consists of follicular cells and a basal chaetoblast with a fibrillar apical structure made up of microvilli. The chaetae grow up by basal apposition of chaetal matrix, which is assembled on the microvilli. Narrow canals

---

remain where the microvilli once had been but, during chaetal development, the central canals become usually larger than the peripheral ones. The construction of hollow canals is responsible for the mechanical properties of the chaetae, since changes in number of canals, wall thickness and diameter could significantly affect their flexibility and hardness (Hausen, 2005).

Amphinomid annelids have always fascinated biologists for the stinging capacity and calcareous nature of their notochaetae (Schroeder, 1984). They are commonly known as "fireworms" because they cause a painful burning sensation when touched (Kicklighter and Hay, 2006). The fireworms belonging to the genera *Eurythoe*, *Hermodice* and *Notopygos* display deterrent capacities against predators due to tufts of notochaetae which are extended when the worms are threatened (Coutinho et al., 2018; Verdes et al., 2018). The amphinomid notochaetae display unique features among annelids: they are needle-like, stiff and fragile. When the worm is contracted, the notochaetae become flared and easily detach from the fireworm body spreading in the seawater, even if no contact triggering the release occurs. The notochaetae could be capillary or may present harpoon-like ends (Fauvel, 1923). In contrast, the neurochaetae are similar to the chaetae of most polychaetes: they are non-stinging and involved in locomotion. The distal part of the neurochaetae has coarse serrations, lacks armor-piercing ends and is flexible and strongly attached to the body (Yáñez-Rivera and Salazar-Vallejo, 2011; Yáñez-Rivera and Brown, 2015; Schulze et al., 2017).

Penetration of *Eurythoe* and *Hermodice* notochaetae in the skin causes immediate intense burning and stinging pain, erythema and paresthesia in the affected area. Rarely, more serious systemic reactions may follow the injury, such as respiratory reactions, nausea and fever (Ottuso, 2013). There is strong debate over the potential toxic properties of the notochaetae, with some authorities suggesting that a venom is associated with them (Nakamura et al., 2008, 2010; Borda et al., 2012; von Reumont et al., 2014). The idea that amphinomids are equipped with hollow chaetae acting as needles to inject poison into predators has been largely supported (Day, 1967; Nakamura et al., 2008; von Reumont et al., 2014; Schulze et al., 2017). Gustafson (1930) reported that the chaetal core was filled with a clear gelatinous substance consisting of fibrils with hexagonal cross-sections. He attributed the toxic nature of the chaetae to this substance and claimed that only the outer layer of the chaetae is calcareous. Schulze et al. (2017) observed that the chaetae core appeared hollow at light microscopy and that a small amount of fluid seemed to be released from the tip of the chaeta.

The first scanning electron microscopic investigation was made by Eckert (1985) on fixed specimens of the amphinomids *Chloeia flava*, *Eurythoe complanata* and *Pherecardia striata*. The close-up of a chaeta section revealed a structure consisting of a large hollow canal surrounded by packed hollow tubules. However, rather than contain toxin they were considered to make chaetae large and conspicuous as deterrents to predators, while the fragmentation of the chaetae in the wound and the microflora on their surface may be responsible for the burning reaction and allergy symptoms. Indeed, no potential poison glands were observed in the parapodia (Eckert, 1985). Based on the chaetogenesis, Tilic et al. (2017) argued that the chaetae of *E. complanata* are not hollow. They assumed that calcium containing inorganic matter, characterized by a structure similar to that of apatite, must be deposited between the canals at a later stage. These depositions cause artificial ruptures of the fine chitinous canals, especially when the chaetae are treated with acid fixatives, and result in the formation of the hollow cavity. Tilic et al. (2017) did not observed any evidence neither for apical or basal pores in the chaetae nor for the presence of poison glands releasing secretions into the chaetal cavity. Thus they rejected the hypothesis of notochaetae as hollow needles for toxin delivering.

In this study, we aimed at clarifying the conflicting evidences related to the structure of the amphinomid chaetae, examining both the external morphology and ultrastructure to unravel their potential role in toxin vehiculation. Furthermore, we defined the chemical and mineralogical composition of the chaetae, which is still almost unexplored and could influence the mechanical properties of the structures. Indeed, despite fireworm chaetae have been frequently defined as calcareous (Fauvel, 1953; Day, 1967; Beesley et al., 2000; Yáñez-Rivera and Salazar-Vallejo, 2011; Borda et al., 2012), just very few, partial studies were published on this issue (e.g. George and Southward, 1973; Schroeder, 1984). We used the bearded fireworm *Hermodice carunculata* (Pallas, 1766) as a model species (see Fig. S1). It is a common, large sized generalist predator/scavenger in Atlantic and Mediterranean rocky reef ecosystems (Simonini et al., 2017, 2018; Righi et al., 2020). The external morphology and the ultrastructure of the chaetae were investigated both in native chaetae (i.e. chaetae not treated with chemical agents), and in chaetae treated with a solution of calcium chelate (EDTA). All these analyses investigated both the noto- and neurochaetae, whose ultrastructure has never been described before to the best of our knowledge for the bearded fireworm. The chemical and mineralogical composition of fireworm chaetae was examined applying crystal-chemical methods. The data gathered provide insights into the structure and composition of the amphinomid chaetae, leading to critical hypotheses on their role in fireworm stinging capacities and hence ecological success.

2. Materials and methods

2.1. Animal collection

H. carunculata specimens were collected along the Apulian coast (Italy) and kept in an aquarium system under controlled conditions (temperature: 24-25 °C; photoperiod: 16 h light / 8 h dark; salinity: 32-36; total volume: 600 L) (Simonini et al., 2018). Before the collection of the chaetae, specimens of *H. carunculata* were anesthetized using a solution of 7% $MgCl_2$ and seawater (1:1) for 2 h. Gills were removed from parapodia and the animals were immersed in distilled water to reduce the excess of inorganic salts.

2.2. Chemical and mineralogical methods

2.2.1. Preparation of the chaeta samples

The noto- and neurochaetae were gently separated from the tissue of the parapodia by pulling with fine tweezers, transferred on filter paper and ground in an agate mortar. The fine, homogeneous powders obtained were washed with Millipore water, dried at 30 °C for 24 h and stored in a dryer until measurement. If not explicitly indicated, no further treatment was carried out before measurements. The removal of the chaetae by pulling forced the detachment of dorsal and ventral cirri (outgrowths with sensory function), that got trapped in the chaeta samples.

2.2.2. Chemical composition assessment

Major elements concentration was measured through Inductively Coupled Plasma-Optical Emission Spectroscopy (ICP-OES, Perkin Elmer Optima 4200 DV) in solutions obtained by acid digestion of the chaeta powders after calcination at 900 °C for 1 h. The calibration of the instrument was carried out with Perkin Elmer certified standard solutions. Given that a valid internal reference standard is not available, major elements concentration was also measured through a wavelength dispersive Philips PW 1480 X-Ray Fluorescence (XRF) spectrometer (Philips, Almelo, The Netherlands) on powder pressed pellets prepared from the same calcinated powder used for ICP-OES measurements. This second analysis was carried out to highlight any interference attributable to matrix effects (Malferrari et al., 2019). The Elemental Analysis (EA) was performed to assess the amount of carbon and nitrogen using a FLASH 2000 Thermo-Fischer Scientific Elemental Analyser. Then, organic carbon was calculated as the difference between total carbon (EA) and carbon bond to carbonates measured through thermal analyses (see the paragraph 2.2.3 "Thermal analyses").

2.2.3. Thermal analyses

Thermogravimetric (TGA) measurements were carried out with a Seiko SSC 5200 thermal analyzer equipped with a quadrupole mass spectrometer (ESS, GeneSys Quadstar 422) to analyze the gas produced during thermal reactions (Evolved Gas Analysis, MSEGA). Gas was sampled via an inert, fused silicon capillary system heated to prevent gases condensing. Background subtraction was applied to obtain the point zero conditions before starting evolved gases analysis. Mass analyses were carried out in multiple ion detection mode measuring the mass-to-charge (m/z) ratios 18, 30, 44, and 64 to detect the release of H_2O, NO, CO_2 and SO_2, respectively; SEM and FARADAY detector were set at 900 V with 0.5 s of integration time on each measured mass.

2.2.4. X-ray powder diffraction

X-Ray Powder Diffraction (XRPD) patterns were recorded from randomly oriented powder grain mounts at room temperature using a Philips X'Pert PRO diffractometer equipped with first generation Real Time Multiple Strip (RTMS) detector. Additional XRPD patterns were recorded from randomly oriented powder grain mounts in the temperature range 25-900 °C (heating rate 10 °C/min) equipping the diffractometer with an HTK16 Anton Paar in situ heating apparatus. The pattern analyses were carried out through the software X-Pert High Score Plus.

Further details on the experimental conditions set are reported in the Supplementary material.

2.3. Structural and ultrastructural analyses

The notopodia and neuropodia (including the chaetal sacs) were carefully dissected from the relaxed animals and rinsed in distilled water.

To analyze the external morphology of the chaetae, the dissected parapodia were air-dried on filter paper and the tips of the chaetae were placed in contact with a double-sided adhesive tape. At the contact with the adhesive surface, the chaetae were naturally pulled out from the parapodium to adhere to the tape. The external morphology of the chaetae was further investigated with a FEI Nova NanoSEM™ scanning electron microscope equipped with an energy dispersive X-ray detector (X-EDS Bruker Quantax-200) (see the Supplementary material for the acquisition conditions).

The inner ultrastructure of the chaetae was examined both in the portion fully emerged from the parapodium (hereafter "distal part") and in the portion embedded into tissues (hereafter "proximal part"). When the distal part was investigated, the parapodia were dissected and grabbed with tweezers from the side of fleshy tissues to avoid damages to the tips of the chaetae due to manipulation. In contrast, when the proximal part was studied, the tips of the chaetae were grabbed with the tweezers and the parapodia were isolated cutting through the tissues far away from the proximal part of the chaetae. To obtain an accurate chemical and mineralogical characterization and limit damages to chaetae morphology, a preparatory procedure without interaction with chemical reagents was adopted. Therefore, the parapodia were dried for 10 min at 50 °C, embedded in epoxy resin for 48 h and cut up using a high-precision wire saw (model AGB9001, from Agar Scientific) equipped with a diamond-coated cutting wire to obtain a surface showing the cross-sections of the distal or proximal part of the chaetae. This method has been applied to annelid chaetae for the first time, but was already used on crustacean cuticles and cirratulid, sabellid, serpulid tubes and vertebrate teeth to prepare polished samples suitable for scanning electron microscopy (Vinn, 2008, 2009; Vinn et al., 2008; Cribb et al., 2009; Vittori et al., 2018; Malferrari et al., 2019). Sub-micrometric (0.05 μm) and chemically inert aluminum oxide and silicon carbide were used to polish the surfaces. Finally, the resin blocks were cleaned in an ultrasonic bath in Millipore water for 3 min and air-dried.

To investigate if decalcification could alter the ultrastructure of the chaetae, a drop of 10% sodium ethylenediaminetetraacetate (EDTA) was deposited on the surface of some parapodia embedded in the resin blocks and removed after 30 min with absorbent paper. All the cross-sections in epoxy resin were gold sputtered and preliminary observed using an Environmental Scanning Electron Microscope (ESEM™). The beam was operated at 25 kV under high vacuum with simultaneous observation of secondary electron (SE) and backscattered (BSE) signals. The elemental and chemical analysis of prominent inorganic constituents was made by electron probe microanalysis with an Energy Dispersive X-ray Spectrometer (X-EDS, Oxford Instruments) equipped with Oxford's INCA Energy 350 software package.

Dimensional changes after EDTA treatment were detected using the software ImageJ on SEM images (Ferreira and Rasband, 2012).

2.4. Decalcification of chaetae

Undamaged notochaetae were obtained by grasping with tweezers the base of the notopodium at chaetigers 9-11 and pushing gently a small cotton swab next to the flared tuft. The notochaetae detached from the parapodium were picked up from the cotton with tweezers under a stereomicroscope and placed in a drop of glycerol prepared on a microscope slide. The neurochaetae did not detach easily and did not remain attached to the cotton. Thus, they were gently separated from the tissues of the parapodium by pulling using tweezers and directly mounted in glycerol on a microscope slide. The procedure was repeated for three worms. To assess the presence of an external calcium carbonate layer, noto- and neurochaetae were obtained from other three fireworms using the same protocol as before but mounting in 10% EDTA:glycerol 1:1 for decalcification. Chaetae from both treatments were measured 1 h after mounting. Since chaetae have a cylindric shape, their boundary could be easily defined under a light microscope with an ocular micrometer (see also Merz and Woodin, 1991). For the notochaetae, the maximum thickness along the length (hereafter "thickness") and the thickness at the last serration of the harpoon were measured. In the case of the neurochaetae, the thickness and the thickness at the spur were measured. The thickness of noto- and neurochaetae in control (glycerol) and decalcification treatments (EDTA-glycerol) was compared by means of one-way ANOVA (n = 27 for both groups). Data analyses were performed using the software PAST (Hammer et al., 2001).

3. Results

3.1. Crystal-chemical characterization of the chaetae

Major elements chemical analyses from ICP-OES (Table 1) are in full agreement with those obtained through XRF (Table S1). These results did not highlight significant differences between noto- and neurochaetae, with the exception of Mg whose concentration is about 30% higher in the neurochaetae. In contrast, EA results indicate that C and N amounts are significantly lower in the neurochaetae rather than in the notochaetae (Table 1). The occurrence of significant amounts of Ca and C in both samples is in nice agreement with XRPD results (Fig. S2). However, XRPD analyses reveal that $CaCO_3$ is the only crystalline phase, thus indicating that a relevant part of the chaetae is formed by amorphous material, including the organic chitinous fraction.

TGA-MSEGA measurements for neuro- and notochaetae are compared in Fig. 1(A-D). The thermal events occurring in the noto- and neurochaetae are basically matching, with some minor and not relevant differences mainly ascribable to the weight loss and to the temperature values of maximum reaction rate.

The first derivative of the thermogravimetric curves (DTG) shows three main reactions (Fig. 1A). The first two occurred in the thermal ranges 25-215 and 215-475 °C and produced a mass variation of 15.5 and 11.1 wt% in the neurochaetae, 13.7 and 12.8 wt% in the notochaetae, respectively (TG curve, Fig. 1A). These reactions are related to the thermal decomposition of chitin, as confirmed by evolved gas mass spectrometry. More in detail, the first reaction corresponds to the release

Table 1

Major constituents (oxide wt%) and elemental (element wt%) chemical analyses of neuro- and notochaetae. Each value is the average of three replicates (*SD*, standard deviation). LOI, Loss On Ignition at 900 °C.

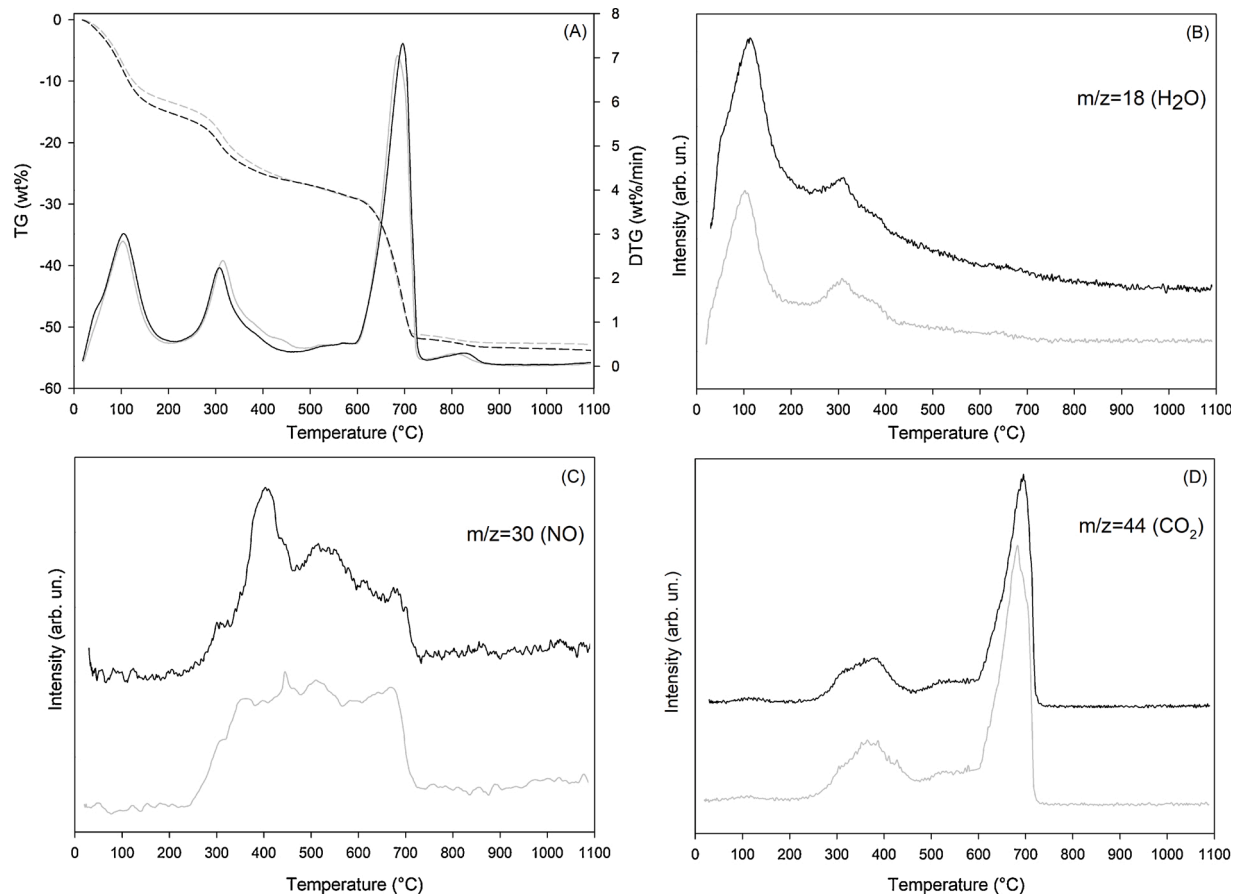|	SiO_2	Al_2O_3	K_2O	Na_2O	MgO	CaO	Fe_2O_3	MnO	P_2O_5	TiO_2	LOI	N	C
Neurochaetae	0.017	0.005	0.165	1.811	4.920	31.66	0.015	0.006	7.580	0.001	53.74	1.21	12.5
SD	*0.012*	*0.001*	*0.008*	*0.109*	*0.135*	*0.34*	*0.004*	*0.001*	*0.036*	*0.001*	*0.19*	*0.03*	*0.01*
Notochaetae	0.013	0.005	0.170	1.932	3.801	32.46	0.021	0.004	7.680	0.001	53.67	1.45	13.3
SD	*0.006*	*0.001*	*0.013*	*0.098*	*0.147*	*0.49*	*0.007*	*0.002*	*0.086*	*0.001*	*0.24*	*0.05*	*0.04*

Fig. 1. Thermogravimetric (TG) and evolved gas mass analysis (MSEGA) as a function of temperature in the notochaetae (grey lines) and in the neurochaetae (black lines). (A) TG (dashed lines) and its first derivative (DTG, solid lines); (B-D) MSEGA detecting the release of H_2O (m/z = 18; B), NO (m/z = 30; C) and CO_2 (m/z = 44; D).

of H_2O (m/z = 18, Fig. 1B), both weakly bound (physically adsorbed, see the shoulder in the DTG curve at about 45 °C well visible in the neurochaetae) and strongly bound (hydrogen bond with the polysaccharide chain, maxima in the DTG curves at about 108 °C) (Fig. 1A,B). The second reaction (release of H_2O, NO and CO_2, m/z = 18, 30, and 44, respectively; Fig. 1B,C,D) is related to the depolymerization of the molecular structure of the polysaccharide. The third reaction, occurring between 595 and 745 °C (neurochaetae: maximum at 698 °C, mass loss of 23.1 wt%; notochaetae: maximum at 687 °C, mass loss 22.3 wt%) is due to the thermal decomposition of $CaCO_3$ with the consequent release of CO_2 (m/z = 44; Fig. 1D), according to the reaction $CaCO_3 \rightarrow CaO + CO_2$ (1) and in agreement with chemical analyses and XRPD measurements.

Three other minor thermal events may be observed in the thermal ranges 420-460, 485-595, and 760-870 °C (Fig. 1D). The first one, marked by a shoulder in the DTG curve is also related to thermal decomposition of chitin, as confirmed by the release of NO and CO_2 (m/z = 30 and 44, respectively; Fig. 1C,D); the associated weight losses are 0.69 and 1.11 wt% in neuro- and notochaetae, respectively. The second

event (485-495 °C), as once again proved by the release of NO and CO_2 (Fig. 1C,D), could be ascribed to the thermal decomposition of remnants of the dorsal and ventral cirri. The associated weight losses are 2.41 and 2.33 wt% in the neuro- and notochaetae respectively. The third event (760-870 °C) may be ascribed to the thermal decomposition of residues of partially decomposed organic/inorganic material (Fig. 1A). None of the monitored gases were emitted during this reaction, suggesting the possible release of radicals or complex molecules by sublimation.

3.2. Chaetae external morphology and Ca-P mapping

The notopodia of *H. carunculata* bear tufts of simple tapering capillary and harpoon notochaetae, the latter characterized by close serrations at the apex (Fig. 2A). The stout neurochaetae have a spur at the base of the blade (Fig. 2B). Most of the notochaetae presents a short extension attached to the basis [n = 7, 22.47 ± 5.77 μm in length (mean ± standard deviation); Fig. 2C]. The notochaetae lacking this extension have a tricuspid basis (Fig. 2C and caption). The basis of the neurochaetae always has an elongated, in-relief extension with smooth surface
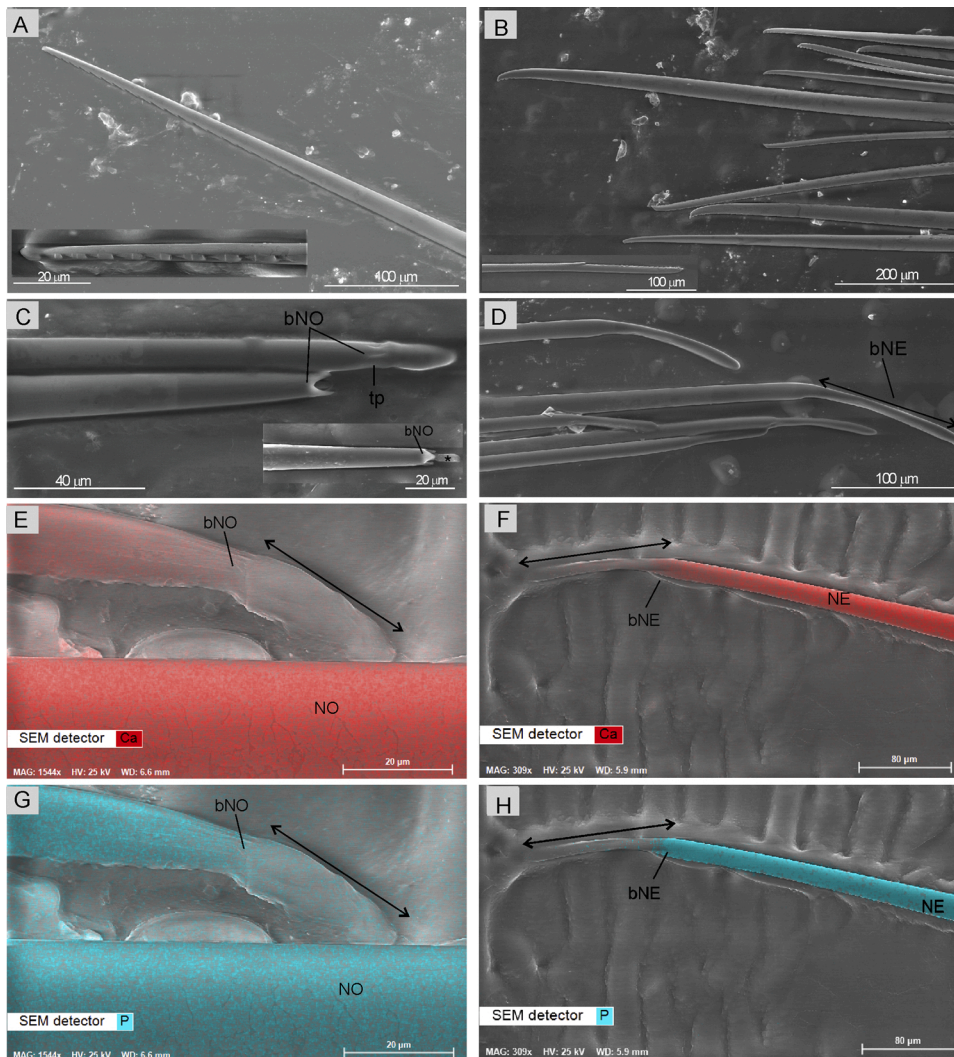
Fig. 2. Scanning electron micrographs of chaetae external morphology with Ca and P distribution revealed by X-EDS detector. (A) Apex of notochaetae showing harpoon serrations (inlet). (B) Apex of bifurcate neurochaetae. Inlet: spur at the base of the blade. (C) Basal portion of two notochaetae (bNO) with a tricuspid ending and with a short extension (double-headed arrow) attached to the basis with tentacular projections (tp). Inlet: detail of a tricuspid base (bNO) and presumably remnants of tissue at the insertion point (*). (D) Elongated extension (double-headed arrow) attached to the basis of the neurochaetae (bNE). (E, G) Maps of Ca (E) and P (G) distribution at the basis of the notochaeta (double-headed arrow) and along the adjacent notochaeta (NO). (F,H) Maps of Ca (F) and P (H) distribution at the basis of the neurochaeta (double-headed arrow) and along the chaeta.

(n = 6, 90.01 $\pm$ 23.43 µm in length; Fig. 2D). In both noto- and neurochaetae, a constriction seems present between the extension and the rest of the chaeta (Fig. 2C,D).

Inorganic constituents were not detected in the basis and in the extension of the chaetae (Fig. 2E-H; Fig. S3). Upwards, the linescans and maps of chaetal element distribution detected Ca as prominent inorganic constituent, together with C, O_2 and P, both in noto- and neurochaetae. The distribution patterns of Ca and P, which are nearly overlaid, showed that their concentration quickly increased along the chaetae and then stabilized (see the central portion of a notochaeta and at about 100 µm from the basis of a neurochaeta reported in Fig. 2E,G and Fig. 2F,H, respectively).

In the chaetae mounted in glycerol (control), the thickness was 19.7 $\pm$ 1.3 µm and 19 $\pm$ 1.9 µm for the noto- and the neurochaetae, respectively. The thickness at the last serration of the harpoon was 11.3 $\pm$ 1.7 µm, while the thickness at the spur was 12.6 $\pm$ 2.2 µm. In chaetae subjected to the decalcification treatment, the thickness was 19.3 $\pm$ 1.6 µm and 19.4 $\pm$ 2.4 µm for the noto- and the neurochaetae, respectively. The thickness at the spur was 13.1 $\pm$ 2.1 µm, while harpoon serrations completely disappeared, thus no measures were possible.

One-way ANOVA did not reveal significant effects of decalcification in the thickness of the notochaetae (F = 1.07, p > 0.31) and the neurochaeta (F = 0.39, p > 0.53), and in the thickness at the spur of the neurochaetae (F = 0.82, p > 0.37).

3.3. Ultrastructure of the chaetae

The embedding of the chaetae in the epoxy resin led to transverse sections showing different chaetal structure and developmental stages, since the chaetae slipped between tissues very easily. The proximal part of the notochaetae presents a well-defined honeycomb hexagonal pattern. Running from the base to the apex, the cavity enlarges and the pattern of the hexagonal canals progressively disappears, giving way to an outer layer made of a multitude of thin packed tubules (Fig. 3A,B). In the distal part, the hexagonal canals are completely replaced by a large cavity surrounded by the thick ring-shaped arrangement of tubules with extremely small lumina (Fig. 3B and inlets).

In the neurochaetae, hexagonal canals are not present either in the proximal part or in the distal part and a cavity can be observed enlarging from the base to the apex (Fig. S5). The cavity is surrounded by a thick ring-shaped arrangement of tubules with extremely small lumen, as previously observed for the distal part of the notochaetae (Fig. 3B).

No polygonal or nodular structures were found inside the cavities and no pore was observed towards the apex of both the noto- and neurochaetae. Qualitative chemical analyses provided by the X-EDS detector coupled with the microscope detected Ca as a prominent inorganic constituent, together with C and P in the noto- and neurochaetae (observed in 50 and 28 points analyses, respectively). In the notochaetae, Ca and P were present both in the ring-shaped arrangement of tubules and in the canals (Fig. S4). After treatment with EDTA, the
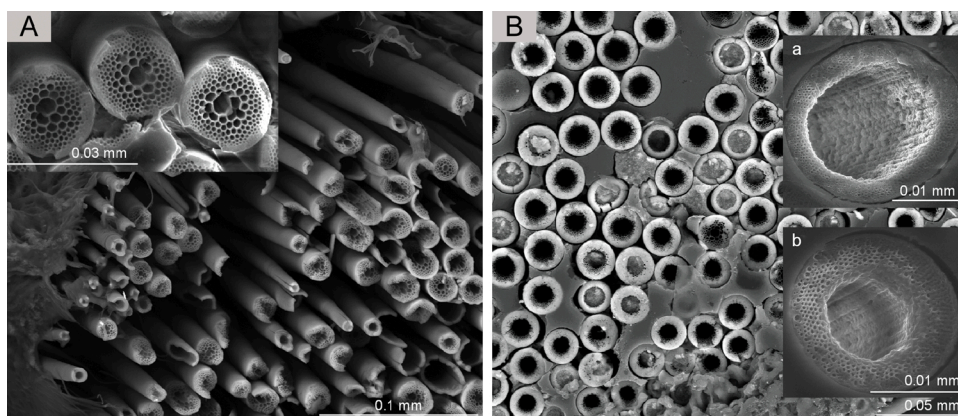
Fig. 3. (A) Well-defined honeycomb hexagonal pattern in the proximal part of the notochaetae. Inlet: details of the honeycomb pattern. (B) Distal part of the notochaetae with a central cavity surrounded by the thick ring-shaped arrangement of tubules with extremely small lumina. Moving up-wards along the notochaetae, the honeycomb pattern progressively disappears starting from the center, leaving a central cavity surrounded by the thick ring-shaped arrangement of tubules with extremely small lumina (see the inlets "a" and "b" as details).

external layer of tubules in the notochaetae decreased in thickness, while the ring-shaped arrangement of tubules towards the central large cavity was not visible anymore. In the neurochaetae, the reduction of the layer of the tubules after EDTA was less marked.

4. Discussion

4.1. H. carunculata chaetae constituents

The experimental results highlighted that fireworm chaetae are composed by organic and inorganic material both in crystalline and amorphous phases. The noto- and neurochaetae of the fireworm *H. carunculata* contain chitin. Indeed, the first two thermal reactions observed with TGA-MSEGA are related to the dehydration of polysaccharide rings and polymerization/thermal decomposition of the acetylated and de-acetylated units of chitin (i.e., deacetylation and cleavage of the glycosidic bond; Kacurakova et al., 1998; Paulino et al., 2006; Wang et al., 2013; Moussout et al., 2016). The first minor thermal events may be attributed to the difference in intermolecular hydrogen bonds of the samples, as already observed by Gbenebor et al. (2017) in the chitin of periwinkle shells.

It has long been assumed that amphinomid chaetae contain $CaCO_3$ in addition to chitin. TGA measurements allowed to calculate the exact amount of $CaCO_3$ present in the noto- and neurochaetae, regardless of whether it is completely crystalline or even partially amorphous. Considering the amount of CO_2 released during the thermal event occurring between 595 and 745 °C (Fig. 1A,D) and according to reaction (1), neuro- and notochaetae consist for 52.5% and 50.7% of $CaCO_3$, respectively. The amounts of Ca calculated for the neuro- and notochaetae (29.4 and 28.4 CaO wt%, respectively) are lower than those found through chemical measurements (Table 1), suggesting that part of the Ca could form other compounds. The amounts of organic C obtained by subtracting C bond to $CaCO_3$ from total C are 0.51708 and 0.59853 mol/100 g for neuro- and notochaetae, respectively. The derived ratios between organic C and N (C/N) are 5.98 and 5.80 for neurochaetae and notochaeteae, respectively. These values are very close each other, but lower than those of pure chitin (C/N = 8), confirming that part of C and N derive from other organic tissues, probably the cirri, in accordance with the second minor thermal event (Fig. 1). Part of C and N could also form a protein matrix, as in cuticular structures of arthropods chitin is frequently associated with specific chitin-binding-proteins into regularly arranged fibrils (Chandran et al., 2016).

Tilic et al. (2017) observed the presence of granules with a dense core in the ultrastructure of the chaetae of *E. complanata*. They interpreted these granules as "carbonated apatite nodules", due to their pseudo-hexagonal morphology. Our XRPD and TGA measurements confirmed that $CaCO_3$ is abundant in *H. carunculata*, but no evidence for crystalline apatite was found. In contrast, chemical measurements

indicated that neuro- and notochaetae contain a significant quantity of P (Table 1), an element characterizing the main anionic site of apatite $[Ca_5(PO_4)_3(OH)]$. Hence, we hypothesized the occurrence of amorphous nanoparticles in the chaetae. Ren et al. (2013) demonstrated that amorphous phosphate nanoparticles may gradually transform into crystalline apatite when heated. Therefore, we carried out *in-situ* XRPD measurements at non-ambient temperature collecting a spectrum after each reaction showed by the thermogravimetric measurements. The results showed that no significant structural and mineralogical transformation occur up to 475 °C (i.e. before the beginning of the decarbonation reaction and after the decomposition of chitin; Fig. 4), even if after thermal decomposition of chitin the peaks of $CaCO_3$ are better evident. In contrast, after the decarbonation reaction, not only the XRPD signal of CaO substituted those of $CaCO_3$ according to reaction (1), but also appeared peaks related to the formation of hydroxyapatite (Fig. 4).

To provide better resolved data, two additional spectra were collected on powder chaetae after calcinating at 900 °C for 1 h and cooling under vacuum (to avoid any possible carbonation and hydroxylation effect). The spectra highlighted the occurrence of MgO in addition to apatite and CaO (Fig. S6). The regular shape of the DTG peak

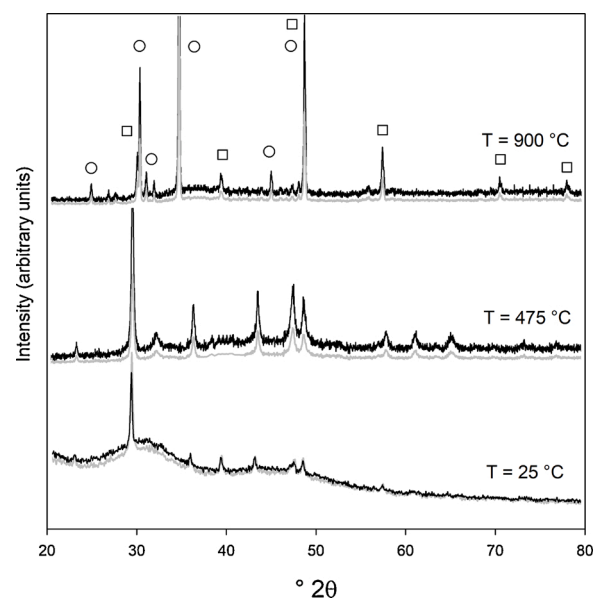**Fig. 4.** XRPD pattern *in-situ* measured at 25, 475, and 900 °C of neuro- (black lines) and notochaetae (grey lines). In the spectrum measured at 900 °C the main peaks of hydroxyapatite and CaO are labeled with circles and squares, respectively. Due to the high signal-to-noise ratio occurring when spectra are collected *in-situ* at high temperature, the peaks related to MgO (Fig. S6) here are not observable.

related to decarbonation (Fig. 1A) allowed to exclude the presence of amorphous $MgCO_3$. From a strictly abiotic and crystallographic point of view, substitutions of Ca with Mg in the $CaCO_3$ structure are very limited. On the other hand, Mg is a very common additive in biogenic carbonate and high-Mg calcite crystals, which are a thermodynamically unstable phase under ambient conditions, are frequently found in the hard tissues of many marine organisms (Long et al., 2014 for a review). The mechanical properties of calcium carbonate are strongly related to the Mg content (Ma et al., 2008; Elstnerova et al., 2010; Moureaux et al., 2010; Kunitake et al., 2013), as high Mg concentration not only facilitates the crystallization of calcite, but also greatly enhances its mechanical properties (Wang et al., 1997; Moureaux et al., 2010). These findings are in nice agreement with the higher Mg content found in the neurochaetae of *H. carunculata* compared to the notochaetae (Table 1), with reference to their involvement in locomotion (see Paragraph 4.2). Besides, Mg may be accommodated in the apatite structure contributing to its stabilization (Bigi et al., 1992; Sader et al., 2013; Farzadi et al., 2014). Considering the quite homogeneous distribution of Mg along the chaetae (Fig. S3), it is possible that part of the Mg contributed also to the formation of the phosphate cluster, but cannot be fully included in the framework when apatite crystallizes. However, as pointed out by Long et al. (2014), the biomineralization processes occurring in marine worms with calcareous tubes (such as those belonging to the Serpulidae family) have not been studied extensively yet.

Other elements (mainly K and Na) are probably remnants of seawater solvated with chitin; these elements may partially enter the structure of apatite (hetero-valent substitutions for Ca), and/or form amorphous material as no proper phases were detected through XRPD. Similar considerations concern also the very limited amounts of Si, Al, Fe, Mn, Ti.

4.2. External morphology of entire chaetae

The SEM images showing the external morphology of the distal ends of noto- and neurochaetae are coherent with those reported in literature for *H. carunculata* (Yáñez-Rivera and Salazar-Vallejo, 2011; Yáñez-Rivera and Brown, 2015; Schulze et al., 2017). The relation between the external structure and the function of the chaetae has already been addressed: the dorsal harpoons are sharp needles displaying strong serrations to harm prey and predators. The ventral chaetae have a slightly curved distal end with denticulations and locomotory function (Yáñez-Rivera and Salazar-Vallejo, 2011; Yáñez-Rivera and Brown, 2015; Schulze et al., 2017; Simonini et al., 2018).

Although several studies investigated the distal ends of fireworm chaetae, to the best of our knowledge the detailed morphology of the basis remains poorly described. Schulze et al. (2017) analyzed the notochaetae released after mechanical irritation of the animals, observing pieces of tissue adhering to the base that they interpreted to be the chaetoblasts. Our scanning electron micrographs and the chemical analyses provided by X-EDS support this hypothesis. The notochaetae show a short in-relief extension with tentacular, shrunken, joint-like connection to the rest of the chaeta (Fig. 2C). Probably, the tricuspid basis observed in some distal ends is the result of the short extension having been ripped of during the dissection process. Chemical data did not detect inorganic constituents in the extension (particularly Ca and P as in the rest of the chaetae; Fig. 2E,G). Besides, it seems to adhere to the chaetae by means of tentacular projections (Fig. 2B), consistently with remnants of the cells (chaetoblasts and/or chaetal follicles embedded within parapodial tissues) at the basis of the chaetae, that may remain attached entirely (Fig. 2C) or in traces (Fig. 2C inlet; Schulze et al., 2017). This short extension could be the insertion point of the notochaetae in the notopodium. In this case, the notochaetae would be anchored at the parapodial tissue through a very small surface, explaining the ease with which they are naturally released when fireworms are threatened.

Inorganic constituents like Ca and P were not detected even in the

elongated extension of the neurochaetae (Fig. 2F,H), further proving that it completely consists of organic material as pieces of tissue. The different morphology, size and resistance to release between the extension of the noto- and neurochaetae may be attributed to the function of these latter: since neurochaetae are used for locomotion, they are never released and remained completely attached to the chaetoblasts even when pulled out from the parapodia with tweezers (Fig. 2B).

Our qualitative crystal-chemical analyses provided by the X-EDS detector, ICP-OES and XRF supported that noto- and neurochaetae are largely constitute by crystalline $CaCO_3$ and clusters of amorphous apatite. The treatments with EDTA did not modify the diameters of noto- and neurochaetae, thus suggesting that the outer sheath of the chaetae is mainly made of chitin, while carbonate (and phosphate) concentration slightly increases moving from the cortex toward the center of the chaetae (Fig. S4C,D). Therefore, our findings do not agree with Gustafson 1930 remark that the outer sheath of the chaetae is calcareous. However, they corroborate his observations about calcareous harpoon ends in the notochaetae. Indeed, the denticulations completely disappeared after exposure to EDTA. The $CaCO_3$ could make the harpoons sharper, enabling them to penetrate tissues of prey and predators. On contrary, the spur and denticulations in the distal end of the neurochaetae seemed to be completely overlain by chitin, reducing the erosion due to locomotion.

4.3. Cross-sections in epoxy resin

Tilic et al. (2017) investigated cross-sections of the notochaetae of *E. complanata*, the sister taxon of *H. carunculata* (Borda et al., 2015). They found that the proximal part of the chaetae was characterized by a bright center with wider chitinous tubules, and much smaller ones in the cortex. They assumed that the fixatives used for observation at TEM dissolved calcareous elements deposited between the chitinous lamellae, leaving nodular remnants which caused the formation of artificial cavities.

The analyses of the sections in resin allowed us to explore the ultrastructure of native chaetae, unaffected by any chemical treatment. The distal part of noto- and neurochaetae and the proximal part of the ventral chaetae showed the same structure: a large hollow cavity surrounded by a thick ring-shaped arrangement of tubules. On contrary, the sections of the proximal part of the notochaetae displayed the typical pattern of annelid chaetae, consisting of central canals with a hexagonal pattern, getting smaller in the cortex. Running from the base to the apex of the notochaetae the canals progressively create a large hollow cavity surrounded by a multitude of thin packed tubules in the cortex. The large hexagonal canals could progressively collapse over the length of the notochaeta, or most likely they could decrease in diameter and become part of the chaeta wall. These observations are coherent with those of Tilic et al. (2017), but confirm that the chaetae of *H. carunculata* are hollow under natural conditions. Besides, the X-EDS point analyses revealed that the reticules are rich in Ca and P. Given that the central canals disappeared after treatment with EDTA, we assumed that mineral constituents are more abundant in the central part of the chaetae and gradually decrease towards the ring-shaped arrangement of tubules in the cortex where chitin matrix is prominent. The morphology of the sections (Fig. 2, S5) together with the chemical analyses provided by X-EDS (Fig. 3, S4) and ICP-OES (Table 1) support that $CaCO_3$ is not deposited in the central core of the canals in a later stage (Tilic et al., 2017), but it is a prominent inorganic constituent of the chaetae.

Given the absence of poison glands highlighted by Eckert (1985) and Tilic et al. (2017), it is our belief that chemicals could be produced by the chaetoblasts themselves, or by other body districts and then transported to the chaetoblasts which incorporate venoms and store them within the chaetae during the chaetogenesis. By this way, the presence of a cavity without an apical pore allows to store material inside the chaetae, as supported by their strong stinging effects (Ottuso, 2013;

Schulze et al., 2017). The large hollow cavity of the chaetae could confer them high resistance to pressure (see for examples Karam and Gibson, 1994; Schmitt et al., 2018). Foam-like infill and honeycomb pattern are also widely utilized as biological strategies to increase structural stiffness and resistance to local buckling (Schmitt et al., 2018). On contrary, the increase of slenderness ratio lead to a reduction in buckling resistance (Schmitt et al., 2018). Perhaps, in the case of the notochaetae, the honeycomb pattern confers them resistance to compressive stresses in the proximal part of the chaeta, while in the distal part the marked slenderness and the progressive disappearance of the hexagonal core facilitate their high sensitivity to breakage on contact. In the neurochaetae, the high Mg content could greatly enhance their mechanical properties, increasing toughness and resistance (Long et al., 2014).

5. Conclusions

We have demonstrated that the chemical composition of the chaetae and their fine ultrastructure in *H. carunculata* differ from the other annelids; however, as these structures have been investigated in a few amphinomid species so far, we hesitate to speculate on whether they are truly exceptional within fireworms. *H. carunculata* is a mobile and brightly colored species crawling on hard substrates, potentially exposed to epibenthic predators. It turned out to be a generalist predator of several benthic invertebrates, displaying powerful defensive capacities to ensure predator escape and opportunistic feeding habits (Simonini et al., 2018, 2017). *H. carunculata* can feed on large defended prey like sea urchins and anemones (Simonini et al., 2017, 2018) and is not threatened by predation. It is free to forage for long periods on a wide range of invertebrates living in Mediterranean and Central Atlantic coastal habitats, potentially influencing the distribution and abundance of its prey (Schulze et al., 2017; Simonini et al., 2017, 2018; Righi et al., 2019). Noteworthy, the characteristics and morphologies of the notochaetae described here well support this lifestyle. They are hollow and able to release compounds. Their strong deterrent effect against consumers and harmful for prey should be mediated by mechanical injury combined with inflammatory substances, supporting the success of fireworms in marine benthic environments (Simonini et al., 2020).

These results shed light on the relation between the structure, composition and function of *H. carunculata* chaetae, which underpins fireworm defensive and offensive strategies and pursues their ecological success. Future studies could further elucidate the organization of chaeta constituents and determine their chemical properties and structure, for instance affecting bending stiffness and axial stiffness (Kryvi and Sørvig, 1990; Merz and Woodin, 1991).

Declaration of Competing Interest

The authors report no declarations of interest.

References

Beesley, P.L., Ross, G.J.B., Glasby, C.J., 2000. Polychaeta, Myzostomida, Pogonophora, Echiura, Sipuncula, Polychaetes & Allies: The Southern Synthesis. Fauna of Australia, Vol. 4. CSIRO Publishing, Melbourne.

Bigi, A., Foresti, E., Gregorini, R., Ripamonti, A., Roveri, N., Shah, J.S., 1992. The role of magnesium on the structure of biological apatites. Calcif. Tissue Int. 50, 439–444.

Borda, E., Kudenov, J.D., Bienhold, C., Rouse, G.W., 2012. Towards a revised Amphinomidae (Annelida, Amphinomida): description and affinities of a new genus and species from the Nile Deep-sea Fan, Mediterranean Sea. Zool. Scr. 41, 307–325.

Borda, E., Yáñez-Rivera, B., Ochoa, G.M., Kudenov, J.D., Sanchez-Ortiz, C., Schulze, A., Rouse, G.W., 2015. Revamping Amphinomidae (Annelida: Amphinomida), with the inclusion of *Notopygos*. Zool. Scr. 44, 324–333.

Chandran, R., Williams, L., Hung, A., Nowlin, K., LaJeunesse, D., 2016. SEM characterization of anatomical variation in chitin organization in insect and arthropod cuticles. Micron 82, 74–85.

Coutinho, M.C.L., Teixeira, V.L., Santos, C.S.G., 2018. A review of "Polychaeta" chemicals and their possible ecological role. J. Chem. Ecol. 44, 2–94.

Cribb, B.W., Rathmell, A., Charters, R., Rasch, R., Huang, H., Tibbetts, I.R., 2009. Structure, composition and properties of naturally occurring non-calcified crustacean cuticle. Arthropod Struct. Dev. 38, 173–178.

Day, J.H., 1967. A Monograph On The Polychaeta Of Southern Africa. British Museum (Natural History) Publication. B.M. (N.H.), London, pp. 1–878, 656.

Eckert, G.J., 1985. Absence of toxin-producing parapodial glands in amphinomid polychaetes (fireworms). Toxicon. 23, 350–353.

Elstnerova, P., Friak, M., Fabritius, H.O., Lymperakis, L., Hickel, T., Petrov, M., Nikolov, S., Raabe, D., Ziegler, A., Hild, S., Neugebauer, J., 2010. Ab initio study of thermodynamic, structural, and elastic properties of Mg-substituted crystalline calcite. Acta Biomater. 6, 4506–4512.

Farzadi, A., Bakhshi, F., Solati-Hashjin, M., Asadi-Eydivand, M., abu Osman, N.A., 2014. Magnesium incorporated hydroxyapatite: synthesis and structural properties characterization. Ceram. Int. 40, 6021–6029.

Fauchald, K., 1977. The polychaete worms. Definitions and keys to the orders, families and genera. Nat. Hist. Mus. Los Angeles Cty. Sei. Ser. 28, 1–188.

Fauvel, P., 1923. Polychètes Errantes. Faune de France, 5. Librairie de la Faculte des Sciences, Paris, pp. 1–488.

Fauvel, P., 1953. The Fauna of India including Pakistan, Ceylon, Burma and Malaya. Annelida Polychaeta. The Indian Press, Allahabad.

Ferreira, T., Rasband, W., 2012. ImageJ user guide. ImageJ/Fiji, 1.

Gbenebor, O.P., Akpan, E.I., Adeosun, S.O., 2017. Thermal, structural and acetylation behavior of snail and periwinkle shells chitin. Prog. Biomater. 6, 97–111.

George, J.D., Southward, E.C., 1973. A comparative study of the setae of Pogonophora and polychaetous Annelida. J. Mar. Biol. Assoc. U.K. 53, 403–424.

Gustafson, G., 1930. Anatomische Studien über die Polychäten-Familien Amphinomidae und Euphrosynidae. Zoologiska Bidrag Fran Uppsala. 12, 305–471.

Hammer, R., Harper, D., Ryan, P., 2001. PAST: Paleontological Statistics Software Package for Education and Data Analysis. Palaeontol. Electron. 4.

Hausen, H., 2005. Chaetae and chaetogenesis in polychaetes (Annelida). Hydrobiologia. 535, 37–52.

Kacurakova, M., Belton, P.S., Hirsch, J., Ebringerova, A., 1998. Hydration properties of xylan-type structures: An FTIR study of xylooligosaccharides. J. Sci. Food Agric. 77, 38–44.

Karam, G.N., Gibson, L.J., 1994. Biomimicking of animal quills and plant stems: natural cylindrical shells with foam cores. Mat. Sci. Eng. C-Mater. 2 (1), 113–132.

Kicklighter, C.E., Hay, M.E., 2006. Integrating prey defensive traits: contrasts of marine worms from temperate and tropical habitats. Ecol. Monograph. 76, 195–215.

Kryvi, H., Sørvig, T., 1990. Internal organization of limbate polychaete setae (*Sabella penicillus*), with notes on bending stiffness. Acta Zool. 71, 25–31.

Kunitake, M.E., Mangano, L.M., Peloquin, J.M., Baker, S.P., Estroff, L.A., 2013. Evaluation of strengthening mechanisms in calcite single crystals from mollusk shells. Acta Biomater. 9, 5353–5359.

Long, X., Ma, Y., Qi, L., 2014. Biogenic and synthetic high magnesium calcite - A review. J. Struct. Biol. 185, 1–14.

Ma, Y.R., Cohen, S.R., Addadi, L., Weiner, S., 2008. Sea urchin tooth design: an "allcalcite" polycrystalline reinforced fiber composite for grinding rocks. Adv. Mater. 20, 1555–1559.

Malferrari, D., Ferretti, A., Mascia, M.T., Savioli, M., Medici, L., 2019. How much can we trust major element quantification in bioapatite investigation? ACS Omega 4, 17814–17822.

Merz, R., Woodin, S.A., 1991. The stiffness of capillary setae: a comparison among sedentariate polychaetes. Ophelia (suppl). 5, 615–623.

Moureaux, C., Perez-Huerta, A., Compere, P., Zhu, W., Leloup, T., Cusack, M., Dubois, P., 2010. Structure, composition and mechanical relations to function in sea urchin spine. J. Struct. Biol. 170, 41–49.

Moussout, H., Ahlafi, H., Aazza, M., Bourakhouadar, M., 2016. Kinetics and mechanism of the thermal degradation of biopolymers chitin and chitosan using thermogravimetric analysis. Polym. Degrad. Stabil. 130, 1–9.

Nakamura, K., Tachikawa, Y., Kitamura, M., Ohno, O., Suganuma, M., Uemura, D., 2008. Complanine, an inflammation-inducing substance isolated from the marine fireworm *Eurythoe complanata*. Org. Biomol. Chem. 6, 2058–2060.

Nakamura, K., Tachikawa, Y., Ohno, O., Kitamura, M., Suganuma, M., Uemura, D., 2010. Neocomplanines A and B, a complanine family isolated from the marine fireworm. J. Nat. Prod. 73, 303–305.

Ottuso, P., 2013. Aquatic dermatology: encounters with the denizens of the deep (and not so deep) a review. Part I: the invertebrates. Int. J. Dermatol. 52, 136–152.

Paulino, A.T., Simionato, J.I., Garcia, J.C., Nozaki, J., 2006. Characterization of chitosan and chitin produced from silkworm chrysalides. Carbohyd. Polym. 64, 98–103.

Ren, F., Leng, Y., Ding, Y., Wang, K., 2013. Hydrothermal growth of biomimetic carbonated apatite nanoparticles with tunable size, morphology and ultrastructure. CrystEngComm. 15, 2137–2146.

Righi, S., Maletti, I., Maltagliati, F., Castelli, A., Barbieri, M., Fai, S., Prevedelli, D., Simonini, R., 2019. Morphometric and molecular characterization of an expanding Ionian population of the fireworm *Hermodice carunculata* (Annelida). J. Mar. Biol. Assoc. U.K. 99, 1569–1577.

Righi, S., Prevedelli, D., Simonini, R., 2020. Ecology, distribution and expansion of a Mediterranean native invader, the fireworm *Hermodice carunculata* (Annelida). Mediterr. Mar. Sci. 21, 558–574.

Rouse, G., Pleijel, F., 2001. Polychaetes. Oxford university press.

Sader, M.S., Lewis, K., Soares, G.A., LeGeros, R.Z., 2013. Simultaneous incorporation of magnesium and carbonate in apatite: effect on physico-chemical properties. Mater. Res. 16, 779–784.

Schmitt, M., Büscher, T.H., Gorb, S.N., Rajabi, H., 2018. How does a slender tibia resist buckling? Effect of material, structural and geometric characteristics on buckling behaviour of the hindleg tibia in stick insect postembryonic development. J. Exp. Biol. 221 (4) jeb173047.

Schroeder, P.C., 1984. Chaetae. In: Bereiter-Hahn, J., Matoltsy, A.G., Richards, K.S. (Eds.), Biology of the Integument. 1. Invertebrates. Springer, Berlin, pp. 297–309.

Schulze, A., Grimes, C.J., Rudek, T.E., 2017. Tough, armed and omnivorous: *Hermodice carunculata* (Annelida: Amphinomidae) is prepared for ecological challenges. J. Mar. Biol. Assoc. U.K. 97, 1075–1080.

Simonini, R., Righi, S., Maletti, I., Fai, S., Prevedelli, D., 2017. Bearded versus thorny: the fireworm *Hermodice carunculata* preys on the sea urchin *Paracentrotus lividus*. Ecology. 98, 2730–2732.

Simonini, R., Maletti, I., Righi, S., Fai, S., Prevedelli, D., 2018. Laboratory observations on predator–prey interactions between the bearded fireworm (*Hermodice*

carunculata) and Mediterranean benthic invertebrates. Mar. Freshwater Behav. Physiol. 51, 145–158.

Simonini, R., Maggioni, F., Zanetti, F., Fai, S., Forti, L., Prevedelli, D., Righi, S., 2020. Synergy between mechanical injury and toxins triggers the urticating system of marine fireworms. J. Exp. Mar. Biol. Ecol. Accepted.

Tilic, E., Pauli, B., Bartolomaeus, T., 2017. Getting to the root of fireworms' stinging chaetae—chaetal arrangement and ultrastructure of *Eurythoe complanata* (Pallas, 1766) (Amphinomida). J. Morphol. 278, 865–876.

Verdes, A., Simpson, D., Holford, M., 2018. Are fireworms venomous? Evidence for the convergent evolution of toxin homologs in three species of fireworms (Annelida, Amphinomidae). Genome Biol. Evol. 10, 249–268.

Vinn, O., 2008. Tube ultrastructure of the fossil genus *Rotularia Defrance*, 1827 (Polychaeta, Serpulidae). J. Paleontol. 82, 206–212.

Vinn, O., 2009. The ultrastructure of calcareous cirratulid (Polychaeta, Annelida) tubes. Est. J. Earth Sci. 58, 153–156.

Vinn, O., Mutvei, H., ten Hove, H.A., Kirsimäe, K., 2008. Unique Mg-calcite skeletal ultrastructure in the tube of the serpulid polychaete *Ditrupa*. Neues Jahrb. Geol. Paläontol. Abh. 248, 79–89.

Vittori, M., Srot, V., Bussmann, B., Predel, F., van Aken, P.A., Štrus, J., 2018. Structural optimization and amorphous calcium phosphate mineralization in sensory setae of a terrestrial crustacean (Isopoda: Oniscidea). Micron 112, 26–34.

von Reumont, B.M., Campbell, L.I., Richter, S., Hering, L., Sykes, D., Hetmank, J., Jenner, R.A., Bleidorn, C., 2014. A polychaete's powerful punch: venom gland transcriptomics of *Glycera* reveals a complex cocktail of toxin homologs. Genome Biol. Evol. 6, 2406–2423.

Wang, R.Z., Addadi, L., Weiner, S., 1997. Design strategies of sea urchin teeth: structure, composition and micromechanical relations to function. Philos. Trans. R. Soc. London, B 352, 469–480.

Wang, Y., Chang, Y., Yu, L., Zhang, C., Xu, X., Xue, Y., Li, Z., Xue, C., 2013. Crystalline structure and thermal property characterization of chitin from Antarctic krill (*Euphausia superba*). Carbohydr. Polym. 92, 90–97.

Yáñez-Rivera, B., Brown, J., 2015. Fireworms (Amphinomidae: Annelida) from Ascension and Saint Helena Island, Central South Atlantic Ocean. Mar. Biodivers. Rec. 8, e149.

Yáñez-Rivera, B., Salazar-Vallejo, S.I., 2011. Revision of *Hermodice* Kinberg, 1857 (Polychaeta: Amphinomidae). Sci. Mar. 75, 251–262.

APPENDIX

Supplementary Material

Table S1. Major constituents (oxide wt%) concentration in neuro- and notochaetae obtained through XRF measurements. Each value is the average of three replicates (*SD*, standard deviation). LOI, Loss On Ignition at 900°C (the same reported in Table 1). Symbol < denotes concentrations below the detection limit (value after the symbol "<").

	SiO_2	Al_2O_3	K_2O	Na_2O	MgO	CaO	Fe_2O_3	MnO	P_2O_5	TiO_2	LOI
Neurochaetae	< 0.1	< 0.1	0.14	1.74	4.71	31.0	< 0.1	< 0.01	7.01	< 0.01	53.74
SD	-	-	*0.01*	*0.02*	*0.14*	*0.22*	-	-	*0.11*	-	*0.19*
Notochaetae	< 0.1	< 0.1	0.13	1.88	3.66	31.9	< 0.1	< 0.01	7.12	< 0.01	53.67
SD	-	-	*0.02*	*0.02*	*0.11*	*0.44*	-	-	*0.12*	-	*0.24*

Caption of Supplementary Figure S1 (A-B). The fireworm *Hermodice carunculata*. (A) Notochaetae (NO) and neurochaetae (NE). (B) Flared notochaetae. Additional images are available at http://www.marinespecies.org/aphia.php?p=taxdetails&id=129831#images

Caption of Supplementary Figure S2. X-ray Powder Diffraction patterns measured at room temperature of neuro- (black line) and notochaetae (grey line). The two spectra well show the main peaks of $CaCO_3$ at about 30 °2θ.

Caption of Supplementary Figure S3 (A-C). SEM images and line maps of the insertion points of the chaetae. (A) Short extension and basis of a notochaeta. (B) Extension at the base of a neurochaeta. (C) Basis of a neurochaeta. Arrows highlight the trend of Ca.

Caption of Supplementary Figure S4 (A-D). Elemental composition of the proximal part of the notochaetae. (A) Point analysis in the cortex of a cross-section and relative X-EDS spectrum showing Ca and P as major compounds. (B) Point analysis in the honeycomb

pattern and relative X-EDS spectrum rich in Ca and P. (C) Elemental map of Ca and of P (D) overlaid with the SEM images of the honeycomb pattern.

Caption of Supplementary Figure S5 (A-C). ESEM and SEM images of the cross-sections of the neurochaetae. (A) Distal part of the neurochaetae with a large central cavity surrounded by the thick ring-shaped arrangement of tubules with extremely small lumina. (B) Proximal part of the neurochaetae showing a ring-shaped arrangement of tubules thicker than the distal part. (C) General aspect of a cross-section of the distal part of the neurochaetae showing hollow tubules.

Caption of Supplementary Figure S6. X-ray Powder diffraction patterns of neuro- (black line) and notochaetae (grey line) measured after calcinating at 900 °C for 1 h and cooling under vacuum. The main peaks of hydroxyapatite, CaO and MgO are labeled by circles, squares and triangles, respectively.
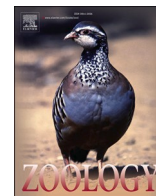
Commentary on: "Unravelling the ultrastructure and mineralogical composition of fireworm stinging bristles" by Righi et al. 2020

Ekin Tilic *, Thomas Bartolomaeus

Institute of Evolutionary Biology and Animal Ecology, University of Bonn, An der Immenburg 1, 53121, Bonn, Germany

ABSTRACT

In a recent paper published in Zoology, Righi et al. (2020) investigated the chaetae of the venomous fireworm *Hermodice carunculata* (Amphinomida, Annelida) and revived the hypothesis of venom injection by hollow chaetae. This conclusion reached by Rigihi et al. (2020) contradicts previously published results, and in our opinion, it is also not supported by their data. We propose the idea that broken chaetae cause lesions and unprotected exposure to venomous epidermal mucous. Herein we also provide further data that show the artificial nature of the empty core of the calcareous bristles. We further emphasise that there is no evidence for venom storage within the chaetae. The idea that fireworm's chaetae are equipped with a venom delivery mechanism, analogous to hypodermic needles, must be considered as refuted. We hope our commentary may help future clarification of venom delivery in fireworms.

Fireworms (Annelida: Amphinomida) are known to cause painful injuries upon contact with their calcareous bristles (Halstead, 1978). The core axis of these chaetae appear to be hollow, which led many researchers to assume that they must be filled with venom (Day, 1967; Penner, 1970). This idea of a defence mechanism that is analogous to a hypodermic needle was quickly accepted by the scientific community and also became dominant in everyday language (Burke, 1997; Harrison, 1992; Nakamura et al., 2008; von Reumont et al., 2014; Smith, 2002). However, as spectacular as it may sound, there is no evidence for such a venom delivery apparatus (Eckert, 1985; Tilic et al., 2017). A recently published paper in *Zoology* on the ultrastructure and mineralogical composition of these stinging bristles by Righi et al. (2020) argues that this is the case, which led us to write this commentary.

In their study, Righi et al. (2020) employ scanning electron microscopy and energy dispersive X-ray spectrometry (X-EDS) for measuring the chemical composition of the chaetae. The authors show that chaetae of *Hermodice carunculata* consist mainly of $CaCO_3$ in addition to chitin and possibly amorphous apatite. These results are a valuable contribution to our knowledge on amphinomid chaetae since an empiric demonstration of their elemental composition was lacking. We have investigated the ultrastructure of chaetae in *Eurythoe complanata* (Fig. 1A) and also published ultrastructural evidence on their calcification (Tilic et al., 2017). Both *E. complanata* and *H. carunculata* are closely related species of Amphinominae (Borda et al., 2015). Similar

investigations on the chemical composition of chaetae in Archinominae and more importantly Euphrosinidae are warranted to confirm that calcareous chaetae are an autapomorphy of Amphinomida.

Furthermore, Righi et al. (2020) also test the effects of decalcification on the chaetae. This was also a central part of Tilic et al., 2017, where we concluded that the empty appearance of chaetae is in many cases a result of decalcification as most aldehyde fixatives used in morphology are slightly acidic. The outer barbs (Fig. 1D) of the harpoon-like chaetae disappear once they are treated with an acidic medium. We also observed this in *Eurythoe complanata* (Tilic et al., 2017) (Fig. 1B, C). Righi et al. (2020), also corroborate our results on the lack of a basal pore and an apical pore (Fig. 1D, F). The core of a chaeta is in its native condition filled with calcareous granules, which disappear when treated with an acidic medium (Fig. 1B, E). The empty appearance of the core is a result of the calcification process, which leads the delicate chitinous lamellae to rupture (Tilic et al., 2017). Similarly the strong mechanical forces Righi et al. (2020) applied while preparing the native, unfixed delicate chaetae for SEM studies, may also explain the central cavity inside the notochaetae (Righi et al., 2020: Fig. 3). Some of the chaetae are ruptured during this process (Righi et al., 2020: Fig 3A), while others still contain an amorphous filling (Righi et al., 2020: Fig 3A).

Oddly enough, Righi et al. (2020) still conclude that the chaetae can deliver and store venom. They state that "*chemicals could be produced by*
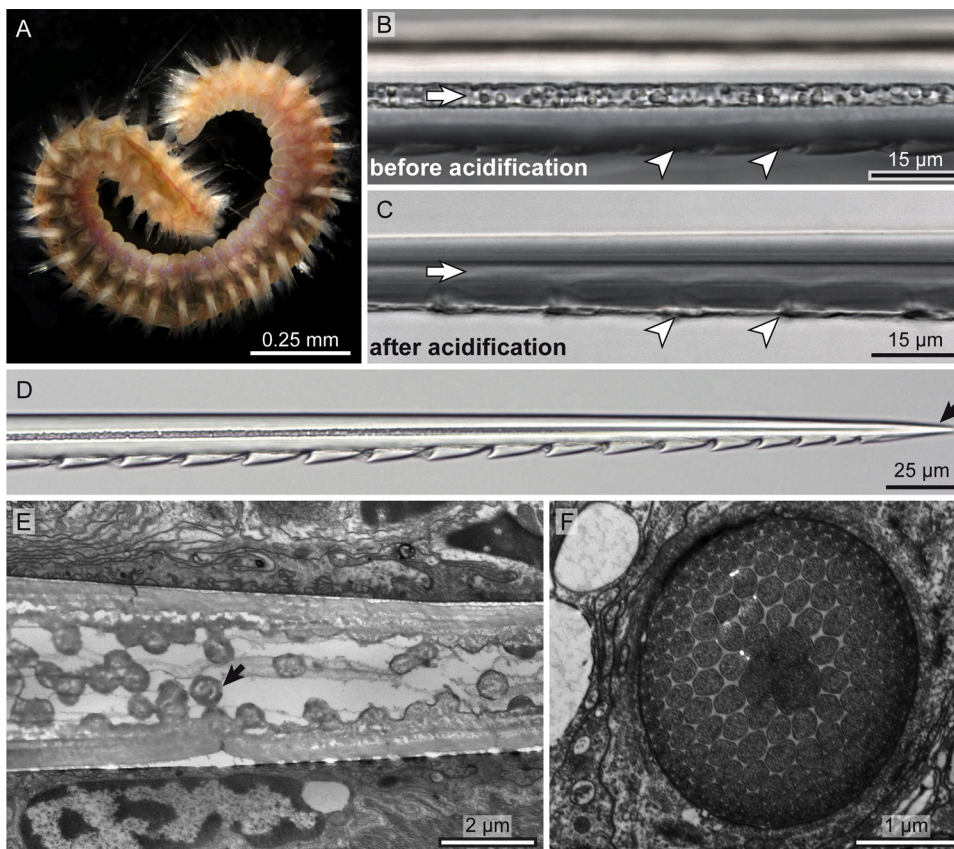

Fig. 1. A The fireworm *Eurythoe complanata*. Note the animal curling into a defensive posture, erecting its calcareous notopodial chaetae. **B** and **C** show the same isolated chaeta before and after acidification. The arrows point at the calcareous granules in the centre that dissolve during acidification. Note that the barbs (arrowheads) also dissolve. **D** An isolated harpoon-like bristle of the fireworm. There is no pore at the tip of the chaeta to release any venom. **E** Transmission electron micrograph showing the calcareous granules (arrow) in the core of the chaeta. **F** Transmission electron micrograph showing the basis of the bristle that is not hollow and not connected to a venom gland.

the chaetoblasts themselves, or by other body districts and then transported to the chaetoblasts which incorporate venoms and store them within the chaetae during the chaetogenesis." (pg. 7). This statement is not only speculative but also lacks a fundamental understanding of the structure of a chaetal follicle and expertise in cell biology. There is no histological (Eckert, 1985) or ultrastructural evidence (Tilic et al., 2017) of a venom gland that is associated with the chaetae or the chaetal sac, nor is there any ultrastructural evidence that the chaetoblast is involved in secretions other than chitin or N-acetylglucosamine. One has to keep in mind that glandular secretory cells have a distinct ultrastructure even visible under the SEM (Saglam et al., 2020). These secretory cells produce and store secretions if unicellular, or store secretions in a commonly formed extracellular space if multicellular (Hausen, 2005; Rößger et al., 2015, and references therein). There is also no evidence for any transport process from surrounding tissue layers across the perifollicular extracellular matrix and the follicle cells into the inner of the chaeta. This, in our opinion, unequivocally shows that venom delivery does not occur through chaetal injections.

It is evident that fireworms can secrete inflammation-inducing chemical compounds (Nakamura et al., 2010, 2008) and might even use a complex mixture of toxins for defence (Verdes et al., 2018). However, it is beyond reason to argue that venom is stored and delivered through chaetae. The most straight-forward and plausible explanation is that venom (or inflammatory chemicals) are secreted through epidermal glands. The entire animal, including the chaetae, is covered with mucousy secretions. The calcified, brittle nature of chaetae allow them to break easily, wounding the predator and exposing it to the possibly venomous or at least inflammatory substances. Until the opposite is proven — either by localised expression of toxin genes or by a chemical analysis of components from within the intrachaetal cavity — the idea that amphinomid chaetae function as hypodermic needles should be considered refuted.

Declaration of Competing Interest

Both authors declare no conflict of interest.

Acknowledgements

References

Borda, E., Yáñez-Rivera, B., Ochoa, G.M., Kudenov, J.D., Sanchez-Ortiz, C., Schulze, A., Rouse, G.W., 2015. Revamping Amphinomidae (Annelida: Amphinomida), with the inclusion of *Notopygos*. Zool. Scr. https://doi.org/10.1111/zsc.12099.

Burke, W.A., 1997. Cutaneous hazards of the coast. Dermatol. Nurs. 9, 163–170.

Day, J.H., 1967. Polychaeta of Southern Africa. Part 2. Sedentaria. British Museum (Natural History) London.

Eckert, G.J., 1985. Absence of toxin-producing parapodial glands in amphinomid polychaetes (fireworms). Toxicon 23, 350–353.

Halstead, B.W., 1978. Poisonous and Venomous Marine Animals of the World, rev. ed. Darwin Press, Princeton N.J.

Harrison, L.J., 1992. Dangerous marine life. J. Fla. Med. Assoc. 79, 633–641.

Hausen, H., 2005. Comparative structure of the epidermis in polychaetes (Annelida). In: Bartolomaeus, T., Purschke, G. (Eds.), Morphology, Molecules, Evolution and Phylogeny in Polychaeta and Related Taxa, pp. 25–35. Hydrobiologia 535/536.

Nakamura, K., Tachikawa, Y., Kitamura, M., Ohno, O., Suganuma, M., Uemura, D., 2008. Complanine, an inflammation-inducing substance isolated from the marine fireworm *Eurythoe complanata*. Org. Biomol. Chem. 6, 2058–2060.

Nakamura, K., Tachikawa, Y., Ohno, O., Kitamura, M., Suganuma, M., Uemura, D., 2010. Neocomplanines A and B, a complanine family isolated from the marine fireworm. J. Nat. Prod. 73, 303–305.

Penner, L.R., 1970. Bristleworm stinging in a natural environment. University of Connecticut Occasional Papers (Biological Sciences Series) 1, 275–280.

Righi, S., Savioli, M., Prevedelli, D., Simonini, R., Malferrari, D., 2020. Unravelling the ultrastructure and mineralogical composition of fireworm stinging bristles. Zoology, 125851.

Rößger, A., Meißner, K., Bick, A., Müller, C.H., 2015. Histological and ultrastructural reconstruction of ventral epidermal glands of *Spio* (Polychaeta, Spionidae, Annelida). Zoomorphology 134 (3), 367–382.

Saglam, N., Saunders, R., Shain, D.H., Saidel, W.M., 2020. Detailed ultrastructure of the *Hirudo* (Annelida: Hirudinea) salivary gland. Micron, 102887.

Smith, M.L., 2002. Cutaneous problems related to coastal and marine worms. Dermatol. Ther. 15, 34–37.

Tilic, E., Pauli, B., Bartolomaeus, T., 2017. Getting to the root of fireworms' stinging chaetae—chaetal arrangement and ultrastructure of *Eurythoe complanata* (Pallas, 1766) (Amphinomida). J. Morphol. 278. https://doi.org/10.1002/jmor.20680.

Verdes, A., Simpson, D., Holford, M., 2018. Are fireworms venomous? Evidence for the convergent evolution of toxin homologs in three species of fireworms (Annelida, Amphinomidae). Genome Biol. Evol. 10, 249–268.

von Reumont, B.M., Campbell, L.I., Jenner, R.A., 2014. Quo vadis venomics? A roadmap to neglected venomous invertebrates. Toxins 6, 3488–3551.
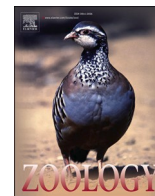
Response to Tilic and Bartolomaeus's Commentary on the original Research Paper "Unravelling the ultrastructure and mineralogical composition of fireworm stinging bristles" (Zoology, 144)

Sara Righi [a,b,*], Martina Savioli [b], Daniela Prevedelli [a], Roberto Simonini [a], Daniele Malferrari [b]

[a] *Department of Life Sciences, University of Modena and Reggio Emilia, Via Campi 213/D, 41125 Modena, Italy*
[b] *Department of Chemical and Geological Sciences, University of Modena and Reggio Emilia, Via Campi 103, 41125 Modena, Italy*

ARTICLE INFO

ABSTRACT

In their Commentary to our paper recently published in Zoology (Righi et al., 2021a), Tilic and Bartolomaeus question our findings that the chaetae of *Hermodice carunculata* (Annelida) are hollow and able to store and deliver venoms. They sustain the idea that inflammatory chemicals are secreted through epidermal glands and possibly exposed to predator trough wounds caused by the brittle chaetae. We provide evidence-based arguments in support of our considerations. The sample preparation procedures did not affect the native inner structure of unfixed fireworm chaetae, which is clearly hollow as supported by both ultrastructure observation and crystal-chemical analysis of constituents. Furthermore, our previous and more recent feeding bioassays and chemical analysis indicate both that chaetae retain strong deterrent capacities even when isolated from the body of *H. carunculata*, and that they contain venoms. The cellular mechanisms involved in fireworm chaeta storage and deliver of chemicals are still unstudied. We strongly believe that this lack of knowledge should draw further attention on *H. carunculata* biology, pursuing new hypotheses and studies based on the noteworthy information which has been obtained so far.

In the present response we would clarify some concerns raised in the Commentary by Tilic and Bartolomaeus (2021). They question our evidence that the chaetae of *Hermodice carunculata* (Annelida) are hollow and able to store and deliver venoms (Righi et al., 2021a).

For the first point, Tilic and Bartolomaeus (2021) state that the chaeta core of *Eurythoe complanata* is filled with calcareous granules in native condition. However, they observed chaetae subjected to preparation for TEM and no data on their elemental composition were provided.

Furthermore, recalling a paper listed among our references (Tilic et al., 2017), the authors suggest that the cavity we observed may be a consequence of mechanical forces applied while preparing the unfixed chaetae for SEM. Aware of the potential artifacts, we analyzed a wide range of samples and all those altered by sectioning were discarded. Importantly, when the parapodium remained perfectly orthogonal to the wall of the resin block, the epoxy resin itself conferred stability to the chaetae leaving them unaltered. In this way, the chaeta inner structure was well visible and resulted hollow. Some particles were present above some chaeta section during the inspection, but energy dispersive X-ray

spectrometry (X-EDS) analyses confirmed that they derived from the aluminum oxide and silicon carbide we used to polish the surfaces of the resin blocks. Consistently, X-EDS point analyses never revealed any constituents in the central black cavity of the chaetae.

For the second point, no conclusive evidence is available on how venom could reach the hollow chaeta cavity, thus other mechanisms than those considered by Tilic and Bartolomaeus (2021) could be possible. Our previous and more recent LC-HRMS and NMR analyses indicate the presence of venom inside the chaeta (Simonini et al., 2021; Righi, 2021 unpublished data; Righi et al., 2021b), unpublished data), and reinforce our results on palatability tests and feeding bioassays on teleost and cnidarians, respectively (Simonini et al., 2021). Further studies concerning the transport process of venom into the chaetae are necessary, but nonetheless the hollow structure of *H. carunculata* chaetae and their chemical storage capacity should no longer be considered as putative.

It is a matter of fact that the notochaetae mediate predator-prey interactions, as already demonstrated by our studies on *H. carunculata* sinecology: when chaetae become flared, they protect the entire

---

* Corresponding author at: Department of Life Sciences, University of Modena and Reggio Emilia, Via Campi 213/D, 41125 Modena, Italy.
E-mail address: sara.righi@unimore.it (S. Righi).

fireworm body from contact, creating a barrier that harms prey and triggers avoidance behaviour in predators, which cannot touch fireworm tissues (Simonini et al., 2018, 2021). The key issue is that our considerations on fireworm stinging capacity derive from an integrated framework of studies about *H. carunculata* biology (Simonini et al., 2018, 2021; Righi, 2021, unpublished data; Righi et al., 2021b, unpublished data).

As an additional information, after years of contact with living *H. carunculata*, we can state that the notochaetae remain stinging for days after fireworm death, beaching (Simonini et al., 2021), or when released inside the aquaria as free chaetae. The painful reactions we experienced lightly touching the free chaetae in the water column disagree with the explanation of Tilic and Bartolomaeus (2021) that chemicals are secreted through epidermal glands, but never delivered from the chaetae. Indeed, even though venoms are not necessarily related only to the chaetae, our data strongly support that *H. carunculata* stores and delivers toxins *via* the hollow chaetae.

Declaration of Competing Interest

The authors report no declarations of interest.

References

Simonini, R., Maletti, I., Righi, S., Fai, S., Prevedelli, D., 2018. Laboratory observations on predator–prey interactions between the bearded fireworm (*Hermodice carunculata*) and Mediterranean benthic invertebrates. Mar. Freshwater Behav. Physiol. 51, 145–158.

Righi, S., 2021. Ecology and physico-chemical weapons of the Mediterranean range-expanding fireworm *Hermodice carunculata* (Annelida). Doctoral Thesis, Dissertation programmed for May 2021. University of Modena and Reggio Emilia (UNIMORE), Modena (Italy).

Righi, S., Savioli, M., Prevedelli, D., Simonini, R., Malferrari, D., 2021a. Unravelling the ultrastructure and mineralogical composition of fireworm stinging bristles. Zoology 144 (125851). https://doi.org/10.1016/j.zool.2020.125851.

Righi, S., Forti, L., Simonini, R., Prevedelli, D., Mucci, A., 2021b. Novel complanine-related compounds and their anatomical distribution in the stinging fireworm *Hermodice carunculata* (Annelida). Manuscript in preparation.

Simonini, R., Maggioni, F., Zanetti, F., Fai, S., Forti, L., Prevedelli, D., Righi, S., 2021. Synergy between mechanical injury and toxins triggers the urticating system of marine fireworms. J. Exp. Mar. Biol. Ecol. 534, 151487.

Tilic, E., Bartolomaeus, T., 2021. Commentary on: "Unravelling the ultrastructure and mineralogical composition of fireworm stinging bristles" by Righi et al. 2021. Zoology 144.

Tilic, E., Pauli, B., Bartolomaeus, T., 2017. Getting to the root of fireworms' stinging chaetae—chaetal arrangement and ultrastructure of *Eurythoe complanata* (Pallas, 1766) (Amphinomida). J. Morphol. 278, 865–876.

CHAPTER IV

Looking inside the structure and chemical composition of bioapatite in fossils

This chapter summarizes the main results related to the chemical and structural characterization of bioapatite in fossils and reports specific conclusions. Like for previous chapter the full set of results is reported in the published papers attached at the end of the chapter (Annexes 3-5).

Annex-3: *Mineralogy and crystallization patterns in conodont bioapatite from first occurrence (Cambrian) to extinction (end-Triassic).*

As previously mentioned, conodonts dominated the ancient ocean from over 300 million years from the Cambrian to the Triassic. Being extinct, it is not possible to obtain reliable information about their pristine composition and structure as the conodont elements have undergone fossilization and diagenesis. We measure and compare bioapatite crystallographic cell parameters in conodonts of different age, taxonomic assignment, geographic provenance and CAI. Furthermore, cell parameters of conodonts were compared with those of other phosphatic fauna from the same residue, like brachiopods, bryozoans, fish teeth and ostracods, in order to detect additional bioapatite signals and to exclude effects of diverse preparations technique and diagenesis. The goal of this work is to find possible interferences of diagenesis and fossilization after biomineralization.

This research added to the classical morphological characterization, achievable through optical and electronic microscopy, typical of the paleontological approach also a crystallographic approach, based on X-ray microdiffraction to gain structural information on conodonts bioapatite. As well known, cell parameter dimensions strongly depend on the different isomorphic substitutions in bioapatite lattice. Our data reveal that cell parameters calculated for paraconodonts significantly differ from those of euconodonts (Fig. 4.1).
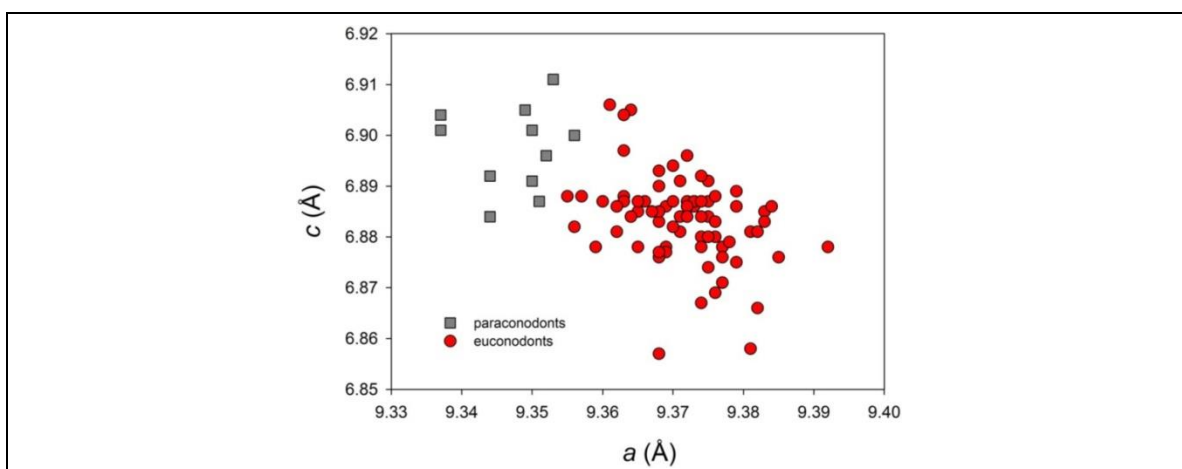

Fig. 4.1 - Binary plot of bioapatite crystallographic unit-cell parameters *c* vs *a* for euconodonts (red circles) and paraconodonts (grey squares) (*Medici et al., 2020*).

Paraconodonts bear, in fact, smaller cell parameters *a* and higher cell parameters *c*, very close to the highest values of *c* of euconodonts. Moreover, cell parameters calculated for both paraconodonts and euconodonts appear to be independent from age, taxonomic assignment, geographic provenance and, for euconodonts, CAI (i.e., heating occurred during fossilization). Other phosphatic/phosphatized material from the same residues producing conodonts are characterized by values of the cell parameters that, in a preliminary way, appear to be mainly correlated with the type of organism even if, for some of them, a correlation also with age cannot be completely ruled out. It is therefore conceivable that major element content strongly depends not only on fossilization, diagenesis and metasomatism, but mostly on the primary bioapatite composition. In other words, from a close crystal-chemical point of view, it is not possible to univocally conclude, for example, that the cell parameter *a*, smaller in paraconodonts than in euconodonts, is the direct consequence of a sort of "francolitization" process (i.e., the formation, for progressive and successive isomorphic substitutions, of the end-member "francolite" that, as already pointed out, was never proved) during fossilization and/or diagenesis.

With this work, we can conclude that primary biomineralization provides an indelible footprint, only mediated by fossilization and diagenetic processes.

Annex-4: *Zooming in REE and other trace elements on conodonts: Does taxonomy guide diagenesis?*

Bioapatite has been used since Cambrian times to build hard tissues and structures either by vertebrates and invertebrates. In the past, content of Rare Earth Elements (REE) and trace elements in fossil bioapatite was generally assumed to be a reliable archive of sea-water composition (*Song et al., 2019; Pietsch & Bottjer, 2010; Girard & Albarède, 1996; Granjean-Lécuyer et al., 1993; Granjeean et al., 1987; Wright et al., 1984*). However, as early as the 1990s, concrete hypothesis began to be advanced in which minor elements concentration in bioapatite could have been considerably affected by other parameters (*Picard et al., 2002; Armstrong et al., 2001; Reynard et al., 1999; Holser, 1997; Toyoda & Tokonami, 1990*), in particular by the mineralogical and chemical composition of the diagenetic environment (*Trotter & Eggins, 2006; Kocsis et al., 2010; Herwarts et al., 2013, 2011; Zhao et al., 2013; Chen et al., 2015; Trotter et al., 2016; Zhang et al., 2016; Liao et al, 2019; Zigaite et al., 2020*).

The agreement about this hypothesis is not unanimous (*Liao et al., 2019*) and in the present work we tried to look inside this unsolved question analysing samples (conodonts) recovered from the same stratigraphic horizon, thus nearly eliminating any issue that could be dependent on the provenance and, therefore, possible influenced by differences (far from to be improbable) occurred during fossilization and diagenesis. Assuming thus all samples have undergone an identical diagenetic history, we have assessed if conodont taxonomy (and morphology) impacts not only HFSE uptake, but also the crystallinity index (CI); in fact, CI of bioapatite should be linearly dependent on diagenetic alteration (the greater and longer a crystal is exposed to high temperature and pressure, the greater the crystallinity index becomes).

Results evidenced that the sample signals are critically affected by diagenetic overprints. Diagenesis leads to an increase in the total REE content, dominantly derived from pore waters of the embedding sediments. Conodont MREE enrichment, already reported in literature (*Bright et al., 2009*), is well evident in our samples, but with a clear distinction between the different conodont genera that we have considered: *Scabbardella*, *Sagittodontina* and *Amorphognathus*. In other words, all the taxa have marked diagenetic imprints, but REE enrichment deeply marks some taxa rather than others. Since all the specimens realistically have been submitted by the same diagenetic conditions, taxonomy, although minimally, appears to control the degree of chemical fractionation.

Other matters of critical importance concern crystallinity. The calculation method of the CI, rarely used in paleontological research, should be carefully considered as it strongly depends on sample preparation and textures, the latter mostly when measurements are not taken on powder. In fact, powder provides an average result which may fail in predicting the true rate of geochemical alteration when it is achieved mainly through the growth of authigenic apatite, as a powder diffraction pattern cannot distinguish between the relative proportion of biogenic and authigenic apatite. Actually, here we have found that a crystallinity index (CI-M3 in Annex 4) calculated considering also the effects of preferential orientations (in turn possibly dependent on taxonomy) is directly relate with ΣHREE which is dependent on the diagenetic imprint (Fig. 4.2).

Fig. 4.2 - Correlations: (a) ΣREE vs CI-M3; (b) [log (ΣREE/Th)] vs 1/(CI-M1); (c) La/Y vs CI-M2. Symbols: *Scabbardella altipes*, circles; *Sagittodontina robusta*, triangles; *Amorphognathus* sp. (Pa), squares; *Amorphognathus* sp. (Pb), diamonds; *Amorphognathus* sp. (Sb), exagons (*Medici et al., 2021*). CI-M1, CI-M2 and CI-M3 are different way used to calculate crystallinity index; please see Annex-4 for details.
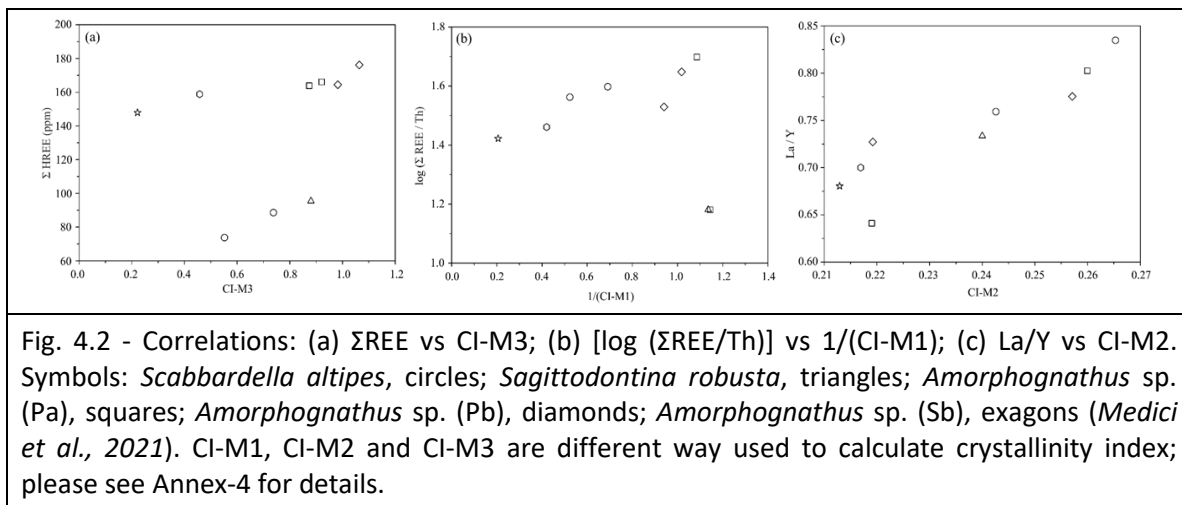
Annex-5: *"Conodont pearls" do not belong to conodonts*

To verify the validity of the "conodont-signature", we check if the so called "conodont-pearls" belong to conodonts. "Conodont pearls" are enigmatic sub-millimetric spherules that are mostly made of apatite and are commonly recovered together with conodonts in the residue derived from the carbonate matrix dissolution (see paragraph 2.2, Chapter II); thus, their stratigraphic distributions is similar to that of conodonts. They were recovered for the first time over a century ago (*Oakley, 1934*) and a lot of different hypotheses regarding their origin has been proposed, but a final answer on their nature is far from being reached. With the aim to shed more light on this controversy, we decided to reverse the analytical prospective analysing

material from a single stratigraphic horizon restricted to a specific time-span and analysing all the phosphatic specimens recovered with the enigmatic microspherules after acid digestion.

Spherules revealed a considerable variation in size (between 0.2 and 0.5 mm), shape and colour. Some specimens reveal a depression on one side and some are associated together: naturally broken and polished spherules display a fine lamination, with micrometric-thick laminae that are continuous and do not reveal to follow a regular pattern. Some microspherules appear to have a rounded nucleus, not always preserved. From a chemical point of view, the composition of spherules is homogeneous, with Ca and P as main elements. Sometimes, also peaks of F were detected and some specimens have an aluminosilicate cover on the phosphatic surface. In general, apatite is the dominant mineralogical phase, some samples are partially coated by chlorite.
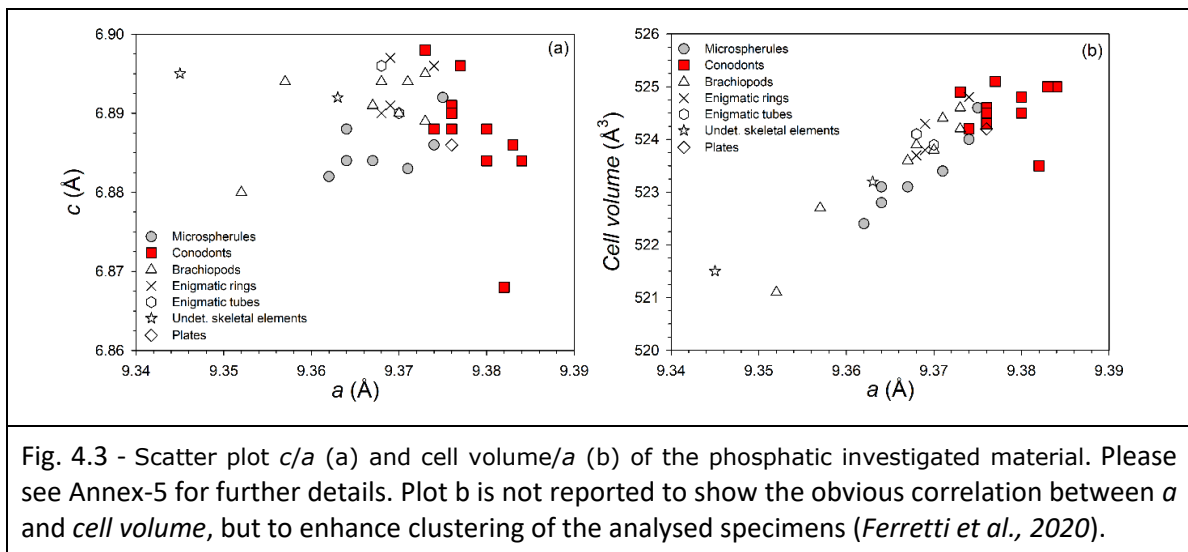
Fig. 4.3 - Scatter plot c/a (a) and cell volume/a (b) of the phosphatic investigated material. Please see Annex-5 for further details. Plot b is not reported to show the obvious correlation between a and *cell volume*, but to enhance clustering of the analysed specimens (*Ferretti et al., 2020*).

Plotting c and a cell parameters (Fig. 4.3), it is clear that conodonts and microspherules occupy two distinct areas regarding parameter a in particular because conodont values are significantly higher. Clusters of enigmatic spherules and tubes are narrow and disjunct from those of conodonts and microspherules, both for parameters a and c. Brachiopods analysed in the exterior surface of the valve cluster in an area overlapping rings and tubes, but clearly separate from conodonts. It is possible to identify four areas of the graphs respectively occupied by conodonts, microspherules, brachiopods and the association of enigmatic rings and tubes.

Phosphatic microspherules have been commonly associated to conodonts because of their similar composition (fluorapatite) and a stratigraphical distribution (Cambrian to early Carboniferous) overlapping that of conodonts (Cambrian to the Triassic/Jurassic transition). However, we cannot rule out that the lack of microspherule records beyond the stratigraphical range of conodonts could be an artefact resulting by the reduction of acid-processing of post-Triassic materials by non-conodont workers. Furthermore, an accurate selection should be done in post-Triassic phosphate spherules, that were previously excluded by investigation as younger than conodonts, to test if any could fit with these enigmatic bodies.

ANNEX-3

Mineralogy and crystallization patterns in conodont bioapatite from first occurrence (Cambrian) to extinction (end-Triassic).

Luca Medici, Daniele Malferrari, Martina Savioli & Annalisa Ferretti

Mineralogy and crystallization patterns in conodont bioapatite from first occurrence (Cambrian) to extinction (end-Triassic)

Luca Medici[a], Daniele Malferrari[b], Martina Savioli[b], Annalisa Ferretti[b,*]

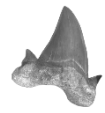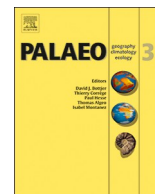[a] National Research Council of Italy, Institute of Methodologies for Environmental Analysis, C.da S. Loja–Zona Industriale, 85050 Tito Scalo, Potenza, Italy
[b] Department of Chemical and Geological Sciences, University of Modena and Reggio Emilia, Via Campi 103, 41125 Modena, Italy

ARTICLE INFO

ABSTRACT

Bioapatite represents an important acquisition in the evolution of life, both in the seas and on land. Vertebrates applied calcium-phosphate biominerals to grow their skeletal support and to shape their teeth, while some invertebrates sheltered their soft parts within apatite shells. Conodonts were the first among vertebrates to experiment with skeletal biomineralization of tooth-like elements in their feeding apparatus. Spanning a time record of over 300 million years, they offer a unique tool to test possible variation in bioapatite structure from the experimentation of a very primitive biomineralization type to a more evolute pattern just before going extinct. X-ray microdiffraction carried out through an X-ray micro-diffractometer, integrated with environmental scanning electron microscopy coupled with chemical microanalyses (ESEM-EDX), has been applied in this study to investigate conodont element crystal structure throughout the entire stratigraphic range of these organisms. In particular, bioapatite crystallographic cell parameters have been calculated for about one hundred conodont elements ranging from the late Cambrian to the Late Triassic. Resulting data clearly indicate two distinct distribution plots of cell parameters for paraconodonts and euconodonts. In contrast, age, taxonomy, geographic provenance and CAI do not affect the dimension of the bioapatite crystal cells. Conodont bioapatite crystallographic cell parameters have been compared with cell parameters resulting from phosphatic/phosphatized material (ostracodes, brachiopods, bryozoans, and fish teeth) present in the same residues producing conodonts. Resulting values of the cell parameters are, in general, mainly correlated with the type of organisms even if, for some of them, a correlation also with age cannot be completely ruled out. According to our data, primary bioapatite appears to imprint a key signature on fossil crystal-chemistry (crystal structure and major chemical element contents), while the contribution of fossilization and diagenetic processes seems less relevant.

1. Introduction

Several present and fossil organisms, among both invertebrates and vertebrates, share the use of bioapatite for the formation of their mineralized structures. Bioapatite has peculiar features that make it suitable to act as a structural support for the body (skeleton), to allow mechanical grinding (teeth), and to provide protection for the soft tissues (*e.g.*, shell in brachiopods and skull of vertebrates) (Kallaste and Nemliher, 2005; Pasteris et al., 2008; Liu et al., 2013). Furthermore, bioapatite is an important reserve for phosphorus, a fundamental element for life that is also present in biological molecules such as DNA, RNA and many proteins, and is one of the main components of ATP (adenosine triphosphate), an essential molecule for the metabolism of living organisms.

Biomineralized structures in biological systems are made up of an organic and an inorganic component. The latter is typically nanocrystalline (10^{-9} m), with nanometric assemblies of atoms with dimensions ranging from ions (10^{-10} m) to macroscopic forms (Banfield and Zhang, 2001). However, there are significant differences between teeth and bones. Teeth are in fact provided with cells completely different from those involved in ossification processes, being odontoblasts specialized in the dentin formation process and ameloblasts in the formation of the enamel. Dentin consists of collagen and nanocrystals of bioapatite, and it is not subject to remodeling during the lifetime of the individual. Mature enamel contains only 2% of proteins and bears bioapatite crystals significantly larger (up to 1000 times greater) than in bones. These differences probably reflect the adaptive capacity of vertebrates that parallels changes imposed by evolution (LeGeros and

Table 1

Conodont taxa analyzed in the present paper, referred to geographic location/formation, age, and most relevant literature. P: paraconodont; E: euconodont.

Code	n° elements	Conodont taxa	Locality/formation	Age	P/E	CAI	Reference paper(s)/collection
A18-A19	2	*Furnishina alata* Szaniawski, 1971	Żarnowiec (Poland)	Cambrian Miaolingian (Guzhangian)	P		Szaniawski, 1971
A11-A12, A90-A91	4	*Westergaardodina* sp.	Kinnekulle, Västergötland (Sweden)	Cambrian Furongian (Paibian)	P		Müller and Hinz, 1991
A13-A14, A88-A89, A110	5	*Furnishina* sp.	Kinnekulle, Västergötland (Sweden)	Cambrian Furongian (Paibian)	P		Müller and Hinz, 1991
A15	1	unrecognizable fragment	Kinnekulle, Västergötland (Sweden)	Cambrian Furongian (Paibian)	P		Müller and Hinz, 1991
A5-A6	2	*Paltodus deltifer deltifer* (Lindström, 1955)	Öland (Sweden)	Early Ordovician (Tremadocian)	E	1.5	IPUM Collection
A10	1	unrecognizable fragment	Öland (Sweden)	Early Ordovician (Tremadocian)	E	1.5	IPUM Collection
A20-A21	2	*Paltodus deltifer pristinus* (Viira, 1970)	Northern Estonia	Early Ordovician (Tremadocian)	E	1.5	Viira, 1970
A30-A31, A98-A99	4	*Amorphognathus* sp. (Pa)	Keisley, Westmorland (UK)	Late Ordovician (Katian)	E	4	Bergström and Ferretti, 2015
A27-A29	3	*Amorphognathus* sp. (Pb)	Keisley, Westmorland (UK)	Late Ordovician (Katian)	E	4	Bergström and Ferretti, 2015
A32-A34, A74-A75	5	*Scabbardella altipes* (Henningsmoen, 1948)	Keisley, Westmorland (UK)	Late Ordovician (Katian)	E	4	Bergström and Ferretti, 2015
A38, A66-A67	3	*Amorphognathus* sp. (Pa)	Cannamenda, Sardinia (Italy)	Late Ordovician (Katian)	E	5	Ferretti and Serpagli, 1999
A37, A41, A68, A72	4	*Amorphognathus* sp. (Pb)	Cannamenda, Sardinia (Italy)	Late Ordovician (Katian)	E	5	Ferretti and Serpagli, 1999
A39-A40, A69-A70	4	*Scabbardella altipes* (Henningsmoen, 1948)	Cannamenda, Sardinia (Italy)	Late Ordovician (Katian)	E	5	Ferretti and Serpagli, 1999
A49-A51	3	*Amorphognathus* sp. (Pa)	Saint-Hilaire-la-Gérard, Normandy (France)	Late Ordovician (Katian)	E	4-5	Ferretti et al., 2014a
62, A52, A107-A108	4	*Amorphognathus* sp. (Pb)	Saint-Hilaire-la-Gérard, Normandy (France)	Late Ordovician (Katian)	E	4-5	Ferretti et al., 2014a
17	1	*Amorphognathus* sp. (Sd)	Saint-Hilaire-la-Gérard, Normandy (France)	Late Ordovician (Katian)	E	4-5	Ferretti et al., 2014a
68, 82	2	*Hamarodus brevirameus* (Walliser, 1964) (M)	Saint-Hilaire-la-Gérard, Normandy (France)	Late Ordovician (Katian)	E	4-5	Ferretti et al., 2014a
49	1	*Hamarodus brevirameus* (Walliser, 1964) (Sc)	Saint-Hilaire-la-Gérard, Normandy (France)	Late Ordovician (Katian)	E	4-5	Ferretti et al., 2014a
21	1	*Icriodella* sp.	Saint-Hilaire-la-Gérard, Normandy (France)	Late Ordovician (Katian)	E	4-5	Ferretti et al., 2014a
20, 56, A53	3	*Panderodus* sp.	Saint-Hilaire-la-Gérard, Normandy (France)	Late Ordovician (Katian)	E	4-5	Ferretti et al., 2014a
24, 41	2	*Sagittodontina robusta* Knüpfer, 1967 (Pa)	Saint-Hilaire-la-Gérard, Normandy (France)	Late Ordovician (Katian)	E	4-5	Ferretti et al., 2014a
46	1	*Sagittodontina robusta* Knüpfer, 1967 (Sd)	Saint-Hilaire-la-Gérard, Normandy (France)	Late Ordovician (Katian)	E	4-5	Ferretti et al., 2014a
45, 59-60, 91, 103, A54, A109	7	*Scabbardella altipes* (Henningsmoen, 1948)	Saint-Hilaire-la-Gérard, Normandy (France)	Late Ordovician (Katian)	E	4-5	Ferretti et al., 2014a
A22	1	*Rhipidognathus symmetricus* Branson, Mehl and Branson, 1951	Saluda Dolomite (USA)	Late Ordovician	E	1	IPUM Collection
A23	1	*Panderodus* sp.	Saluda Dolomite (USA)	Late Ordovician	E	1	IPUM Collection
A104	1	*Belodina* sp.	Kimmswick Formation, Missouri (USA)	Late Ordovician	E	1	IPUM Collection
A105	1	*Plectodina* sp.	Kimmswick Formation, Missouri (USA)	Late Ordovician	E	1	IPUM Collection
A106	1	*Panderodus* sp.	Kimmswick Formation, Missouri (USA)	Late Ordovician	E	1	IPUM Collection
A1	1	*Zieglerodina planilingua* (Murphy and Valenzuela-Ríos, 1999)	U Topolů (Bohemia)	Early Devonian (Lochkovian)	E	3	Chlupáč et al., 1980
A2	1	*Lanea omoalpha* (Murphy and Valenzuela-Ríos, 1999)	U Topolů (Bohemia)	Early Devonian (Lochkovian)	E	3	Chlupáč et al., 1980
A82	1	*Palmatolepis* sp.	Pramosio A, Carnic Alps (Italy)	Late Devonian (Frasnian)	E	4.5	Spalletta and Perri, 1998a
A83	1	*Polygnathus decorosus* Stauffer, 1938	Pramosio A, Carnic Alps (Italy)	Late Devonian (Frasnian)	E	4.5	Spalletta and Perri, 1998a
A80	1	unrecognizable fragment	Casera Collinetta di Sotto A, Carnic Alps (Italy)	Late Devonian (Famennian)	E	4.5	Perri and Spalletta, 1998
A81	1	*Branmehla werneri* (Ziegler, 1957)	Casera Collinetta di Sotto A, Carnic Alps (Italy)	Late Devonian (Famennian)	E	4.5	Perri and Spalletta, 1998
A101	1	*Palmatolepis triangularis* Sannemann, 1955	Texas (USA)	Late Devonian (Famennian)	E	2	IPUM Collection
A102	1	*Palmatolepis subperlobata* Branson and Mehl, 1934	Texas (USA)	Late Devonian (Famennian)	E	2	IPUM Collection
A103	1	*Icriodus* sp.	Texas (USA)	Late Devonian (Famennian)	E	2	IPUM Collection
A76-A77, A100	3	unrecognizable fragments	Dolina, Carnic Alps (Italy)	Carboniferous Early Mississippian (Tournaisian)	E	4.5	Spalletta and Perri, 1998b

Table 1 (*continued*)

Code	n° elements	Conodont taxa	Locality/formation	Age	P/E	CAI	Reference paper(s)/collection
A78-A79	2	*Gnathodus* sp.	Dolina, Carnic Alps (Italy)	Carboniferous Middle Mississippian (Visean)	E	4–4.5	Spalletta and Perri, 1998b
A86-A87	2	*Pachycladina obliqua* Staesche, 1964	Cencenighe Galleria, Dolomites (Italy)	Early Triassic (Olenekian)	E	5.5–6	Perri and Andraghetti, 1987
A84-A85	2	unrecognizable fragments	Sotto le Rive, Dolomites (Italy)	Middle Triassic (Anisian)	E	1.5	Kovaçs et al., 1996; Farabegoli and Perri, 1998
A42-A44	3	*Carnepigondolella pseudodiebeli* (Kozur, 1972)	Pizzo Mondello, Sicani Mountains, Sicily (Italy)	Late Triassic (Carnian)	E	1.5	Mazza et al., 2012; Mazza and Martínez-Pérez, 2015

LeGeros, 1984; Mann, 2001; Skinner, 2005; Glimcher, 2006).

From the crystal-chemical point of view, apatite crystallizes in the hexagonal system and its crystallographic cell parameters, which define the geometry of the crystal lattice in three dimensions by the two parameters a (base) and c (height), vary in size in close correlation with the isomorphic iso- and hetero-valent substitutions that may occur in the various coordination sites (Hughes et al., 1989) that, additionally, impart distinctive features to bones and teeth as well. For example, there is a close correlation between the solubility of bioapatite and the partial substitution of the phosphate anion by carbonate. It is not accidental that teeth, more subject to the attack of acids, contain much less carbonate than bones in order to be less soluble. Moreover, there is an inverse proportionality ratio between concentration of carbonate and hydroxyl ions in bioapatite, as the substitution of phosphate $(PO_4)^{3-}$ with carbonate $(CO_3)^{2-}$ is counterbalanced by removal of calcium from the lattice and limiting the concentration of hydroxyl ions. As a consequence of these substitutions, the lattice is distorted and crystal growth interrupted (*i.e.*, small sized crystals are formed). The first direct consequence is a drastic increase of the surface-to-volume ratio and, thus, of the reactivity toward external molecules (Cazalbou et al., 2004; Wopenka and Pasteris, 2005; Glimcher, 2006; Boskey, 2007).

The effects of these chained events significantly affect the overall biomineralization process. Bioapatite crystal formation is, in fact, ruled by appropriate nucleation or crystallization inhibitors and crystal growth depends on the presence of biological fluids saturated with hydroxyapatite and possibly also various trace elements that can be incorporated within the bioapatite frame (Skinner, 2005; Pasteris et al., 2008). When such inhibitors are removed, mineral growth occurs only from extracellular fluids, whose composition reflects the surrounding environment. Hence several studies, involving bioapatite as a biological and/or environmental marker, have been carried out on fossil remains or Recent organisms (see Keenan, 2016 for a comprehensive review).

This paper focuses on conodonts, which dominated the ancient oceans for over 300 million years from the Cambrian to the Triassic. Being extinct, it is not possible to obtain reliable information about their original composition and structure as the elements have undergone fossilization and diagenesis. Conodonts, for a long time considered enigmatic, represent an extinct group of jawless vertebrates, that were the first among the group to experiment skeletal biomineralization with tooth-like elements in their feeding apparatus (Martínez-Pérez et al., 2014). These elements, ranging in average size from 0.1 to 5 mm, consist of bioapatite with a francolite-like structure, and are arranged in a bilaterally-symmetrical apparatus within the cephalic part of the animal. Conodonts, owing to their rapid evolution and diversity of habitats, represent a fundamental biostratigraphical tool within carbonate depositional environments. Moreover, as bioapatite may archive sea water chemistry information, their chemical composition encourages palaeoenvironmental investigations on ocean geodynamics and climates (Holmden et al., 1996; Trotter et al., 1999; Wenzel et al., 2000).

In the face of these advantages offered by conodont chemical composition, it seems that fossilization and diagenetic processes can affect some trace element incorporation following the biomineralization process. For example, Trotter and Eggins (2006), through comparative analyses of contemporaneous bioapatites and Holocene and Recent fish material, found a linear relationship between their respective REE, Y, Pb, Th, and U incorporations, with repercussions for their possible liability to diagenesis. A similar argument also applies to vertebrate enamel which, in general, is subject to isomorphic substitutions much less than other mineralized vertebrate tissues (Kohn et al., 1999; Trueman and Tuross, 2002).

Notwithstanding the numerous studies that accounted for trace element (and isotope) incorporations in conodont bioapatite, little or nothing regarding the structural variations of bioapatite in conodont elements has been published. In fact it has been widely demonstrated

INTERNATIONAL CHRONOSTRATIGRAPHIC CHART

IUGS   www.stratigraphy.org   International Commission on Stratigraphy   v 2018/08
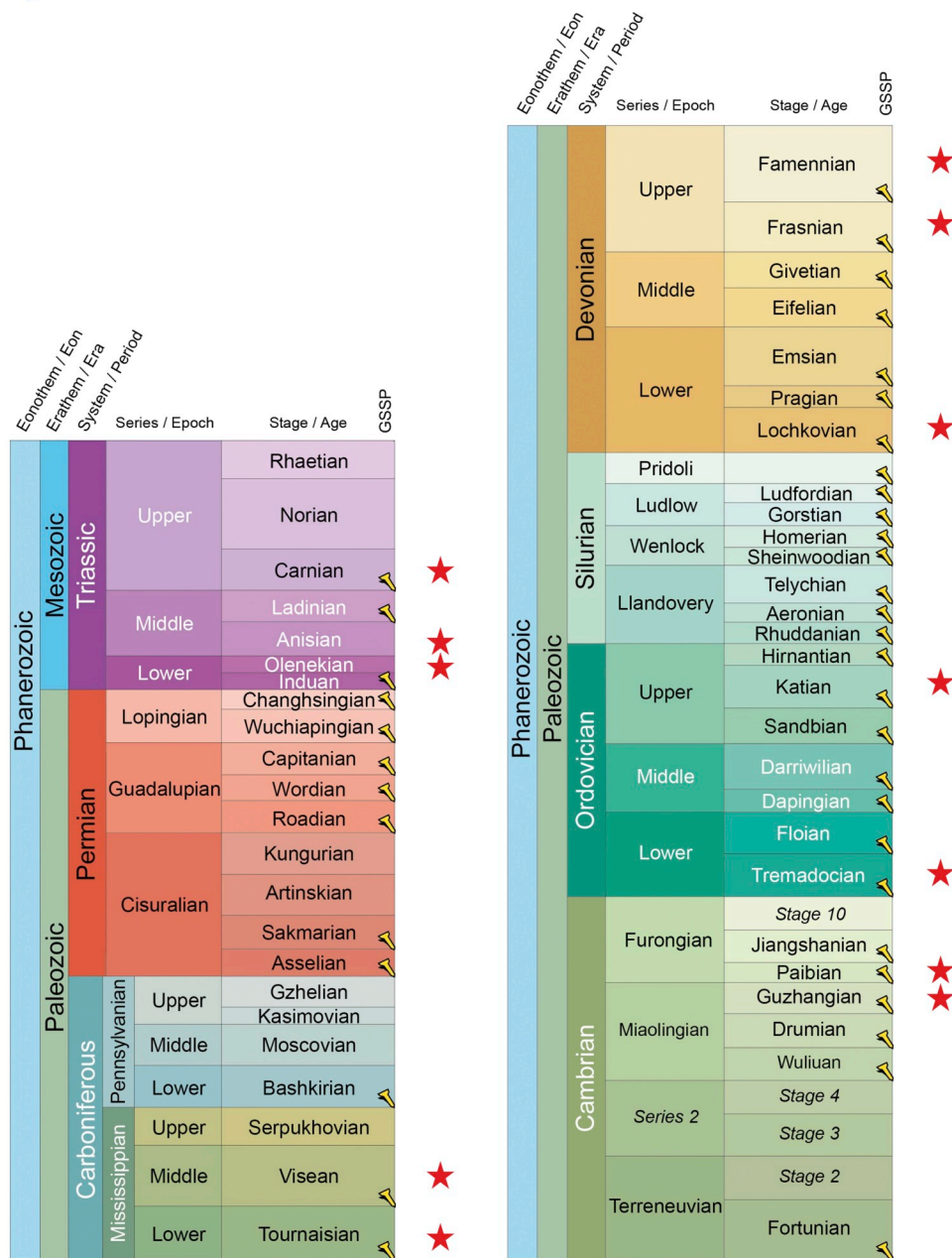
Fig. 1. Different time frames investigated in this study (red stars) plotted on the latest version of the International Commission on Stratigraphy Chronostratigraphic Chart (2018/08: http://www.stratigraphy.org/index.php/ics-chart-timescale; see Cohen et al., 2013, updated 2018).

that isomorphic substitutions of major elements in apatite significantly affect the dimension of cell parameters (McConnell, 1973; Hughes et al., 1989; Hughes and Rakovan, 2002; Rodríguez-Lorenzo et al., 2003). Conversely, their measure can provide a nice approximation of the quantitative chemical composition of major elements that, in conodonts, is not easily measurable due to their small size and a lack of proper certified analytical standards with a phosphatic matrix. For example, it has been observed that the cell parameter a calculated for a pure fluorapatite (obtained by synthesis) is significantly lower than that of natural bioapatites which contain both hydroxyl and carbonate ions. Likewise, a progressive decrease of the same cell parameter in a continuous series of crystals reflects progressive substitutions of hydroxyl with fluorine (Hughes and Rakovan, 2002).

In this paper we measure and compare bioapatite crystallographic cell parameters in conodonts of different age (Cambrian to Triassic), taxonomic assignment, geographic provenance and CAI. Furthermore, cell parameters of conodont bioapatite are compared with those of coeval phosphatic or phosphatized fossils recovered from the same residue resulting from conodont preparation (i.e., brachiopods, bryozoans, fish teeth, and ostracodes). The output of the comparison will be related to a possible interference of fossilization and diagenesis after biomineralization. As demonstrated (Ferretti et al., 2017), the calculation of the cell parameters of a single conodont element can be successfully achieved through the employment of micro X-ray diffraction (μ-XRD) measurements which allow to obtain *in-situ* diffraction patterns.

Fig. 2. Some of the conodont elements analyzed in this study. A: *Westergaardodina* sp., late Cambrian, specimen no. A11, IPUM 29101, Västergötland (Sweden); B: *Furnishina alata* Szaniawski, 1971, late Cambrian, specimen no. A18, IPUM 29102, Żarnowiec (Poland); C: *Furnish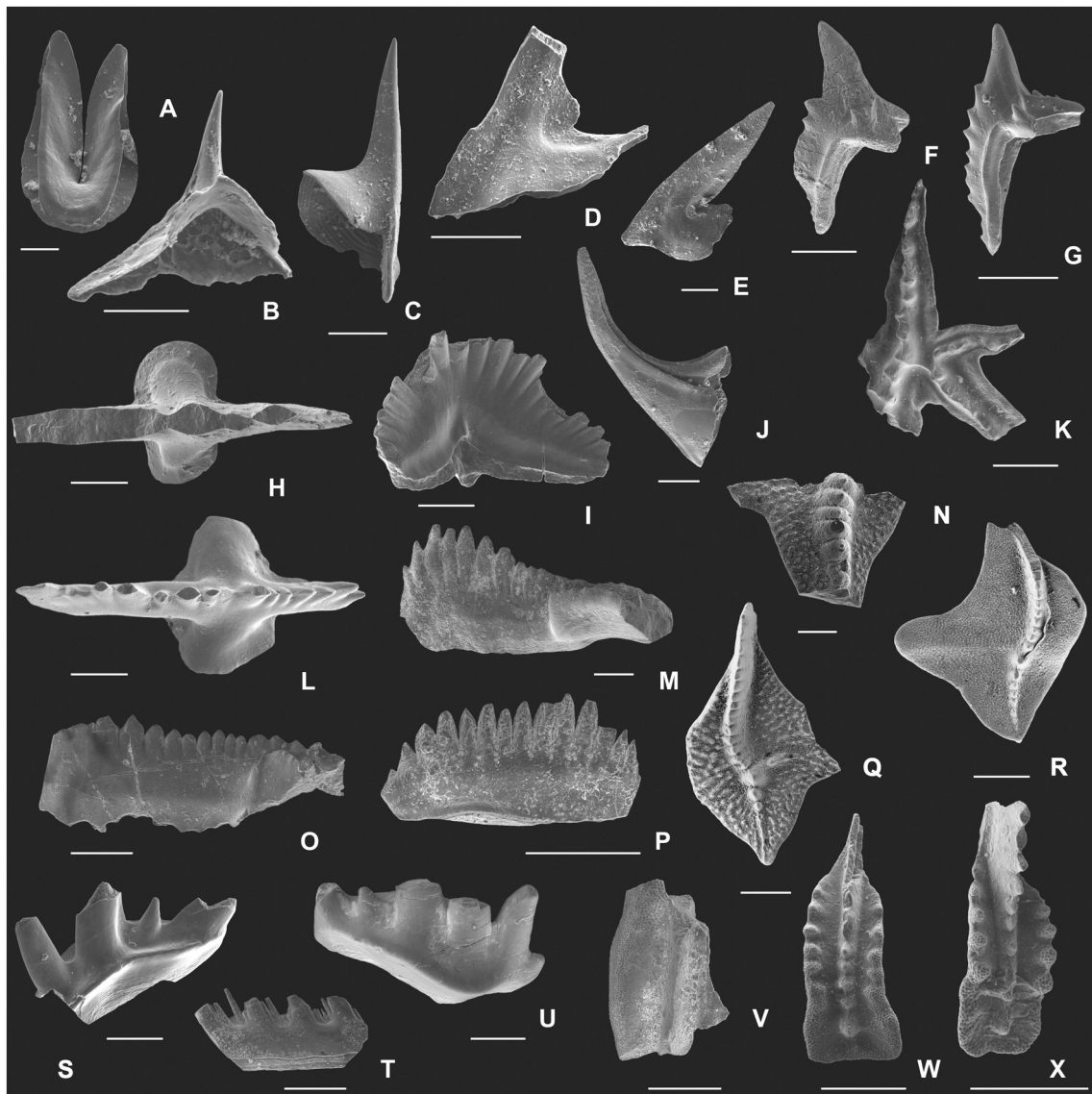ina* sp., late Cambrian, specimen no. A14, IPUM 29103, Västergötland (Sweden); D: *Paltodus deltifer deltifer* (Lindström, 1955), Early Ordovician, specimen no. A6, IPUM 29104, Öland (Sweden); E: *Hamarodus brevirameus* (Walliser, 1964), M element, Late Ordovician, specimen no. 82, IPUM 29105, Normandy (France); F: *Amorphognathus* sp., Pb element, Late Ordovician, specimen no. A41, IPUM 29106, Sardinia (Italy); G: *Amorphognathus* sp., Pb element, Late Ordovician, specimen no. A27, IPUM 29107, Westmorland (UK); H: *Lanea omoalpha* (Murphy and Valenzuela-Ríos, 1999), Early Devonian, specimen no. A2, IPUM 29108, U Topolů (Bohemia); I: *Rhipidognathus symmetricus* Branson, Mehl and Branson, 1951, Late Ordovician, specimen no. A22, IPUM 29109, Saluda Dolomite (USA); J: *Scabbardella altipes* (Henningsmoen, 1948), Late Ordovician, specimen no. 45, IPUM 29110, Normandy (France); K: *Amorphognathus* sp., Pa element, Late Ordovician, specimen no. A98, IPUM 29111, Westmorland (UK); L: *Zieglerodina planilingua* (Murphy and Valenzuela-Ríos, 1999), Early Devonian, specimen no. A1, IPUM 29112, U Topolů (Bohemia); M: *Polygnathus decorosus* Stauffer, 1938, Late Devonian, specimen no. A83, IPUM 29113, Carnic Alps (Italy); N: *Palmatolepis* sp., Late Devonian, specimen no. A82, IPUM 29114, Carnic Alps (Italy); O: *Gnathodus* sp., Middle Mississippian, specimen no. A78, IPUM 29115, Carnic Alps (Italy); P: *Branmehla werneri* (Ziegler, 1957), Late Devonian, specimen no. A81, IPUM 29116, Carnic Alps (Italy); Q: *Palmatolepis triangularis* Sannemann, 1955, Late Devonian, specimen no. A101, IPUM 29117, Texas (USA); R: *Palmatolepis subperlobata* Branson and Mehl, 1934, Late Devonian, specimen no. A102, IPUM 29118, Texas (USA); S, U: *Pachycladina obliqua* Staesche, 1964, Early Triassic, specimens no. A87 and A86, IPUM 29119 and IPUM 29121, Dolomites (Italy); T: unrecognizable fragment, Early Mississippian, specimen no. A77, IPUM 29120, Carnic Alps (Italy); V: unrecognizable fragment, Middle Triassic, specimen no. A84, IPUM 29122, Dolomites (Italy); W–X: *Carnepigondolella pseudodiebeli* (Kozur, 1972), Late Triassic, specimens no. A44 and A43, IPUM 29123 and IPUM 29124, Sicily (Italy). Scale bars correspond to 200 μm.

2. Material and methods

2.1. Study materials

Material investigated herein derives from conodont collections organized at the University of Modena and Reggio Emilia (IPUM Collection) in his long career by Enrico Serpagli, from material prepared by one of us (AF) in her study on Late Ordovician faunas as well as from specimens kindly provided by other conodont workers. A conodont assemblage of about one hundred elements (Table 1), spanning in age from the Cambrian to the Triassic (Fig. 1) and including both paraconodonts and euconodonts (Fig. 2), was investigated in this paper. Material results from standard conodont processing techniques.

In order to make comparisons between the bioapatite signal of the

Table 2
Other phosphatic/phosphatized fauna (OPF) analyzed in the present paper, referred to geographic location and age.

Code	Faunal element	Locality	Age
A16	ostracod	Kinnekulle, Västergötland (Sweden)	Cambrian Furongian (Paibian)
A17	ostracod	Kinnekulle, Västergötland (Sweden)	Cambrian Furongian (Paibian)
A92	ostracod	Kinnekulle, Västergötland (Sweden)	Cambrian Furongian (Paibian)
A93	ostracod	Kinnekulle, Västergötland (Sweden)	Cambrian Furongian (Paibian)
A94	ostracod	Kinnekulle, Västergötland (Sweden)	Cambrian Furongian (Paibian)
A95	undetermined	Kinnekulle, Västergötland (Sweden)	Cambrian Furongian (Paibian)
A96	undetermined	Kinnekulle, Västergötland (Sweden)	Cambrian Furongian (Paibian)
A97	undetermined	Kinnekulle, Västergötland (Sweden)	Cambrian Furongian (Paibian)
A7	brachiopod	Öland (Sweden)	Early Ordovician (Tremadocian)
A8	brachiopod	Öland (Sweden)	Early Ordovician (Tremadocian)
A9	brachiopod	Öland (Sweden)	Early Ordovician (Tremadocian)
A25	brachiopod	Keisley, Westmorland (UK)	Late Ordovician (Katian)
A26	brachiopod	Keisley, Westmorland (UK)	Late Ordovician (Katian)
A73	brachiopod	Cannamenda, Sardinia (Italy)	Late Ordovician (Katian)
A36	brachiopod	Cannamenda, Sardinia (Italy)	Late Ordovician (Katian)
A55	brachiopod	Saint-Hilaire-la-Gérard, Normandy (France)	Late Ordovician (Katian)
A64	brachiopod	Saint-Hilaire-la-Gérard, Normandy (France)	Late Ordovician (Katian)
A3	brachiopod	U Topolů (Bohemia)	Early Devonian (Lochkovian)
A4	brachiopod	U Topolů (Bohemia)	Early Devonian (Lochkovian)
A35	bryozoan	Cannamenda, Sardinia (Italy)	Late Ordovician (Katian)
A71	bryozoan	Cannamenda, Sardinia (Italy)	Late Ordovician (Katian)
A58	bryozoan	Saint-Hilaire-la-Gérard, Normandy (France)	Late Ordovician (Katian)
A61	bryozoan	Saint-Hilaire-la-Gérard, Normandy (France)	Late Ordovician (Katian)
A65	bryozoan	Saint-Hilaire-la-Gérard, Normandy (France)	Late Ordovician (Katian)
A24	bryozoan	Saluda Dolomite (USA)	Late Ordovician
A45	fish tooth	Pizzo Mondello, Sicani Mountains, Sicily (Italy)	Late Triassic (Carnian)
A46	fish tooth	Pizzo Mondello, Sicani Mountains, Sicily (Italy)	Late Triassic (Carnian)
A47	fish tooth	Pizzo Mondello, Sicani Mountains, Sicily (Italy)	Late Triassic (Norian)

conodont elements and those of other fossil organisms, the same analytical procedure was applied to other phosphatic/phospatized organisms selected from the same residues producing conodonts. In this way the investigation has included brachiopods, bryozoans, ostracods and fish teeth (Table 2; Fig. 3).

All analyzed material is housed in the Palaeontological Collections of the University of Modena and Reggio Emilia: under accession prefix IPUM at the Department of Chemical and Geological Sciences, University of Modena and Reggio Emilia, Modena, Italy.
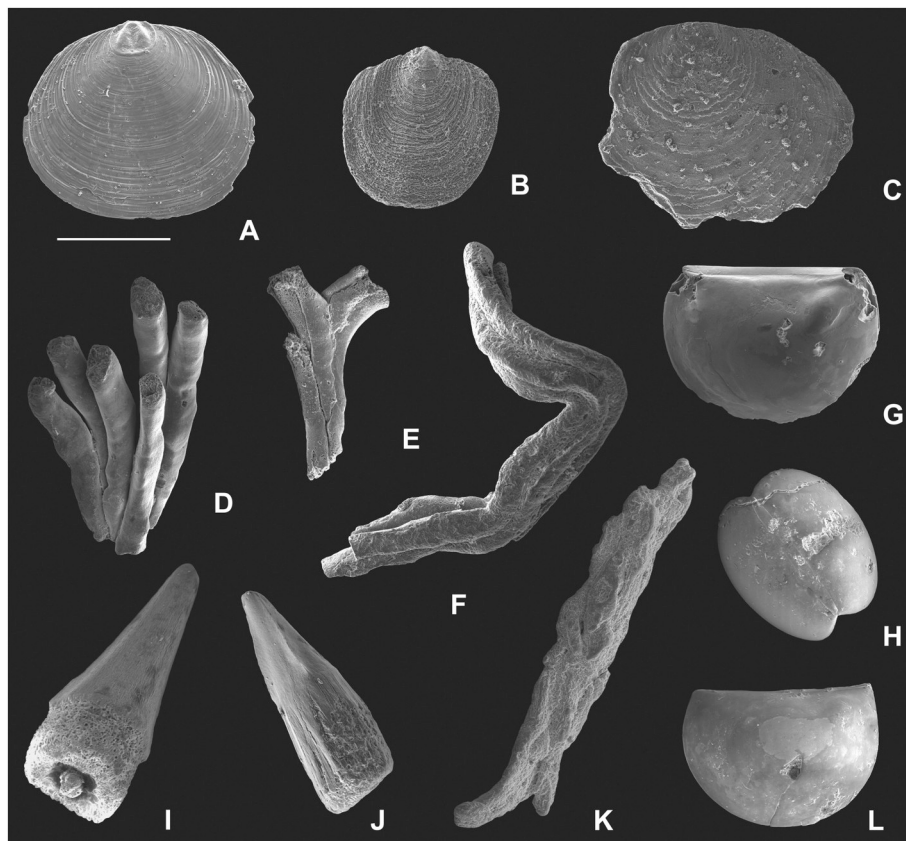
Fig. 3. Some of the other phosphatic fauna (OPF) analyzed in this study. A–C: brachiopods, Early Devonian (A) and Late Ordovician (B–C−), specimens no. A3, A26 and A36, IPUM 29125–29127, U Topolů (Bohemia), Westmorland (UK) and Sardinia (Italy), respectively; D–E: bryozoans, Late Ordovician, specimens no. A24 and A61, IPUM 29128 and IPUM 29129, Saluda Dolomite (USA) and Normandy (France), respectively; F, K: undetermined phosphatic material, late Cambrian, specimens no. A95 and A96, IPUM 29130 and IPUM 29135, Västergötland (Sweden); G–H, L: ostracodes, late Cambrian, specimens no. A17, A94 and A93, IPUM 29131, IPUM 29132 and IPUM 29136, Västergötland (Sweden); I–J: fish teeth, Late Triassic, specimens no. A45 and A46, IPUM 29133 and IPUM 29134, Sicily (Italy).
Scale bars correspond to 500 μm except for G (400 μm) and H, L (300 μm).

2.2. SEM/ESEM microscopy

Conodonts elements and associated phosphatic fossils were initially analyzed and photographed under optical and electron microscopy. For non-conodont material, the presence of bioapatite was preliminarily tested. Specimens were mounted on aluminum stubs previously covered with carbon-conductive adhesive tape. Au-coated and non-coated elements were observed using an Environmental Scanning Electron Microscope (ESEM) FEI ESEM-Quanta 200, equipped with an Oxford EDX INCA 300 X-ray energy dispersive spectrometer and by a Scanning Electron Microscope (SEM) Nova NanoSEM FEI 450 equipped with a X-EDS Bruker QUANTAX-200 detector. ESEM observations were performed in high and low vacuum (low vacuum brackets 1 and 0.5 Torr) with an accelerating voltage between 5 and 25 keV for imaging and between 5 and 15 keV for elemental analyses. SEM observations were in high vacuum with an accelerating voltage between 15 and 25 keV for imaging and between 15 and 25 keV for elemental analyses.

2.3. X-ray microdiffraction (μ-XRD)

X-ray diffraction measurements were carried out with a micro X-ray diffractometer. This instrument is extremely versatile and allows the non-destructive study of structural properties of the material such as, for example, the mineralogical composition of the crystalline phases, the degree of crystallinity, the size of crystallites, the detection of preferential orientation, *etc.*, with the same accuracy obtainable with conventional diffractometers, but with the advantage of detecting measurements on very small portions of the sample and, thus, on small-sized fossils. Here, μ-XRD measurements were performed on elements mounted on small plane surfaces. Data were acquired using a Rigaku D/ MAX RAPID diffraction system, operating at 40 kV and 30 mA equipped with a CuKα source, curved-image-plate detector, flat graphite monochromator, variety of beam collimators, motorized stage and

microscope for accurate positioning of the sample. Measurements were performed in reflection mode using a 300-μm collimator and collection times of 30 min and by varying the Omega and Phi angles between one sample and the other to fit with the instrument geometry and thus to obtain a significant number of diffraction effects with a maximized signal-to-noise ratio. The μ-XRD data were collected as two-dimensional images and then converted into 2θ-I profiles using the Rigaku R-AXIS Display software. A 300-μm collimator was suitable to obtain mean values of bioapatite cell parameters representative of the conodont elements in their wholeness.

Even though a previous study demonstrated that apatite overgrowth perfectly replicates the original structure (Ferretti et al., 2017), when possible each point was selected to avoid analyses on newly formed crystals. After measurement, unit-cell parameters were refined using UnitCell software (Holland and Redfern, 1997). All diffraction spots shown in the two-dimensional images were excluded due to the fact that they were related to single crystals (Ferretti et al., 2017).

Optical microscopy and ESEM-EDX analyses were performed at the Scientific Instruments Facility (CIGS) of the University of Modena and Reggio Emilia (Modena, Italy), whereas X-ray diffraction measurements were made at the Institute of Methodologies for Environmental Analysis of the National Research Council of Italy of Tito Scalo (Potenza, Italy).

3. Results

3.1. Conodont faunal data

A collection of about one hundred conodont elements spanning in age from the late Cambrian to the Late Triassic and including both paraconodonts and euconodonts was analyzed in this study. Elements were carefully selected and most were from well-known and published sequences biostratigraphically firmly constrained in order to refer to specific time frames. Only specimens with a good preservation state
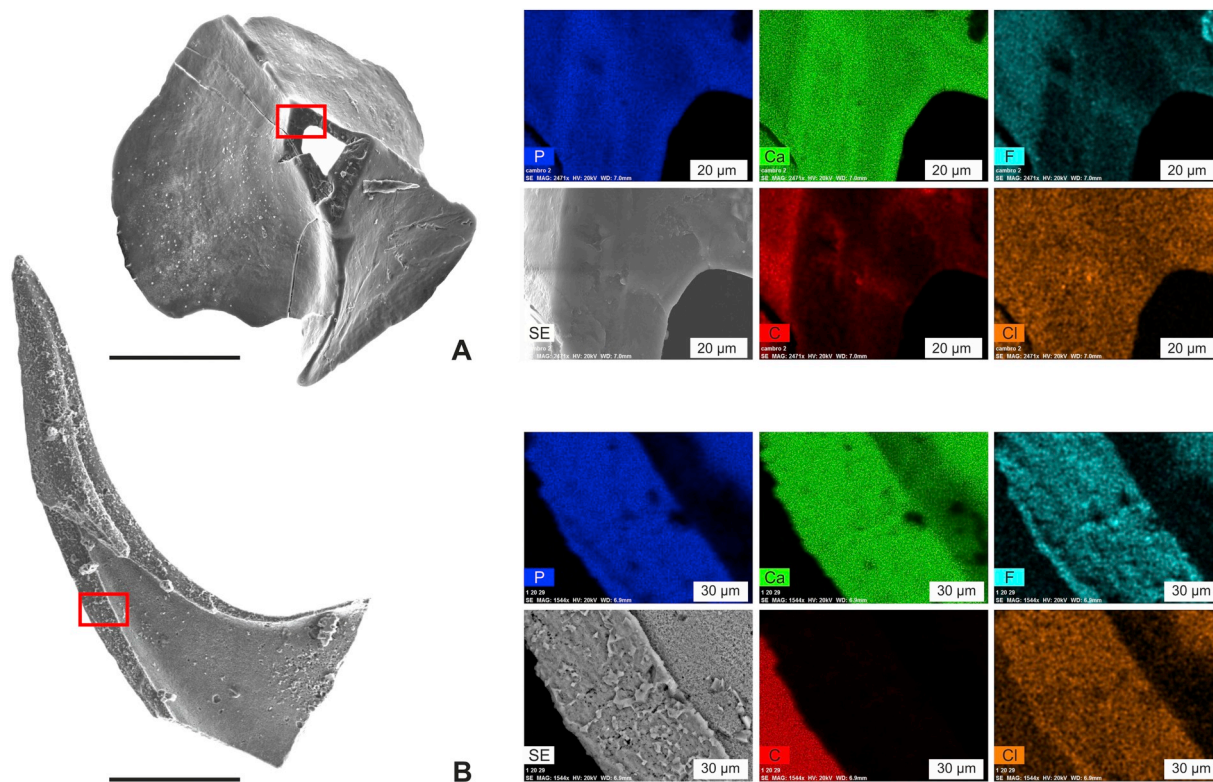

Fig. 4. Chemical composition. ESEM image and SEM-EDS elemental maps (P, Ca, F, C, and Cl). A: *Furnishina* sp., late Cambrian, specimen no. A110, IPUM 29137, Västergötland (Sweden). B: *Scabbardella altipes* (Henningsmoen, 1948), Late Ordovician; specimen no. A109, IPUM 29138, Normandy (France). Scale bars correspond to 200 μm.

were analyzed. CAI covered of our conodont fauna ranges from 1 to 6.

For a precise interval (Late Ordovician; *Amorphognathus ordovicicus* Zone), elements occupying different positions in the same apparatus were processed in order to test possible contrasting signals. Pa, Pb and Sd elements of *Amorphognathus* sp., Pa and Sd elements of *Sagittodontina robusta* Knüpfer, 1967, and M and Sc elements of *Hamarodus brevirameus* (Walliser, 1964) were investigated for this purpose. Furthermore, results from the widely-distributed taxa *Amorphognathus* sp. and *Scabbardella altipes* (Henningsmoen, 1948) were compared from three geographic areas: Sardinia (Domusnovas Formation, Italy; Ferretti and Serpagli, 1999) and Normandy (Vaux Limestone, France; Ferretti et al., 2014a) located along the peri-Gondwana margin and Westmorland (Keisley Limestone, UK; Bergström and Ferretti, 2015) located in Avalonia. For a more global assessment of the Late Ordovician conodont faunas, refer to Ferretti et al. (2014b).

3.1.1. ESEM and SEM characterization

Conodont elements were preliminarily investigated in order to monitor distribution of major elements. Environmental scanning electron microscopy coupled with microanalyses (SEM/ESEM-EDX) was applied to the entire surface of the conodont specimens, with special attention to detect variations through the element wall thickness. Broken elements were carefully analyzed and scanned for this purpose. Maps of major element (P, Ca, F, C, Cl, K, Na, Ba, Fe, Pb, S) distribution do not vary significantly through the element wall, both for para-

conodonts (Fig. 4A) and euconodonts (Fig. 4B). These findings support the presence of the same carbonate-fluoroapatite in the conodont element.

3.1.2. μ-XRD measurements and cell parameter refinements

Table SI–1 reports calculated cell parameters for conodonts (Table SI–1a) and non-conodonts (Table SI–1b) listed in Tables 1–2. If analyzed globally, our data enhance an overall considerable dispersion of the cell parameter *a* of the bioapatite. The cell parameter *c*, differently, appears to be highly variable among the euconodonts (Table SI–1a), and more stable in the other fossil groups, in particular paraconodonts (Table SI–1a) and brachiopods (Table SI–1b). Selected data are plotted and discussed in the following sections.

Fig. 5 plots the bioapatite crystallographic cell parameters *c vs a* for euconodonts and paraconodonts. It is remarkable that paraconodonts and euconodonts clearly occupy two different and non-overlapping fields of the plot. More in detail, the comparison clearly highlights that: i) the cell parameter *a* is smaller in paraconodonts than in euconodonts and it ranges between 9.337(6) and 9.392(6) (Table SI–1a, specimens A14 and A21, respectively); ii) values of the cell parameter *c* of all paraconodonts are very close to the highest values of *c* of the euconodonts that ranges between 6.857(6) and 6.911(2) (Table SI–1a, specimens A1 and A89, respectively). Fig. 6 plots the bioapatite crystallographic cell parameters *c vs a* for conodonts according to their age, spanning from the late Cambrian (Guzhangian) to the Late Triassic (Carnian). It is highly evident that age does not affect cell parameter distribution. In fact, from a chronological point of view, some values of the cell parameter *a* calculated for the youngest euconodonts (Carboniferous and Triassic) are surprisingly much closer to Cambrian paraconodonts than to Ordovician euconodonts. Fig. 7 plots the bioapatite crystallographic cell parameters *c vs a* for selected Late Ordovician conodonts according to their taxonomic assignment (Fig. 7A) and geographic area (Fig. 7B). No correlation is evident in either plots: neither taxonomy (including position occupied within the apparatus architecture) nor geographic location appear to influence cell parameter values.

3.2. Other phosphatic fauna (OPF)

Phosphatic/phosphatized material was picked exactly from the same residues that had produced the conodont elements that were analyzed, in order to detect additional bioapatite signals and to exclude effects of diverse preparation technique and diagenesis. Well preserved phosphatized ostracodes (Fig. 3G–H, L) and undetermined material (Fig. 3F, K) were picked from the same late Cambrian residue so to offer possible comparison with paraconodonts. A wider age range was covered by the analyzed brachiopods (Fig. 3A–C), spanning from the Early
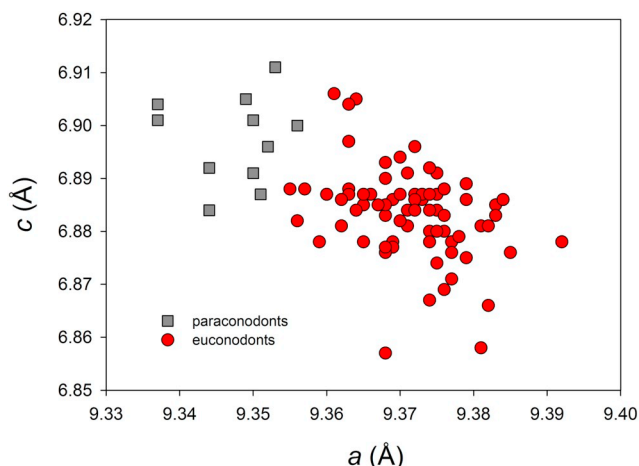
Fig. 5. Binary plot of bioapatite crystallographic unit-cell parameters *c vs a* for euconodonts and paraconodonts.
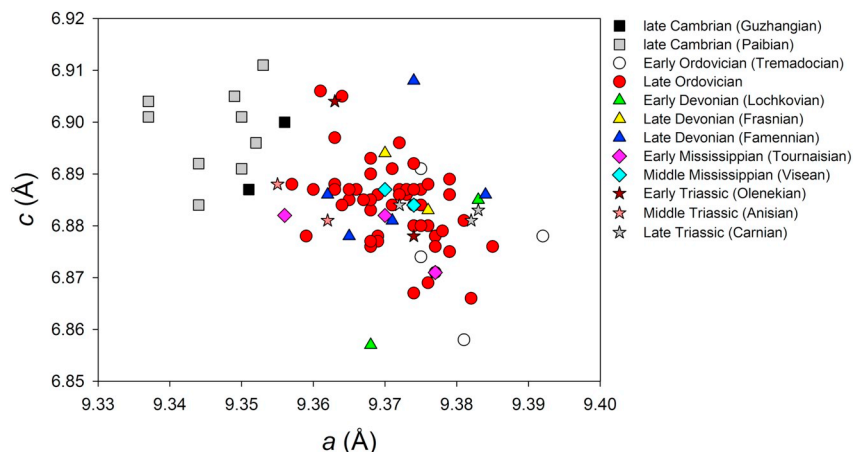
Fig. 6. Binary plot of bioapatite crystallographic unit-cell parameters *c vs a* of conodonts by age.
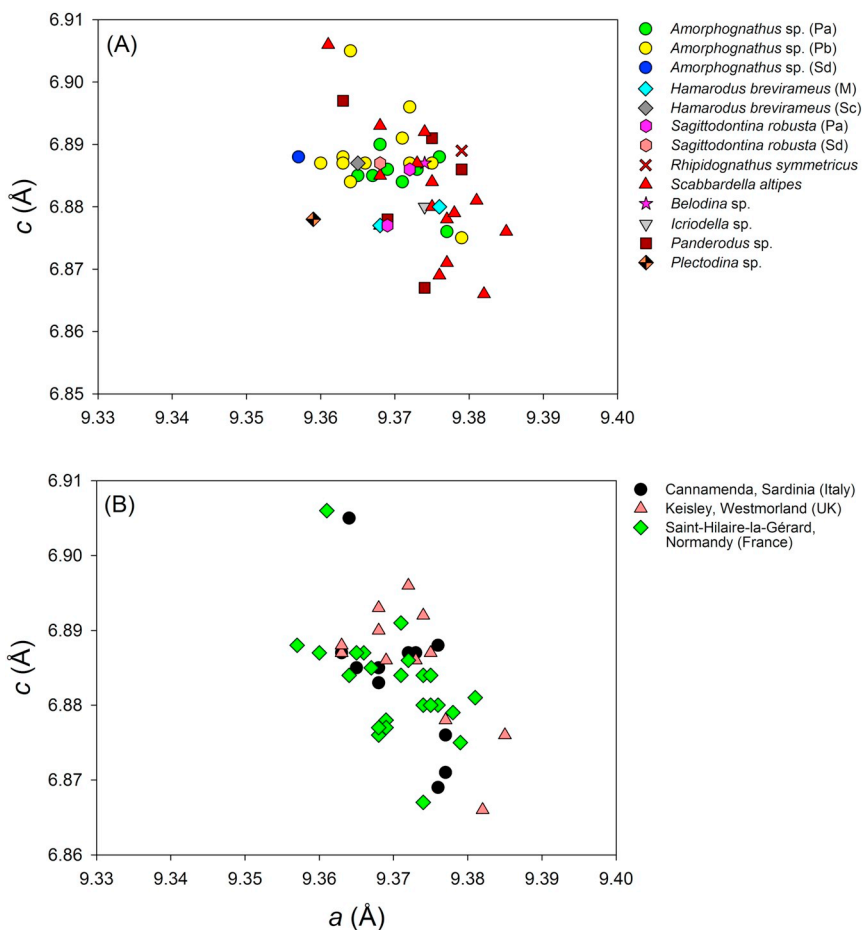
Fig. 7. Binary plot of bioapatite crystallographic unit-cell parameters *c vs a* of Late Ordovician conodonts by taxonomy (A) and geographic provenance (B).

Ordovician to the Early Devonian. Particular effort was made to document brachiopods from the three Late Ordovician areas (Sardinia, Normandy and Westmoreland) investigated in detail also with conodonts. Only Late Ordovician bryozoans (Fig. 3D–E), but from three geographic sectors, were processed for investigation. Finally, a few fish teeth (Fig. 3I–J) from Upper Triassic residues were measured. The presence of bioapatite was preliminarily tested by ESEM and SEM techniques so as to exclude non-phosphatic material. No further chemical detailed analysis was attempted.

3.2.1. *μ-XRD measurements and unit cell parameter refinements*

Fig. 8 reports bioapatite crystallographic cell parameters for all analyzed OPF. For simplicity, the age-average values of cell parameters calculated for conodonts are reported as well. Main terms of the comparison are: i) values of the cell parameter *a* calculated for all the OPF are generally lower (or, at least, very close) than those calculated for euconodonts, with the exception of a Late Triassic fish tooth (specimen A47; Norian); ii) on the opposite, values of cell parameter *c* calculated for all the OPF are significantly higher (or, at least, very close) than those calculated for euconodonts, with the exception of a Late Ordovician brachiopod (specimen A55; Katian); iii) late Cambrian OPF

Fig. 8. Binary plot of bioapatite crystallographic unit-cell parameters *c vs a* for other phosphatic/phosphatized fauna (ostracodes, brachiopods, bryozoans and fish teeth) compared with average values of conodonts by age.
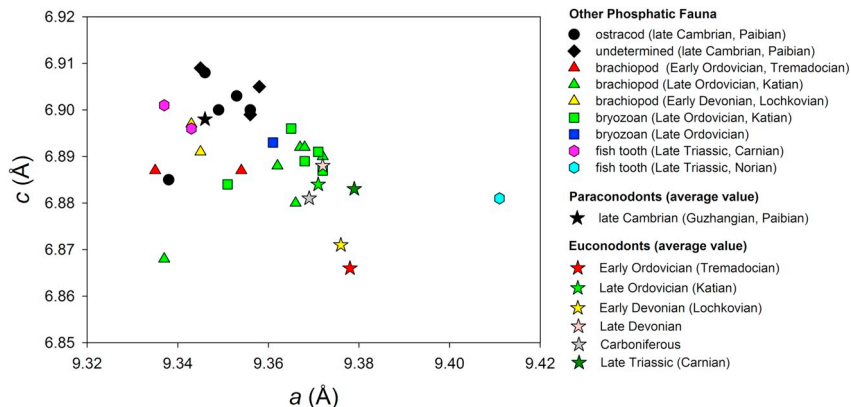
(ostracodes and undetermined material) share similar values of both cell parameters with paraconodonts, with the exception of an ostracod (specimen A94; Paibian); iv) similar values were calculated also for Early Devonian (Lochkovian) brachiopods and a Late Triassic (Carnian) fish tooth.

All results will be further discussed below. However, any conclusion from OPF should be regarded as preliminary since the number of analyzed OPF specimens is significantly lower than conodonts and because we could preliminarily test provenance effects on cell parameters only for bryozoans and brachiopods and age only for brachiopods.

4. Discussion

Bioapatites are generally classified as francolites [$Ca_5(PO_4, CO_3)_3F$)] or as dahllites [$Ca_5(PO_4, CO_3)_3(OH)$]. From a strict mineralogical point of view, these are no longer valid nomenclature forms (discredited by the IMA in 2008) as carbonate is not the dominant species in tetrahedral isomorphic substitutions (type B substitutions) (Wopenka and Pasteris, 2005). Moreover, numerous studies carried out to-date (see Liu et al., 2013 for a review) have shown that many other isomorphic substitutions occur in bioapatites and, in consequence, the chemical formulas of francolite and dahllite cannot be considered completely exhaustive for the composition of these biomaterials. As mentioned in the Introduction, isomorphic substitutions of major elements in apatite significantly affect crystallographic cell parameter dimensions. For example, substitutions of $(CO_3)^{2-}$ for $(PO_4)^{3-}$ results in an increase of the cell parameter *c* and a contraction of the cell parameter *a*, whereas $(CO_3)^{2-}$ for $(OH)^-$ substitution produces the opposite results (LeGeros, 1981). Therefore, even if to-date there is no evidence that francolite and dahllite can be considered as the end-members of a continuous solid solution, it is unquestionable that the measurement of cell parameters can provide a nice approximation of major element chemical composition. This approach could be mandatory when both the presence of the C element and small size of the sample prevents a more detailed chemical characterization than semi-quantitative EDS or EDX techniques.

Nemliher et al. (2004) combined X-ray diffraction on powdered sample and chemical EDX measurements on fragments of Recent fish and marine mammal skeletons, phosphatic brachiopods and oceanic phosphorites. Data were compared with fossil material and phosphorites of Cretaceous, Miocene and Holocene age. The authors observed a reduction of the cell parameter *a* in fossil material and related this both to the increase of carbonate content and to the decrease in the hydroxyl-ion content subsequent to the recrystallization of apatite. More specifically, they proposed that the substitutions of OH with F are contextual to the progressive decrease in cell volume, evidence that also suggests that these substitutions do not significantly affect cell parameter *c*. Zhang et al. (2017), through a multi-analytical approach combining Raman spectroscopy, high resolution X-ray diffraction and chemical analyses on well-preserved Ordovician coniform conodonts from South China, documented several chemical substitutions occurring during diagenesis that affect conodont tissue types (albid and hyaline crown, and basal body) differently. Such observations were previously highlighted by Trotter et al. (2007) in their examination of hyaline and albid crown tissues using transmission electron microscopy.

The absence of significant correlation in our euconodonts between bioapatite cell parameters and taxonomic assignment, age, and geographic provenance of the elements supports the hypothesis that isomorphic substitutions are not exclusively correlated with the age of the fossil. Triassic elements are, in fact, much more deviated compared to the Ordovician ones (Fig. 7). On the other hand, euconodont cell parameters define a higher range of values than paraconodonts (Fig. 5), even if Ordovician euconodonts are closer in age to paraconodonts than to Early Triassic euconodonts. The existence of two clearly separate distribution fields of cell parameters, one for paraconodonts and one for euconodonts, is further strengthened plotting values of bioapatite cell

volume (Fig. SI–1). Again, two distinct distributions appear, one for paraconodonts and one for euconodonts. These results improve the knowledge of these elements which were previously studied and distinguished using synchrotron radiation X-ray tomographic microscopy to characterize and compare the microstructure of morphologically similar euconodont and paraconodont elements (Murdock et al., 2013).

Transformation of an original bioapatite could also occur by dissolution/recrystallization processes or by metasomatic substitutions. Dissolution/recrystallization drives to the formation of large-size crystals with high crystallinity, whereas metasomatic substitutions normally lead to a reduction of the crystallinity and do not affect crystal size. Notwithstanding which of the two is the main promoter of the transformation, there is general agreement that temperature should favor isomorphic substitution. By restricting the observation to euconodonts, it was thus surprising to find no significant correlation between cell parameters and CAI (Fig. SI–2). Similar conclusions are supported by Zhang et al. (2017) by the analysis of conodonts exhibiting CAI of 1–3, but with no significant relationship between CAI and chemical composition, Raman spectroscopic features, and crystallinity.

Comparison of our data and those available in similar studies on conodonts (Fig. SI–3) provides a foremost endorsement of our interpretation. Unfortunately, conodont cell parameters available in the literature are extremely scarce. With the exception of those reported in our previous paper (Ferretti et al., 2017) and here considered, to our knowledge only two researches (Pietzner et al., 1968; Nemliher and Kallaste, 2012) provide this information. Results from Pietzner et al. (1968) were not plotted as information about measurements, and data management are missing. Nemliher and Kallaste (2012) applied an experimental approach, different from ours, but that undoubtedly provides us a useful comparison tool. In fact, the authors calculated cell parameters from X-ray spectra measured on powders produced grinding various specimens of different taxa belonging to different biozones (ranging from the Early Ordovician to the Silurian). Detected cell parameters could therefore be considered as an average value representative of each biozone. Fig. SI–3 shows that there is a nice agreement with our data, including average values calculated for Ordovician elements, and those from the cited authors.

Further support of the absence of a close relationship between cell parameter values and age/geographic provenance is provided by comparing signals of conodonts and other phosphatic fauna (OPF) (Fig. 8). In fact, excluding the out of range cell parameter values above mentioned among OPF (specimens A47 and A55), remaining data could be better sorted considering the fossil group rather than its age or locality.

Lack of additional material does not allow definitive conclusions to be formulated without speculation. However, if our preliminary data are confirmed by further measurements on larger and more varied faunal collections, including also Recent material and with diverse preservation (Ferretti et al., 2012), it appears that primary biomineralization provides an indelible footprint, only mediated by fossilization and diagenetic processes.

5. Conclusions

This research has added to routine morphological and chemical qualitative characterization, achievable through optical and electronic microscopy, by integrating a crystallographic approach based on X-ray microdiffraction (μ-XRD) to gain enhanced structural information about conodonts and other bioapatite fossils. Microdiffraction measurements, recently introduced in conodont studies by our research group, is, in fact, a powerful tool for obtaining crystallographic information when dealing with small-sized samples like conodont elements. Moreover, μ-XRD is a non-destructive technique for dealing with irreplaceable material. The methodological approach and the results here obtained were additionally strengthened by comparison with data from the literature that had been obtained through conventional methods (X-ray powder diffraction) that parallel our findings.

As reported in the literature, bioapatite crystallographic cell parameters strongly depend on different isomorphic substitutions. Our data reveal that cell parameters calculated for paraconodonts significantly differ from those derived for euconodonts. In fact, paraconodonts bear smaller cell parameters *a* and higher cell parameters *c*, very close to the highest values of *c* of euconodonts. Moreover, cell parameters calculated for both paraconodonts and euconodonts appear to be independent of age, taxonomic assignment, geographic provenance and, for euconodonts, CAI (*i.e.*, temperature). Other phosphatic/phosphatized material from the same residues producing conodonts are characterized by values of the cell parameters that, in a preliminary way, appear to be mainly correlated with the type of organism even if, for some of them, a correlation also with age cannot be completely ruled out.

It is, therefore, conceivable that major element content strongly depends not only on fossilization, diagenesis and metasomatism, but mostly on the primary bioapatite composition. In other words, from a close crystal-chemical point of view, it is not possible to unequivocally conclude, for example, that the cell parameter *a*, smaller in paraconodonts than in euconodonts, is the direct consequence of a sort of "francolitization" process (*i.e.*, the formation, for progressive and successive isomorphic substitutions, of the end-member francolite that, as already pointed out, was never proved) during fossilization and/or diagenesis.

Acknowledgements

Appendix A. Supplementary data

Supplementary data to this article can be found online at https://doi.org/10.1016/j.palaeo.2019.02.024.

References

Banfield, J.F., Zhang, H., 2001. Nanoparticles in the environment. Rev. Mineral. Geochem. 44 (1), 1–58.

Bergström, S.M., Ferretti, A., 2015. Conodonts in the Upper Ordovician Keisley Limestone of northern England: taxonomy, biostratigraphical significance and biogeographical relationships. Pap. Palaeont. 93, 1–32.

Boskey, A., 2007. Mineralization of bones and teeth. Elements 3, 385–391.

Cazalbou, S., Combes, C., Eichert, D., Rey, C., 2004. Adaptive physico-chemistry of bio-related calcium phosphates. J. Mater. Chem. 14, 2148–2153.

Chlupáč, I., Kříž, J., Schönlaub, H.P., 1980. Field trip E, ECOS II, Barrandian. Abh. Geol. Bundesanst. 35, 147–180.

Cohen, K.M., Finney, S.C., Gibbard, P.L., Fan, J.-X., 2013. The ICS international chronostratigraphic chart. In: Episodes. 36. pp. 199–204 (updated 2018).

Farabegoli, E., Perri, M.C., 1998. Scythian and Anisian conodonts from the Sotto le Rive section (Southern Alps, Italy). Giorn. Geol. 60, 254–259.

Ferretti, A., Serpagli, E., 1999. Late Ordovician conodont faunas from southern Sardinia, Italy: biostratigraphic and paleogeographic implications. Boll. Soc. Paleontol. Ital. 37 (2–3), 215–236.

Ferretti, A., Cavalazzi, B., Barbieri, R., Westall, F., Foucher, F., Todesco, R., 2012. From black-and-white to colour in the Silurian. Palaeogeogr. Palaeoclimatol. Palaeoecol. 367–368, 505–519.

Ferretti, A., Messori, A., Bergström, S.M., 2014a. Composition and significance of the Katian (Upper Ordovician) conodont fauna of the Vaux Limestone ("Calcaire des Vaux") in Normandy, France. Est. J. Earth Sci. 63 (4), 214–219.

Ferretti, A., Bergström, S.M., Barnes, C.R., 2014b. Katian (Upper Ordovician) conodonts from Wales. Palaeontology 57 (4), 801–831.

Ferretti, A., Malferrari, D., Medici, L., Savioli, M., 2017. Diagenesis does not invent anything new: Precise replication of conodont structures by secondary apatite. Sci. Rep. 7 (1), 1624–1632.

Glimcher, M.J., 2006. Bone: nature of the calcium phosphate crystals and cellular, structural, and physical chemical mechanisms in their formation. Rev. Mineral. Geochem. 64, 223–282.

Holland, T.J.B., Redfern, S.A.T., 1997. Unit cell refinement from powder diffraction data: the use of regression diagnostics. Mineral. Mag. 61, 65–77.

Holmden, C., Creaser, R.A., Muehlenbachs, K., Bergström, S.M., Leslie, S.A., 1996. Isotopic and elemental systematics of Sr and Nd in 454 Ma biogenic apatites: implications for paleoseawater studies. Earth Planet. Sci. Lett. 142, 425–437.

Hughes, J.M., Rakovan, J., 2002. The crystal structure of apatite, Ca5(PO4)3(F,OH,Cl). Rev. Mineral. Geochem. 48, 1–12.

Hughes, J.M., Cameron, M., Crowley, K.D., 1989. Structural variations in natural F, OH, and Cl apatites. Am. Mineral. 74, 870–876.

Kallaste, T., Nemliher, J., 2005. Apatite varieties in extant and fossil vertebrate mineralized tissues. J. Appl. Crystallogr. 38, 587–594.

Keenan, S.W., 2016. From bone to fossil: a review of the diagenesis of bioapatite. Am. Mineral. 101 (9), 1943–1951.

Kohn, M.J., Schoeninger, M.J., Barker, W.W., 1999. Altered states: effects of diagenesis on fossil tooth chemistry. Geochim. Cosmochim. Acta 63 (18), 2737–2747.

Kovács, S., Papsova, J., Perri, M.C., 1996. New Middle Triassic conodonts of the *Gondolella szabòi-G. trammeri* lineage from the West Carpathian Mts and from the Southern Alps. Acta Geol. Hung. 39 (1), 101–128.

LeGeros, R.Z., 1981. Apatites in biological systems. Prog. Cryst. Growth Charact. Mater. 4, 1–2), 1–45.

LeGeros, R.Z., LeGeros, J.P., 1984. Phosphate minerals in human tissue. In: Nriagu, J.O., Moore, P.B. (Eds.), Phosphate Minerals. Springer-Verlag, New York, pp. 351–395.

Liu, Q., Huang, S., Pekka Matinlinna, J., Chen, Z., Pan, H., 2013. Insight into biological apatite: physiochemical properties and preparation approaches. Biomed. Res. Int. 929, 7–48.

Mann, S., 2001. Biomineralization: Principles and Concepts in Bioinorganic Materials Chemistry. Oxford University Press, Oxford, pp. 1–198.

Martínez-Pérez, C., Rayfield, E.J., Purnell, M.A., Donoghue, P.C.J., 2014. Finite element, occlusal, microwear and microstructural analyses indicate that conodont microstructure is adapted to dental function. Palaeontology 57 (5), 1059–1066.

Mazza, M., Martínez-Pérez, C., 2015. Unravelling conodont (Conodonta) ontogenetic processes in the Late Triassic through growth series reconstructions and X-ray microtomography. Boll. Soc. Paleontol. Ital. 54 (3), 161–186.

Mazza, M., Rigo, M., Gullo, M., 2012. Taxonomy and stratigraphic record of the Upper Triassic conodonts of the Pizzo Mondello section (Western Sicily, Italy), GSSP candidate for the base of the Norian. Riv. It. Paleont. Strat. 118 (1), 85–130.

McConnell, D., 1973. Apatite – its crystal chemistry, mineralogy, utilization and geological and biological occurrences. In: Applied Mineralogy. Springer-Verlag, Wien, pp. 1–111.

Müller, K.J., Hinz, I., 1991. Upper Cambrian conodonts from Sweden. Fossils Strata 28, 1–153.

Murdock, D.J.E., Dong, X.-P., Repetski, J.E., Marone, F., Stampanoni, M., Donoghue, P.C.J., 2013. The origin of conodonts and of vertebrate mineralized skeletons. Nature 502, 546–549.

Nemliher, J., Kallaste, T., 2012. Conodont bioapatite resembles vertebrate enamel by XRD properties. Est. J. Earth Sci. 61 (3), 191–192.

Nemliher, J.G., Baturin, G.N., Kallaste, T.E., Murdmaa, I.O., 2004. Transformation of hydroxyapatite of bone phosphate from the ocean bottom during fossilization. Lithol. Miner. Resour. 39 (5), 468–479.

Pasteris, J.D., Wopenka, B., Valsami-Jones, E., 2008. Bone and tooth mineralization: why apatite? Elements 4 (2), 97–104.

Perri, M.C., Andraghetti, M., 1987. Permian–Triassic boundary and Early Triassic conodonts from the Southern Alps, Italy. Riv. It. Paleont. Strat. 93 (3), 291–328.

Perri, M.C., Spalletta, C., 1998. Latest Devonian and Early Carboniferous conodonts from the Casera Collinetta di Sotto A section (Carnic Alps, Italy). Giorn. Geol. 60, 168–181.

Pietzner, H., Vahl, J., Werner, H., Ziegler, W., 1968. Zur chemischen Zuzammensetzung und Mikromorphologie der Conodonten. Palaeontographica 128, 115–152.

Rodríguez-Lorenzo, L.M., Hart, J.N., Gross, K.A., 2003. Structural and chemical analysis of well-crystallized hydroxyfluorapatites. J. Phys. Chem. B 107, 8316–8320.

Skinner, H.C.W., 2005. Biominerals. Mineral. Mag. 69, 621–641.

Spalletta, C., Perri, M.C., 1998a. The Frasnian-Famennian boundary at the Pramosio A section (Carnic Alps, Italy). Giorn. Geol. 60, 198–205.

Spalletta, C., Perri, M.C., 1998b. Lower Carboniferous conodonts at the Tournaisian/Visean boundary in the Dolina section (Carnic Alps, Italy). Giorn. Geol. 60, 244–253.

Szaniawski, H., 1971. New species of Upper Cambrian conodonts from Poland. Acta Palaeontol. Pol. XVI (4), 401–413.

Trotter, J.A., Eggins, S.M., 2006. Chemical systematics of conodont apatite determined by laser ablation ICPMS. Chem. Geol. 233 (3), 196–216.

Trotter, J.A., Korsch, M.J., Nicoll, R.S., Whitford, D.J., 1999. Sr isotopic variation in single conodont elements: implications for defining the Sr seawater curve. Boll. Soc. Paleontol. Ital. 37 (2–3), 507–514.

Trotter, J.A., Fitz Gerald, J.D., Kokkonen, H., Barnes, C.R., 2007. New insights into the ultrastructure, permeability, and integrity of conodont apatite determined by transmission electron microscopy. Lethaia 40 (2), 97–110.

Trueman, C.N., Tuross, N., 2002. Trace elements of recent and fossil bone apatite. Rev. Mineral. Geochem. 48, 489–521.

Viira, V., 1970. Conodonts of the Varangu Member (Estonian Upper Tremadoc). Eesti NSV Tead. Akad. Toim. Keemia Geol. 19, 224–233.

Wenzel, B., Lécuyer, C., Joachimski, M.M., 2000. Comparing oxygen isotope records of Silurian calcite and phosphate–δ18O compositions of brachiopods and conodonts. Geochim. Cosmochim. Acta 64 (11), 1859–1872.

Wopenka, B., Pasteris, J.D., 2005. A mineralogical perspective on the apatite in bone. Mater. Sci. Eng. C 25, 131–143.

Zhang, L., Cao, L., Zhao, L., Algeo, T.J., Chen, Z.Q., Li, Z., Lv, Z., Wang, X., 2017. Raman spectral, elemental, crystallinity, and oxygen-isotope variations in conodont apatite during diagenesis. Geochim. Cosmochim. Acta 210 (1), 184–207.

Supplementary data

Mineralogy and crystallization pattern in conodonts bioapatite from first occurrence (Cambrian) to extinction (end-Triassic)

Luca Medici[a], Daniele Malferrari[b], Martina Savioli[b], Annalisa Ferretti[b,*]

[a]*National Research Council of Italy, Institute of Methodologies for Environmental Analysis, C.da S. Loja–Zona Industriale, I–85050 Tito Scalo (Potenza), Italy*

[b]*Department of Chemical and Geological Sciences, University of Modena and Reggio Emilia, Via Campi 103, I–41125 Modena, Italy*

[*] Corresponding author.

E-mail addresses: luca.medici@imaa.cnr.it (L. Medici), daniele.malferrari@unimore.it (D. Malferrari), martina.savioli@unimore.it (M. Savioli), ferretti@unimore.it (A. Ferretti).
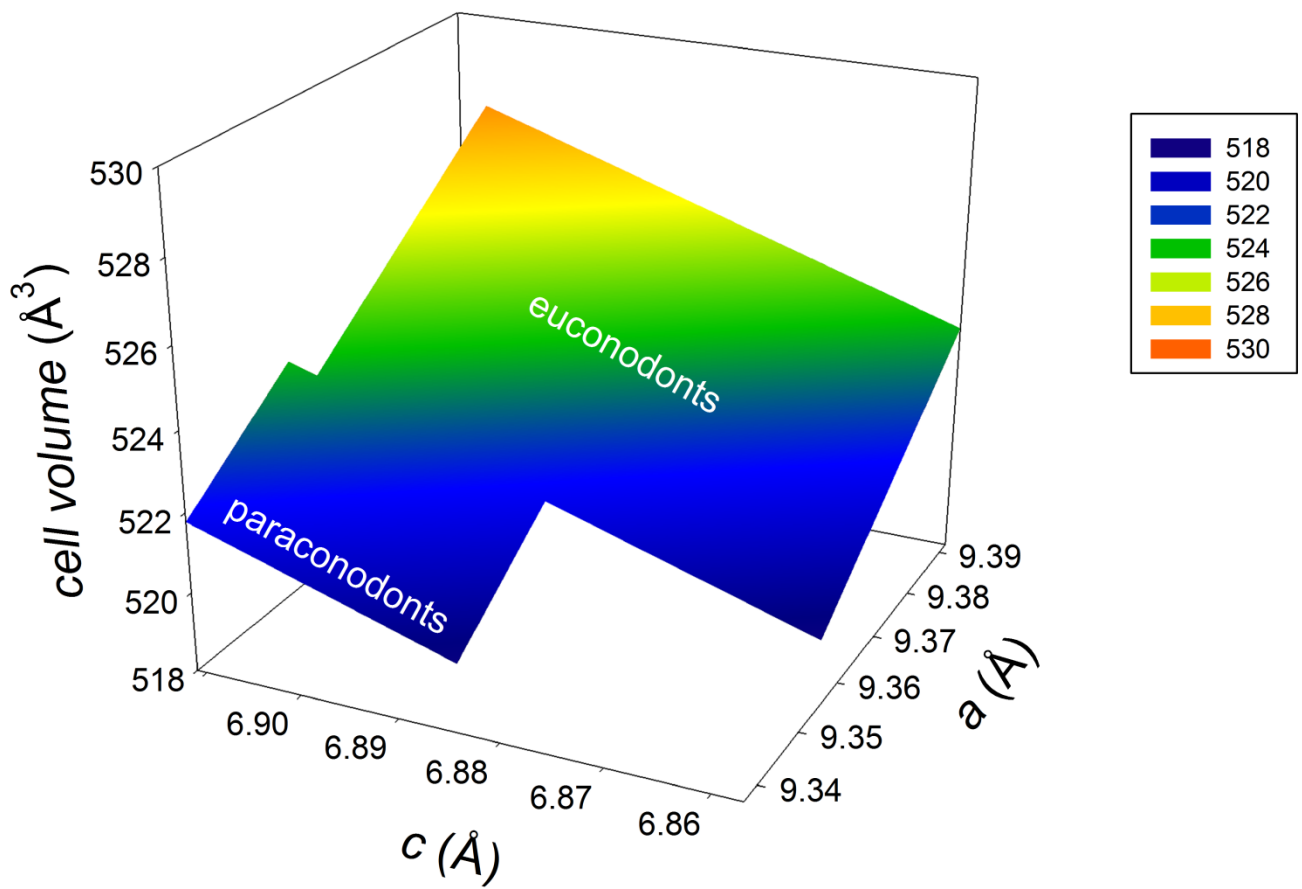
Figure SI-1. Bioapatite cell volume distribution surface calculated for paraconodonts and euconodonts.
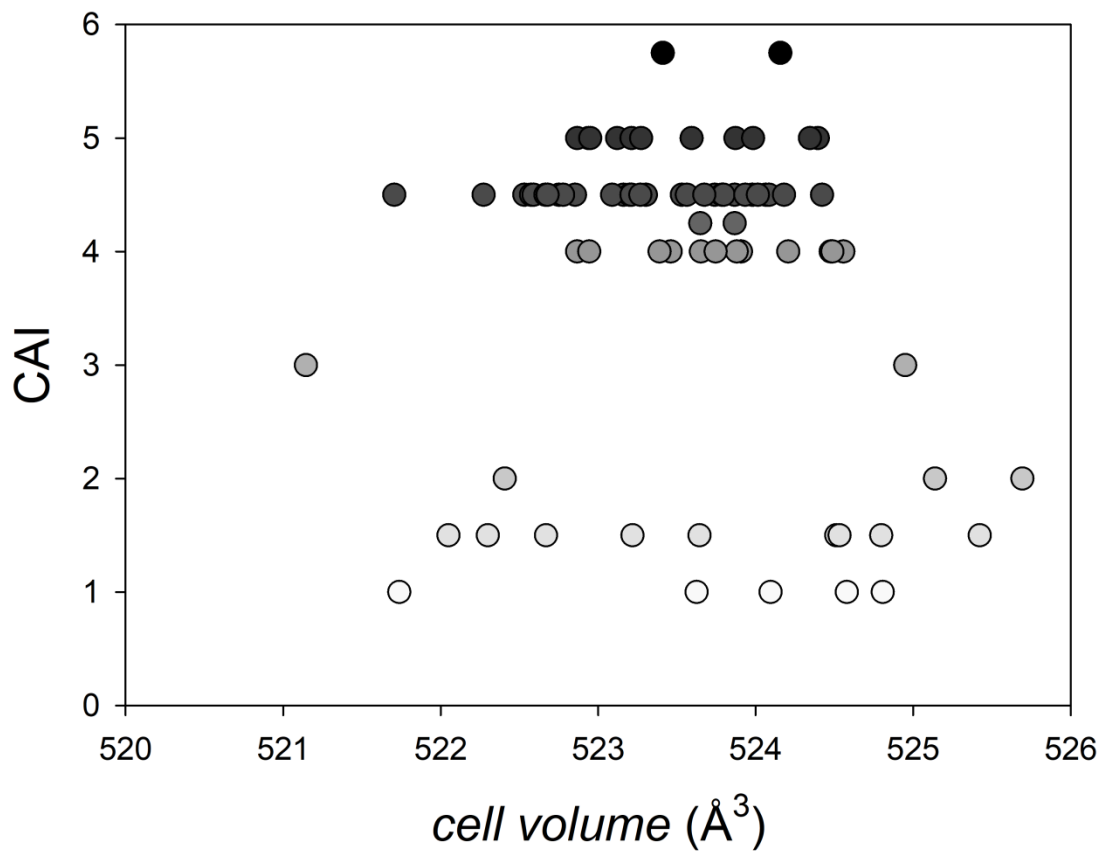
Figure SI-2. Distribution of bioapatite cell volumes calculated for euconodonts in function of the CAI. Grey tones are used exclusively to facilitate reading and grade to dark grey for high CAI values.
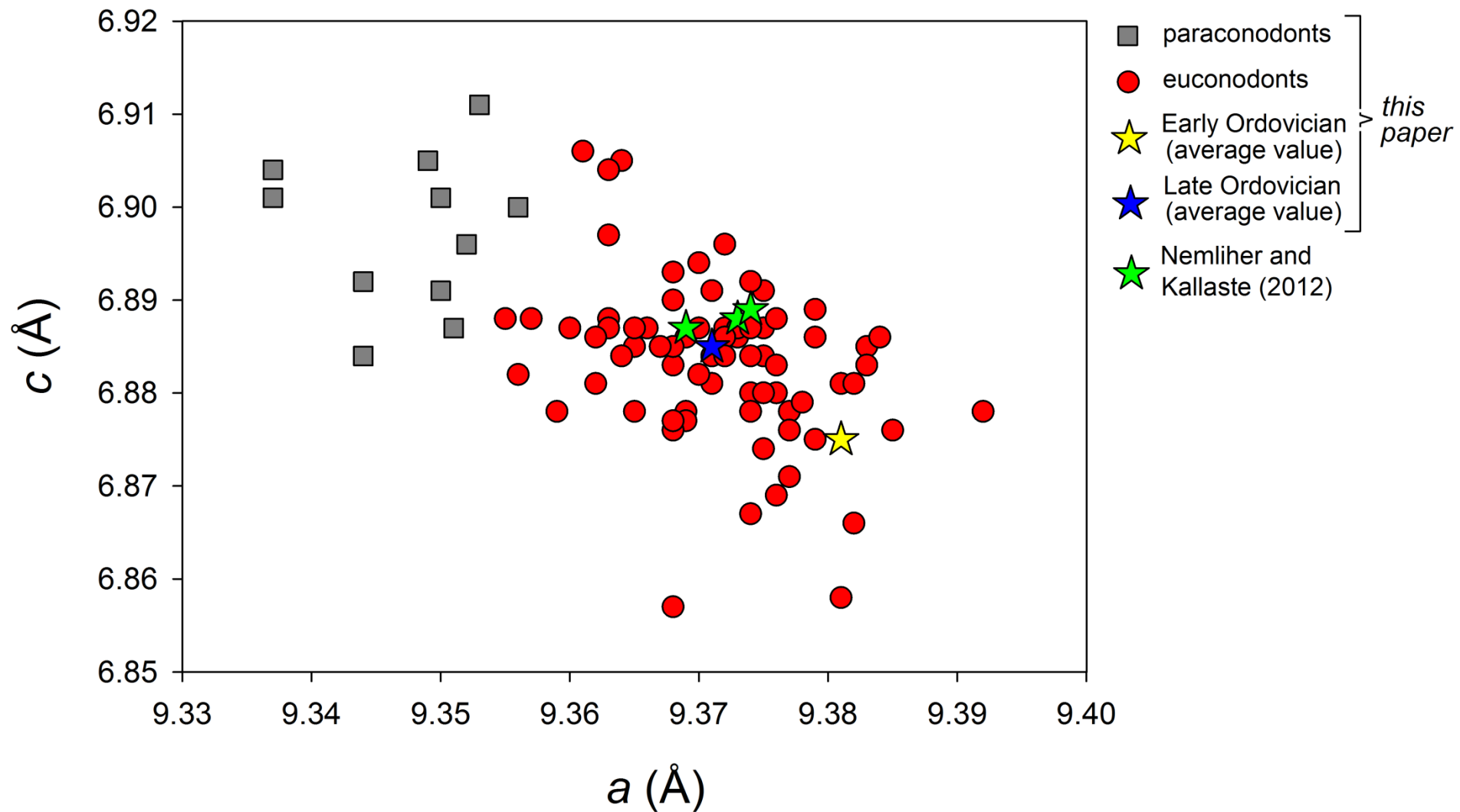
Figure SI-3. Binary plot of bioapatite unit-cell parameters *c vs a* for euconodonts and paraconodonts analysed in this study compared with literature data (green stars).

Table SI-1a. Bioapatite cell parameters calculated for conodonts. For additional details, see Table 1. P: paraconodont; E: euconodont.

Code	a (Å)	c (Å)	Taxa	Locality/Formation	Age	P / E	CAI
A18	9.356(6)	6.900(4)	*Furnishina alata* Szaniawski, 1971	Żarnowiec (Poland)	Cambrian Miaolingian (Guzhangian)	P	
A19	9.351(4)	6.887(4)	*Furnishina alata* Szaniawski, 1971	Żarnowiec (Poland)	Cambrian Miaolingian (Guzhangian)	P	
A11	9.344(4)	6.892(4)	*Westergaardodina* sp.	Kinnekulle, Västergötland (Sweden)	Cambrian Furongian (Paibian)	P	
A12	9.344(3)	6.884(3)	*Westergaardodina* sp.	Kinnekulle, Västergötland (Sweden)	Cambrian Furongian (Paibian)	P	
A90	9.350(4)	6.891(3)	*Westergaardodina* sp.	Kinnekulle, Västergötland (Sweden)	Cambrian Furongian (Paibian)	P	
A91	9.352(4)	6.896(4)	*Westergaardodina* sp.	Kinnekulle, Västergötland (Sweden)	Cambrian Furongian (Paibian)	P	
A13	9.349(2)	6.905(2)	*Furnishina* sp.	Kinnekulle, Västergötland (Sweden)	Cambrian Furongian (Paibian)	P	
A14	9.337(6)	6.901(5)	*Furnishina* sp.	Kinnekulle, Västergötland (Sweden)	Cambrian Furongian (Paibian)	P	
A88	9.350(3)	6.901(5)	*Furnishina* sp.	Kinnekulle, Västergötland (Sweden)	Cambrian Furongian (Paibian)	P	
A89	9.353(2)	6.911(2)	*Furnishina* sp.	Kinnekulle, Västergötland (Sweden)	Cambrian Furongian (Paibian)	P	
A15	9.337(3)	6.904(2)	unrecognizable fragment	Kinnekulle, Västergötland (Sweden)	Cambrian Furongian (Paibian)	P	
A5	9.375(3)	6.874(5)	*Paltodus deltifer deltifer* (Lindström, 1955)	Öland (Sweden)	Early Ordovician (Tremadocian)	E	1.5
A6	9.381(2)	6.858(6)	*Paltodus deltifer deltifer* (Lindström, 1955)	Öland (Sweden)	Early Ordovician (Tremadocian)	E	1.5

A20	9.375(2)	6.891(4)	*Paltodus deltifer deltifer* (Lindström, 1955)	Northern Estonia	Early Ordovician (Tremadocian)	E	1.5
A21	9.392(6)	6.878(6)	*Paltodus deltifer deltifer* (Lindström, 1955)	Northern Estonia	Early Ordovician (Tremadocian)	E	1.5
A30	9.363(2)	6.887(3)	*Amorphognathus* sp. (Pa)	Keisley, Westmorland (UK)	Late Ordovician (Katian)	E	4
A31	9.368(5)	6.890(3)	*Amorphognathus* sp. (Pa)	Keisley, Westmorland (UK)	Late Ordovician (Katian)	E	4
A98	9.369(2)	6.886(4)	*Amorphognathus* sp. (Pa)	Keisley, Westmorland (UK)	Late Ordovician (Katian)	E	4
A99	9.373(3)	6.886(4)	*Amorphognathus* sp. (Pa)	Keisley, Westmorland (UK)	Late Ordovician (Katian)	E	4
A27	9.375(2)	6.887(3)	*Amorphognathus* sp. (Pb)	Keisley, Westmorland (UK)	Late Ordovician (Katian)	E	4
A28	9.372(2)	6.896(2)	*Amorphognathus* sp. (Pb)	Keisley, Westmorland (UK)	Late Ordovician (Katian)	E	4
A29	9.363(3)	6.888(6)	*Amorphognathus* sp. (Pb)	Keisley, Westmorland (UK)	Late Ordovician (Katian)	E	4
A32	9.382(3)	6.866(6)	*Scabbardella altipes* (Henningsmoen, 1948)	Keisley, Westmorland (UK)	Late Ordovician (Katian)	E	4
A33	9.374(3)	6.892(5)	*Scabbardella altipes* (Henningsmoen, 1948)	Keisley, Westmorland (UK)	Late Ordovician (Katian)	E	4
A34	9.368(2)	6.893(4)	*Scabbardella altipes* (Henningsmoen, 1948)	Keisley, Westmorland (UK)	Late Ordovician (Katian)	E	4
A74	9.385(4)	6.876(5)	*Scabbardella altipes* (Henningsmoen, 1948)	Keisley, Westmorland (UK)	Late Ordovician (Katian)	E	4
A75	9.377(2)	6.878(4)	*Scabbardella altipes* (Henningsmoen, 1948)	Keisley, Westmorland (UK)	Late Ordovician (Katian)	E	4
A38	9.365(3)	6.885(2)	*Amorphognathus* sp. (Pa)	Cannamenda, Sardinia (Italy)	Late Ordovician (Katian)	E	5
A66	9.377(2)	6.876(3)	*Amorphognathus* sp. (Pa)	Cannamenda, Sardinia (Italy)	Late Ordovician (Katian)	E	5

A67	9.376(2)	6.888(3)	*Amorphognathus* sp. (Pa)	Cannamenda, Sardinia (Italy)	Late Ordovician (Katian)	E	5
A37	9.363(3)	6.887(4)	*Amorphognathus* sp. (Pb)	Cannamenda, Sardinia (Italy)	Late Ordovician (Katian)	E	5
A41	9.364(2)	6.905(3)	*Amorphognathus* sp. (Pb)	Cannamenda, Sardinia (Italy)	Late Ordovician (Katian)	E	5
A68	9.368(3)	6.883(4)	*Amorphognathus* sp. (Pb)	Cannamenda, Sardinia (Italy)	Late Ordovician (Katian)	E	5
A72	9.372(3)	6.887(6)	*Amorphognathus* sp. (Pb)	Cannamenda, Sardinia (Italy)	Late Ordovician (Katian)	E	5
A39	9.377(2)	6.871(6)	*Scabbardella altipes* (Henningsmoen, 1948)	Cannamenda, Sardinia (Italy)	Late Ordovician (Katian)	E	5
A40	9.376(2)	6.869(5)	*Scabbardella altipes* (Henningsmoen, 1948)	Cannamenda, Sardinia (Italy)	Late Ordovician (Katian)	E	5
A69	9.368(4)	6.885(8)	*Scabbardella altipes* (Henningsmoen, 1948)	Cannamenda, Sardinia (Italy)	Late Ordovician (Katian)	E	5
A70	9.373(2)	6.887(4)	*Scabbardella altipes* (Henningsmoen, 1948)	Cannamenda, Sardinia (Italy)	Late Ordovician (Katian)	E	5
A49	9.364(2)	6.884(3)	*Amorphognathus* sp. (Pa)	Saint-Hilaire-la-Gérard, Normandy (France)	Late Ordovician (Katian)	E	4-5
A50	9.367(3)	6.885(4)	*Amorphognathus* sp. (Pa)	Saint-Hilaire-la-Gérard, Normandy (France)	Late Ordovician (Katian)	E	4-5
A51	9.371(2)	6.884(2)	*Amorphognathus* sp. (Pa)	Saint-Hilaire-la-Gérard, Normandy (France)	Late Ordovician (Katian)	E	4-5
62	9.366(3)	6.887(3)	*Amorphognathus* sp. (Pb)	Saint-Hilaire-la-Gérard, Normandy (France)	Late Ordovician (Katian)	E	4-5
A52	9.371(2)	6.891(3)	*Amorphognathus* sp. (Pb)	Saint-Hilaire-la-Gérard, Normandy (France)	Late Ordovician (Katian)	E	4-5
A107	9.360(3)	6.887(3)	*Amorphognathus* sp. (Pb)	Saint-Hilaire-la-Gérard, Normandy (France)	Late Ordovician (Katian)	E	4-5
A108	9.364(3)	6.884(4)	*Amorphognathus* sp. (Pb)	Saint-Hilaire-la-Gérard, Normandy (France)	Late Ordovician (Katian)	E	4-5

17	9.357(4)	6.888(5)	*Amorphognathus* sp. (Sd)	Saint-Hilaire-la-Gérard, Normandy (France)	Late Ordovician (Katian)	E	4-5
68	9.379(2)	6.875(3)	*Hamarodus brevirameus* (Walliser, 1964) (M)	Saint-Hilaire-la-Gérard, Normandy (France)	Late Ordovician (Katian)	E	4-5
82	9.376(2)	6.880(3)	*Hamarodus brevirameus* (Walliser, 1964) (M)	Saint-Hilaire-la-Gérard, Normandy (France)	Late Ordovician (Katian)	E	4-5
49	9.365(2)	6.887(9)	*Hamarodus brevirameus* (Walliser, 1964) (Sc)	Saint-Hilaire-la-Gérard, Normandy (France)	Late Ordovician (Katian)	E	4-5
21	9.374(2)	6.880(2)	*Icriodella* sp.	Saint-Hilaire-la-Gérard, Normandy (France)	Late Ordovician (Katian)	E	4-5
20	9.374(4)	6.884(4)	*Panderodus* sp.	Saint-Hilaire-la-Gérard, Normandy (France)	Late Ordovician (Katian)	E	4-5
56	9.374(4)	6.867(6)	*Panderodus* sp.	Saint-Hilaire-la-Gérard, Normandy (France)	Late Ordovician (Katian)	E	4-5
A53	9.369(3)	6.878(6)	*Panderodus* sp.	Saint-Hilaire-la-Gérard, Normandy (France)	Late Ordovician (Katian)	E	4-5
24	9.369(2)	6.877(3)	*Sagittodontina robusta* Knüpfer, 1967 (Pa)	Saint-Hilaire-la-Gérard, Normandy (France)	Late Ordovician (Katian)	E	4-5
41	9.372(2)	6.886(5)	*Sagittodontina robusta* Knüpfer, 1967 (Pa)	Saint-Hilaire-la-Gérard, Normandy (France)	Late Ordovician (Katian)	E	4-5
46	9.368(6)	6.876(5)	*Sagittodontina robusta* Knüpfer, 1967 (Sd)	Saint-Hilaire-la-Gérard, Normandy (France)	Late Ordovician (Katian)	E	4-5
45	9.375(3)	6.884(5)	*Scabbardella altipes* (Henningsmoen, 1948)	Saint-Hilaire-la-Gérard, Normandy (France)	Late Ordovician (Katian)	E	4-5
59	9.375(4)	6.880(3)	*Scabbardella altipes* (Henningsmoen, 1948)	Saint-Hilaire-la-Gérard, Normandy (France)	Late Ordovician (Katian)	E	4-5
60	9.381(2)	6.881(2)	*Scabbardella altipes* (Henningsmoen, 1948)	Saint-Hilaire-la-Gérard, Normandy (France)	Late Ordovician (Katian)	E	4-5
91	9.368(2)	6.877(4)	*Scabbardella altipes* (Henningsmoen, 1948)	Saint-Hilaire-la-Gérard, Normandy (France)	Late Ordovician (Katian)	E	4-5
103	9.374(3)	6.908(4)	*Scabbardella altipes* (Henningsmoen, 1948)	Saint-Hilaire-la-Gérard, Normandy (France)	Late Ordovician (Katian)	E	4-5

A54	9.361(2)	6.906(5)	*Scabbardella altipes* (Henningsmoen, 1948)	Saint-Hilaire-la-Gérard, Normandy (France)	Late Ordovician (Katian)	E	4-5
A22	9.379(2)	6.889(2)	*Rhipidognathus symmetricus* Branson, Mehl and Branson, 1951	Saluda Dolomite (USA)	Late Ordovician	E	1
A23	9.363(3)	6.897(4)	*Panderodus* sp.	Saluda Dolomite (USA)	Late Ordovician	E	1
A104	9.374(3)	6.887(4)	*Belodina* sp.	Kimmswick Formation, Missouri (USA)	Late Ordovician	E	1
A105	9.359(3)	6.878(4)	*Plectodina* sp.	Kimmswick Formation, Missouri (USA)	Late Ordovician	E	1
A106	9.379(2)	6.886(4)	*Panderodus* sp.	Kimmswick Formation, Missouri (USA)	Late Ordovician	E	1
A1	9.368(4)	6.857(6)	*Zieglerodina planilingua* (Murphy & Valenzuela-Ríos, 1999)	U Topolů (Bohemia)	Early Devonian (Lochkovian)	E	3
A2	9.383(3)	6.885(3)	*Lanea omoalpha* (Murphy & Valenzuela-Ríos, 1999)	U Topolů (Bohemia)	Early Devonian (Lochkovian)	E	3
A82	9.370(3)	6.894(3)	*Palmatolepis* sp.	Pramosio A, Carnic Alps (Italy)	Late Devonian (Frasnian)	E	4.5
A83	9.376(2)	6.883(6)	*Polygnathus decorosus* Stauffer, 1938	Pramosio A, Carnic Alps (Italy)	Late Devonian (Frasnian)	E	4.5
A80	9.362(3)	6.886(4)	unrecognizable fragment	Casera Collinetta di Sotto A, Carnic Alps (Italy)	Late Devonian (Famennian)	E	4.5
A81	9.371(3)	6.881(6)	*Branmehla werneri* (Ziegler, 1957)	Casera Collinetta di Sotto A, Carnic Alps (Italy)	Late Devonian (Famennian)	E	4.5
A101	9.365(2)	6.878(3)	*Palmatolepis triangularis* Sannemann, 1955	Texas (USA)	Late Devonian (Famennian)	E	2
A102	9.384(1)	6.886(2)	*Palmatolepis subperlobata* Branson and Mehl, 1934	Texas (USA)	Late Devonian (Famennian)	E	2
A103	9.378(2)	6.879(3)	*Icriodus* sp.	Texas (USA)	Late Devonian (Famennian)	E	2
A76	9.377(2)	6.871(3)	unrecognizable fragment	Dolina, Carnic Alps (Italy)	Carboniferous Early Mississippian (Tournaisian)	E	4.5

A77	9.356(2)	6.882(2)	unrecognizable fragment	Dolina, Carnic Alps (Italy)	Carboniferous Early Mississippian (Tournaisian)	E	4.5
A100	9.370(2)	6.882(3)	unrecognizable fragment	Dolina, Carnic Alps (Italy)	Carboniferous Early Mississippian (Tournaisian)	E	4.5
A78	9.374(2)	6.884(3)	*Gnathodus* sp.	Dolina, Carnic Alps (Italy)	Carboniferous Middle Mississippian (Visean)	E	4-4.5
A79	9.370(2)	6.887(4)	*Gnathodus* sp.	Dolina, Carnic Alps (Italy)	Carboniferous Middle Mississippian (Visean)	E	4-4.5
A86	9.374(2)	6.878(3)	*Pachycladina obliqua* Staesche, 1964	Cencenighe Galleria, Dolomites (Italy)	Early Triassic (Olenekian)	E	5.5-6
A87	9.363(2)	6.904(5)	*Pachycladina obliqua* Staesche, 1964	Cencenighe Galleria, Dolomites (Italy)	Early Triassic (Olenekian)	E	5.5-6
A84	9.355(3)	6.888(3)	unrecognizable fragment	Sotto le Rive, Dolomites (Italy)	Middle Triassic (Anisian)	E	1.5
A85	9.362(4)	6.881(5)	unrecognizable fragment	Sotto le Rive, Dolomites (Italy)	Middle Triassic (Anisian)	E	1.5
A42	9.372(2)	6.884(2)	*Carnepigondolella pseudodiebeli* (Kozur, 1972)	Pizzo Mondello, Sicani Mountains, Sicily (Italy)	Late Triassic (Carnian)	E	1.5
A43	9.383(3)	6.883(4)	*Carnepigondolella pseudodiebeli* (Kozur, 1972)	Pizzo Mondello, Sicani Mountains, Sicily (Italy)	Late Triassic (Carnian)	E	1.5
A44	9.382(2)	6.881(3)	*Carnepigondolella pseudodiebeli* (Kozur, 1972)	Pizzo Mondello, Sicani Mountains, Sicily (Italy)	Late Triassic (Carnian)	E	1.5

Table SI-1b. Bioapatite cell parameters calculated for other phosphatic fauna (OPF). Brachiopod A9 was lose before X-ray measurements.

Code	*a* (Å)	*c* (Å)	Taxa	Locality/Formation	Age
A16	9.356(4)	6.900(4)	ostracod	Kinnekulle, Västergötland (Sweden)	Cambrian Furongian (Paibian)
A17	9.353(4)	6.903(3)	ostracod	Kinnekulle, Västergötland (Sweden)	Cambrian Furongian (Paibian)
A92	9.349(4)	6.900(3)	ostracod	Kinnekulle, Västergötland (Sweden)	Cambrian Furongian (Paibian)
A93	9.346(6)	6.908(6)	ostracod	Kinnekulle, Västergötland (Sweden)	Cambrian Furongian (Paibian)
A94	9.338(7)	6.885(7)	ostracod	Kinnekulle, Västergötland (Sweden)	Cambrian Furongian (Paibian)
A95	9.358(5)	6.905(4)	undetermined	Kinnekulle, Västergötland (Sweden)	Cambrian Furongian (Paibian)
A96	9.345(2)	6.909(3)	undetermined	Kinnekulle, Västergötland (Sweden)	Cambrian Furongian (Paibian)
A97	9.356(6)	6.899(4)	undetermined	Kinnekulle, Västergötland (Sweden)	Cambrian Furongian (Paibian)
A7	9.354(1)	6.887(2)	brachiopod	Öland (Sweden)	Early Ordovician (Tremadocian)
A8	9.335(5)	6.887(5)	brachiopod	Öland (Sweden)	Early Ordovician (Tremadocian)
A25	9.367(2)	6.892(2)	brachiopod	Keisley, Westmorland (UK)	Late Ordovician (Katian)
A26	9.368(3)	6.892(3)	brachiopod	Keisley, Westmorland (UK)	Late Ordovician (Katian)
A73	9.366(2)	6.880(2)	brachiopod	Cannamenda, Sardinia (Italy)	Late Ordovician (Katian)
A36	9.362(2)	6.888(2)	brachiopod	Cannamenda, Sardinia (Italy)	Late Ordovician (Katian)
A55	9.337(3)	9.868(3)	brachiopod	Saint-Hilaire-la-Gérard, Normandy (France)	Late Ordovician (Katian)
A64	9.372(2)	6.890(2)	brachiopod	Saint-Hilaire-la-Gérard, Normandy (France)	Late Ordovician (Katian)
A3	9.343(3)	6.897(3)	brachiopod	U Topolů (Bohemia)	Early Devonian (Lochkovian)
A4	9.345(3)	6.891(3)	brachiopod	U Topolů (Bohemia)	Early Devonian (Lochkovian)
A35	9.365(1)	6.896(2)	bryozoan	Cannamenda, Sardinia (Italy)	Late Ordovician (Katian)
A71	9.351(2)	6.884(4)	bryozoan	Cannamenda, Sardinia (Italy)	Late Ordovician (Katian)
A58	9.368(3)	6.889(3)	bryozoan	Saint-Hilaire-la-Gérard, Normandy (France)	Late Ordovician (Katian)

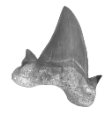| A61	9.371(2)	6.891(2)	bryozoan	Saint-Hilaire-la-Gérard, Normandy (France)	Late Ordovician (Katian)
A65	9.372(3)	6.887(4)	bryozoan	Saint-Hilaire-la-Gérard, Normandy (France)	Late Ordovician (Katian)
A24	9.361(2)	6.893(3)	bryozoan	Saluda Dolomite (USA)	Late Ordovician
A45	9.337(3)	6.901(3)	fish tooth	Pizzo Mondello, Sicani Mountains, Sicily (Italy)	Late Triassic (Carnian)
A46	9.343(5)	6.896(4)	fish tooth	Pizzo Mondello, Sicani Mountains, Sicily (Italy)	Late Triassic (Carnian)
A47	9.411(6)	6.881(5)	fish tooth	Pizzo Mondello, Sicani Mountains, Sicily (Italy)	Late Triassic (Norian)

ANNEX-4

Zooming in REE and other trace elements on conodonts: Does taxonomy guide diagenesis?

Luca Medici, Martina Savioli, Annalisa Ferretti & Daniele Malferrari

Zooming in REE and Other Trace Elements on Conodonts: Does Taxonomy Guide Diagenesis?

Luca Medici[1], **Martina Savioli**[2], **Annalisa Ferretti***[2], **Daniele Malferrari**[2]

1. *National Research Council of Italy, Institute of Methodologies for Environmental Analysis,*
C. da S. Loja-Zona Industriale, 85050 Tito Scalo, Potenza, Italy
2. *Department of Chemical and Geological Sciences, University of Modena and Reggio Emilia,*
Via Campi 103, 41125 Modena, Italy

Luca Medici: https://orcid.org/0000-0001-9426-4653; Martina Savioli: https://orcid.org/0000-0001-6358-4320;
Annalisa Ferretti: https://orcid.org/0000-0002-1173-8778; Daniele Malferrari: https://orcid.org/0000-0002-0879-1703

ABSTRACT: Conodont elements are calcium phosphate (apatite structure) mineralized remains of the cephalic feeding apparatus of an extinct marine organism. Due to the high affinity of apatite for rare earth elements (REE) and other high field strength elements (HFSE), conodont elements were frequently assumed to be a reliable archive of sea-water composition and changes that had occurred during diagenesis. Likewise, the crystallinity index of bioapatite, i.e., the rate of crystallinity of biologically mediated apatite, should be generally linearly dependent on diagenetic alteration as the greater (and longer) the pressure and temperature to which a crystal is exposed, the greater the resulting crystallinity. In this study, we detected the uptake of HFSE in conodont elements recovered from a single stratigraphic horizon in the Upper Ordovician of Normandy (France). Assuming therefore that all the specimens have undergone an identical diagenetic history, we have assessed whether conodont taxonomy (and morphology) impacts HFSE uptake and crystallinity index. We found that all conodont elements are characterized by a clear diagenetic signature, with minor but significant differences among taxa. These distinctions are evidenced also by the crystallinity index values which show positive correlations with some elements and, accordingly, with diagenesis; however, correlations with the crystallinity index strongly depend on the method adopted for its calculation.
KEY WORDS: bioapatite, crystallinity index, HFSE, laser ablation, mass spectrometry, microdiffraction, Normandy, Ordovician.

0 INTRODUCTION

Conodont elements are the mineralized remains of the cephalic feeding apparatus of an extinct marine organism whose taxonomic attribution has been strongly debated in the past before being finally assessed among Vertebrates (see Sweet and Donoghue, 2001 for a review). Conodonts lived in the ancient oceans for over 300 Ma from the Cambrian to the Triassic/Jurassic transition. Thanks to their rapid evolution and diversity of habitats, conodonts represent a fundamental tool for biostratigraphic assignments and a valuable aid in paleogeographic reconstructions (Ferretti et al., 2020a). Elements, organized in apparatuses, reveal an extreme morphological inter- and intra-apparatus variability, but with elements sharing two main phosphatic and crystallized parts: (i) a basal body, rarely preserved and characterized by a low to medium tissue density; (ii) a hyaline and an albid crown, both variably distributed within cusps and denticles and characterized

by a medium (hyaline) to high (albid) tissue density (e.g., Li et al., 2017; Zhao et al., 2013; Trotter et al., 2007; Trotter and Eggins, 2006).

Conodonts are constituted by bioapatite, a name generally used to indicate an apatite of strictly biochemical origin. The chemical formula usually assigned to bioapatite is $Ca_5(PO_4,CO_3)_3(F,OH)$. According to the amount of substitutions in the anionic sites, bioapatite was also referred in the past with different mineral names (e.g., francolite, dahllite) which, however, have been now discredited by the Commission on New Minerals and Mineral Names (CNMMN). In spite of these formal aspects, a certainty remains: different iso- and heterovalent substitutions occur in the bioapatite framework both in the anionic and cationic sites (LeGeros, 1981). The cationic replacements can be relevant or minor, with Ca respectively substituted by major elements (mostly Na and Mg; e.g., Keenan and Engel, 2017; Keenan, 2016; Brigatti et al., 2004) or by REE and other trace elements (e.g., Li et al., 2017; Zhao et al., 2013; Trotter et al., 2007; Trotter and Eggins, 2006; Trueman and Tuross, 2002; Reynard et al., 1999; Grandjean-Lécuyer et al., 1993).

The replacing cations are incorporated during *in-vivo* biologically-mediated crystal growth or during *post-mortem* bur-

ial and diagenesis. In the past, content of rare earth elements (REE) and trace elements (mostly others high field strength elements, HFSE) in fossil bioapatite was generally assumed to be a reliable archive of sea-water composition (e.g., Song et al., 2019; Pietsch and Bottjer, 2010; Girard and Albarède, 1996; Grandjean-Lécuyer et al., 1993; Grandjean et al., 1987; Wright et al., 1984). However, as early as the 1990s, concrete hypotheses began to be advanced in which HFSE concentration in bioapatite could have been considerably affected by other parameters (Picard et al., 2002; Armstrong et al., 2001; Reynard et al., 1999; Holser, 1997; Toyoda and Tokonami, 1990), generally triggered by the geochemistry (i.e., overall chemical and mineralogical composition) of the diagenetic environment (Žigaitė et al., 2020; Liao et al., 2019; Trotter et al., 2016; Zhang et al., 2016; Chen et al., 2015; Herwartz et al., 2013, 2011; Zhao et al., 2013; Kocsis et al., 2010; Trotter and Eggins, 2006). Although there is still no unanimous agreement (Liao et al., 2019), the hypothesis of a diagenetic imprint is undoubtedly more likely (Trotter et al., 2016; Zhang et al., 2016; Chen et al., 2015; Kim et al., 2012; Lécuyer et al., 2004), and Zhang et al. (2016) even suggested that all researches in which bioapatite has been considered as a proxy being based exclusively on HFSE concentration and REE anomalies should be reviewed.

Bioapatite may record a REE signature from sea-water (hydrogenous signature) which is usually characterized by low ΣREE (sum of all REEs content) and marked LREE (light REEs, i.e., La, Ce) deficit (Webb et al., 2009; Lécuyer et al., 2004; Nothdurft et al., 2004; Webb and Kamber, 2000; Grandjean-Lécuyer et al., 1993; Wright et al., 1987). Later, in the burial environment, the uptake of REE will be controlled by diagenesis which imparts a signature (pore-water signature) several orders higher than the hydrogenous one (Zhang et al., 2016; Chen et al., 2015; Pattan et al., 2005). Reliable information on the hydrogenous signature is provided by Y/Ho as, in modern ocean water, Ho is adsorbed or complexed at about twice the rate of Y (Xin et al., 2016; Nozaki et al., 1997; Zhang and Nozaki, 1996; Zhang et al., 1994), generating a Y/Ho ratio for sea-water about twice that of terrigenous materials (McLennan, 2001). Therefore, higher Y/Ho represents a larger fraction of sea-water derived (hydrogenous) REE, and lower Y/Ho indicates a larger fraction of terrigenous derived (lithogenous) REE. On the other hand, the pore-water signature is usually marked by high ΣREE and strong Th and LREE enrichment (a lithogenous signal mainly from clay minerals; Shen et al., 2012; Peppe and Reiners, 2007; McLennan, 2001; Wright and Colling, 1995) and, more rarely by MREE (middle REEs, i.e., Pr, Nd, Sm, Eu) and HREE (heavy REEs, i.e., Gd, Tb, Dy, Ho, Er, Tm, Yb, Lu) enrichments related to an authigenic phosphate signal (Bright et al., 2009; Reynard et al., 1999; Sholkovitz and Shen, 1995). Actually, a rapid assessment of REE sources can be made on the basis of Th *vs.* ΣREE and Y/Ho *vs.* ΣREE cross-plots (Li et al., 2017).

In addition to HFSE, another parameter that can be related to the degree of diagenesis is the crystallinity index (CI), although applied less frequently and sometimes leading to questionable results (Trueman et al., 2008; Pucéat et al., 2004). The CI is a measure of the structural order within crystals. Several methods for CI assessment are described in the literature (e.g., Pucéat et al., 2004; Person et al., 1995), all generally based on the shape and intensity of selected X-ray powder diffraction peaks which mainly depend on crystal size, structural order, texture and amount/type of iso- and hetero-valent major substitutions. The correlation between CI and diagenesis should be that the greater (and longer) the pressure and temperature to which a crystal is exposed, the greater the resulting crystallinity. In fact, during *in-vivo* biologically-mediated crystal growth, bioapatite crystallites are intimately associated and intergrown with the organic matrix. After death, the organic phase is more or less rapidly decomposed and the inorganic phosphate crystals may be re-arranged and distributed in the empty spaces. This structural and textural re-organization should generally imply an increase of CI (Trueman et al., 2008). At the same time, the breakdown of the organic component also enhances the diffusion of water (Collins et al., 2002) and, consequently, increases as well the rate and amount of exchange/adsorption reactions occurring at the solid/water interface. It is reasonable to expect, therefore, that high CI values should pair high ΣREE, LREE, Th concentrations and, conversely, low CI values couple low ΣREE, marked LREE deficit and high Y/Ho ratio. Literature reports several evidences that the ultrastructure of bioapatite, which is strongly related to CI, plays a relevant role in HFSE uptake rate and extension (Kohn and Moses, 2013; Herwartz et al., 2011; Trueman et al., 2008; Pucéat et al., 2004; Trueman and Tuross, 2002; Toyoda and Tokonami, 1990), but rarely (Žigaitė et al., 2020) focusing on conodont taxonomy and/or element morphology.

In this study, we detected the uptake of HFSE in conodont elements from the Upper Ordovician of Normandy ("Vaux Limestone", outcropped close to the village of Saint-Hilaire-la-Gérard). Assuming that the material has undergone an identical diagenetic history (specimens come from the same stratigraphic horizon), we have assessed whether conodont taxonomy and element morphology impacts HFSE uptake. We then compared resulting data with CI values previously detected exactly in the same positions where the chemical measurements were collected.

1   MATERIALS AND METHODS
1.1   Samples and Sample Preparation

Material investigated in this study was collected in Normandy (NW France) and described by Ferretti et al. (2014c), who sampled in 2006 and 2007 the locality reported by Weyant et al. (1977) located about 2 km SW of Saint-Hilaire-la-Gérard in the Sées syncline (Fig. 1). The area hosts nowadays the Normandie-Maine Regional Natural Park, a protected area that will preserve the outcrop for the future. Ferretti et al. (2014c) tried to test the paleogeographic affinity of the Late Ordovician conodont fauna from Normandy, a geographic sector located aside Brittany (e.g., Paris et al., 1981; Lindström and Pelhate, 1971) in a key-position between the British Isles (for updated conodont references see Bergström and Ferretti, 2015; Ferretti et al., 2014a, b), Baltoscandia (e.g., Dzik, 2020, 1999, and references therein) and Continental Europe (see, among others, Del Moral and Sarmiento, 2008; Ferretti and Schönlaub, 2001; Ferretti and Serpagli, 1999, 1991; Ferretti and Barnes, 1997).

A total of 90 kg of limestone was processed in formic acid using standard methods of conodont extraction. The conodont association described by Ferretti et al. (2014c) was assigned to

the middle Katian and resulted dominated by *Amorphognathus* and *Scabbardella*, with *Sagittodontina* and *Hamarodus* common as well. Just the presence of the latter, concentrated in some levels, is significant as the genus is absent from Brittany. The authors confirmed the *Sagittodontina robusta-Scabbardella altipes* biofacies already proposed by Sweet and Bergström (1984).

Among this material, we selected specimens of the three main documented genera (Fig. 2): *Sagittodontina* (one specimen; P element), *Scabbardella* (two elements) and *Amorphognathus* (six elements: two Pa elements, two Pb elements, one Sb element and one Sc element). All these elements were collected from the same stratigraphic horizon and, more specifically, from the same sample (level W2).

All analysed material is housed in the Paleontological Collections of the University of Modena and Reggio Emilia: under accession prefix IPUM at the Department of Chemical and Geological Sciences, University of Modena and Reggio Emilia, Modena, Italy.

1.2 Instruments and Analytical Methods

1.2.1 Chemical measurements

Tuning the ablation parameters is of paramount relevance in this kind of studies as their value strictly rules the quantity of material (i.e., bioapatite) removed by the laser beam. The various mineralized tissues react differently to the laser impulses (Malferrari et al., 2019) and the amount of ablated bioapatite depends on crystallites density, crystals size and morphology, overall chemical composition and sample shape. Nevertheless, it is not even possible to know *a priori* the point-by-point re-

sponse of the sample to the laser impulses so to fine-tune the ablation parameters accordingly. This issue is further amplified by the lack of a true matrix-matched (composition and hardness) calibration standard for LA-ICPMS measurements on fossil bioapatite. The NIST SRM 1400 Bone Ash and NIST SRM 1486 Bone Meal could represent possible compromise, even if they are specifically designed to prepare liquid standard solutions and, moreover, have concentrations of most trace elements considerably lower than those usually found in fossils. Hence, the NIST SRM 610 and NIST SRM 612, despite their silica-glass matrix, have often been preferred, mediating through the development of opportune calibration strategies and discussing element ratios, or other relationships, rather than elements absolute concentrations.

Here we adopted a calibration strategy encompassing both silica and phosphatic standards and using the ICP-MS X Series II (Thermo Fisher Scientific) equipped with the 213 nm laser ablation device UP-213 (New Wave Research). Prior to optimizing laser ablation parameters for the conodont elements, the instrument was tuned using the NIST SRM 610 and NIST SRM 612 glasses measuring, at instrument-optimized working conditions, the intensity of the signals from U and Th (U/Th *vs.* U). Later, according to methods already adopted in past researches (e.g., Ferretti et al., 2020b; Malferrari et al., 2019; Nardelli et al., 2016), we prepared a pressed tablet with the NIST SRM 1400 and, using the NIST SRM 610 and NIST SRM 612 as calibrating standards, we modulated the ablation parameters up to gain for NIST SRM 1400 tablet (considered as unknown sample) the concentrations of selected trace elements which amount in NIST SRM 1400 is
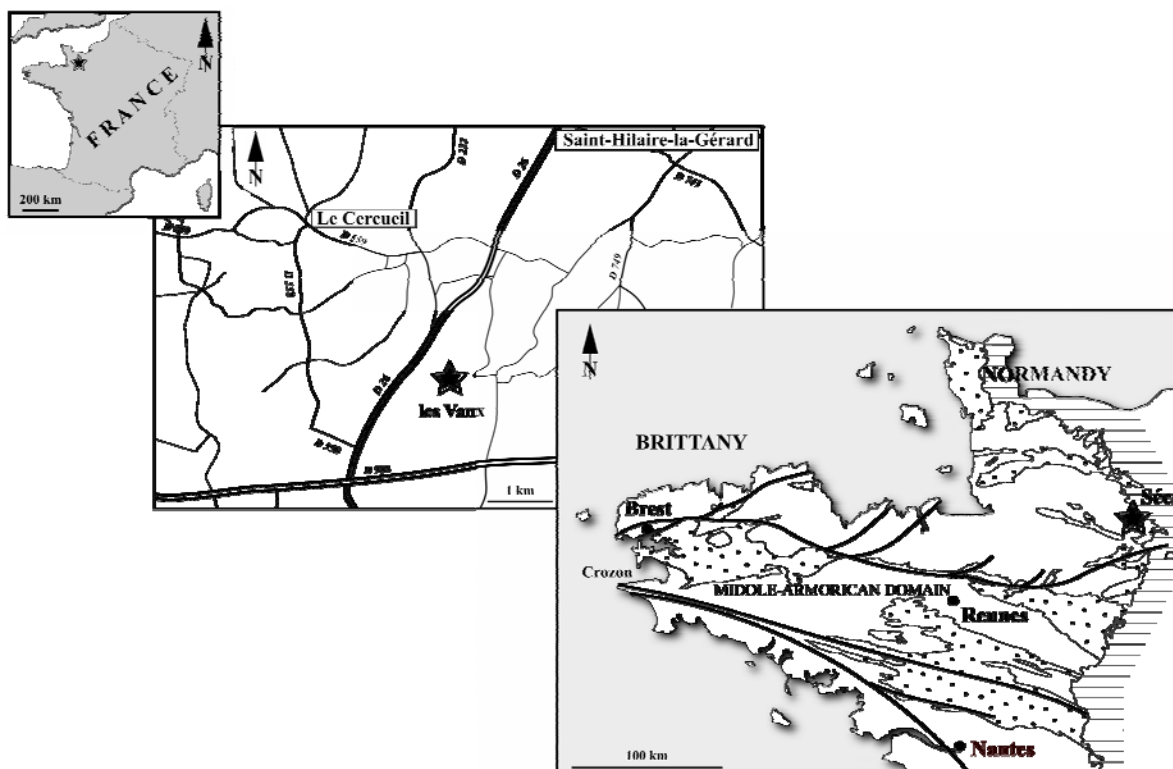
Figure 1. Geographical and geological maps of the sampling area located about 2 km SW of Saint-Hilaire-la-Gérard in the Sées syncline. The outcrop is now part of the Normandie-Maine Regional Natural Park (48°35'14"N, 0°02'33"E). Modified after Vidal et al. (2011) and Ferretti et al. (2014c). Stippling indicates Paleozoic units, horizontal lines represent Mesozoic units, white refers to Proterozoic and Cadomian units and to igneous Variscan units.

Figure 2. Selected specimens (after laser ablation) of the three main genera documented in the "Vaux Limestone", Late Ordovician, Normandy. (1), (2) *Scabbardella altipes* (Henningsmoen, 1948), lateral views of elements IPUM 29850 and IPUM 29851, respectively. (3), (4) *Amorphognathus* sp., upper view of Pa element IPUM 29852 and lateral view of Sb element IPUM 29853, respectively. (5) *Sagittodontina robusta* Knüpfer, 1967, lateral view of P element IPUM 29854. Frames illustrate details of selected ablated areas. Scale bars correspond to 100 µm.

bracketed by (i.e., Sr and K) or close to (i.e., Fe, Mn, Pb and Zn) those of NIST SRM 612 and NIST SRM 1400. The obtained optimized ablation parameters (Table S1) were later applied to standards (NIST SRM 610 and NIST SRM 612) and samples (conodont elements). However, as already pointed out by Zhang et al. (2017), this method leaves unsolved the lack of a univocal internal standard as Ca and/or P (the most used references) in conodonts can vary significantly for isomorphic substitutions.

Another thing to carefully consider is the type of tissue to be analyzed. Various authors (e.g., Trotter et al., 2016; Zhang et al., 2016; Frank-Kamenetskaya et al., 2014; Zhao et al., 2013;

Wheeley et al., 2012; Trotter and Eggins, 2006) reported that the albid tissue, in view of its high hardness and low porosity, is usually better and more frequently preserved and, in comparison mostly to the basal body (or basal cavity), it is less affected by chemical contamination from detrital residues (Trotter et al., 2007; Wenzel et al., 2000; Holmden et al., 1996). Nevertheless, Zhang et al. (2017) observed that the albid and hyaline crowns are more affected by recrystallization (as proxied by the sharp of X-ray diffraction peaks) rather than the basal body; consequently, they concluded that the practice of selectively utilizing the albid crown for geochemical studies of conodonts should be

carefully re-evaluated.

We agree that, in comparing absolute concentrations of HFSE in conodonts from different geographic areas, it is crucial to take the measurements always on the same type of tissue, so to reduce the number of variables. On the other hand, when comparing and correlating the HFSE uptake among conodont elements within the same fauna, average values between diverse tissues are probably preferable, especially whether high CAI may prevent a clear tissue distinction. For the same reason, we processed our material by small ablation lines (Table S1) rather than points in order to gain more signal to integrate and, consequently, mitigate any density anomalies.

1.2.2 X-ray microdiffraction (μ-XRD)

The μ-XRD measurements (described below) used to calculate CI were collected in the same element areas which were later ablated and chemically characterized. The analytical technique and the instrument are already described in the literature (e.g., Medici et al., 2020; Ferretti et al., 2017). The experimental conditions here applied are reported in Table S1. The crystallinity index values were calculated following three different procedures.

The first one, referred as CI-M1, was primary described by Person et al. (1995) and later refined by Pucéat et al. (2004) to determine the degree of chemical alteration of biogenic apatite. The CI value is calculated considering the heights H, where $H[211]$ is the height of the (211) reflection, $H[112]$ $H[300]$ $H[202]$ represent the difference between the top of the peak and the value of the minimum separating it from the previous peak, for the (112), (300), (202) reflections, respectively. The formula can be summarized as $CI=\Sigma\{H[202], H[300], H[112]\}/H[211]$.

The second index (CI-M2), is more commonly employed in crystallography and considers the full width at half maximum (FWHM), which is the width of an XRD peak measured between those two points (2θ) that are at half of the maximum intensity of the peak. This method is sensitive to the variation in microstructure and stress/strain accumulation in the material and it is inversely correlated to the degree of crystallinity. It is

usually calculated as the sum (e.g., Zhang et al., 2017) or the average (this study) of the values measured for some selected reflections—here we considered the (300), (222), (132) and (321) as they are better defined in all the nine elements studied.

Both methods are indicative of the crystallinity rate. The main difference is that the former allows direct comparison also with measurements from previous studies (although so far absent for conodonts), while the latter is strictly dependent on the instrument and on the applied experimental conditions.

The crystallinity index by Person et al. (1995) refers to data obtained by powdered samples; on the contrary, here X-ray microdiffraction data were measured in specific areas of the samples (i.e., those after chemically characterized) without any pre-treatment. Therefore, measurements could be affected by the morphologies of the elements and by crystal preferential orientations which could underestimate the intensity of the (211) reflection (Medici et al., 2020). In the light of these considerations, a third crystallinity index (CI-M3) is proposed in this paper as a modification of CI-M1 index. It is calculated as $CI=\Sigma\{H_1, H_2, H_3\}/H_M$, where H_M corresponds to the highest value among $H[211]$, $H[112]$, $H[300]$, and $H[202]$ in CI-M1 crystallinity index by Person et al. (1995) and H_1, H_2, and H_3 represent the other three values.

2 RESULTS

A list of statistically significant relationships among HFSE is reported in Table 1, whereas chemical analyses and normalized concentrations (McLennan, 2001) are given in Table S2.

All the samples are characterized by a substantial enrichment of MREE and HREE as shown by the lower $(La/Sm)_N$ and $(La/Yb)_N$ ratios (Table 1, Fig. S1). Distribution of UCC-normalized (McLennan, 2001) REE (Fig. 3) outlines two patterns which pair *Scabbardella* (Sc) and *Sagittodontina* (Sa) on one side (type I) and the elements (Pa, Pb, Sb and Sc) of *Amorphognathus* (Am) on the other (type II). This distinct behavior is expressed also by the linear distribution of Y *vs.* La, Nd and Yb considered as representative of LREE, MREE and HREE, respectively (Figs. 4, S2) and by the MREE anomaly (MR/MR*, Table 1), i.e., the
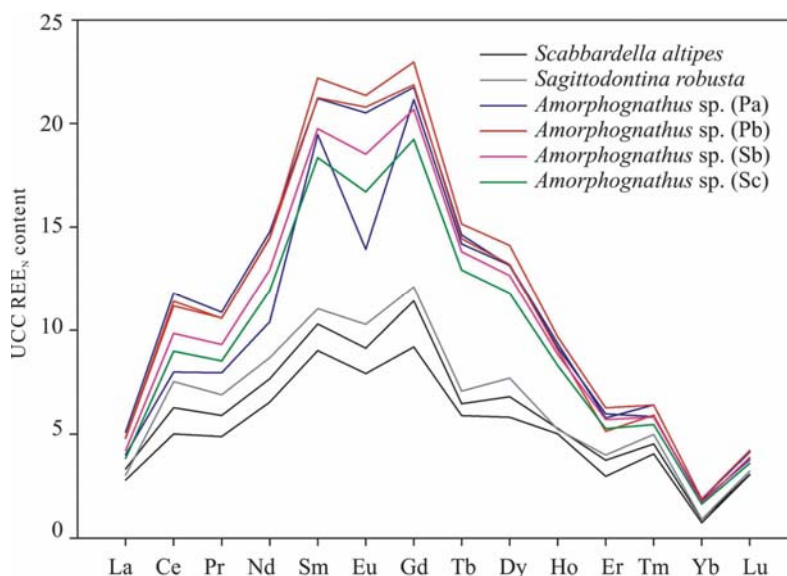

Figure 3. UCC normalized (McLennan, 2001) REE abundance patterns for conodont elements.

Table 1 Statistically significant relationships among HFSE. Sums of REE are in ppm.

	CI-M1	CI-M2	CI-M3	La/Y	La/Yb	Y/Ho	MR/MR*	Pr/Pr*	Ce/Ce*	Gd/Gd*	Eu/Eu*
Scabbardella altipes	1.911	0.243	0.552	0.759	51.71	27.48	0.596	0.845	1.241	1.331	0.870
Scabbardella altipes	1.447	0.265	0.738	0.835	51.82	28.31	0.565	0.846	1.314	1.465	0.841
Sagittodontina robusta	0.880	0.240	0.880	0.734	46.04	29.64	0.559	0.851	1.532	1.396	0.889
Amorphognathus sp. (Pa)	0.921	0.260	0.921	0.803	38.63	25.92	0.606	0.818	1.418	1.238	0.955
Amorphognathus sp. (Pa)	0.874	0.219	0.874	0.641	29.25	25.03	0.635	0.864	1.300	1.505	0.686
Amorphognathus sp. (Pb)	1.063	0.219	1.063	0.727	34.78	25.55	0.632	0.825	1.391	1.258	0.946
Amorphognathus sp. (Pb)	0.982	0.257	0.982	0.775	39.08	25.83	0.617	0.818	1.418	1.241	0.965
Amorphognathus sp. (Sb)	2.379	0.217	0.457	0.700	33.25	25.46	0.638	0.818	1.385	1.279	0.916
Amorphognathus sp. (Sc)	4.864	0.213	0.221	0.680	32.03	25.45	0.643	0.815	1.376	1.299	0.889

	(La/Sm)$_N$	(La/Yb)$_N$	HR/LR	(La+Th)	ΣLREE	ΣMREE	ΣHREE	ΣREE	ΣREE/Th	log (ΣREE)	log (ΣREE/Th)
Scabbardella altipes	0.309	3.792	0.183	104	404	252	74	730	36.51	2.863	1.562
Scabbardella altipes	0.323	3.800	0.177	122	501	295	89	885	39.60	2.947	1.598
Sagittodontina robusta	0.275	3.376	0.167	157	572	333	95	1 001	15.18	3.000	1.181
Amorphognathus sp. (Pa)	0.240	2.833	0.183	186	907	575	166	1 648	49.91	3.217	1.698
Amorphognathus sp. (Pa)	0.206	2.145	0.260	201	631	427	164	1 222	15.16	3.087	1.181
Amorphognathus sp. (Pb)	0.216	2.551	0.205	192	859	571	176	1 606	33.81	3.206	1.529
Amorphognathus sp. (Pb)	0.228	2.866	0.188	181	875	565	164	1 604	44.45	3.205	1.648
Amorphognathus sp. (Sb)	0.213	2.438	0.210	175	756	507	159	1 422	28.91	3.153	1.461
Amorphognathus sp. (Sc)	0.209	2.349	0.214	164	690	468	148	1 306	26.43	3.116	1.422

ratio of the observed to the expected concentration of MREE here is calculated as suggested in Chen et al. (2015). Likewise, similar observations are provided by the crossplots (Fig. S3) of La$_N$ *vs.* Pr$_N$ (i.e., LREE/LREE), La$_N$ *vs.* Gd$_N$ (i.e., LREE/MREE), and La$_N$ *vs.* Yb$_N$ (i.e., LREE/HREE). Ce/Ce* and Eu/Eu* values (here calculated as Ce/Ce*=3Ce$_N$/(2La$_N$+Nd$_N$) and Eu/Eu*= 2Eu$_N$/(Sm$_N$+Gd$_N$), respectively (Shields and Stille, 2001), which mirror the reducing/oxidizing conditions of the burial environment, are relatively consistent (Table 1) and are not clustered, suggesting that the redox environment equally imprints each type of conodont. Eu/Eu* is characterized by values ranging from 0.69 to 0.97 (the average value is 0.88), which indicates a clearly negative Eu anomaly. The Ce/Ce* *vs.* Pr/Pr* plot (Fig. S4), where Pr/Pr*=2Pr$_N$/(Ce$_N$+Nd$_N$), confirms the positive Ce anomaly for all the samples basing on the model from Kowal-Linka et al. (2014).

The (La+Th) and ΣREE *vs.* Y/Ho cross plots may be used to evaluate the REE contribution of terrigenous material as in terrigenous sediments REE and Th are high in concentration, while Y and Ho are more prevalent in sea-water. All the samples show Y/Ho ratios between 25 and 30 (Table 1), clearly indicative of a strong diagenetic contribution, however once again highlighting the distinction between type I and type II (that is *Sagittodontina* and *Scabbardella* on one side, and *Amorphognathus* on the other, Fig. S5). The marked imprint of diagenesis as well as the diversification between the two clusters is here further evidenced by the positive correlations between Y and ΣREE or U (Fig. S6) and by the inverse correlation between Y/Ho and MR/MR* (Fig. S7), whereas less meaningful are the correlations between Y and Th.

Sr is not correlated systematically with any other elements including REE. Although Sr may be taken up *in vivo* (Trotter and Eggins, 2006), high Sr concentrations in fossil apatite usually mirror its solubility in sediment pore-waters and long-term uptake in the burial environment (Martin and Scher, 2004; Holmden et al., 1996).

As far as crystallinity concerns, a relevant relationship, once again highlighting the double clustering evidenced by chemical analyses, was found between ΣHREE and CI-M3 (Fig. 5a). Less significant correlations were found also between log (ΣREE/Th) and 1/(CI-M1) and between La/Y and CI-M2 (Figs. 5b, 5c, respectively), but in this case without paralleling the clustering described above.

3 DISCUSSION

The origin of HFSE incorporated in fossils is not easily constrained. As mentioned in the INTRODUCTION, the HFSE composition of bioapatite has long been used for reconstruction of paleoceanographic conditions based on the shape of normalized REE distributions, REE anomalies and correlation between REE and/or other trace elements. On the other hand, several evidences suggested that also the hydrogenous signal present in fossils could be critically affected by diagenetic overprints. In our samples, diagenesis leads to an increase in the total REE content (Table S2) associated with low Y/Ho ratios (Fig. S5). This result indicates that the REE budget is dominantly derived from the pore-waters of the embedding sediments, as confirmed also by the concomitant increase of U and, in less amount, of Th.

Bright et al. (2009) observed that most of the shale-normalized REE patterns in conodonts is characterized by MREE enrichment, although quantitatively variable among samples. The MREE enrichment, even if peaking to Gd (here assigned to
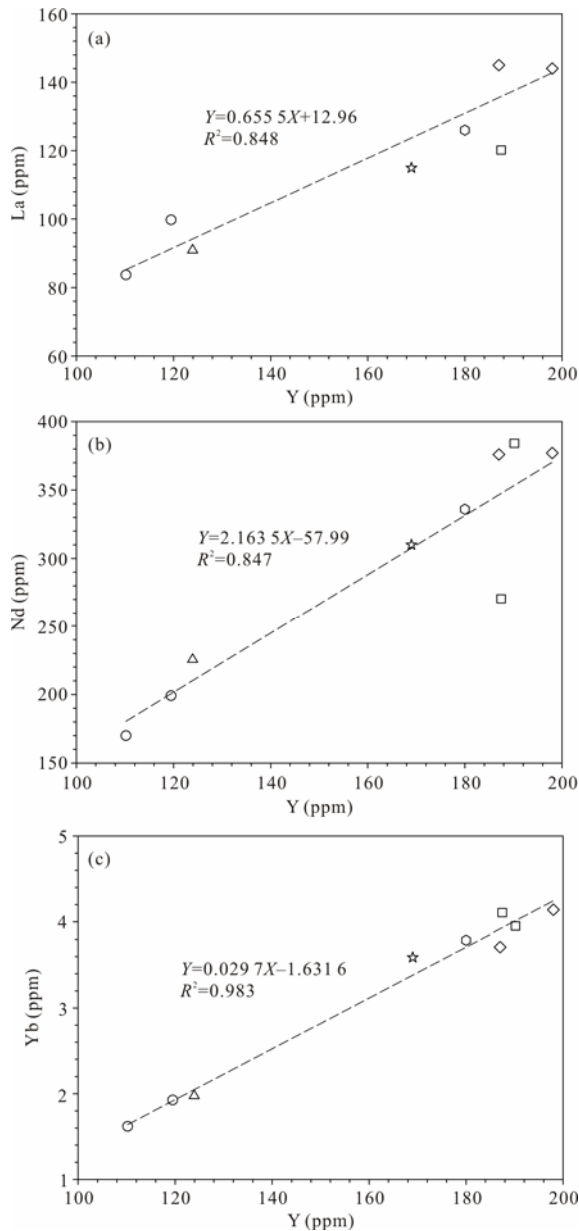
Figure 4. Crossplots of La, Nd, Yb *vs.* Y showing the distribution between types I and II clusters. Symbols: *Scabbardella altipes*, circles; *Sagittodontina robusta*, triangles; *Amorphognathus* sp. (Pa), squares; *Amorphognathus* sp. (Pb), diamonds; *Amorphognathus* sp. (Sb), exagons; *Amorphognathus* sp. (Sc), stars. Dashed lines indicate the linear regression plots (equations and R^2 are reported on the plot).

Figure 5. Diagrams showing the correlations of (a) ΣHREE *vs.* CI-M3; (b) [log (ΣREE/Th)] *vs.* 1/(CI-M1); (c) La/Y *vs.* CI-M2. Symbols are the same as in Fig. 4.

HREE), is well evident also in our samples (bulge pattern, Fig. 3), but with a clear distinction between *Scabbardella* (Sc) and *Sagittodontina* (Sa) on one side (type I) and the elements (Pa, Pb, Sb and Sc) of *Amorphognathus* (Am) on the other (type II). Although this diversification does not question the marked diagenetic imprint for all the samples as proved by the linear correlation between ΣMREE and ΣREE (Fig. S8), it enhances that the REE enrichment deeply marks some taxa rather than others. Such questions arise from several observation, especially as all specimens realistically underwent an identical diagenetic imprint being collected from the same sample. Taxonomy, although minimally, appears to control the degree of chemical fractionation which, therefore, depends not only on the effective

diffusion coefficient, but also on the size of the exposed surface that, due to the small dimensions of conodont elements, otherwise would be reasonably assumed as a negligible parameter.

Various hypotheses have been proposed for several years to explain the MREE enrichment in Paleozoic bioapatite; most of them are mainly ascribable to two main hypotheses: (i) a real seawater MREE enrichment due to a combination of biological and chemical processes which caused a selective uptake and cycling of REE from sea water (e.g., Picard et al., 2002; Girard and Albarède, 1996; Grandjean-Lécuyer et al., 1993); (ii) MREE enrichment resulting from preferential substitution of MREEs for Ca^{2+} in both biogenic and authigenic apatite lattice during diagenetic recrystallization likely masking or delating the original signals (e.g., Trotter and Eggins, 2006; Shields and Webb, 2004; Cruse and Lyons, 2000; Reynard et al., 1999;

McArthur and Walsh, 1984). The latter hypothesis is definitely more accepted (see INTRODUCTION); however, it leaves open the debate about the timing of the enrichment. Our data do not more favorably support one hypothesis or the other as the differentiation we have detected could be linked to both original enrichment as well as diagenesis. Nevertheless, as mentioned above, the linear correlation between MREE and ΣREE (Fig. S8) better supports the diagenetic-dependent imprint. But other than that, very rarely differences in REE concentration among different taxa have been critically zoomed once assessed the diagenetic imprint. To the best of our knowledge, only Bright et al. (2009), comparing MREE concentration in Carboniferous *Idiognathodus* and *Gondolella*, highlighted slight but significant distinctions, however reporting differences less marked compared to ours. As *Idiognathodus* is found both in limestones and shales while *Gondolella* is almost exclusively recovered from phosphatic black shale facies of cyclothems (Heckel and Baesemann, 1975), the resulting differences were associated to the living environment without considering the possible contribution of taxonomy.

Here, in addition to the geochemical markers, we considered also the crystallographic signature. Undoubtedly, the main result is that the double clustering (i.e., types I and II) is paralleled also by the relationship between CI-M3 and ΣHREE, thus suggesting a possible "chemical and structural control" by diagenesis strictly mediated by taxonomy (Fig. 5a). The lack of clustering shown in Figs. 5b–5c suggests that CI-M1 and CI-M2 indexes are not suited for not-powered samples as crystallites could not be randomly distributed, but affected by preferential orientation according to their morphologies (Medici et al., 2020).

Nevertheless, the lack of marked positive correlation between CI and ΣHREE (or, conversely, the lack of an inverse correlation with ΣLREE) can suggest that diagenesis drives crystallinity only up to a "threshold of saturation" as already observed by Pucéat et al. (2004) in fossil biogenic apatites. In the incipient diagenesis the HFSE uptake is mainly controlled by the decomposition of the organic phase and, consequently, by the progressive exposure of the specimen to pore water (Trueman et al., 2008). During burial, CI increases mainly as a response to crystallization of the amorphous part and, in consequence, authigenic apatite crystals grow replicating the unit cell signature of primary bioapatite (Ferretti et al., 2017). In late diagenesis, CI may not significantly increase as the crystal lattice is already formed; at this stage the primary amorphous component is exhausted (i.e., it is crystallized) and the site-specific geochemical conditions become the dominant parameter in controlling chemical substitutions (major and trace elements) at the solid/pore-water interface. At this time the HFSE uptake is no longer limited, breaking down its relationship with CI. Moreover, it should be considered that new authigenic apatite crystals, replicating the original unit cell parameters, are sometimes recognizable only through diffractometric techniques and may form not only in the empty space, but also on the surface (Sanz-López and Blanco-Ferrera, 2012); actually, no significant differences in unit cell parameters were documented between the newly formed apatite crystals and those of the pristine conodont surfaces (Ferretti et al., 2017).

By matching the literature data and those analyzed in this study, a two-step mechanism can be hypothesized.

(1) A *post-mortem* phase in which diffusion of pore-water in the space previously occupied by organic matter occurs simultaneously with a deep recrystallization (Smith et al., 2005; Trueman and Tuross, 2002). This would explain also why the hardest and yet well-crystalized tissues (i.e., albid and hyaline crowns) are less affected by trace element enrichment (Trotter et al., 2016; Zhang et al., 2016; Zhao et al., 2013; Trotter and Eggins, 2006).

(2) A burial and late diagenesis stage in which the pristine bioapatite gets fully recrystallized, but the geochemical imprint goes on. It is in this latter stage that taxonomy appears to play its role, even if the mechanism is still unknown.

The substitutions of REE for Ca^{2+} in original (but organic-free) bioapatite crystal lattice (*post-mortem* phase) are likely several orders of magnitude lower than partition coefficients for REE between pore waters and new apatite crystals (burial and late diagenesis stage). Precipitation of secondary apatite will thus increase the total volume of phosphate mineral, but will not necessarily increase the concentration of REE within the original bioapatite, breaking down the relationship between crystal size and diagenetic trace element content.

In addition to the different partition coefficient of REE between biogenic and authigenic apatite, Trueman et al. (2008) have found that also the rate of closure of intra-crystalline porosity plays a crucial role as it modulates the interactions at the solid/pore-water interface and, therefore, the uptake of REE. The rate of closure of intra-crystalline porosity, which is also a condition for preservation of fossil into deep time, is a multi-parameters dependent factor and it is quite likely that it depends not only on the fossilization and burial environment, but also on the biogenic and taxa-related conformation of the living organism. Although further investigations are needed to provide an experimental demonstration, it is hard to disengage the rate of changing in porosity from geochemical alteration and, therefore, from the loss of a predictive relationship between crystallinity and trace element accumulation.

4   CONCLUSIONS

The Late Ordovician conodont material investigated in this study is undoubtedly characterized by a diagenetic signature, however with minor but significant distinctions among taxa. Differences like these are not relevant for burial environmental interpretations when all the chemical markers converge towards a model of diagenetic enrichment; in contrast, the diagenetic setting can be hardly framed when chemical markers assume values close to the limit typical of the hydrogenous or diagenetic enrichment. How this process develops, and the reasons for this, needs further investigation.

Other matters of critical importance concern crystallinity. The calculation method of the CI, rarely used in paleontological research, should be carefully considered as it strongly depends on sample preparation and textures, the latter mostly when measurements are not taken on powder. In fact, powder provides an average result which may fail in predicting the true rate of geochemical alteration when it is achieved mainly through the growth of authigenic apatite, as a powder diffraction pattern cannot distinguish between the relative proportion of biogenic and authigenic apatite. Actually, the modified crys-

tallinity index CI-M3, which accounts of the effects of preferential orientations (in turn possibly dependent on taxonomy) prove to directly relate with ΣHREE which, in contrast to crystal index, is a well-known and used diagenetic marker.

Regardless of the calculation method, the recrystallization rate of porous and amorphous tissues (basal body) is probably different from that of the hard ones (albid and hyaline crowns), suggesting that the CI "threshold" could be reached first from one tissue rather than the other. Likewise, authigenic crystals grown from solution circulating within a metasomatic environment differs from recrystallization, that is more typical (but not univocal) of an anhydrous environment (Burnett and Hall, 1992).

ACKNOWLEDGMENTS

Electronic Supplementary Materials: Supplementary materials are available in the online version of this article at https://doi.org/ 10.1007/s12583-020-1094-3, (i) the LA-ICPMS and μXRD experimental conditions (ESM I, Table S1); (ii) conodont elements chemical analyses (ESM I, Table S2); (iii) cross-plots showing additional relationships between HFSE (ESM II, Figs. S1–S8).

REFERENCES CITED

Armstrong, H. A., Pearson, D. G., Griselin, M., 2001. Thermal Effects on Rare Earth Element and Strontium Isotope Chemistry in Single Conodont Elements. *Geochimica et Cosmochimica Acta*, 65(3): 435–441. https://doi.org/10.1016/s0016-7037(00)00548-2

Bergström, S. M., Ferretti, A., 2015. Conodonts in the Upper Ordovician Keisley Limestone of Northern England: Taxonomy, Biostratigraphical Significance and Biogeographical Relationships. *Papers in Palaeontology*, 1(1): 1–32. https://doi.org/10.1002/spp2.1003

Bright, C. A., Cruse, A. M., Lyons, T. W., et al., 2009. Seawater Rare-Earth Element Patterns Preserved in Apatite of Pennsylvanian Conodonts?. *Geochimica et Cosmochimica Acta*, 73(6): 1609–1624. https://doi.org/10.1016/j.gca.2008.12.014

Brigatti, M. F., Malferrari, D., Medici, L., et al., 2004. Crystal Chemistry of Apatites from the Tapira Carbonatite Complex, Brazil. *European Journal of Mineralogy*, 16(4): 677–685. https://doi.org/10.1127/0935-1221/2004/0016-0677

Burnett, R. D., Hall, J. C., 1992. Significance of Ultrastructural Features in Etched Conodonts. *Journal of Paleontology*, 66(2): 266–276. https://doi.org/10.1017/s0022336000033783

Chen, J. B., Algeo, T. J., Zhao, L. S., et al., 2015. Diagenetic Uptake of Rare Earth Elements by Bioapatite, with an Example from Lower Triassic Conodonts of South China. *Earth-Science Reviews*, 149: 181–202. https://doi.org/10.1016/j.earscirev.2015.01.013

Collins, M. J., Nielsen-Marsh, C. M., Hiller, J., et al., 2002. The Survival of Organic Matter in Bone: A Review. *Archaeometry*, 44(3): 383–394. https://doi.org/10.1111/1475-4754.t01-1-00071

Cruse, A. M., Lyons, T. W., 2000. Sedimentology and Geochemistry of the Hushpuckney and Upper Tackett Shales Cyclothem Models Revisited. In: Johnson, K. S., ed., Marine Clastics in the Southern Midcontinent, 1997 Symposium. *Oklahoma Geological Survey Circular*, 103: 185–194

Del Moral, B., Sarmiento, G. N., 2008. Conodontos del Katiense (Ordovicico Superior) del Sector Meridional de la Zone Centroibérica (España). *Revista de Micropaleontologia*, 40: 169–245

Dzik, J., 1999. Evolution of Late Ordovician High-Latitude Conodonts and Dating of Gondwana Glaciations. *Bollettino della Società Paleontologica Italiana*, 37(2): 237–253

Dzik, J., 2020. Ordovician Conodonts and the Tornquist Lineament. *Palaeogeography, Palaeoclimatology, Palaeoecology*, 549: 109157. https://doi.org/10.1016/j.palaeo.2019.04.013

Ferretti, A., Bancroft, A. M., Repetski, J. E., 2020a. GECkO: Global Events Impacting Conodont Evolution. *Palaeogeography, Palaeoclimatology, Palaeoecology*, 549: 109677. https://doi.org/10.1016/j.palaeo.2020.109677

Ferretti, A., Malferrari, D., Savioli, M., et al., 2020b. 'Conodont Pearls' do not Belong to Conodonts. *Lethaia*. https://doi.org/10.1111/let.12403

Ferretti, A., Barnes, C. R., 1997. Upper Ordovician Conodonts from the Kalkbank Limestone of Thuringia, Germany. *Palaeontology*, 40(1): 15–42

Ferretti, A., Bergström, S. M., Barnes, C. R., 2014a. Katian (Upper Ordovician) Conodonts from Wales. *Palaeontology*, 57(4): 801–831. https://doi.org/10.1111/pala.12089

Ferretti, A., Bergström, S. M., Sevastopulo, G. D., 2014b. Katian Conodonts from the Portrane Limestone: The First Ordovician Conodont Fauna Described from Ireland. *Bollettino della Società Paleontologica Italiana*, 53(2): 105–119

Ferretti, A., Messori, A., Bergström, S. M., 2014c. Composition and Significance of the Katian (Upper Ordovician) Conodont Fauna of the Vaux Limestone ('Calcaire des Vaux') in Normandy, France. *Estonian Journal of Earth Sciences*, 63(4): 214–219. https://doi.org/10.3176/earth.2014.21

Ferretti, A., Malferrari, D., Medici, L., et al., 2017. Diagenesis does not Invent anything New: Precise Replication of Conodont Structures by Secondary Apatite. *Scientific Reports*, 7(1): 1624. https://doi.org/10.1038/s41598-017-01694-4

Ferretti, A., Schönlaub, H. P., 2001. New Conodont Faunas from the Late Ordovician of the Central Carnic Alps, Austria. *Bollettino della Società Paleontologica Italiana*, 40(1): 3–15

Ferretti, A., Serpagli, E., 1991. First Record of Ordovician Conodonts from Southwestern Sardinia. *Rivista Italiana di Paleontologia e Stratigrafia*, 97(1): 27–34

Ferretti, A., Serpagli, E., 1999. Late Ordovician Conodont Faunas from Southern Sardinia, Italy: Biostratigraphic and Paleogeographic Implications. *Bollettino della Società Paleontologica Italiana*, 37(2/3): 215–236

Frank-Kamenetskaya, O. V., Rozhdestvenskaya, I. V., Rosseeva, E. V., et al., 2014. Refinement of Apatite Atomic Structure of Albid Tissue of Late Devon Conodont. *Crystallography Reports*, 59(1): 41–47. https://doi.org/10.1134/s1063774514010039

Girard, C., Albarède, F., 1996. Trace Elements in Conodont Phosphates from the Frasnian/Famennian Boundary. *Palaeogeography, Palaeoclimatology, Palaeoecology*, 126(1/2): 195–209. https://doi.org/10.1016/s0031-0182(96)00114-9

Grandjean-Lécuyer, P., Feist, R., Albarède, F., 1993. Rare Earth Elements in Old Biogenic Apatites. *Geochimica et Cosmochimica Acta*, 57(11): 2507–2514. https://doi.org/10.1016/0016-7037(93)90413-q

Grandjean, P., Cappetta, H., Michard, A., et al., 1987. The Assessment of REE Patterns and $^{143}Nd/^{144}Nd$ Ratios in Fish Remains. *Earth and Planetary Science Letters*, 84(2/3): 181–196. https://doi.org/10.1016/0012-821x(87)90084-7

Heckel, P. H., Baesemann, J. F., 1975. Environmental Interpretation of Conodont Distribution in Upper Pennsylvanian (Missourian) Megacy-

clothems in Eastern Kansas. *AAPG Bulletin*, 59: 486–509. https://doi.org/10.1306/83d91cb8-16c7-11d7-8645000102c1865d

Henningsmoen, G., 1948. The Tretaspis Series of the Kullatorp Core. In: Waern, B., Thorslund, P., Henningsmoen, G., eds., Deep Boring through Ordovician and Silurian Strata at Kinnekulle, Vestergötland. *Bulletin of the Geological Institution of the University of Uppsala*, 32: 374–432

Herwartz, D., Tütken, T., Jochum, K. P., et al., 2013. Rare Earth Element Systematics of Fossil Bone Revealed by LA-ICPMS Analysis. *Geochimica et Cosmochimica Acta*, 103: 161–183. https://doi.org/10.1016/j.gca.2012.10.038

Herwartz, D., Tütken, T., Münker, C., et al., 2011. Timescales and Mechanisms of REE and Hf Uptake in Fossil Bones. *Geochimica et Cosmochimica Acta*, 75(1): 82–105. https://doi.org/10.1016/j.gca.2010.09.036

Holmden, C., Creaser, R. A., Muehlenbachs, K., et al., 1996. Isotopic and Elemental Systematics of Sr and Nd in 454 Ma Biogenic Apatites: Implications for Paleoseawater Studies. *Earth and Planetary Science Letters*, 142(3/4): 425–437. https://doi.org/10.1016/0012-821x(96)00119-7

Holser, W. T., 1997. Evaluation of the Application of Rare-Earth Elements to Paleoceanography. *Palaeogeography, Palaeoclimatology, Palaeoecology*, 132(1/2/3/4): 309–323. https://doi.org/10.1016/s0031-0182(97)00069-2

Keenan, S. W., 2016. From Bone to Fossil: A Review of the Diagenesis of Bioapatite. *American Mineralogist*, 101(9): 1943–1951. https://doi.org/10.2138/am-2016-5737

Keenan, S. W., Engel, A. S., 2017. Early Diagenesis and Recrystallization of Bone. *Geochimica et Cosmochimica Acta*, 196: 209–223. https://doi.org/10.1016/j.gca.2016.09.033

Kim, J.-H., Torres, M. E., Haley, B. A., et al., 2012. The Effect of Diagenesis and Fluid Migration on Rare Earth Element Distribution in Pore Fluids of the Northern Cascadia Accretionary Margin. *Chemical Geology*, 291: 152–165. https://doi.org/10.1016/j.chemgeo.2011.10.010

Knüpfer, J., 1967. Zur Fauna und Biostratigraphie des Ordoviziums (Gräfenthaler Schichten) in Thüringen. *Freiberger Forschungshefte*, C220: 1–119

Kocsis, L., Trueman, C. N., Palmer, M. R., 2010. Protracted Diagenetic Alteration of REE Contents in Fossil Bioapatites: Direct Evidence from Lu-Hf Isotope Systematics. *Geochimica et Cosmochimica Acta*, 74(21): 6077–6092. https://doi.org/10.1016/j.gca.2010.08.007

Kohn, M. J., Moses, R. J., 2013. Trace Element Diffusivities in Bone Rule out Simple Diffusive Uptake during Fossilization but Explain *in vivo* Uptake and Release. *Proceedings of the National Academy of Sciences*, 110(2): 419–424. https://doi.org/10.1073/pnas.1209513110

Kowal-Linka, M., Jochum, K. P., Surmik, D., 2014. LA-ICP-MS Analysis of Rare Earth Elements in Marine Reptile Bones from the Middle Triassic Bonebed (Upper Silesia, S Poland): Impact of Long-Lasting Diagenesis, and Factors Controlling the Uptake. *Chemical Geology*, 363: 213–228. https://doi.org/10.1016/j.chemgeo.2013.10.038

Lécuyer, C., Reynard, B., Grandjean, P., 2004. Rare Earth Element Evolution of Phanerozoic Seawater Recorded in Biogenic Apatites. *Chemical Geology*, 204(1/2): 63–102. https://doi.org/10.1016/j.chemgeo.2003.11.003

LeGeros, R. Z., 1981. Apatites in Biological Systems. *Progress in Crystal Growth and Characterization* 4(1/2): 1–45

Li, Y., Zhao, L. S., Chen, Z.-Q., et al., 2017. Oceanic Environmental Changes on a Shallow Carbonate Platform (Yangou, Jiangxi Province, South China) during the Permian-Triassic Transition: Evidence from Rare Earth Elements in Conodont Bioapatite. *Palaeogeography, Palaeoclimatology, Palaeoecology*, 486: 6–16. https://doi.org/10.1016/j.palaeo.2017.02.035

Liao, J. L., Sun, X. M., Li, D. F., et al., 2019. New Insights into Nanostructure and Geochemistry of Bioapatite in REE-Rich Deep-Sea Sediments: LA-ICP-MS, TEM, and Z-Contrast Imaging Studies. *Chemical Geology*, 512: 58–68. https://doi.org/10.1016/j.chemgeo.2019.02.039

Lindström, M., Pelhate, A., 1971. Présence de Conodontes dans les Calcaires de Rosan (Ordovicien moyen a Supérieur, Massif Armoricain). Colloque Ordovicien–Silurien, Brest 1971. *Mémoire du Bureau de Recherches Géologiques et Minières*, 73: 89–91

Malferrari, D., Ferretti, A., Mascia, M. T., et al., 2019. How much can We Trust Major Element Quantification in Bioapatite Investigation?. *ACS Omega*, 4(18): 17814–17822. https://doi.org/10.1021/acsomega.9b02426

Martin, E. E., Scher, H. D., 2004. Preservation of Seawater Sr and Nd Isotopes in Fossil Fish Teeth: Bad News and Good News. *Earth and Planetary Science Letters*, 220(1/2): 25–39. https://doi.org/10.1016/s0012-821x(04)00030-5

McArthur, J. M., Walsh, J. N., 1984. Rare-Earth Geochemistry of Phosphorites. *Chemical Geology*, 47(3/4): 191–220. https://doi.org/10.1016/0009-2541(84)90126-8

McLennan, S. M., 2001. Relationships between the Trace Element Composition of Sedimentary Rocks and Upper Continental Crust. *Geochemistry, Geophysics, Geosystems*, 2(4). https://doi.org/10.1029/2000gc000109

Medici, L., Malferrari, D., Savioli, M., et al., 2020. Mineralogy and Crystallization Patterns in Conodont Bioapatite from First Occurrence (Cambrian) to Extinction (end-Triassic). *Palaeogeography, Palaeoclimatology, Palaeoecology*, 549: 109098. https://doi.org/10.1016/j.palaeo.2019.02.024

Nardelli, M. P., Malferrari, D., Ferretti, A., et al., 2016. Zinc Incorporation in the Miliolid Foraminifer *Pseudotriloculina rotunda* under Laboratory Conditions. *Marine Micropaleontology*, 126: 42–49. https://doi.org/10.1016/j.marmicro.2016.06.001

Nothdurft, L. D., Webb, G. E., Kamber, B. S., 2004. Rare Earth Element Geochemistry of Late Devonian Reefal Carbonates, Canning Basin, Western Australia: Confirmation of a Seawater REE Proxy in Ancient Limestones. *Geochimica et Cosmochimica Acta*, 68(2): 263–283. https://doi.org/10.1016/s0016-7037(03)00422-8

Nozaki, Y., Zhang, J., Amakawa, H., 1997. The Fractionation between Y and Ho in the Marine Environment. *Earth and Planetary Science Letters*, 148(1/2): 329–340. https://doi.org/10.1016/s0012-821x(97)00034-4

Paris, F., Pelhate, A., Weyant, M., 1981. Conodontes ashgilliens dans la Formation de Rosan, coupe de Lostmarc'h (Finistère, Massif Armoricain). Conséquences Paléogéographiques. *Bulletin de la Société Géologique et Minéralogique de Bretagne*, 13(2): 15–35

Pattan, J. N., Pearce, N. J. G., Mislankar, P. G., 2005. Constraints in Using Cerium-Anomaly of Bulk Sediments as an Indicator of Paleo Bottom Water Redox Environment: A Case Study from the Central Indian Ocean Basin. *Chemical Geology*, 221(3/4): 260–278. https://doi.org/10.1016/j.chemgeo.2005.06.009

Peppe, D. J., Reiners, P. W., 2007. Conodont (U-Th)/He Thermochronology: Initial Results, Potential, and Problems. *Earth and Planetary Science Letters*, 258(3/4): 569–580. https://doi.org/10.1016/j.epsl.2007.04.022

Person, A., Bocherens, H., Saliège, J. F., et al., 1995. Early Diagenetic Evolution of Bone Phosphate: An X-Ray Diffractometry Analysis. *Journal of Archaeological Science*, 22(2): 211–221. https://doi.org/10.1006/jasc.1995.0023

Picard, S., Lécuyer, C., Barrat, J. A., et al., 2002. Rare Earth Element Contents of Jurassic Fish and Reptile Teeth and Their Potential Relation to Seawater Composition (Anglo-Paris Basin, France and England). *Chemical Geology*, 186(1/2): 1–16. https://doi.org/10.1016/s0009-2541(01)00424-7

Pietsch, C., Bottjer, D. J., 2010. Comparison of Changes in Ocean Chemistry in the Early Triassic with Trends in Diversity and Ecology. *Journal of Earth Science*, 21(S1): 147–150. https://doi.org/10.1007/s12583-010-0195-9

Pucéat, E., Reynard, B., Lécuyer, C., 2004. Can Crystallinity be Used to Determine the Degree of Chemical Alteration of Biogenic Apatites?. *Chemical Geology*, 205(1/2): 83–97. https://doi.org/10.1016/j.chemgeo.2003.12.014

Reynard, B., Lécuyer, C., Grandjean, P., 1999. Crystal-Chemical Controls on Rare-Earth Element Concentrations in Fossil Biogenic Apatites and Implications for Paleoenvironmental Reconstructions. *Chemical Geology*, 155(3/4): 233–241. https://doi.org/10.1016/s0009-2541(98)00169-7

Sanz-López, J., Blanco-Ferrera, S., 2012. Overgrowths of Large Authigenic Apatite Crystals on the Surface of Conodonts from Cantabrian Limestones (Spain). *Facies*, 58(4): 707–726. https://doi.org/10.1007/s10347-012-0295-3

Shen, J., Algeo, T. J., Zhou, L., et al., 2012. Volcanic Perturbations of the Marine Environment in South China Preceding the Latest Permian Mass Extinction and Their Biotic Effects. *Geobiology*, 10(1): 82–103. https://doi.org/10.1111/j.1472-4669.2011.00306.x

Shields, G., Stille, P., 2001. Diagenetic Constraints on the Use of Cerium Anomalies as Palaeoseawater Redox Proxies: An Isotopic and REE Study of Cambrian Phosphorites. *Chemical Geology*, 175(1/2): 29–48. https://doi.org/10.1016/s0009-2541(00)00362-4

Shields, G., Webb, G. E., 2004. Has the REE Composition of Seawater Changed over Geological Time?. *Chemical Geology*, 204: 103–107. https://doi.org/10.1016/j.chemgeo.2003.09.010

Sholkovitz, E., Shen, G. T., 1995. The Incorporation of Rare Earth Elements in Modern Coral. *Geochimica et Cosmochimica Acta*, 59(13): 2749–2756. https://doi.org/10.1016/0016-7037(95)00170-5

Smith, C. I., Craig, O. E., Prigodich, R. V., et al., 2005. Diagenesis and Survival of Osteocalcin in Archaeological Bone. *Journal of Archaeological Science*, 32(1): 105–113. https://doi.org/10.1016/j.jas.2004.07.003

Song, H. J., Wignall, P. B., Song, H. Y., et al., 2019. Seawater Temperature and Dissolved Oxygen over the Past 500 Million Years. *Journal of Earth Science*, 30(2): 236–243. https://doi.org/10.1007/s12583-018-1002-2

Sweet, W. C., Bergström, S. M., 1984. Conodont Provinces and Biofacies of the Late Ordovician. In: Clark, D. L., ed., Conodont Biofacies and Provincialism. *Geological Society of America Special Paper*, 196: 69–87

Sweet, W. C., Donoghue, P. C. J., 2001. Conodonts: Past, Present, Future. *Journal of Paleontology*, 75(6): 1174–1184. https://doi.org/10.1017/s0022336000017224

Toyoda, K., Tokonami, M., 1990. Diffusion of Rare-Earth Elements in Fish Teeth from Deep-Sea Sediments. *Nature*, 345: 607–609. https://doi.org/10.1038/345607a0

Trotter, J. A., Barnes, C. R., McCracken, A. D., 2016. Rare Earth Elements in Conodont Apatite: Seawater or Pore-Water Signatures?. *Palaeogeography*, *Palaeoclimatology*, *Palaeoecology*, 462: 92–100. https://doi.org/10.1016/j.palaeo.2016.09.007

Trotter, J. A., Eggins, S. M., 2006. Chemical Systematics of Conodont Apatite Determined by Laser Ablation ICPMS. *Chemical Geology*, 233(3/4): 196–216. https://doi.org/10.1016/j.chemgeo.2006.03.004

Trotter, J. A., Gerald, J. D. F., Kokkonen, H., et al., 2007. New Insights into the Ultrastructure, Permeability, and Integrity of Conodont Apatite Determined by Transmission Electron Microscopy. *Lethaia*, 40(2): 97–110. https://doi.org/10.1111/j.1502-3931.2007.00024.x

Trueman, C. N., Privat, K., Field, J., 2008. Why do Crystallinity Values Fail to Predict the Extent of Diagenetic Alteration of Bone Mineral? *Palaeogeography*, *Palaeoclimatology*, *Palaeoecology*, 266(3/4): 160–167. https://doi.org/10.1016/j.palaeo.2008.03.038

Trueman, C. N., Tuross, N., 2002. Trace Elements in Recent and Fossil Bone. In: Kohn, M. J., Rakovan, J., Hughes, J. M., eds., Phosphates: Geochemical, Geobiological and Materials Importance. *Review in Mineralogy and Geochemistry*, 48: 489–521

Vidal, M., Dabard, M.-P., Gourvennec, R., et al., 2011. Le Palèozoïque de la Presqu'Île de Crozon, Massif Armoricain (France). *Gèologie de la France*, 1: 3–45

Webb, G. E., Kamber, B. S., 2000. Rare Earth Elements in Holocene Reefal Microbialites: A New Shallow Seawater Proxy. *Geochimica et Cosmochimica Acta*, 64(9): 1557–1565. https://doi.org/10.1016/s0016-7037(99)00400-7

Webb, G. E., Nothdurft, L. D., Kamber, B. S., et al., 2009. Rare Earth Element Geochemistry of Scleractinian Coral Skeleton during Meteoric Diagenesis: A Sequence through Neomorphism of Aragonite to Calcite. *Sedimentology*, 56(5): 1433–1463. https://doi.org/10.1111/j.1365-3091.2008.01041.x

Wenzel, B., Lécuyer, C., Joachimski, M. M., 2000. Comparing Oxygen Isotope Records of Silurian Calcite and Phosphate—δ^{18}O Compositions of Brachiopods and Conodonts. *Geochimica et Cosmochimica Acta*, 64(11): 1859–1872. https://doi.org/10.1016/s0016-7037(00)00337-9

Weyant, M., Dorè, F., Le Gall, J., et al., 1977. Un épisode Calcaire ashgillien dans l'est du Massif Armoricain: Incidence Sur l'âge des Dépôts Glacio-Marins fini-Ordoviciens. *Comptes Rendus de l'Académie des Sciences*, 284(D): 1147–1149

Wheeley, J. R., Smith, M. P., Boomer, I., 2012. Oxygen Isotope Variability in Conodonts: Implications for Reconstructing Palaeozoic Palaeoclimates and Palaeoceanography. *Journal of the Geological Society*, 169(3): 239–250. https://doi.org/10.1144/0016-76492011-048

Wright, J., Schrader, H., Holser, W. T., 1987. Paleoredox Variations in Ancient Oceans Recorded by Rare Earth Elements in Fossil Apatite. *Geochimica et Cosmochimica Acta*, 51(3): 631–644. https://doi.org/10.1016/0016-7037(87)90075-5

Wright, J., Colling, A., 1995. Seawater: Its Composition, Properties and Behavior. Second ed. Pergamon, Oxford. 168

Wright, J., Seymour, R. S., Shaw, H. F., 1984. REE and Nd Isotopes in Conodont Apatite: Variations with Geological Age and Depositional Environment. In: Clark, D. L., ed., Conodont Biofacies and Provincialism. *Geological Society of America Special Paper*, 196: 325–340

Xin, H., Jiang, S. Y., Yang, J. H., et al., 2016. Rare Earth Element Geochemistry of Phosphatic Rocks in Neoproterozoic Ediacaran Doushantuo Formation in Hushan Section from the Yangtze Gorges Area, South China. *Journal of Earth Science*, 27(2): 204–210. https://doi.org/10.1007/s12583-015-0653-5

Zhang, L., Algeo, T. J., Cao, L., et al., 2016. Diagenetic Uptake of Rare Earth Elements by Conodont Apatite. *Palaeogeography*, *Palaeoclimatology*, *Palaeoecology*, 458: 176–197. https://doi.org/10.1016/j.palaeo.2015.10.049

Zhang, L., Cao, L., Zhao, L. S., et al., 2017. Raman Spectral, Elemental, Crystallinity, and Oxygen-Isotope Variations in Conodont Apatite during Diagenesis. *Geochimica et Cosmochimica Acta*, 210: 184–207. https://doi.org/10.1016/j.gca.2017.04.036

Zhang, J., Nozaki, Y., 1996. Rare Earth Elements and Yttrium in Seawater: ICP-MS Determinations in the East Caroline, Coral Sea, and South Fiji Basins of the Western South Pacific Ocean. *Geochimica et Cosmochimica Acta*, 60(23): 4631–4644. https://doi.org/10.1016/s0016-7037(96)00276-1

Zhang, J., Amakawa, H., Nozaki, Y., 1994. The Comparative Behaviors of Yttrium and Lanthanides in the Seawater of the North Pacific. *Geophysical Research Letters*, 21(24): 2677–2680. https://doi.org/10.1029/94gl02404

Zhao, L. S., Chen, Z.-Q., Algeo, T. J., et al., 2013. Rare-Earth Element Patterns in Conodont Albid Crowns: Evidence for Massive Inputs of Volcanic Ash during the Latest Permian Biocrisis?. *Global and Planetary Change*, 105: 135–151. https://doi.org/10.1016/j.gloplacha.2012.09.001

Žigaitė, Ž., Qvarnström, M., Bancroft, A., et al., 2020. Trace and Rare Earth Element Compositions of Silurian Conodonts from the Vesiku Bone Bed: Histological and Palaeoenvironmental Implications. *Palaeogeography*, *Palaeoclimatology*, *Palaeoecology*, 549: 109449. https://doi.org/10.1016/j.palaeo.2019.109449

Zooming in REE and other trace elements on conodonts: Does taxonomy guide diagenesis?

Luca Medici[1], Martina Savioli[2], Annalisa Ferretti[2*], Daniele Malferrari[2]

1. *National Research Council of Italy, Institute of Methodologies for Environmental Analysis, C.da S. Loja-Zona Industriale, 85050 Tito Scalo, Potenza, Italy*
2. *Department of Chemical and Geological Sciences, University of Modena and Reggio Emilia, Via Campi 103, 41125 Modena, Italy*

Luca Medici: https://orcid.org/0000-0001-9426-4653; Martina Savioli: https://orcid.org/0000-0001-6358-4320; Annalisa Ferretti: http://orcid.org/0000-0002-1173-8778; Daniele Malferrari: https://orcid.org/0000-0002-0879-1703.

*Corresponding author: annalisa.ferretti@unimore.it

Table S1 Optimized laser parameters and main µXRD experimental conditions

	Laser intensity (%)	Frequency (Hz)	Ablation line width (µm)	Scan speed (µm/s)	Laser fluence J/cm² (1)
Pre-ablation (2)	25	5	55	25	1.9
Ablation	65	15	55	8	8.6
	Radiation CuKα λ=1.54056Å	XRD Voltage 40 kV	XRD Current 30 mA	Collimator 300 µm	Int. time (3) 30 min

(1) Average value measured for both NIST SRM 610 and NIST SRM 612. (2) Ablation carried out in mild conditions to clean the surface. (3) Optimized by varying the Omega and Phi angles between one sample and the other to fit with the instrument geometry and thus to obtain a significant number of diffraction effects with a maximized signal-to-noise ratio (Medici et al., 2020).

Table S2. Chemical analyses of conodont elements. In green are reported data after normalization (McLennan 2001, second column).

Samples 1–3

	McLennan (2001) - UCC	Sample 1 *Scabbardella altipes*	*Scabbardella altipes*	Sample 2 *Scabbardella altipes*	*Scabbardella altipes*	Sample 3 *Sagittodontina robusta*	*Sagittodontina robusta*
Mg	13300	489	0.037	484	0.036	238	0.018
Sr	350	6277	17.933	4848	13.9	2561	7.316
Y	22.0	110	5.010	120	5.432	124	5.633
La	30.0	83.7	2.789	99.8	3.326	90.9	3.031
Ce	64.0	321	5.009	401	6.268	482	7.523
Pr	7.10	34.6	4.877	41.8	5.894	48.9	6.890
Nd	26.0	170	6.536	199	7.658	226	8.673
Sm	4.500	40.6	9.018	46.3	10.3	49.7	11.0
Eu	0.880	6.966	7.916	8.040	9.136	9.052	10.3
Gd	3.80	34.9	9.189	43.4	11.427	46.0	12.1
Tb	0.640	3.770	5.891	4.134	6.460	4.521	7.064
Dy	3.50	20.3	5.812	23.8	6.797	26.920	7.691
Ho	0.800	4.010	5.013	4.222	5.277	4.181	5.226
Er	2.30	6.818	2.964	8.604	3.741	9.182	3.992
Tm	0.330	1.334	4.043	1.494	4.527	1.645	4.985
Yb	2.20	1.618	0.736	1.925	0.875	1.975	0.898
Lu	0.320	0.974	3.043	0.982	3.067	1.031	3.222
Th	10.7	20.0	1.869	22.3	2.088	66.0	6.165
Pb	17.0	19.0	1.119	9.052	0.532	45.115	2.654
U	2.80	0.913	0.326	1.097	0.392	1.090	0.357

Samples 4–6

	McLennan (2001) - UCC	Sample 4 *Amorphognathus* sp. (Pa)	*Amorphognathus* sp. (Pa)	Sample 5 *Amorphognathus* sp. (Pa)	*Amorphognathus* sp. (Pa)	Sample 6 *Amorphognathus* sp. (Pb)	*Amorphognathus* sp. (Pb)
Mg	13300	1159	0.087	1000	0.075	998	0.075
Sr	350	3313	9.464	3358	9.594	3505	10.014
Y	22.0	190	8.645	187	8.520	198	9.000
La	30.0	153	5.088	120	4.006	144	4.800
Ce	64.0	755	11.8	511	7.982	715	11.2
Pr	7.10	77.2	10.9	56.4	7.946	75.2	10.6
Nd	26.0	384	14.8	271	10.406	377	14.5
Sm	4.500	95.5	21.2	87.6	19.464	99.9	22.2
Eu	0.880	18.1	20.5	12.3	13.932	18.8	21.4
Gd	3.80	82.6	21.7	80.4	21.159	87.3	23.0
Tb	0.640	9.361	14.6	9.078	14.184	9.700	15.2
Dy	3.50	46.0	13.1	46.1	13.160	49.4	14.1
Ho	0.800	7.337	9.171	7.490	9.362	7.750	9.688
Er	2.30	13.7	5.970	13.3	5.778	14.400	6.261
Tm	0.330	1.928	5.841	2.113	6.402	2.110	6.394
Yb	2.20	3.952	1.796	4.108	1.867	4.140	1.882
Lu	0.320	1.204	3.763	1.322	4.130	1.350	4.219
Th	10.7	33.0	3.086	80.6	7.531	47.5	4.439
Pb	17.0	28.7	1.687	51.2	3.010	32.1	1.888
U	2.80	1.075	0.384	1.150	0.411	1.210	0.432

Samples 7–9

	McLennan (2001) - UCC	Sample 7 *Amorphognathus* sp. (Pb)	*Amorphognathus* sp. (Pb)	Sample 8 *Amorphognathus* sp. (Sb)	*Amorphognathus* sp. (Sb)	Sample 9 *Amorphognathus* sp. (Sc)	*Amorphognathus* sp. (Sc)
Mg	13300	1028	0.077	958	0.072	946	0.071
Sr	350	3364	9.611	3199	9.140	2994	8.554
Y	22.0	187	8.500	180	8.182	169	7.682
La	30.0	145	4.833	126	4.200	115	3.833
Ce	64.0	730	11.4	630	9.844	575	8.984
Pr	7.10	75.1	10.6	66.1	9.310	60.5	8.521
Nd	26.0	376	14.5	336	12.9	310	11.9
Sm	4.500	95.6	21.2	88.9	19.8	82.6	18.4
Eu	0.880	18.3	20.8	16.3	18.5	14.7	16.7
Gd	3.80	83.1	21.9	78.6	20.7	73.1	19.2
Tb	0.640	9.240	14.4	8.840	13.8	8.270	12.9
Dy	3.50	46.2	13.2	44.3	12.7	41.3	11.8
Ho	0.800	7.240	9.050	7.070	8.838	6.640	8.300
Er	2.30	11.8	5.130	13.1	5.696	12.1	5.261
Tm	0.330	1.950	5.909	1.920	5.818	1.800	5.455
Yb	2.20	3.710	1.686	3.790	1.723	3.590	1.632
Lu	0.320	1.240	3.875	1.230	3.844	1.150	3.594
Th	10.7	36.1	3.374	49.2	4.598	49.4	4.617
Pb	17.0	30.5	1.794	35.2	2.071	34.9	2.053
U	2.80	1.100	0.393	1.070	0.382	1.010	0.361
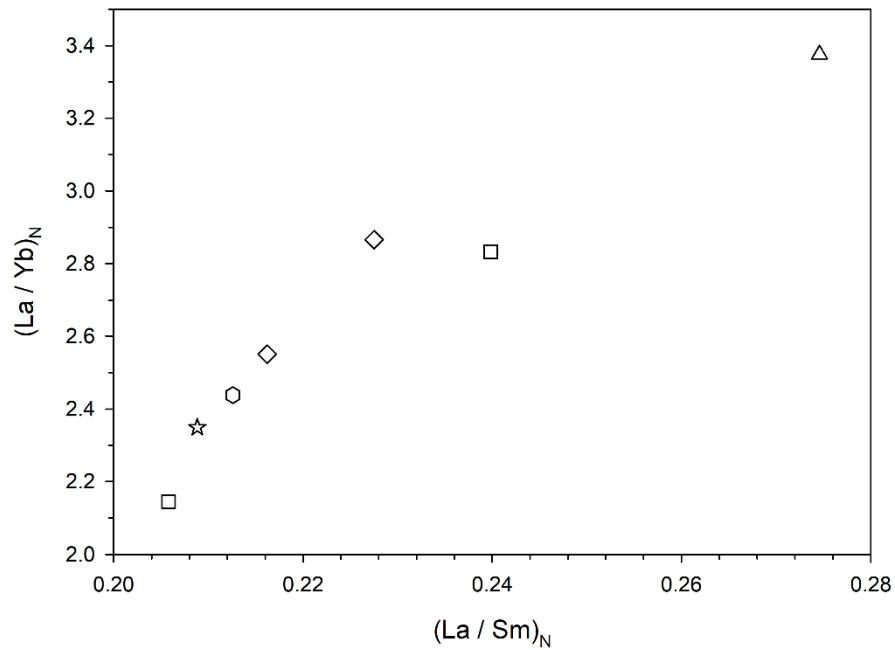
Figure S1. Crossplots of the normalized (McLennan, 2001) ratios of La/Sm and La/Yb (labeled as $(La/Sm)_N$ and $(La/Yb)_N$, respectively). Symbols: *Scabbardella altipes*, circles; *Sagittodontina robusta*, triangle; *Amorphognathus* sp. (Pa), squares; *Amorphognathus* sp. (Pb), diamonds; *Amorphognathus* sp. (Sb), exagon; *Amorphognathus* sp. (Sc), star.
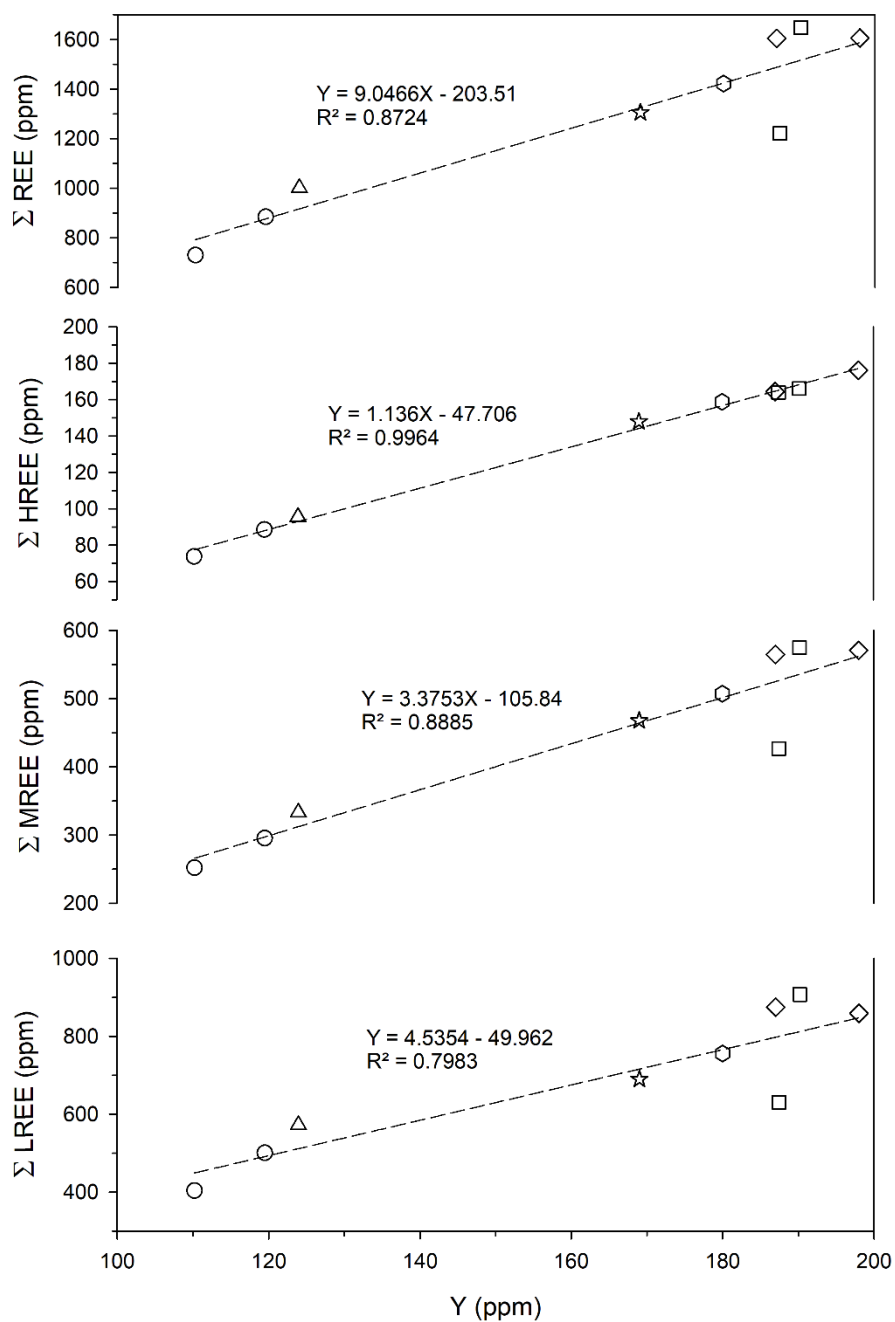
Figure S2. Linear correlations between Y and total REE (ΣREE), sum of light (ΣLREE), middle (Σ MREE) and heavy (ΣHREE) REE. The dashed lines are the linear regression plots (equations and R^2 are reported on each plot). Symbols are like in Figure S1.
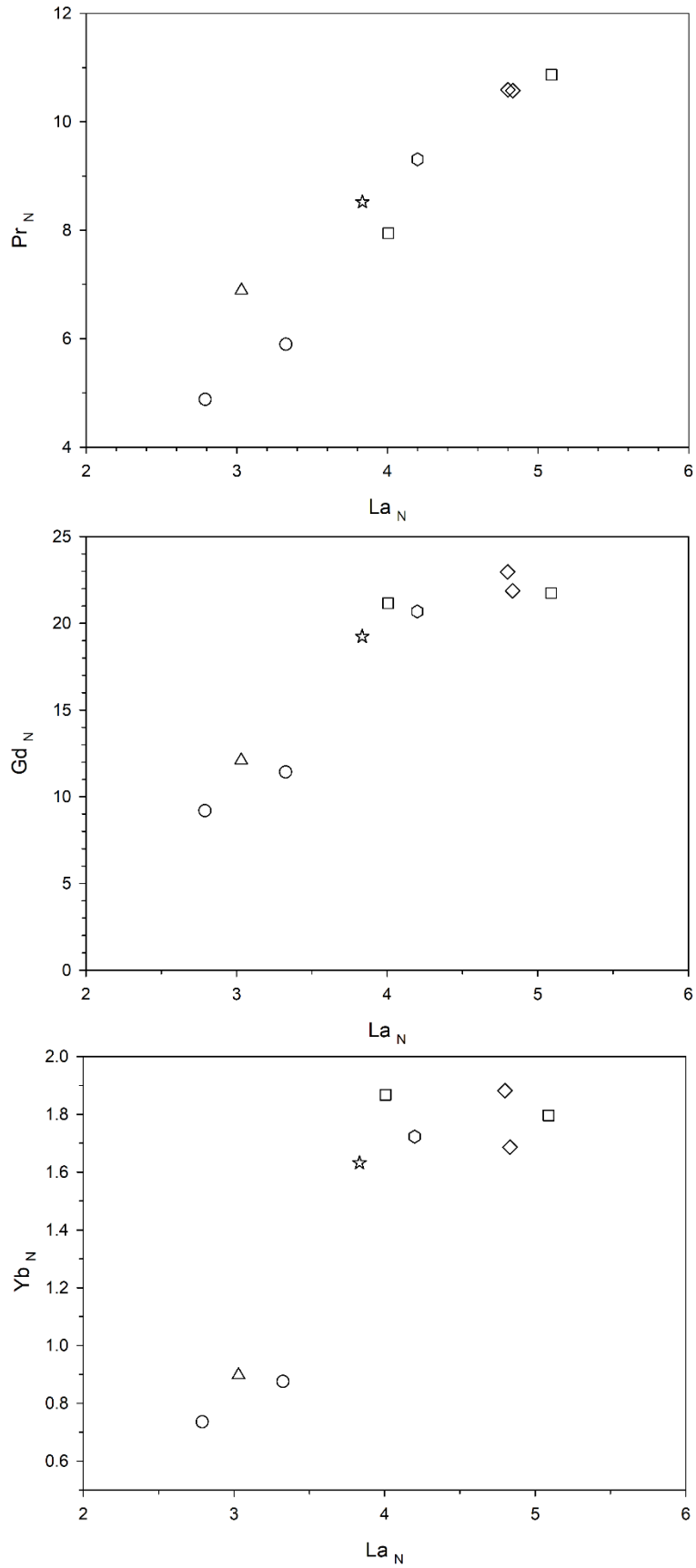
Figure S3. Crossplots of the normalized (McLennan, 2001) concentrations of Pr, Gd and Yb *vs*La. Symbols are like in Figure S1.
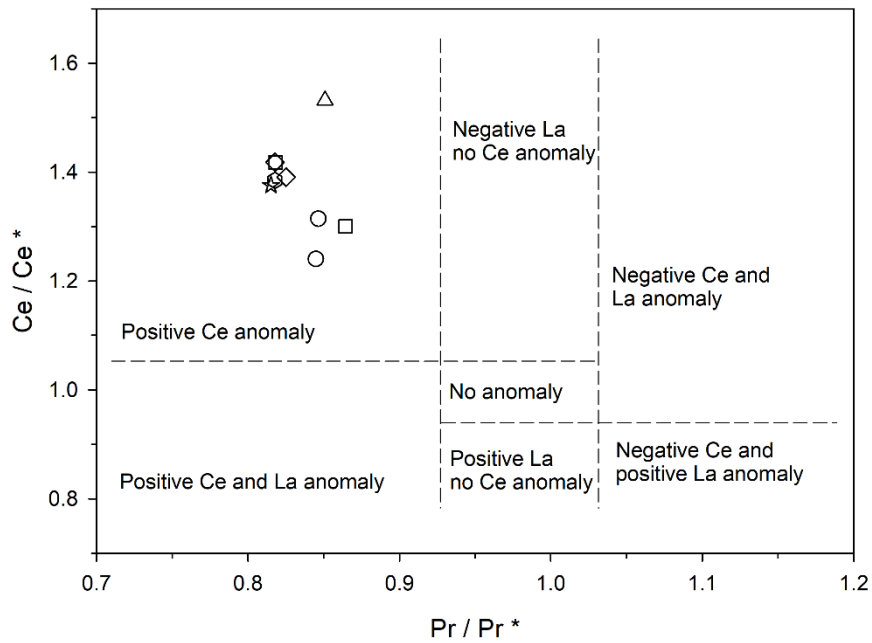
Figure S4. Location of the samples in the McLennan (2001) normalized plots of (Ce/Ce*) *vs* (Pr/Pr*) (labeled as (Ce/Ce*)$_N$ and (Pr/Pr*)$_N$, respectively). Adapted from Kowal-Linka et al. (2014). Symbols are like in Figure S1.
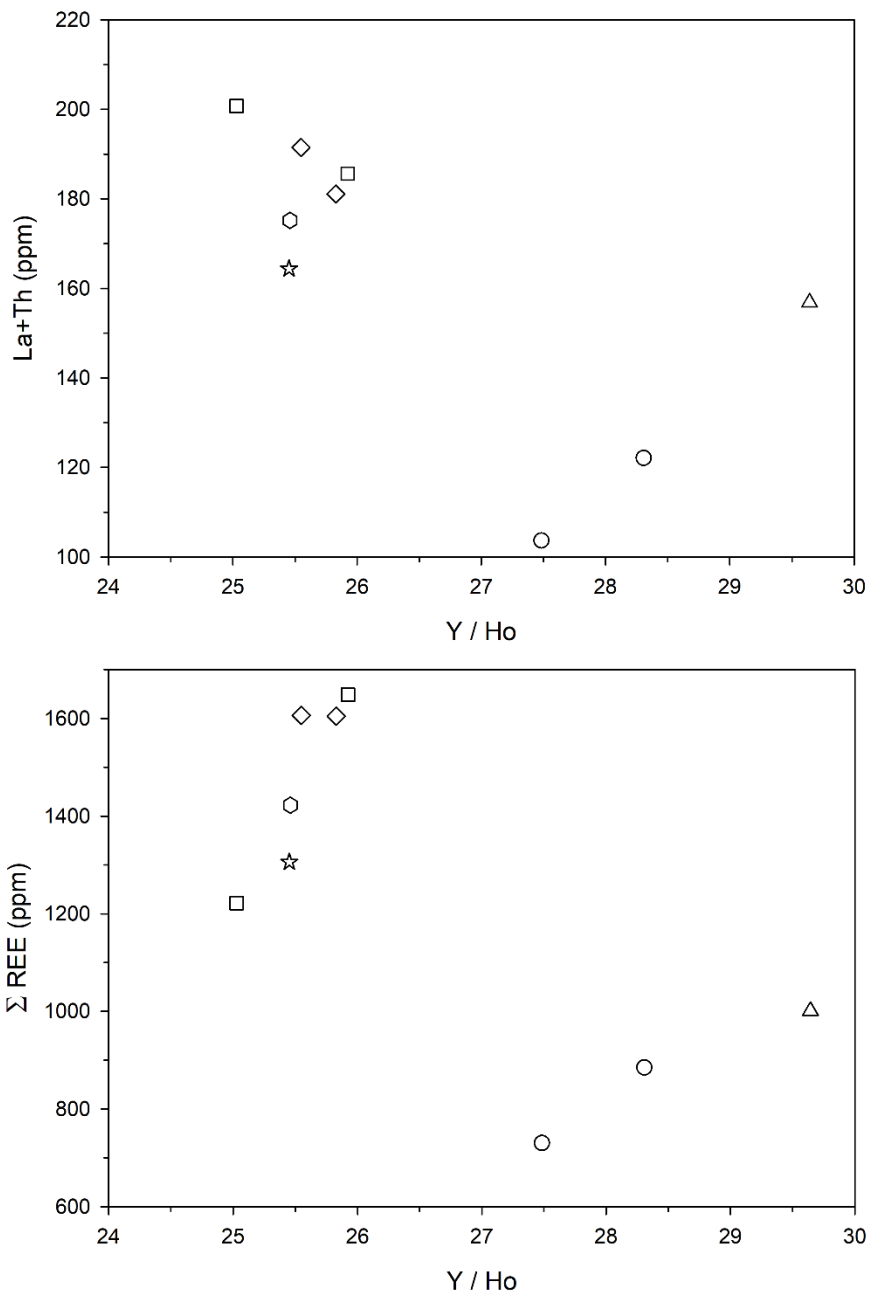
Figure S5. Crossplots of (La+Th) and total REE (ΣREE) contents *vs* (Y/Ho) ratios. Symbols are like in Figure S1.
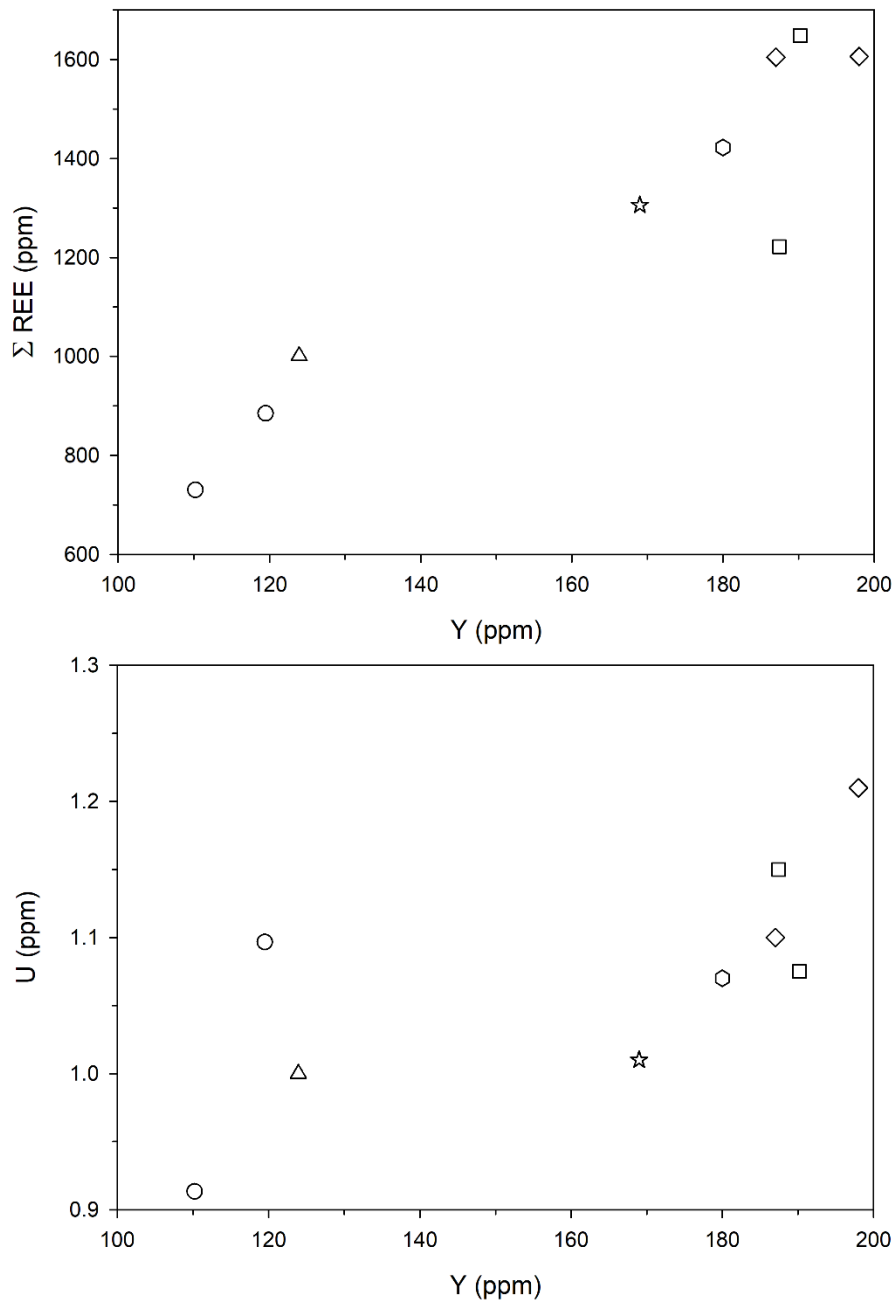
Figure S6. Crossplots of total REE (ΣREE) and U contents *vs*Y contents. Symbols are like in Figure S1.
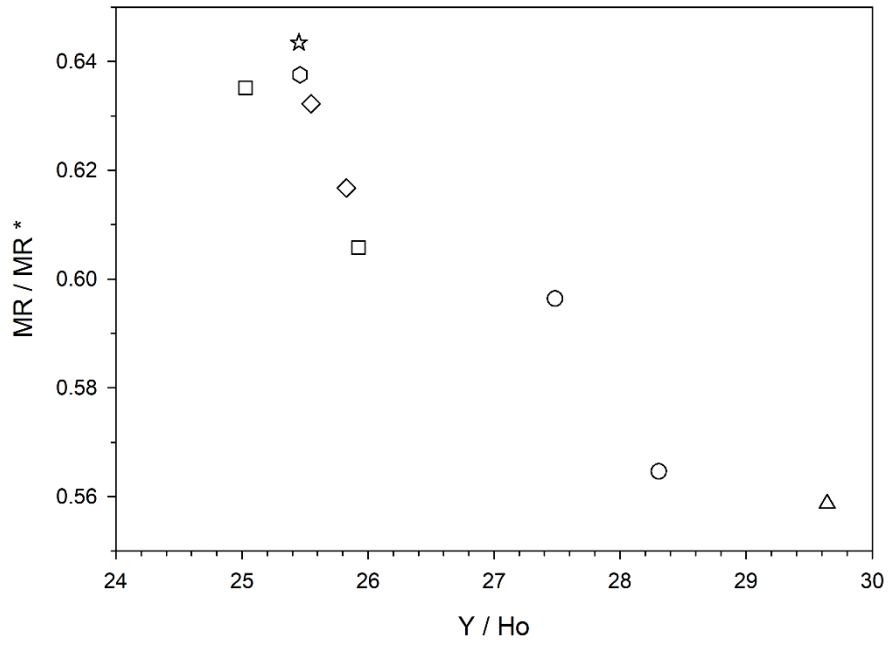
Figure S7. Crossplots of showing the inverse correlation between (Y/Ho) and (MR/MR*). Symbols are like in Figure S1.
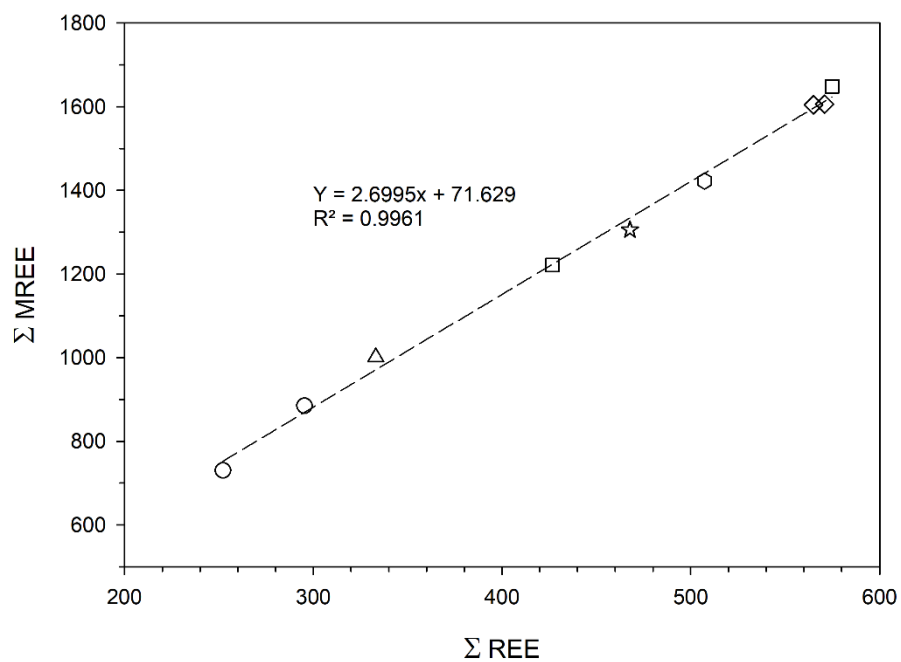
Figure S8. Linear correlation between sum of total (Σ REE) and middle (Σ MREE) REE contents. The dashed line is the linear regression plot (equation and R^2 are reported on the plot). Symbols are like in Figure S1.
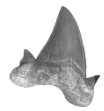
ANNEX-5

"Conodont pearls" do not belong to conodonts

Annalisa Ferretti, Daniele Malferrari, Martina Savioli, Teresa Siepe & Luca Medici

Lethaia (2020)

'Conodont pearls' do not belong to conodonts

ANNALISA FERRETTI, DANIELE MALFERRARI ⦿, MARTINA SAVIOLI, TERESA SIEPE AND LUCA MEDICI

LETHAIA

Ferretti, A., Malferrari, D., Savioli, M., Siepe, T., & Medici, L. 2020: 'Conodont pearls' do not belong to conodonts. *Lethaia*, https://doi.org/10.1111/let.12403.

We investigated the mineralogical and chemical signatures of enigmatic microspherules commonly recovered in conodont residues and referred to in literature as 'conodont pearls.' Comparison between these 'pearls,' associated conodonts and other phosphatic skeletal elements present in the same stratigraphical level was run in an effort to reveal any possible relation between 'conodont pearls' and the joined groups so to finally provide a response on the affinity of these spherules. □ *bioapatite cell parameters, biomineralization, enigmatic microspherules, Ireland, Silurian.*

Annalisa Ferretti [ferretti@unimore.it], Daniele Malferrari✉ [daniele.malferrari@unimore.it], Martina Savioli [martina.savioli@unimore.it], and Teresa Siepe [226411@studenti.unimore.it], Department of Chemical and Geological Sciences, University of Modena and Reggio Emilia, Via Campi 103, Modena 41125, Italy;
Luca Medici [luca.medici@imaa.cnr.it], National Research Council of Italy, Institute of Methodologies for Environmental Analysis, C.da S. Loja-Zona Industriale, 85050 Tito Scalo, Potenza, Italy; manuscript received on 10/06/2020; manuscript accepted on 17/09/2020.

The analysis of conodont residues resulting after acid digestion of collected rocks commonly produces a large set of organisms, other than conodont elements, that share with them a comparable size. Among these, sub-millimetric spherules that are made of apatite and have a stratigraphical distribution similar to conodonts are frequently recovered.

A series of pioneer papers in the thirties and forties of the last century indicated the presence of these spherules mostly in studies dealing with conodont faunas, but providing as well their first description, illustration and attesting hypothesis on their affinity. Many of the following interpretations were proposed when conodont affinity was still a matter of major controversy among specialists. Oakley (1934, p. 299) reported '*spherolith*' inside Silurian Polyzoa as '*concentrically laminated structure with a central nucleus*,' detecting for the first time their phosphatic composition (and not calcareous or siliceous as previously proposed). Their presence within zooecial tubes closed by diaphragms and a shape adapting to the form of the hosting cell excluded a detritic origin. Nuclei were represented by either granular or flocculent material, this latter as possible agglomerated tissue cells (degenerated embryos/aborted larvae). Oakley (1934) excluded these spherules could be bryozoan pearls because having a different chemical composition of the hosting (calcitic) animals and suggested that (p. 306): '*spheroliths are inorganic concretions formed in the coelomic fluid of the zooids by precipitation of phosphate around nuclei, and that they are therefore in many respects comparable with*
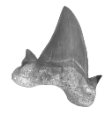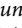
gallstones *and* urinary calculi.' This interpretation of the *spheroliths*, named *oakleyites* by Eisenack (1964), was later confirmed and regarded as a sign of degeneration of genera close to extinction (Oakley 1966).

Stauffer (1935) stated for the first time the occurrence of these spherules in the Ordovician Decorah Shale in Minnesota, Iowa and Illinois, USA and figured three spherules from locality 40 (Minnesota) describing them as: '*bodies … composed of the same material as the teeth* [conodonts]. *They have no special characteristics except a circular or elliptical opening on one side… It is rather hesitatingly suggested that they may be egg cases, but there is no real substantiating evidence*' (Stauffer 1935, p. 620). The same author later reported some more spherules from the Devonian of southern Minnesota advocating an affinity with conodonts (Stauffer 1940, p. 434): '*The exact nature of these bodies or their possible significance is still unknown, but their general appearance, composition and occurrence with the conodonts suggests that they may belong to these animals.*'

Youngquist & Miller (1948) detailed microspherules from the Late Devonian of Iowa, proposing an alternative hypothesis to the conodont one (p. 440): '*They appear to be composed of the same material as conodonts, with which they occur in direct association. Furthermore, their abundance in any given sample is in general directly proportional to the number of conodonts, which, however, are far more numerous… Another possibility is that they are otoliths.*'
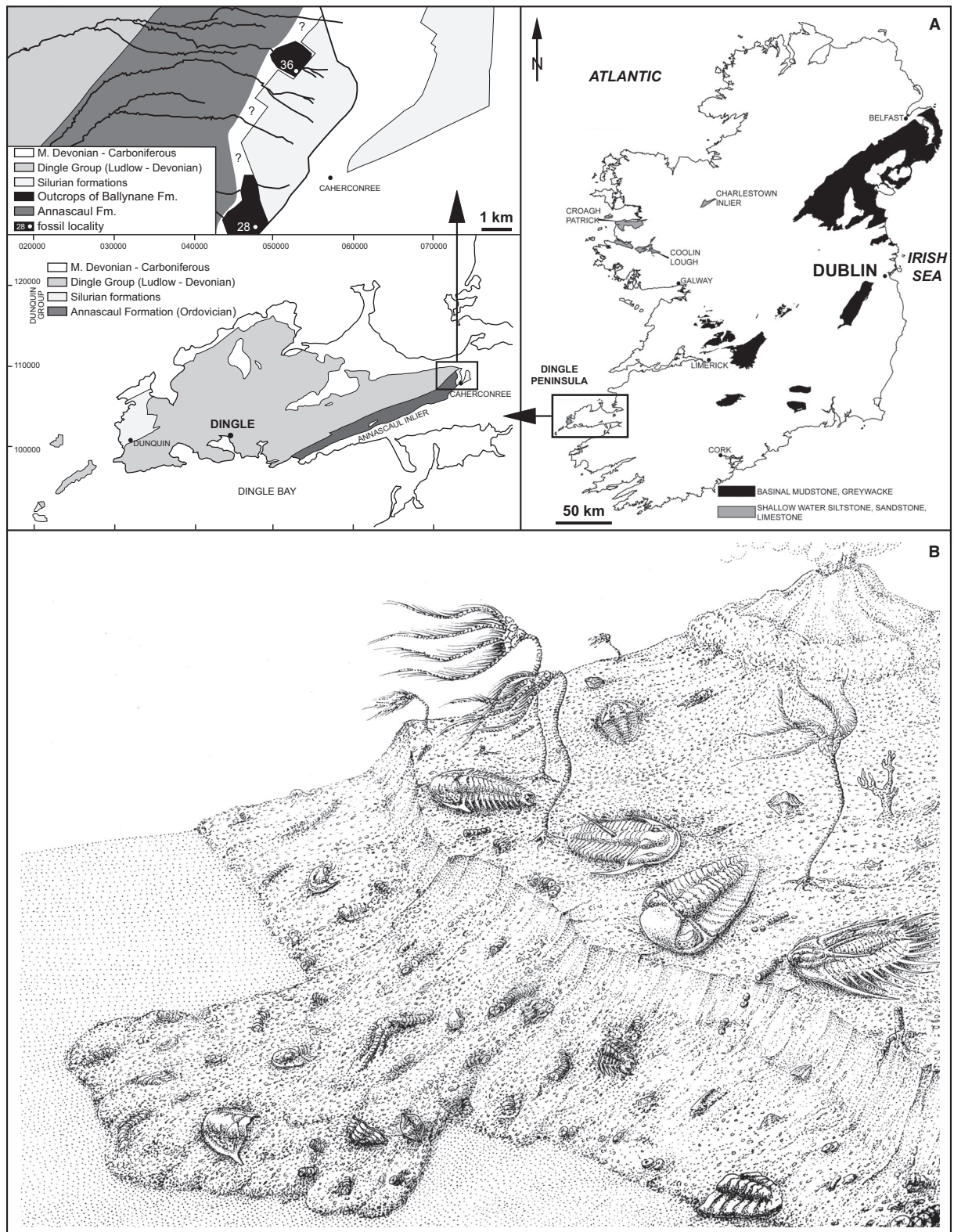
Fig. 1. Geological map and inferred depositional setting of the Dingle material. A, distribution of outcrop/suboutcrop of Silurian rocks of basinal and shallow-water shelf facies in Ireland (large right frame); geology of the Dingle Peninsula showing the location of Caherconree and the Irish 10 km National Grid (bottom left frame); and the exposure of the Ballynane Formation in Localities 28 and 36 (top left frame). Adapted from Parkin (1976), Pracht (1996) and Kaminski *et al.* (2016). B, reconstructed depositional environment of the investigated material. Drawing by artist Giancarlo Leonardi (refigured after Ferretti & Holland 1994).

Lindström (1955) referred to these spherules as 'egg-cases' of Stauffer (1935) in Ordovician strata of South-Central Sweden. Müller (1959) figured spherules ('kugeln') associated to specimens of *Westergaardodina*. Müller & Nogami (1972) compared the lamellar accretion of conodonts with that of '*the brown bodies, 'oakleyite', contained in the Silurian bryozoan genus* Favositella*, which are also composed of calcium-phosphate, but have a mode of growth somewhat different from the conodonts*' (Müller & Nogami 1972, p. 27). Müller *et al.* (1974) suggested an organic origin of the microspherules for the presence of borings.

A second group of papers, starting from the seventies, was exclusively focused on the microspherules. Large collections of specimens of different age and provenance were analysed and compared (in time and space) in the attempt to identify common features and derive a systematic assignment. Leuteritz *et al.* (1972) integrated light, scanning and transmitting electron microscopy and microprobe analysis and, on the basis of structure and chemical composition, suggested that (p. 111): '*a formation within organisms can be excluded. Chemical processes during decay of organic matter have favoured their formation near the sea bottom.*' The detection of organic matter residues at the centre of the spheres, some of which interpreted as fully preserved skeletons of hystrichospheroids, suggested they acted as nuclei of early diagenetic concretions. Bischoff (1973) interpreted Stauffer's spherules as statoliths of medusoid conodont-bearing animals.

Glenister *et al.* (1976) analysed about 2000 microspherules of Silurian and Devonian age from different areas. The authors detailed a lamellar fabric with more than 50 alternately light and darker concentric layers around a distinct nucleus up to 0.1 mm in size. A shallow external concave zone ('dimple'), replicated by successive coatings and regarded as basal, was noticed. Occasionally, spheres were fused together (up to five) and enveloped by outer shells. What had been previously interpreted as possible spines of hystrichospheroids at the centre, were there explained as secondary radial cracks partially or completely filled during diagenesis. X-ray diffraction pattern of the apatite composing the spheres as well as colour revealed to be identical with those of the associated conodonts. According to mineralogical composition, structure, faunal associations, and geological occurrence, the Authors concluded that (p. 571): '*the phosphatic spheres are pearls secreted by the conodont-bearing animal around a particulate or organic irritant.*'

McConnell & Ward (1978) suggested that uroliths present in the urinary tract of extant *Nautilus*, constituted by an amorphous calcium-phosphate hydrogel, could have been transformed by diagenesis in a crystalline form so to correspond to the 'conodont pearls' described by Glenister *et al.* (1976). In their reply, Glenister *et al.* (1978) remarked that (p. 209): '*Unlike the 'pearls,' uroliths display an uneven varicose surface and lack a regularly replicated dimple.*' In addition, the Authors observed that no records of pearls are known in the post-Palaeozoic, a period in which cephalopods were dominant.

Gao *et al.* (1987) and Yin *et al.* (1989) reported apatite spherules from the latest Permian of South China that they interpreted to be of organic origin (Yin *et al.* 1989). These records need further investigation to test if they can extend the stratigraphical range of the microspherule.

Wang & Chatterton (1993) analysed Devonian microspherules picked from conodont residues of Canada and China with a combination of scanning electron microscope, energy dispersive X-ray spectroscopy, X-ray microdiffraction, and electron microprobe analysis. Three groups of natural microspherules were identified. Phosphatic spherules, with a distinctive shallow concave area ('dimple') were regarded as conodont pearls, confirming assumptions of previous authors. Splash-shaped silicate spherules with a glass matrix were interpreted as microtektites of impact origin; black, magnetic iron spherules were assigned to a possible extra-terrestrial origin.

Giles *et al.* (2002) studied over 400 sub-millimetric phosphatic microspherules from the Late Devonian of eastern Nevada and western Utah. Other than conodont elements, residues produced fish teeth, silicified foraminifers, ostracods, brachiopods and echinodermal skeletal debris. Microspherules, fish

Table 1. Main interpretations on the nature of the enigmatic phosphatic spherules according to previous literature.

Interpretation	Reference(s)
Bryozoan calculi	Oakley (1934, 1966)
Egg cases	Stauffer (1935), Lindström (1955)
Conodont affinity	Stauffer (1940), Müller (1959)
Otoliths	Youngquist & Miller (1948), Zhang *et al.* (2017)
Early diagenetic concretions	Leuteritz *et al.* (1972)
Cnidaria (conodont) statoliths	Bischoff (1973)
Conodont pearls	Glenister *et al.* (1976), Wang & Chatterton (1993)
Conodont pearls	Glenister *et al.* (1976), Wang & Chatterton (1993)
Nautiloid uroliths	McConnal & Ward (1978)
Fish otoliths	Giles *et al.* (2002)
Different origins	Lindskog *et al.* (2017)
?Brachiopod pearls	This paper

teeth, and conodonts were further analysed by electron microprobe. The chemical composition of microspherules, regarded as primary biogenic, appeared more similar to fish teeth than to conodonts, with in particular lower concentrations in wt % of P_2O_5, F, SrO and higher concentrations of CaO, SO_2, MgO and Fe_2O_3. For that reason, microspherules were interpreted as possible fish otoliths. However, in modern oceans, otoliths are made of calcium carbonate, typically aragonite, with concentric laminae produced on a daily basis. The unusual phosphatic composition of the Devonian microspherules was explained by the authors as '*related to a major shift in local ocean water composition and temperature during this time*' (Giles *et al.* 2002, p. 120).

Zhang *et al.* (2017) interpreted Late Devonian microspherules from South China as phosphatic otoliths on the basis of 'checks,' 'rhythmic growth patterns' and 'sub-diurnal increments' revealed by quantitative microstructure analysis, with annuli width getting narrower at increasing radius. A maximum value of about 90 annuli was detected in all the specimens. The Authors associated therefore the spherules to a marine organism with a very short lifespan (<90 days).

Lindskog *et al.* (2017) added synchrotron radiation X-ray tomographic microscopy (SRXTM) to routine technique applied by previous Authors. A large collection of microspherules from several localities and stratigraphical (Cambrian to Devonian) levels was investigated. Associated conodont elements were analysed as well. Five different groups with diverse morphological and chemical features were discriminated. *Type 1 spherules* (78 specimens) correspond to the 'classical' conodont pearls described by Glenister *et al.* (1976). *Type 2 spherules* (a single spherule) replicate the previous one but with the additional presence of Si, Al and Fe ('*siliciclastic clay and/or iron oxide*;' Lindskog *et al.* 2017, p. 30) within laminae. *Type 3 spherules* (thousands of specimens) are asymmetrical with polygonal properties and resemble '*spherulites*' reported by Oakley (1934, 1966) within bryozoans. *Type 4 spherules* (six specimens) are similar to *Type 3* but are missing the polygonal properties. *Type 5 spherules* (16 specimens) normally lack cortical lamination and include specimens directly associated with paraconodont *Westergaardodina* and euconodont *Cordylodus*. Chemical analysis revealed that, together with the tendency of spherules and conodonts from the same samples to group together, microspherules and conodont elements create separate clusters, having the former in particular a significantly lower P content than the latter. *Type 1 spherules*, those better matching the 'conodont pearls'

introduced by Glenister *et al.* (1976), were among those most distant from the main conodont cluster. The Authors concluded that phosphatic spherules may have different origin, both inorganic and organic, as also confirmed by so many distant taxonomic attributions by previous literature (Table 1). Furthermore (Lindskog *et al.* 2017, p. 39): '*The only organisms that are unequivocal producers of phosphatic spherules in our sample materials are bryozoans, and the conodonts* Westergaardodina *and* Cordylodus. *The function, if any, of the spherules in both these groups remains unclear, but a pathogenic origin is possible, or even likely. None of the isolated spherules could be tied to other euconodonts with certainty. By contrast, several of the micro-spherules found in euconodont sample residues most likely have a bryozoan origin.*'

After almost one century from the first report of these spherules, a final answer on their nature is far from being reached. With the aim to shed more light on this controversy, we decided to reverse the analytical perspective. Previous works had dealt with as many spherules as possible and covering the largest stratigraphical range. On the contrary, we processed material from a single stratigraphical horizon (Locality 36, Ballynane Formation, Ireland) restricted to a precise time-span (latest Gorstian-early Ludfordian, early Ludlow, Silurian) and analysed all the phosphatic specimens recovered with the enigmatic microspherules after acid digestion. Only in this way, we can be reasonably certain these organisms really belong to the same faunal association.

Geological setting

The actual configuration of Ireland results from the fusion of distinct terranes. Ireland was in fact located in the Silurian at the Iapetus suture zone merging the palaeocontinents of Laurentia, Baltica and Avalonia and still under the influence of Gondwana (Ferretti *et al.* 2014).

Most of the Silurian is there represented by shales and greywackes of basinal facies (Holland 2009). Shallow-water facies are restricted to the west and southwest of Ireland. To the west (Counties Galway, Mayo and Roscommon), a late Llandovery transgression is documented by fossiliferous shallow-water calcareous siltstones and sandstones of Telychian age. The shelly faunas there recovered are dominated by brachiopods. Calcareous rocks are scarce and hardly processable for conodont investigation.

The shallow-water Silurian sediments exposed in the Dingle Peninsula (County Kerry) are represented by calcareous siltstones and sandstones with
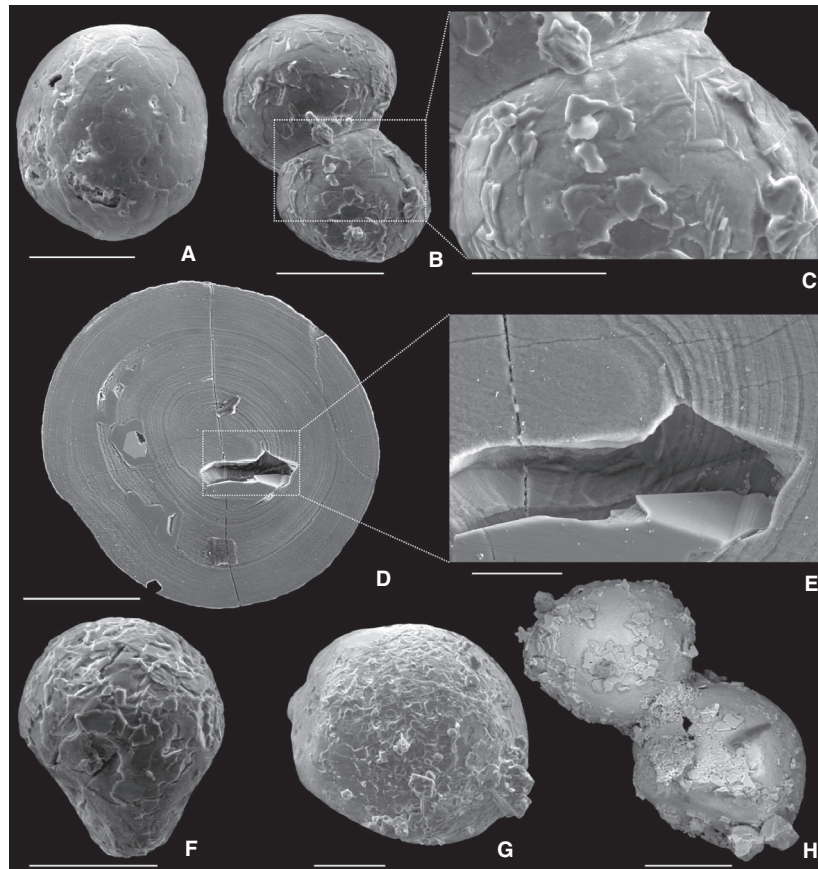
Fig. 2. Phosphatic 'conodont pearls' recovered in the Dingle material. A, microspherule 6, specimen TCD.50767. B, C, microspherule 2, specimen TCD.50768. C, detail of B with contact between the two sub-spherules. D, E, microspherule 53, mounted in epoxy and polished to expose a flat surface to reveal the finely laminated structure, specimen TCD.50769. E, enlargement of a fissure displaying the laminated structure. F, microspherule 7, specimen TCD.50770. G, microspherule 3, specimen TCD.50771. H, microspherule 58, specimen TCD.50772. Scale bar = 100 µm (except for C and E, respectively, 50 and 20 µm).

abundant marine shelly faunas, dominated by brachiopods of Wenlock-Ludlow age. In the Dunquin inlier, at the western end of the Dingle Peninsula, no attempts of dissolving the sparse calcareous rocks revealed to be successful. However, the Annascaul inlier described by Parkin (1976) exposes the Wenlock (Homerian) to Ludlow Ballynane Formation (Pracht 1996), consisting of siltstones, with thin bands and nodular masses of limestone, and fine-grained volcaniclastics (Ferretti & Holland 1994). The younger Caherconree and Derrymore Glen Formations (Ludlow) do not contain limestone. Only two exposures disclose the calcareous nodules of the Ballynane Formation. These small outcrops, known in literature as Localities 28 and 36 of Parkin, are separated each other by one kilometre of unexposed ground (Fig. 1A). Conodonts described by Aldridge (1980) suggested a Wenlock age for Locality 28 and a Ludlow age for Locality 36. A rich trilobite fauna, dominated by odontopleurids, was reported by Siveter (1989), and a mid/late Wenlock-earliest Ludlow age was indicated for Locality 36. Kaminski *et al.*

(2016) proposed an early Ludlow (Gorstian-earliest Ludfordian) age basing on new conodont material extracted from Locality 36. The recovery in this study of new conodont elements and in particular of *Kockelella variabilis ichnusae* Serpagli & Corradini, 1998 allows to further restrict the stratigraphical range of Locality 36 to the latest Gorstian-early Ludfordian: in fact, the taxon ranges from the upper part of the *K. v. variabilis* interval Zone into the *P. siluricus* Zone (Corriga *et al.* 2009; Corradini *et al.* 2015; Gómez *et al.* 2019).

Parkin's Locality 36 exposes about 3 m of grey centimetric carbonate nodules embedded in a finer-grained matrix. Disarticulated trilobites reflecting a thanatocoenosis (Siveter 1989), crinoids (plates, spines, and stems), brachiopods with well-preserved shell-layering and rare bryozoans clearly illustrate benthic communities of shallow and well-ventilated water. They were interpreted as periodical episodes of colonization of the bottom, punctuated by volcanic events and redepositions in deeper-waters (Ferretti & Holland 1994; Fig. 1B). In even deeper and
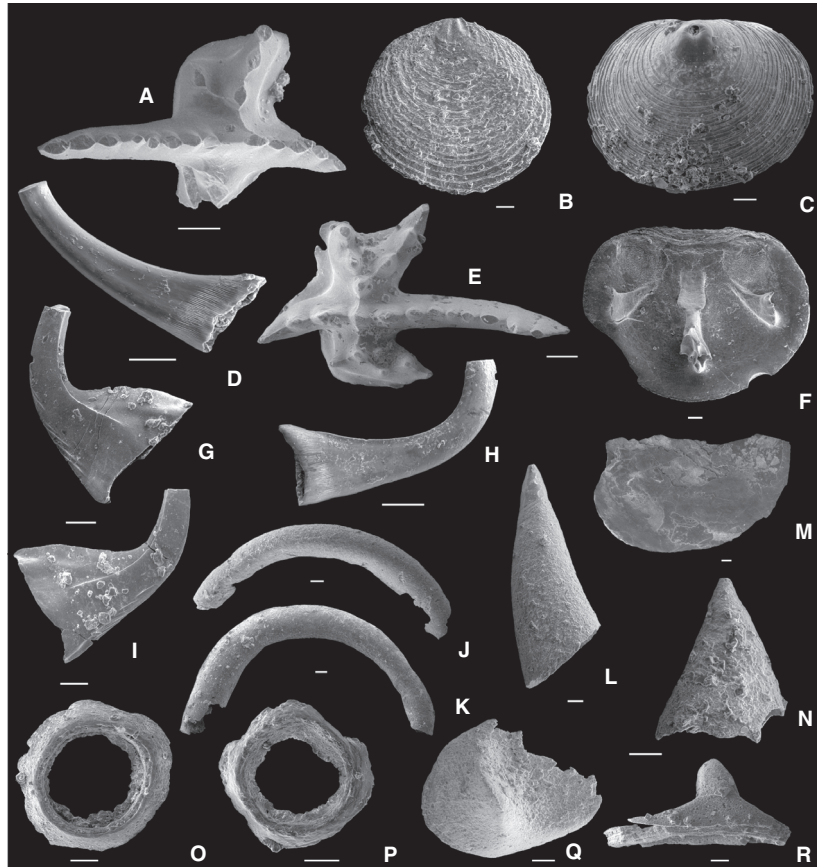
Fig. 3. Main phosphatic skeletal elements recovered in the Dingle material. A, D, E, G–I. Conodonts. A, *Kockelella variabilis ichnusae* Serpagli & Corradini, 1998. Upper view of Pa element 32, specimen TCD.50773. D, H, *Panderodus unicostatus* (Branson & Mehl, 1933), lateral views of elements 38 and 39, specimens TCD.50774 and TCD.50775. E, *Kockelella variabilis ichnusae* Serpagli & Corradini, 1998. Upper view of Pa element 33, specimen TCD.50776. G, I, *Dapsilodus obliquicostatus* (Branson & Mehl, 1933). Lateral views respectively of elements 34 and 29, specimens TCD.50777 and TCD.50778. B, C, F, L-N. Brachiopods. B, C, exterior surface of valves 43 and 16, specimens TCD.50779 and TCD.50780. F, M, interior surface of valves 19 and 15, specimens TCD.50781 and TCD.50782. L, N, exterior surface of valves 51 and 52, specimens TCD.50783 and TCD.50784. J, K, undetermined phosphatic hollow tubes 20 and 21, specimens TCD.50785 and TCD.50786. O, P, upper views of problematic phosphatic rings 24 and 25, specimens TCD.50787 and TCD.50788. Q, R. *Eurytholia* cf. *E. bohemica* Ferretti, Serpagli & Štorch, 2006. Q, upper view of plate 49, specimen TCD.50789. R, lateral view of specimen TCD.60909b. Scale bar = 100 μm.

scarcely oxygenated waters, as documented mostly in the peri-Gondwana area, the typical Silurian black cephalopod limestone biofacies was deposited (Barca *et al.* 1992; Ferretti & Serpagli 1996; Ferretti *et al.* 1998, 2009; Corradini *et al.* 2009a).

Several problematic organisms were recovered from the same locality. Ring-like phosphatic elements, similar to those reported from the Czech Republic by Ferretti *et al.* (2013), and enigmatic plates attributed to *Eurytholia bohemica* already described from the Middle-Late Ordovician of several sites of the Iapetus Ocean (United Kingdom, Sweden, Estonia and Alabama; Sutton *et al.* 2001) and the Silurian of the Czech Republic, the Carnic Alps and Sardinia (Ferretti *et al.* 2006; Ferretti & Serpagli 2008; Corradini *et al.* 2009b) are present also in Ireland (Kaminski *et al.* 2016; this paper). Partially silicified microfossils of uncertain affinity assigned to

Regnellia and *Sandvikina* were described by Ferretti *et al.* (1993). Finally, a low diversity agglutinated foraminiferal assemblage with a clear North American affinity was recently detailed by Kaminski *et al.* (2016).

Material and methods

Lab processing and optical microscopy

A total of about 7 kg of calcareous material collected from Locality 36 was dissolved in diluted formic acid with the standard processing technique used for conodont preparation. The entire residue (light and heavy fractions) was carefully hand-picked under a Zeiss binocular microscope. Spherules and phosphatic associated material (a selection is reported

Table 2. Bioapatite cell parameters *a* and *c* and cell volume calculated for the investigated material, symbol – indicates value that could not be calculated.

Fossil code	Fossil type	a (Å)	c (Å)	cell volume (Å^3)
1	Microspherule	–	–	–
2	Microspherule	9.364 (3)	6.884 (3)	522.8 (3)
3	Microspherule	9.374 (2)	6.886 (2)	524.0 (2)
4	Microspherule	9.364 (3)	6.888 (2)	523.1 (3)
5	Microspherule	–	–	–
6	Microspherule	9.362 (4)	6.882 (3)	522.4 (4)
7	Microspherule	9.367 (3)	6.884 (2)	523.1 (3)
8	Microspherule	9.374 (2)	6.888 (2)	524.2 (2)
9	Undetermined skeletal element	–	–	–
10	Undetermined skeletal element	9.345 (4)	6.895 (5)	521.5 (5)
11	Microspherule	–	–	–
12	Microspherule	9.375 (2)	6.892 (2)	524.6 (2)
13	Undetermined skeletal element	–	–	–
14	Ring	9.374 (2)	6.896 (2)	524.8 (2)
15	Brachiopod (interior surface of the valve)	9.352 (1)	6.880 (2)	521.1 (2)
16	Brachiopod (exterior surface of the valve)	9.373 (4)	6.889 (4)	524.2 (4)
17	Inorganic material	–	–	–
18	Inorganic material	–	–	–
19	Brachiopod (interior surface of the valve)	9.357 (2)	6.894 (3)	522.7 (2)
20	Undefined hollow tube	9.368 (2)	6.896 (2)	524.1 (2)
21	Undefined hollow tube	9.370 (1)	6.890 (2)	523.9 (1)
22	Ring	9.369 (2)	6.891 (2)	523.8 (2)
23	Ring	9.369 (2)	6.891 (2)	523.8 (2)
24	Ring	9.369 (2)	6.897 (2)	524.3 (2)
25	Ring	9.368 (2)	6.890 (3)	523.7 (2)
26	Undetermined skeletal element	9.363 (2)	6.892 (2)	523.2 (2)
27	Undetermined skeletal element	–	–	–
28	Conodont (*Kockelella*)	9.384 (1)	6.884 (1)	525.0 (1)
29	Conodont (*Dapsilodus*)	9.383 (1)	6.886 (2)	525.0 (2)
30	Conodont (*Panderodus*)	9.382 (2)	6.868 (4)	523.5 (3)
31	Conodont (*Kockelella*)	9.380 (1)	6.888 (2)	524.8 (1)
32	Conodont (*Kockelella*)	9.380 (2)	6.884 (2)	524.5 (2)
33	Conodont (*Kockelella*)	9.376 (1)	6.891 (2)	524.6 (1)
34	Conodont (*Dapsilodus*)	9.376 (1)	6.888 (1)	524.4 (1)
35	Conodont (*Dapsilodus*)	9.376 (1)	6.890 (2)	524.5 (1)
36	Conodont (*Dapsilodus*)	9.373 (1)	6.898 (3)	524.9 (2)
37	Conodont (*Panderodus*)	9.376 (2)	6.888 (4)	524.3 (2)
38	Conodont (*Panderodus*)	9.374 (2)	6.888 (3)	524.2 (2)
39	Conodont (*Panderodus*)	9.377 (3)	6.896 (4)	525.1 (3)
41	Brachiopod (exterior surface of the valve)	9.373 (2)	6.895 (2)	524.6 (2)
42	Brachiopod (exterior surface of the valve)	9.371 (1)	6.894 (1)	524.4 (1)
43	Brachiopod (exterior surface of the valve)	9.367 (2)	6.891 (2)	523.6 (2)
49	Plate	9.376 (1)	6.886 (1)	524.2 (2)
51	Brachiopod (exterior surface of the valve)	9.370 (2)	6.890 (3)	523.8 (2)
52	Brachiopod (exterior surface of the valve)	9.368 (4)	6.894 (4)	523.9 (3)
69	Microspherule	9.371 (1)	6.883 (1)	523.4 (1)

respectively in Figs 2, 3) were collected in this way. The latter material resulted to be represented by conodonts, brachiopods, enigmatic rings, problematic plates and unassigned curved tubes. All recovered pearls (56 specimens) were investigated under SEM/ESEM analysis as their minute dimensions prevent a study under optical microscopy. Eleven pearls were further characterized through X-Ray microdiffraction (μXRD). Among other phosphatic material, most complete specimens with no secondary recrystallization were selected (Fig. 3). Twelve conodont elements belonging to the genera *Kockelella* (four Pa elements; Fig. 3A, E), *Panderodus* (four elements; Fig. 3D, H) and *Dapsilodus* (four elements; Fig. 3G, I), eight brachiopod valves (two analysed in the interior surface of the valve, Fig. 3F, M; six in the exterior surface of the valve, Fig. 3B-C, L, N), five enigmatic rings (Fig. 3O, P), two curved tubes (Fig. 3 J, K) and one plate (Fig. 3Q) were chosen. Material processed under X-Ray microdiffraction and resulting data are detailed in Table 2.

Illustrated specimens are deposited in the collections of the Trinity College of Dublin (TCD), Ireland, under repository numbers TCD.50767–TCD.50795.

SEM/ESEM microscopy

Specimens were mounted on aluminium stubs previously covered with carbon-conductive adhesive tape. Au-coated and non-coated specimens were observed
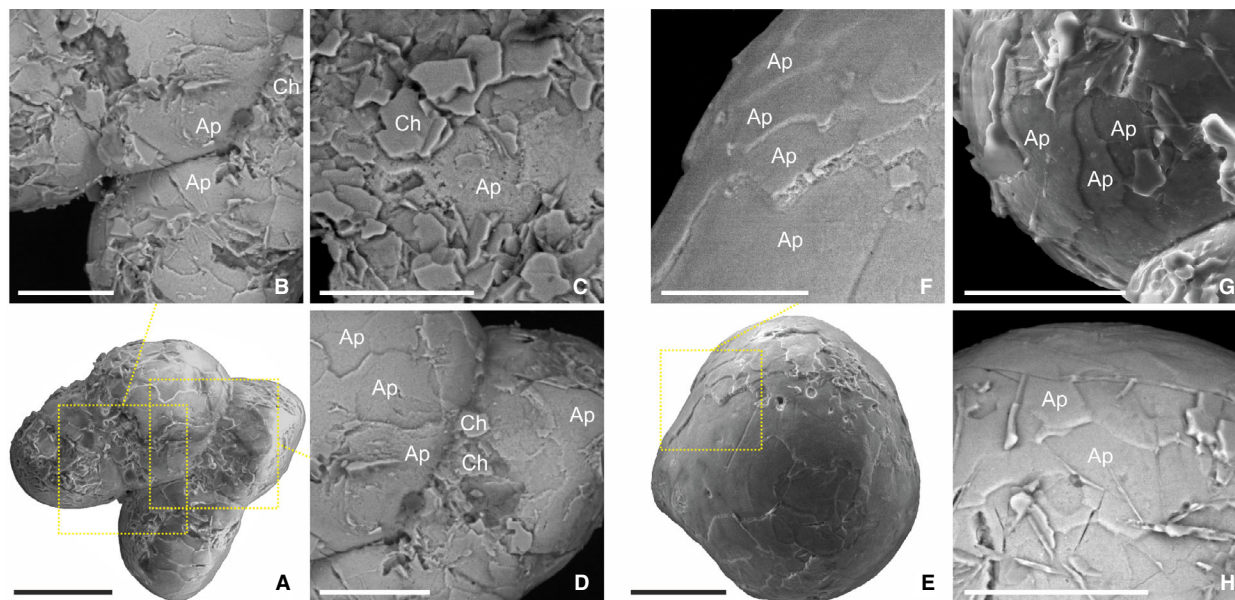
Fig. 4. External surface of the 'conodont pearls.' A-B, D, microspherule 63, specimen TCD.50790. C, microspherule 4, specimen TCD.50791. E-F, microspherule 8, specimen TCD.50792. G-H, microspherule 2, specimen TCD.50768. Scale bar = 100 μm.

using an Environmental Scanning Electron Microscope (ESEM) FEI ESEM-Quanta 200, equipped with an Oxford EDX INCA 300 X-ray energy dispersive spectrometer and a Scanning Electron Microscope (SEM) Nova NanoSEM FEI 450 equipped with a XEDS Bruker QUANTAX-200 detector. ESEM observations were performed in high and low vacuum (low vacuum brackets 1 and 0.5 Torr) with an accelerating voltage between 5 and 25 keV for imaging and between 5 and 15 keV for elemental analyses. SEM observations were in high vacuum with an accelerating voltage between 15 and 25 keV for imaging and between 15 and 25 keV for elemental analyses.

Some microspherules were embedded in epoxy resin for 48 h and finely polished with chemically inert aluminium oxide and silicon carbide to expose their cross-section (see Malferrari *et al.* 2019 for the method). The resin blocks were finally cleaned in an ultrasonic bath in Millipore water for 3 min and air dried. Sectioned specimens mounted in epoxy were gold sputtered and observed under ESEM/SEM investigation as described above.

X-ray microdiffraction (μ-XRD)

An X-ray microdiffraction study was carried out on selected material. XRD patterns were obtained using a Rigaku D-max Rapid microdiffractometer operating at 40 kV and 30 mA. This instrument is equipped with a CuKα source, curved-image-plate
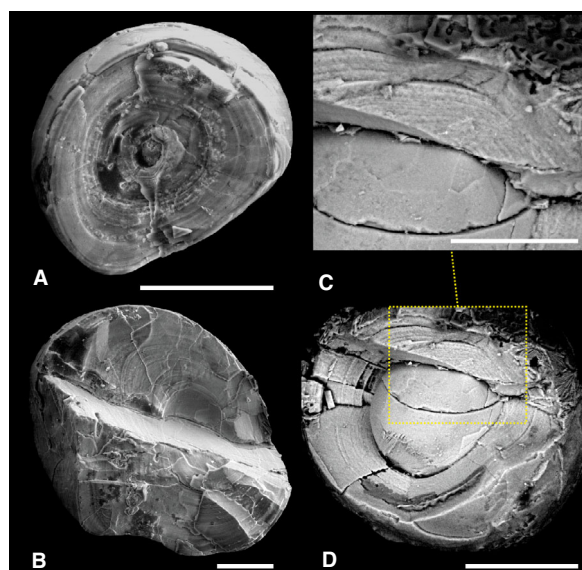
Fig. 5. Inner laminated fabric of the microspherules. A, detail of naturally broken microspherule 60 revealing a fine lamination, specimen TCD.50793. B, microspherule 61 exposing a laminated coating, specimen TCD.50794. C-D, microspherule 62, specimen TCD.50795. The scale bar is 100 μm in A-B, D and 50 μm in C.

detector, flat graphite monochromator, variety of beam collimators, motorized stage and microscope for accurate positioning of the sample. The motorized stage allows two angular movements (rotation Φ and revolution ω). Data were measured in reflection mode using various sample-to-beam geometries and operating conditions. In particular, specimens were

mounted on small plane surfaces and analysed with 0.3 mm (collection time: 10 min), 0.1 mm (collection time: 1 h), and 0.05 mm (collection time: 3 h) collimators; both Φ and ω were maintained fixed. XRD data were measured as two-dimensional images and converted into I-2θ profiles using the Rigaku R-AXIS Display software. Mineralogical data, expressed by parameters *a* and *c*, respectively, width (=length) and height of the apatite crystallographic cell (unit cell parameters), were refined using UnitCell software (Holland & Redfern 1997). The use of the microdiffractometer has the advantage of detecting measurements on small sized fossils and even minor portions of them. This instrument allows a non-destructive mineralogical study, with both qualitative and quantitative analysis of crystalline phases, and determination of additional mineralogical properties like degree of crystallinity, size of crystallites and preferential orientations.

Lab processing, optical microscopy and ESEM-EDX analyses were performed at the Scientific Instruments Facility (CIGS) of the University of Modena and Reggio Emilia (Modena, Italy), whereas X-ray microdiffraction measurements were run at the Institute of Methodologies for Environmental Analysis of the National Research Council of Italy of Tito Scalo (Potenza, Italy).

Results

Size, shape and structure

Spherules recovered in the Irish material reveal a considerable variation both in size and in shape. Size of the microspherules ranges between 0.2 and 0.5 mm. Sub-spherical shapes (Fig. 2A, D) are the most abundant, associated with oblong (Fig. 2F), polygonal or irregular ones. Colour is extremely variable, from a porcelaneous white to grey or black. Surfaces of the microspherules are either dull or bright, with some specimens having iridescent properties. Some microspherules reveal a depression on one side (Fig. 2G), as originally observed by Glenister *et al.* (1976, 1978) and later reported by, among others, Wang & Chatterton (1993), Giles *et al.* (2002), Lindskog *et al.* (2017) and Zhang *et al.* (2017). Associations of multiple microspherules, up to four, were recovered as well (Fig. 2B, C, H). At higher magnification spherules show either a smooth external surface (Fig. 4E) or a rough appearance (Fig. 4A), due to the presence of equidimensional scattered 'frakes' spread all over the outermost layer.

Naturally broken material and polished microspherules display a very fine lamination, with
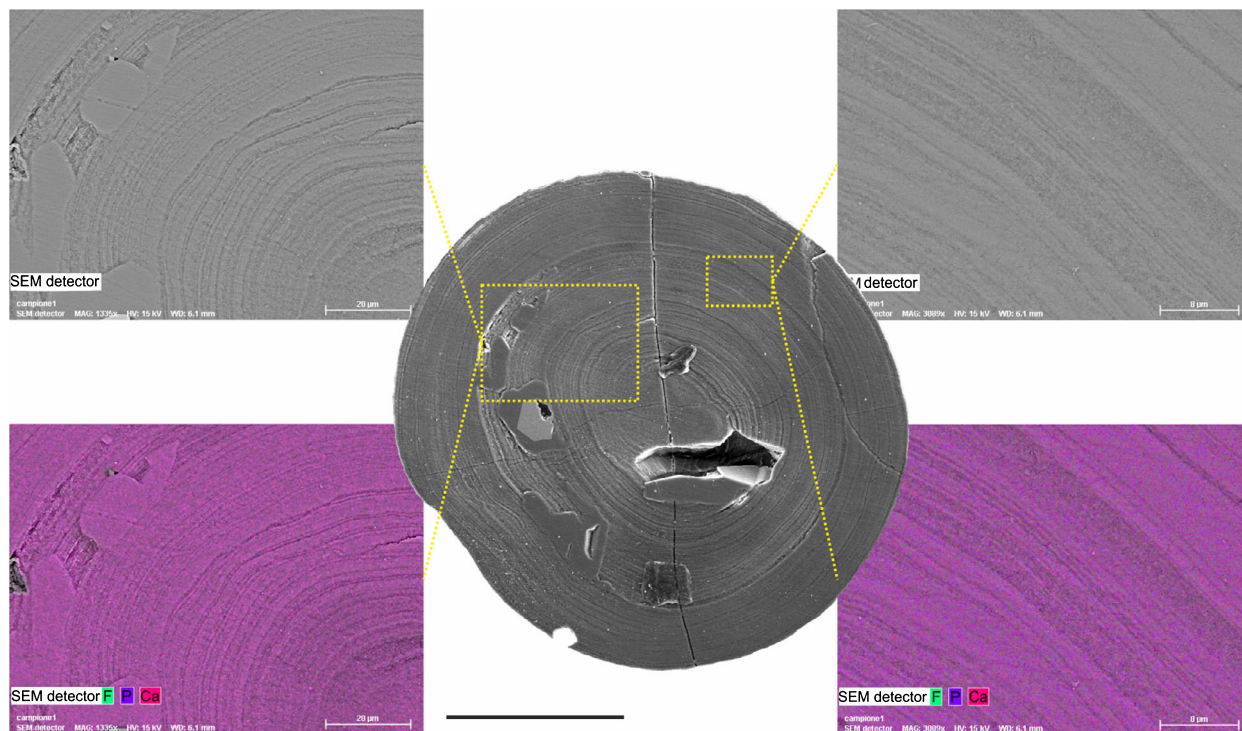
Fig. 6. Chemical composition. SEM-EDS elemental maps (Ca, P and F) of two areas of microspherule 53 (specimen TCD.50769) revealing a general compositional uniformity within the cortex of the microspherule. Scale bar = 100 μm.

micrometric-thick laminae. Laminae are continuous and do not apparently reveal to follow a regular pattern (e.g., decrease/increase in thickness from the centre to the outer rim of the microspherule).

Multiple microspherules are composed of singularly coated ones, further enveloped by additional laminae strictly replicating the geometry of the aggregated material. Adhesion surfaces of fused spherules are planar (Figs 2B-C, 4A-B, D) which suggests a simultaneous growth of each microspherule and not a later adhesion. Compound specimens where single constituents keep a spherical shape (Fig. 2H) might reflect on the contrary a posthumous aggregation.

Some microspherules appear to have a rounded nucleus, not always preserved (Fig. 5A, B). A laminated fabric (Fig. 2E) is detectable even in the innermost part of the microspherule, so it is not excluded that the 'nucleus' simply represents a weaker detachment surface within the coating (Fig. 5C, D). Other sectioned specimens do not reveal a definite nucleus, perhaps also because the innermost part of the microspherule was not exposed by the polishing.

SEM/ESEM-EDX chemical characterization

Spherules and other associated material were preliminarily investigated in order to monitor distribution of major elements. Environmental scanning electron microscopy coupled with microanalyses (SEM/ESEM-EDX) revealed that Ca and P are the main chemical elements of the external surface of the microspherules; a weak, but significant peak of F was also detected; likewise, EDX analyses on the exposed laminae (Fig. 4F) of smooth microspherules showed identical chemical composition. In contrast, rough microspherules (Fig. 4C) revealed the occurrence of scattered 'frakes' of an aluminosilicate partially covering the phosphatic surface, as documented by the comparison in the EDX spectra of the signals from Fe, Si, Al and Mg.

Naturally broken material and polished microspherules were carefully mapped to detail also the innermost parts. No significant changes in chemical composition of major elements appeared from core to rim (Fig. 6) confirming a compositional homogeneity throughout the entire coating.

µ-XRD measurements and cell parameter refinement

µ-XRD revealed that polycrystalline apatite and chlorite are the two main mineralogical phases, as highlighted by the well-defined diffraction arcs for each

XRD reflection. The frequent occurrence of sub-microscopic single-crystals of quartz, randomly distributed on the surfaces of many skeletal elements, were evidenced by the presence of single-crystal diffraction spots (for the meaningfulness of diffraction arcs and diffraction spots, see Ferretti *et al.* 2017 and Medici *et al.* 2020).

Apatite is the dominant mineralogical phase; however, as reported above, a large part of the analysed samples is partially coated by chlorite. The coating was so diffused in some skeletal elements (e.g., specimens 1, 5, 9, 11, 13, 17, 18, 27) to hamper definition of bioapatite unit cell parameters. XRD reflections allowed to detail the type of chlorite as a Fe-rich clinochlore or chamosite (Brigatti *et al.* 2011), in agreement with EDX analyses that detected in the same points the signals of Mg and Fe. Nevertheless, some samples are chlorite-free, such as microspherules 6 and 8, and the majority of conodonts (specimens 28, 29, 31, 32, 33, 35, 39).

Single-crystals of quartz were detected in mostly all skeletal elements; in particular, strong signals were found in microspherules 1, 5, 6, 11, 69, in undetermined skeletal elements 9 and 13, in enigmatic rings

Fig. 7. Scatter plot *c/a* (A) and cell volume/*a* (B) of the phosphatic material investigated in this study.

14, 22 and 24, in brachiopods 15, 16, 42, 43 and 52, in inorganic material 17, in undefined tube 20, in plate 49, and in conodonts 30, 34, 37, 38. No signals emphasized the presence of polycrystalline quartz.

The crystallographic unit cell parameters a and c (considering the hexagonal crystal system) of apatite (for the samples for which it was possible to meas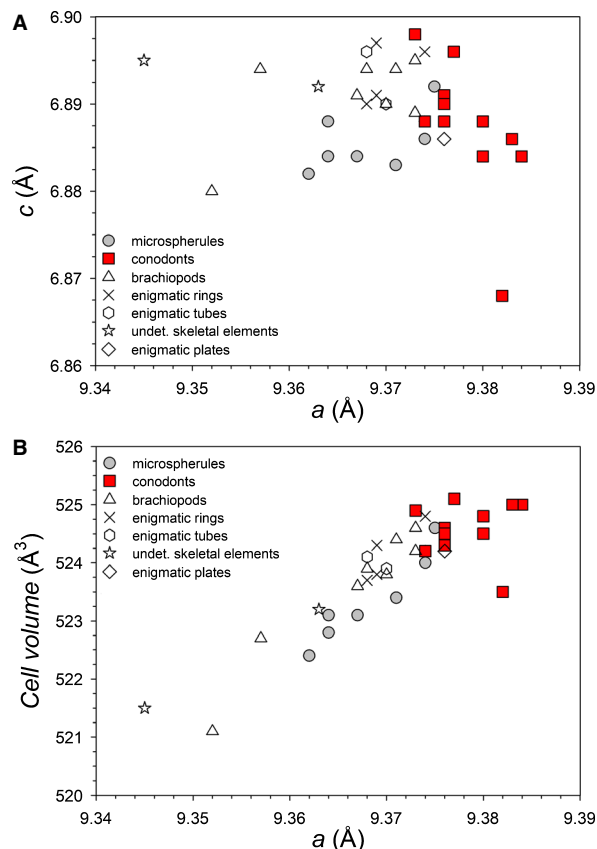ure an adequate number of diffraction peaks) were calculated to compare the mineralogical composition of microspherules and other skeletal elements (Table 2). The results, once again in agreements with EDX analyses, indicated unit cell parameters for bioapatite materials close to those typical of carbonate-fluorapatite minerals with, however, important ranges of variability: a: 9.352 ÷ 9.384 Å, c: 6.868 ÷ 6.898 Å, cell volume: 521.1 ÷ 525.1 Å^3. Actually, these ranges were not randomly distributed, but allowed to strictly focus on the aims of our study (see discussion below).

Discussion

Pearls today

In modern environments, pearls are secreted solely by shell-bearing molluscs (Murr & Ramirez 2012), that surround irritating particles inside the shell with concentric layers of calcium carbonate alternating with conchiolin, the same substances which compose the molluscan shell.

Pearls exhibit a remarkable variation in size (up to over 20 cm in diameter) and shape (spherical, irregular, droplet, fused, etc.), with those mostly approaching a spherical shape as the most precious in the jewellery market. Final shape reflects the position of the pearl (e.g. attached to the shell or free in the mantle) within the mollusc shell. Pearls originally free may be later enveloped by shell growth. Hemispherical pearls, that is pearls having a flat surface, are not rare. Murr & Ramirez (2012) report alteration of the pearl curvature in cultured freshwater pearls: their external surface flattens when the mantle seed used to trigger pearl growth is inserted too close to the shell surface. Colour varies from white pearl to pink, or blue up to the rare black ones. Iridescent properties are common, but not exclusive.

Fossil analogues to pearls were reported from other organisms, such as inoceramids (Brown 1940), brachiopods (Chatterton 1975), conulariids (Babcock 1990), gastropods (Schäffer *et al.* 1997), and ammonoids (De Baets *et al.* 2011), where pearls are composed of the same substance that builds the other hard parts of the organism. Macintyre *et al.* (2000, p. 456) reported '*uniserial individual spheres resembling a string of pearls*' made of a carbonate hydroxyl-apatite in one family of modern gorgonian octocorals (and possibly in the fossil counterpart).

Oakley (1934) excluded that '*spherolites*' could represent bryozoan pearls on the basis both of their mode of origin and different chemical composition (phosphatic *versus* calcareous). It appears highly reasonable that, whatever is the function of the microspherules, the organisms they belong used in creating them the same substance (e.g., bioapatite) already processed for building other skeletal parts. Basing on this assumption, the only phosphatic organisms recovered in the investigated residue, or revealed in thin-sections, were conodonts, brachiopods and enigmatic material in the form of rings, plates and hollow tubes.

Crystallographic signature

Chemical and diffractometric characterization allowed to classify the phosphatic material as a carbonate-fluorapatite and its Si-, Al-, Fe-, Mg-rich coating (if any) as a Fe-rich clinochlore (or chamosite) for all the samples.

The calculation of the crystallographic cell parameters a and c and of the cell volume for the bioapatite of microspherules, conodonts and the other phosphatic fauna associated in the conodont residue, further refines the distinction between various organisms. Results are summarized in Fig. 7 and commented below.

c/a plot. – Figure 7A plots the c vs a cell parameters for all the phosphatic material. Separate clusters clearly emerge for the different groups. In particular, conodonts and microspherules occupy two distinct areas regarding parameter a, being conodont values significantly higher (a for conodonts: 9.373 ÷ 9.384 Å; a for microspherules: 9.362 ÷ 9.375 Å). On the contrary, c variability of conodonts seems to incorporate that of microspherules (c for conodonts: 6.868 ÷ 6.898 Å; c for microspherules: 6.882 ÷ 6.892 Å). The enigmatic plate (a: 9.376, c: 6.886 Å) occurs at the border between these two groups. Nevertheless, data resulting from a single specimen are too limited to allow further considerations. Clusters of enigmatic rings and hollow tubes are narrow and disjunct from those of conodonts and microspherules, both for a (a for rings: 9.368 ÷ 9.374 Å; a for tubes: 9.368 ÷ 9.370 Å) and c (c for rings: 6.890 ÷ 6.897 Å; c for tubes: 6.890 ÷ 6.896 Å). Remarkable is the distribution of brachiopod cell parameters. Brachiopods analysed in the exterior surface of the valve cluster in an area overlapping rings and tubes, but clearly separate from conodonts (a for

brachiopods: $9.367 \div 9.373$ Å; c for brachiopods: $6.889 \div 6.895$ Å). Two brachiopods analysed in the interior surface of the valve cluster at lower a values 9.352 and 9.357 Å (and c parameters 6.880 Å and 6.894 Å).

Accordingly, the graph can be divided in four areas, respectively occupied by conodonts, microspherules, brachiopods and the association of enigmatic rings and hollow tubes. Brachiopod cluster overlaps that of microspherules. Rings and tubes have a values inside the range of variability of microspherules, whereas c values match those of conodonts. Crystallographic data collected from three different conodont genera (*Kockelella*, *Panderodus* and *Dapsilodus*) suggest that taxonomy does not influence a and c distribution.

Cell volume/a plot. – The correlation between bioapatite cell volumes and cell parameters a (Fig. 7B) confirms all remarks already expressed in Fig. 7A by a different point of view. Despite variability of cell volume, the four main areas previously highlighted are even more evident in this plot.

Microspherules display a wide range of variability both of a and cell volume ($522.4 \div 524.6$ Å^3). Brachiopod cell volume ($521.1 \div 524.6$ Å^3) and parameter a overlap those of microspherules. Rings ($523.7 \div 524.8$ Å^3) and hollow tubes ($523.9 \div 524.1$ Å^3) cluster at a marginal area of the microspherule distribution. On the contrary, conodonts clearly display different a parameters and cell volumes ($523.5 \div 525.1$ Å^3), clustering in a separate field from those of microspherules and the other phosphatic elements. The enigmatic plate (volume: 524.2 Å^3) shows values very close to some conodont ones.

Conclusions

Phosphatic microspherules have been commonly associated to conodonts because of their similar composition (fluorine apatite) and a stratigraphical distribution (Cambrian to early Carboniferous) overlapping that of conodonts (Cambrian to the Triassic/Jurassic transition). However, we cannot rule out that the lack of microspherule records beyond the stratigraphical range of conodonts could be an artefact resulting by the reduction of acid-processing in the post-Triassic by non-conodont workers. Furthermore, an accurate selection should be done in post-Triassic phosphate spherules, that were previously excluded by investigation as younger than conodonts, to test if any could fit with these enigmatic bodies.

We are aware that some organisms had (and have) a dual mineralization strategy with the co-existence of carbonate and phosphate mineralization, such as bryozoans secreting phosphatic linings (Martinsson 1965; Conti & Serpagli 1988) and brown calcitic bodies (Key *et al.* 2008), fishes producing teeth and otholiths, or some crustaceans producing phosphate gastroliths or mandibular teeth and calcareous bulk skeletal reinforcements (Bentov *et al.* 2016). Nevertheless, if interpreted of organic origin (pearls, calculi, otoliths, other?), we regard more reasonable to assume that these microspherules were constituted by the same substance already in use by the organism for building other major skeletal parts. On this basis, a combined chemical and mineralogical approach may be the key to reveal the nature of the microspherules.

Our study indicates that microspherules and conodonts recovered from the same stratigraphical horizon (Locality 36, Ballynane Formation, Ireland) and of the same age (latest Gorstian-early Ludfordian, early Ludlow, Silurian) have a different bioapatite crystallographic lattice configuration, both for cell parameters a and c, and cell volume. Conodonts, in addition, appear to exhibit a separate signature from that shown by the other phosphatic investigated specimens. Microspherule crystallographic parameters only partially overlap those of enigmatic rings, plates and tubes and, more importantly, appear to be included within the variability of bioapatite crystallographic lattice configuration of brachiopods. The affinity with the latter group needs to be analysed in greater detail in the future to test if non-Lingulida organophosphatic brachiopods, diffused in the Cambrian-Late Devonian interval, could have been producing pearls in the Palaeozoic as molluscs do today.

References

Aldridge, R.J. 1980: Notes on some Silurian conodonts from Ireland. *Journal of Earth Sciences Royal Dublin Society 3*, 127–132.

Babcock, L. 1990: Conulariid pearls. In Boucot, A.J. (ed): *Evolutionary Paleobiology of Behavior and Coevolution*, 68–71. Elsevier, Amsterdam, 725 pp.

Barca, S., Ferretti, A., Massa, P. & Serpagli, E. 1992: The Hercynian Arburese tectonic unit of SW Sardinia. New stratigraphic and structural data. *Rivista Italiana di Paleontologia e Stratigrafia 98*, 119–136.

Bentov, S., Aflalo, E.D., Tynyakov, J., Glazer, L. & Sagi, A. 2016: Calcium phosphate mineralization is widely applied in crustacean mandibles. *Scientific Reports 6*, 22118.

Bischoff, G.C.O. 1973: On the nature of the conodont animal. *Geologica et Palaeontologica 7*, 147–174.

Branson, E.B. & Mehl, M.G. 1933: Conodonts from the Bainbridge Formation (Silurian) of Missouri. *University of Missouri Studies 8*, 39–52.

Brigatti, M.F., Malferrari, D., Laurora, A. & Elmi, C. 2011: Structure and mineralogy of layer silicates: recent perspectives and new trends. In: *Layered mineral structures and their application in advanced technologies*. The Mineralogical Society of Great Britain and Ireland *11*, 1–71.

Brown, R.W. 1940: Fossil pearls from the Colorado group of western Kansas. *Washington Academy Science 30*, 365–374.

Chatterton, B.D.E. 1975: A commensal relationship between a small filter feeding organism and Australian Devonian spiriferid brachiopods. *Paleobiology 1*, 371–378.

Conti, S. & Serpagli, E. 1988: Bimineralic (calcareous and phosphatic) skeleton in Late Ordovician Bryozoa from Sardinia: Geological implications. *Bollettino della Società Paleontologica Italiana 27*, 129–162.

Corradini, C., Corriga, M.G., Ferretti, A. & Leone, F. 2009a: The Silurian of the Foreland Zone (southwestern Sardinia). *Rendiconti della Società Paleontologica Italiana 3*, 51–56.

Corradini, C., Corriga, M.G., Männik, P. & Schönlaub, H.P. 2015: Revised conodont stratigraphy of the Cellon section (Silurian, Carnic Alps). *Lethaia 48*, 56–71.

Corradini, C., Ferretti, A., Corriga, M.G. & Serpagli, E. 2009b: The reference section of the Sardinian Ockerkalk: the Silius Section. *Rendiconti della Società Paleontologica Italiana 3*, 209–216.

Corriga, M.G., Corradini, C. & Ferretti, A. 2009: Silurian conodonts from Sardinia: an overview. *Rendiconti della Società Paleontologica Italiana 3*, 95–107.

De Baets, K., Klug, C. & Korn, D. 2011: Devonian pearls ammonoid-endoparasite co-evolution. *Acta Palaeontologica Polonica 56*, 159–180.

Eisenack, A. 1964: Mikrofossilien aus dem Silur Gotlands Phosphatische Reste. *Paläontologische Zeitschrift 38*, 170–179.

Ferretti, A., Bergström, S.M. & Sevastopulo, G.D. 2014: Katian conodonts from the Portrane Limestone: the first Ordovician conodont fauna described from Ireland. *Bollettino della Società Paleontologica Italiana 53*, 105–119.

Ferretti, A., Cardini, A., Crampton, J., Serpagli, E., Sheets, H.D. & Štorch, P. 2013: Rings without a lord? Enigmatic fossils from the lower Palaeozoic of Bohemia and the Carnic Alps. *Lethaia 46*, 211–221.

Ferretti, A., Corradini, C. & Serpagli, E. 1998: The Silurian and Devonian sequence in SW Sardinia. *Giornale di Geologia 60, Special Issue*, 57–61.

Ferretti, A. & Holland, C.H. 1994: Biofacies and palaeoenvironmental analysis of a limestone lens, unique in the Irish Silurian, from the Dingle Peninsula, County Kerry. *Irish Journal of Earth Sciences 13*, 83–89.

Ferretti, A., Holland, C.H. & Syba, E. 1993: Problematic microfossils from the Silurian of Ireland and Scotland. *Palaeontology 36*, 771–783.

Ferretti, A., Malferrari, D., Medici, L. & Savioli, M. 2017: Diagenesis does not invent anything new: Precise replication of conodont structures by secondary apatite. *Scientific Reports 7*, 1624–1632.

Ferretti, A. & Serpagli, E. 1996: Geological outline, community sequence and paleoecology of the Silurian of Sardinia. *Rivista Italiana di Paleontologia e Stratigrafia 102*, 353–362.

Ferretti, A. & Serpagli, E. 2008: *Eurytholia* plates (Problematica) from the late Silurian of the Austrian Carnic Alps. *Revue de Micropaleontologie 51*, 183–187.

Ferretti, A., Serpagli, E. & Štorch, P. 2006: Problematic phosphatic plates from the Silurian-Early Devonian of Bohemia, Czech Republic. *Journal of Paleontology 80*, 1026–1031.

Ferretti, A., Storch, P. & Corradini, C. 2009: The Silurian of Sardinia: facies development and palaeoecology. *Rendiconti della Società Paleontologica Italiana 3*, 57–65.

Gao, Z., Xu, D., Zhang, Q. & Sun, Y. 1987: Discovery and study of microspherules at the Permian-Triassic boundary of the Shangsi section, Guangyuan, Sichuan. *Geological Review 33*, 203–211 [In Chinese].

Giles, K.A., McMillan, N.J. & McCarson, B.L. 2002: Geochemical analysis and paleoecological implications of phosphatic microspherules (otoliths?) from Frasnian-Famennian boundary strata in the Great Basin, USA. *Palaeogeography, Palaeoclimatology, Palaeoecology 181*, 111–125.

Glenister, B.F., Klapper, G. & Chauff, K.M. 1976: Conodont pearls? *Science 193*, 571–573.

Glenister, B.F., Klapper, G. & Chauff, K.M. 1978: Nautiloid uroliths composed of phosphatic hydrogel (Reply). *Science 199*, 209.

Gómez, M.J., Mestre, A., Garcías, Y. & Corradini, C. 2019: First documentation of the *Polygnathoides siluricus* conodont Zone (Ludfordian) in South America (Argentina) and the stratigraphic significance of the younger species of *Kockelella* (Conodonta). *Geological Journal 54*, 3455–3467.

Holland, C.H. 2009: Silurian. In Holland, C.H. & Sanders, I.S. (eds): *The Geology of Ireland*. 2nd edn, 568 pp. Dunedin Press, Edinburgh.

Holland, T.J.B., & Redfern, S.A.T. 1997: Unit cell refinement from powder diffraction data use of regression diagnostics. *Mineralogical Magazine 61*, 65–77.

Kaminski, M.A., Ferretti, A., Messori, F., Papazzoni, C.A. & Sevastopulo, G. 2016: Silurian agglutinated foraminifera from the Dingle Peninsula, Ireland. *Bollettino della Società Paleontologica Italiana 55*, 127–138.

Key Jr, M.M., Wyse Jackson, P.N., Miller, K.E. & Patterson, W.P. 2008: A stable isotopic test for the origin of fossil brown bodies in trepostome bryozoans from the Ordovician of Estonia. In Hageman, S.J., Key, M.M. & Winston, J.E. (eds): *Bryozoan Studies 2007. Proceedings of the 14th International Bryozoology Association conference, Boone, North Carolina, Martinsville, Virginia*, Virginia Museum of Natural History Special Publication Number 15, 75–84.

Leuteritz, K., Pietzner, H., Vahl, J. & Ziegler, W. 1972: Aufbau, Zusammensetzung und Entstehung von Calciumphosphat-Sphären in paläozoischen Kalken. *Geologica et Palaeontologica 6*, 111–113.

Lindskog, A., Eriksson, M.E., Bergström, S.M., Terfelt, F. & Marone, F. 2017: Palaeozoic 'conodont pearls' and other phosphatic micro-spherules. *Lethaia 50*, 26–40.

Lindström, M. 1955: Conodonts from the lowermost Ordovician strata of South-Central Sweden. *Geologiska Foereningan i Stockholm. Foerhandlingar 76*, 517–604.

Macintyre, I.G., Bayer, F.M., Logan, M.A.V. & Skinner, H.C.W. 2000: Possible vestige of early phosphatic biomineralization in gorgonian octocorals (Coelenterata). *Geology 28*, 455–458.

Malferrari, D., Ferretti, A., Mascia, M.T., Savioli, M. & Medici, L. 2019: How much can we trust major element quantification in bioapatite investigation? *ACS Omega 4*, 17814–17822.

Martinsson, A. 1965: Phosphatic linings in bryozoan zooecia. *Geologiska Föreningen i Stockholm Förhandlingar 86*, 404–408.

McConnell, D. & Ward, P. 1978: Nautiloid uroliths composed of phosphatic hydrogel. *Science 199*, 208–209.

Medici, L., Malferrari, D., Savioli, M. & Ferretti, A. 2020: Mineralogy and crystallization patterns in conodont bioapatite from first occurrence (Cambrian) to extinction (end-Triassic). *Palaeogeography, Palaeoclimatology, Palaeoecology 549*, 109098.

Müller, K.J. 1959: Kambrische Conodonten. *Zeitschrift der Deutschen Geologischen Gesellschaft 111*, 434–485.

Müller, K.J. & Nogami, Y. 1972: Growth and function of conodonts. 24th International Geological Congress 7, Montreal, 20–27.

Müller, K.J., Nogami, Y. & Lenz, H. 1974: Phosphatische Ringe als Mikrofossilien im Altpaleozoikum. *Palaeontographica Abteilung A 146*, 79–99.

Murr, L.E. & Ramirez, D.A. 2012: The microstructure of the cultured freshwater pearl. *JOM Journal of the Minerals Metals and Materials Society 64*, 469–474.

Oakley, K.P. 1934: Phosphatic Calculi in Silurian Polyzoa. *Proceedings of the Royal Society of London. Series B Biological Sciences 116*, 296–314.

Oakley, K.P. 1966: Some Pearl-Bearing Ceramoporidae (Polyzoa). *Bulletin of the British Museum (Natural History). Geology 14*, 1–20.

Parkin, J. 1976: Silurian rocks of the Bull's Head, Annascaul and Derrymore Glen inliers, Co., Kerry. *Proceedings of the Royal Irish Academy Series B 76*, 577–606.

Pracht, M. 1996: *Geology Of Dingle Bay: A Geological Description to Accompany the Bedrock Geology 1:100,00 Map Series, Sheet 20, Dingle Bay, With Contributions By G. Wright, P. O'Connor, K. Claringbold & W.P. Warren*, 58 pp. Geological Survey of Ireland.

Schäffer, T.E., Ionescu-Zanetti, C., Proksch, R., Fritz, M., Walters, D.A., Almqvist, N., Zaremba, C.M., Belcher, A.M., Smith, B.L., Stucky, G.D., Morse, D.E. & Hansma, P.K. 1997: Does abalone nacre form by heteroepitaxial nucleation or by growth through mineral bridges? *Chemistry of Materials 9*, 1731–1740.

Serpagli, E. & Corradini, C. 1998: New taxa of *Kockelella* (Conodonta) from Late Wenlock-Ludlow (Silurian) of Sardinia. *Giornale di Geologia 60, Special Issue*, 79–83.

Siveter, D.J. 1989: Silurian trilobites from the Annascaul inlier, Dingle Peninsula, Ireland. *Palaeontology 32*, 109–161.

Stauffer, C.R. 1935: The conodont fauna of the Decorah Shale (Ordovician). *Journal of Paleontology 9*, 596–620.

Stauffer, C.R. 1940: Conodonts from the Devonian and associated clays of Minnesota. *Journal of Paleontology 14*, 417–435.

Sutton, M.D., Holmer, L.E. & Cherns, L. 2001: Small problematic phosphate sclerites from the Ordovician of Iapetus. *Journal of Paleontology 75*, 1–8.

Wang, K. & Chatterton, B.D.E. 1993: Microspherules in Devonian sediments: origins, geological significance, and contamination problems. *Canadian Journal of Earth Sciences 30*, 1660–1667.

Yin, H., Huang, S., Zhang, K., Yang, F., Ding, M., Bi, X. & Zhang, S. 1989: Volcanism at the Permian-Triassic boundary in South China and its effects on mass extinction. *Acta Geologica Sinica 63*, 169–181.

Youngquist, W. & Miller, A.K. 1948: Additional conodonts from the Sweetland Creek Shale of Iowa. *Journal of Paleontology 22*, 440–450.

Zhang, X.-S., Huang, C. & Gong, Y.-M. 2017: Late Devonian dimpled phosphatic microspherules associated with conodonts are possible otoliths of short-lived and opportunistic organisms. *Lethaia 50*, 486–494.

CHAPTER V

Bioapatite in time: dead, fossil or alive?

Like for previous chapters, below we summarize the results which are fully reported in Annex-6, a paper recently (March 2021) submitted for publication. Please see Annex-6 for further details.

As the last step of this thesis work (but not of this line of research) we considered living, dead and fossil apatite biomineralizing organisms, both vertebrates and invertebrates, ranging from the Cambrian to the Recent, a time-lapse spanning over 500 million years. We detected bioapatite crystal chemistry of the major phosphatic phyla (brachiopods, arthropods, bryozoans, and chordates: the latter including conodonts, cartilaginous and bony fishes, amphibians, reptiles, birds and mammals). Our aim was to explore the real effect of fossilization and diagenesis on bioapatite in different phyla over geological time.

We initially investigated recent phosphatic materials (dead and alive) so to exclude any diagenetic imprinting. Fresh or material exposed to up to 50 years of weathering was processed. We distinguished as well between *in-vivo* and *ex-vivo* bioapatite, to test if vital effect is able to affect the signal. In the following, we compared results with those detected from the fossil counterparts.
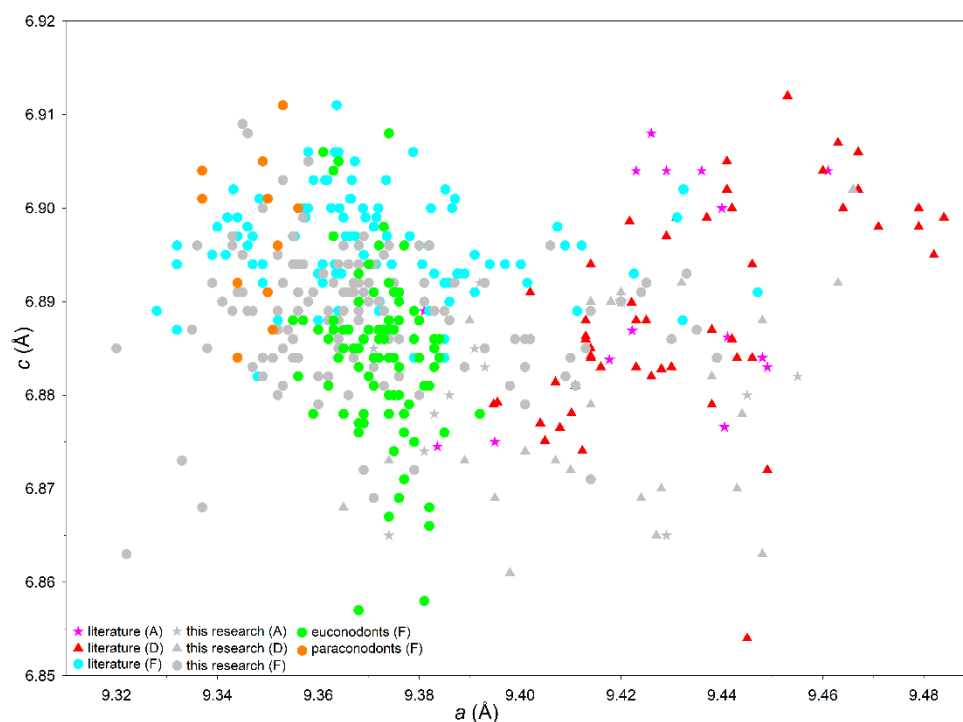
Fig. 5.1 - Binary plot of bioapatite crystallographic unit-cell parameters *c vs a* integrating our data with literature. In legend (F) denotes fossil material, (D/A) dead or alive material. Please see Annex-6 for references related to literature data.

We have found that the distribution of c versus a parameters denotes a general marked separation between fossil and non-fossil (dead/alive) material, being fossil bioapatite characterized by lower values of the cell parameter a. Cell parameter c appears to be more stable. The distinction between fossil and dead/alive bioapatite cell parameters gets even more evident when we integrate our data with measurements derived from literature (Fig. 5.1). Fossil bioapatite, again, clusters in the left part of the diagram, with a values significantly lower, and dead/alive bioapatite occupies the right part of the plot, with higher values of a.

It is necessary to light up that not all the taxonomic groups gave the same response. For example, cell parameters of mammals from fossil and recent samples greatly overlap, in particular if they derive from teeth enamel. This tissue is very hard and scarcely porous and has high crystallinity and low organic matter content. As a consequence, teeth enamel is less affected by fossilization-related isomorphic substitution and better preserves the original cell dimension (high a values) of bioapatite. On the opposite, dentin and bones in living animals are more porous, less crystalline and have a higher content of organic matter which, decomposing, leaves exposed the inorganic tissue increasing the incorporation of carbon into the bioapatite framework during fossilization and re-crystallization (*Trueman et al., 2008*; *Keenan et al., 2015*; *Medici et al., 2021*). The reduction of a cell parameter dimension is mostly due to the tetrahedral $(CO_3)^{2-}$ for $(PO_4)^{3-}$ substitutions, being the ionic radius of C^{4+} smaller than that of P^{5+}.

ANNEX-6

Dead, Fossil or Alive: bioapatite diagenesis and fossilization

Annalisa Ferretti, Luca Medici, Martina Savioli, Maria Teresa Mascia & Daniele Malferrari

Submitted

Palaeogeography, Palaeoclimatology, Palaeoecology

Dead, Fossil or Alive: bioapatite diagenesis and fossilization

--Manuscript Draft--

Abstract:	Calcium carbonate, silica and calcium phosphate have been selectively used by organisms in the production of mineralized hard parts throughout the Phanerozoic. Among these materials, bioapatite has enabled fundamental acquisitions in the evolution of life. Despite the remarkable biological success, the crystallography of bioapatite and the eventual modification of lattice parameters over a wide range of geologic time have in contrast been scarcely investigated. In our study we analyzed living, dead and fossil remains of apatite biomineralizing organisms, both vertebrates and invertebrates, ranging from the Cambrian to the Recent, a time-lapse spanning over 500 million years. We detected the bioapatite crystal features of the major phosphatic phyla (Brachiopoda, Arthropoda, Bryozoa, and Chordata: the latter including conodonts, cartilaginous and bony fishes, amphibians, reptiles, birds and mammals). Groups were investigated using either fossil or recent material (dead and alive, the latter referring to material extracted from living organisms). Our study reveals that living and dead organisms, and their fossil remains, have a distinct geometric signature in terms of bioapatite lattice cell parameters mirroring atom re-arrangements within the crystal lattice which drive to a general reduction of the cell volume (i.e., the volume of the hexagonal crystalline cell frame) over time. These changes initiate at the death of the organism, and attain overall stability only in the ultimate stages of fossilization.

Suggested Reviewers:	Živilė ŽIGAITĖ Uppsala University: Uppsala Universitet zivile.zigaite@ebc.uu.se specialist in chemical composition and structure of conodont elements
	Manuel RIGO University of Padua: Universita degli Studi di Padova manuel.rigo@unipd.it specialist in conodont geochemistry and paleoclimatology
	Andrey V. ZHURAVLEV Institute of Geology Komi Scientific Centre of the Ural Branch of the Russian Academy of Sciences: Institut geologii Komi naucnogo centra Ural'skogo otdelenia Rossijskoj akademii nauk micropalaeontology@gmail.com specialist in bioapatite ultrastructure
	Sarah W. KEENAN South Dakota School of Mines and Technology Sarah.Keenan@sdsmt.edu

	specialist in bioapatite diagenesis and fossilization
	Gianfranco ULIAN University of Bologna: Universita di Bologna gianfranco.ulian2@unibo.it expert in microscopic methods, bioapatite crystallography and mineralogy
Opposed Reviewers:	

Consiglio Nazionale delle Ricerche
Istituto di Metodologie per l'Analisi Ambientale

imaa

Dear Editor-in-Chief,

I am pleased to submit a manuscript entitled:

"**Dead, Fossil or Alive: bioapatite diagenesis and fossilization**"
by Annalisa Ferretti, Luca Medici, Martina Savioli, Maria Teresa Mascia and Daniele Malferrari

This manuscript presents a novel in-depth study of bioapatite in living, dead and the fossil remains of apatite biomineralizing organisms, both vertebrates and invertebrates, in a time-lapse spanning over 500 million years, using a multi-analytical (chemical, microscopic and diffractometric) and interdisciplinary (crystallography and paleontology) approach. We discovered that the bioapatite spatial arrangement within a common hexagonal crystal cell undergoes re-modeling over time of the basal crystallographic cell frame with a general reduction of the cell volume, mirroring chemical variations. We demonstrate that these changes start at the death of the organism and reach an overall stability only in the later stages of fossilization.

We are confident that our methodology and findings can also be applied globally across diverse geological disciplines, ages and environments as our study suggests caution regarding the use of bioapatite as a geochemical tracer without prior investigation of the fossilization/diagenetic overprinting. We consider therefore that publication of these exciting results in *Palaeogeography, Palaeoclimatology, Palaeecology* will ensure their diffusion among a broad audience and thus will facilitate the use of this approach in promoting further studies within many disciplinary fields.

All the authors have reviewed and approved this submission and confirm that this manuscript is not under consideration for publication elsewhere nor have its contents been published previously. In order to meet the standards required the English of the manuscript has been revised by a professional native English-speaking geoscientific editor.

A list of potential reviewers is reported below and has been submitted.

1) **Živilė ŽIGAITĖ**, Department of Organismal Biology, Uppsala University, Norbyv. 18A, 752 36 Uppsala, Sweden: zivile.zigaite@ebc.uu.se (specialist in chemical composition and structure of conodont elements);
2) **Manuel RIGO**, Department of Geosciences, University of Padua, Via Gradenigo 6, 35131 Padua, Italy: manuel.rigo@unipd.it (specialist in conodont geochemistry and paleoclimatology);
3) **Andrey V. ZHURAVLEV**, Institute of Geology Komi SC, UrB RAS, Pervomayskaya 54, 167000 Syktyvkar, Russia: micropalaeontology@gmail.com (specialist in bioapatite ultrastructure);
4) **Sarah W. KEENAN**, Department of Geology and Geological Engineering, South Dakota School of Mines and Technology, Rapid City, South Dakota, United States of America: Sarah.Keenan@sdsmt.edu (specialist in bioapatite diagenesis and fossilization);
5) **Gianfranco ULIAN**, Department of Biological, Geological and Environmental Sciences, University of Bologna, Italy: gianfranco.ulian2@unibo.it (expert in microscopic methods, bioapatite crystallography and mineralogy).

Thank you very much for your consideration.

Best regards,

Luca Medici

Potenza, 19/03/2021
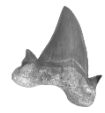
Dead, fossil or alive: bioapatite diagenesis and fossilization

Annalisa Ferretti, Luca Medici, Martina Savioli, Maria Teresa Mascia, Daniele Malferrari

Highlights

- Bioapatite crystallographic cell parameters c and a are variable.
- Cell parameters of fossils differ from cell parameters of dead and alive material.
- Bioapatite crystallographic cell volume reduces during diagenesis and fossilization.
- Volume reduction occurs in the first million years.

1   Dead, fossil or alive: bioapatite diagenesis and fossilization

2   Annalisa Ferretti[a], Luca Medici[b,*], Martina Savioli[a], Maria Teresa Mascia[c], Daniele

3   Malferrari[a]

4

5   *[a]Department of Chemical and Geological Sciences, University of Modena and Reggio*

6   *Emilia, Via Campi 103, I-41125 Modena, Italy*

7   *[b]National Research Council of Italy, Institute of Methodologies for Environmental*

8   *Analysis, C.da S. Loja–Zona Industriale, I–85050 Tito Scalo, Potenza, Italy*

9   *[c]Department of Maternal-Child and Adult Medical and Surgical Sciences, University of*

10   *Modena and Reggio Emilia, Via del Pozzo 71, I–41125 Modena, Italy*

11

12   * Corresponding author.

13   *E-mail addresses:* ferretti@unimore.it (A. Ferretti), luca.medici@imaa.cnr.it (L. Medici),

14   martina.savioli@unimore.it (M. Savioli), mariateresa.mascia@unimore.it (M.T. Mascia),

15   daniele.malferrari@unimore.it (D. Malferrari).

16

17   *Key words:* Calcium phosphate, skeletal material, fossil, unit cell parameters,

18   crystallography.

19

20   **Highlights**

21   •   Bioapatite crystallographic cell parameters c and a are variable.

22   •   Cell parameters of fossils differ from cell parameters of dead and alive material.

23 •   Bioapatite crystallographic cell volume reduces during diagenesis and

24 fossilization.

25 •   Cell volume reduction occurs in the first million years.

26

27 **ABSTRACT**

28

29 Calcium carbonate, silica and calcium phosphate have been selectively used by

30 organisms in the production of mineralized hard parts throughout the Phanerozoic.

31 Among these materials, bioapatite has enabled fundamental acquisitions in the evolution

32 of life. Despite the remarkable biological success, the crystallography of bioapatite and

33 the eventual modification of lattice parameters over a wide range of geologic time have in

34 contrast been scarcely investigated.

35   In our study we analyzed living, dead and fossil remains of apatite biomineralizing

36 organisms, both vertebrates and invertebrates, ranging from the Cambrian to the Recent, a

37 time-lapse spanning over 500 million years. We detected the bioapatite crystal features of

38 the major phosphatic phyla (Brachiopoda, Arthropoda, Bryozoa, and Chordata: the latter

39 including conodonts, cartilaginous and bony fishes, amphibians, reptiles, birds and

40 mammals). Groups were investigated using either fossil or recent material (dead and

41 alive, the latter referring to material extracted from living organisms). Our study reveals

42 that living and dead organisms, and their fossil remains, have a distinct geometric

43 signature in terms of bioapatite lattice cell parameters mirroring atom re-arrangements

44 within the crystal lattice which drive to a general reduction of the cell volume (i.e., the

45 volume of the hexagonal crystalline cell frame) over time. These changes initiate at the

2

46 death of the organism, and attain overall stability only in the ultimate stages of

47 fossilization.

48

49 **1. Introduction**

50

51   Bioapatite has facilitated the evolution of living organisms for over five hundred

52 million years. In utilizing calcium phosphate minerals, animals learnt how to construct

53 new body architectures with a rigid skeletal frame, to shelter soft body parts from

54 predation within a shell, to defend themselves from attack with menacing weapons, and

55 to process food with teeth. By the use of efficient structural designs that optimized

56 mechanical properties through a combination of evolutionary processes and functional

57 adaptations, bioapatite has enabled vertebrates to acquire large body sizes in the sea, on

58 land and in the air.

59   Vertebrates opted for apatite to mineralize teeth and bones from the first appearance of

60 the group (Pasteris et al., 2008; Georgiadis et al., 2016), but phosphate was in use also in

61 the invertebrates such as the Small Shelly Faunas that developed at the

62 Precambrian/Cambrian transition and represented the 'first major appearance of hard

63 skeletal material in the fossil record, some 10 myr before the first trilobite evolved'

64 (Benton and Harper, 2020, p. 294).

65   The reorganization of aragonite within the more stable isomorph calcite during

66 diagenesis is well documented and the mechanisms involved have been widely described

67 in precise detail. On the contrary, recent researches (e.g., Keenan, 2016; Emmons et al.,

68 2020) have indicated that bioapatite is far from being a stable mineralogical form, and our

3

69 knowledge with respect to bioapatite transformation is still biased by several uncertainties

70 and gaps in the scientific dataset (Keenan et al., 2015).

71   (Bio)apatite crystallizes within a hexagonal system with crystallographic cell

72 parameters a and c outlining the geometry of the crystal lattice in three dimensions

73 (Brigatti et al., 2004). Cell parameter a, equal to b, defines the base of the

74 crystallographic cell, while cell parameter c measures its height (Fig. 1). In vivo,

75 bioapatite consists of inorganic mineral fractions with interlayered organic components.

76 This configuration may be subject to frequent modification triggered by biostratinomic

77 processes and diagenesis that produce isomorphic iso- and hetero-valent substitutions

78 occurring at the various coordination sites (Medici et al., 2020), so as to justify the

79 nickname 'Nature's trashcan', a term often used when referring to bioapatite.

80   Silurian monospecific associations of conodonts, an extinct group of jawless

81 vertebrates, had highlighted variation in the a/c ratio of nanocrystallites and of their

82 ordering (mosaicity) (Shohel et al., 2020). In general, such changes have been attributed

83 to ontogeny and element positioning within the conodont apparatus, and these findings

84 suggest caution regarding the use of bioapatite as a palaeoceanographic tracer within

85 geochemical investigations. Furthermore, overgrowths of diagenetic bioapatite crystals

86 upon conodont elements were observed to have the same crystallographic signature as the

87 conodont elements (Ferretti et al., 2017), emphasizing and again suggesting caution with

88 respect to an additional role played by diagenesis.

89

90   In this paper we detect bioapatite crystallographic cell parameters in phosphate

91 mineralizing organisms of different age (Cambrian to Recent), and compare data

92 resulting from fossil and recent material (dead and alive). Aim of the comparison is to

93 detect any possible interference of fossilization and diagenesis on bioapatite crystal lattice

94 configuration.

95

96 **2. Material and methods**

97

98 *2.1. Material under investigation*

99

100 Based on an extremely heterogeneous sampling dataset covering the major phosphatic

101 phyla (Brachiopoda, Arthropoda, Bryozoa and Chordata – more specifically conodonts,

102 cartilaginous and bony fishes, amphibians, reptiles, birds and mammals), we analyzed

103 material consisting of living, dead and fossil phosphatic remains ranging in age from the

104 Cambrian to the Recent (see Table S1 for a detailed list). In order to explore the true

105 effect of diagenesis, we examined recent phosphatic materials so as to exclude diagenetic

106 imprinting. Fresh and dead phosphatic biomaterial, exposed for up to 50 years of

107 weathering, was processed. We distinguished in this way between in-vivo and ex-vivo

108 bioapatite, to test whether vital effects impacted the signal. We then compared these

109 results with findings detected from the fossil counterparts.

110

111 *2.2. Analytical methods and approach*

112

113 We applied in this study a consolidated protocol of analyses (Ferretti et al., 2017,

114 2020; Medici et al., 2020, 2021) integrating optical and scanning electron microscopy

115 coupled with chemical microanalyses (ESEM-EDX and SEM-EDS) and micro X-ray

116 diffraction (μ-XRD).

117   Microscopy was used for the preliminary selection and characterization of the

118 samples; for example, samples with an evident pattern of re-crystallization as well as

119 bearing diffuse chemical impurities were discarded even if they appeared to be well

120 preserved. After that, μ-XRD was applied to gain the bioapatite cell parameters, which

121 are the smallest repeating units having the full symmetry of the crystal structure.

122 Utilization of a micro X-ray diffractometer (see below for a detailed description) allows

123 the detection of structural properties of the material, such as mineralogical composition of

124 the crystalline phases, degree of crystallinity, size of crystallites, preferential orientation,

125 etc., as do standard powder diffractometers, but with the advantage of being non-

126 destructive and of processing very small portions of the sample and, thus, also facilitating

127 study of small-sized specimens.

128

129 *2.3. Instrument and experimental conditions*

130

131   Au-coated and non-coated phosphatic remains were observed using an Environmental

132 Scanning Electron Microscope FEI ESEM-Quanta 200, equipped with the Oxford EDX

133 INCA 300 X-ray energy dispersive spectrometer and by a Scanning Electron Microscope

134 Nova NanoSEM FEI 450 equipped with a X-EDS Bruker QUANTAX-200 detector.

135 Measurements were performed on Au-coated samples mounted on aluminum stubs

136 previously covered with carbon-conductive adhesive tape. ESEM-EDX observation were

137 in high and low vacuum (low vacuum brackets 1 and 0.5 Torr) with an accelerating

6

138 voltage between 5 and 25 keV for imaging and between 5 and 15 keV for elemental

139 analyses. SEM-EDS observations were in high vacuum with an accelerating voltage

140 between 15 and 25 keV both for imaging and elemental analyses.

141

142   A Rigaku D-max Rapid microdiffractometer was used to obtain X-ray diffraction

143 patterns by non-destructive procedures. This instrument operates at 40 kV and 30 mA and

144 is equipped with a Cu*K*α source, curved-image-plate detector, flat graphite

145 monochromator, variety of beam collimators, motorized stage and microscope for

146 accurate positioning of the sample. Data were measured in reflection mode using various

147 sample-to-beam geometries and operating conditions. Specimens were mounted on small

148 plane surfaces and analyzed with 0.3 mm collimator (collection time: 10 min). X-ray

149 diffraction data were measured as two-dimensional images and converted into I-2θ

150 profiles using the Rigaku R-AXIS Display software. Mineralogical data were refined

151 using UnitCell software (Holland and Redfern, 1997).

152

153   SEM/ESEM microscopy analyses were performed at the Scientific Instruments

154 Facility (CIGS) of the University of Modena and Reggio Emilia (Modena, Italy), whereas

155 μ-XRD measurements were made at the Institute of Methodologies for Environmental

156 Analysis of the National Research Council of Italy of Tito Scalo (Potenza, Italy).

157

158 **3. Results**

159

Cell parameters measure and calculation was firstly applied to conodonts (Ferretti et al., 2020; Medici et al., 2020) across their full stratigraphic range (late Cambrian to Late Triassic). The experimental results revealed that bioapatite cell parameter a is significantly higher for euconodonts (a = 9.355÷9.392 Å) than for paraconodonts (a = 9.337÷9.356 Å); however, age, provenance and position of the conodont element within the animal apparatus did not appear to influence the basic cell geometry.

The variability of unit cell parameters a and c for all the analyzed material (dead, fossil and alive) is shown in Fig. 2 which sums up the response of all the investigated groups. The signal deriving from still living organisms (alive) is hardly detectable due to the low crystallinity of the bioapatite. The bioapatite crystallographic signature becomes more visible as a result of amplification due to death and fossilization. The distribution of c versus a parameters denotes a general marked separation between fossil and non-fossil (dead/living) material, fossil bioapatite being characterized by lower values of the cell parameter a (a = 9.320÷9.439 Å for fossil bioapatite, a = 9.355÷9.466 Å for dead/living material). Cell parameter c appears to be more stable in dead, fossil and living material (c = 6.857÷6.911 Å for fossil bioapatite, c = 6.861÷6.902 Å for dead/living material).

The distinction between fossil and dead/living organism bioapatite cell parameters is emphasized on integration of our data with measurements derived from literature (Fig. 3; Table S2). Fossil bioapatite, as in previous analyses, forms clusters in the left part of the diagram, with values a being significantly lower while dead/living organism bioapatite occupies the right part of the plot, i.e., higher values of a.

Despite the findings above, the response of single taxonomic groups is not uniform, with mammals and cartilaginous fishes deviating somewhat from the rule. Bioapatite

183 crystallographic cell parameters partially overlap for fossil (a = 9.339÷9.439 Å, c =

184 6.869÷6.894 Å, cell volume = 520.6÷531.3 Å^3) and recent (a = 9.374÷9.455 Å, c =

185 6.865÷6.892 Å, cell volume = 522.4÷532.8 Å^3) mammals. In particular, this behavior is

186 highlighted by mammal teeth enamel where fossil materials (a = 9.424÷9.439 Å, c =

187 6.884÷6.891 Å, cell volume = 530.0÷531.1 Å^3) show only slightly lower a parameters

188 and cell volumes with respect to the recent samples (a = 9.439÷9.455 Å, c = 6.880÷6.884

189 Å, cell volume = 531.2÷532.8 Å^3). As regards the cartilaginous fishes, the oldest fossil

190 material again forms clusters at lower a values; nonetheless some a values obtained by

191 the analyses of teeth enamel of fossil (a = 9.366÷9.386 Å, c = 6.872÷6.896 Å, cell

192 volume = 522.4÷525.7 Å^3) and recent (a = 9.355÷9.393 Å, c = 6.868÷6.881 Å, cell

193 volume = 521.6÷526.0 Å^3) bioapatite appear to overlap.

194

195 **4. Discussion**

196

197   The explanation for a partial overlap of bioapatite crystallographic cell parameters for

198 fossil and recent mammals and, likewise, for the fairly 'deviation from the rule' of

199 cartilaginous fish teeth, lies in the physical and chemical features of teeth enamel. Enamel

200 is a very hard tissue with a low degree of porosity, high crystallinity and low organic

201 matter content (Combes et al., 2016). As a consequence, enamel is less affected by

202 fossilization-related isomorphic substitutions and better preserves the original bioapatite

203 crystal cell. In contrast, dentin and bones in living mammals are more porous, less

204 crystalline and have a higher content of organic matter whose decomposition involves the

205 incorporation of carbon, i.e., $(CO_3)^{2-}$, into the bioapatite framework, triggering a

206   biostratinomic/fossilization (re)crystallization (Trueman et al., 2008; Keenan et al., 2015;

207   Margariti et al., 2019; Medici et al., 2021). In this context, the reduction of the cell

208   parameter a is mostly due to tetrahedral $(CO_3)^{2-}$ for $(PO_4)^{3-}$ substitutions, as the ionic

209   radius of C^{4+} is smaller than that of P^{5+} (McLellan and Lehr, 1969). Anionic substitutions

210   of $(CO_3)^{2-}$ for $(OH)^-$ and F^- may also occur (Wopenka and Pasteris, 2005), but less

211   affecting cell dimension changes (Pan and Fleet, 2002).

212   In order to account for the role played by time in the structural reorganization of the

213   bioapatite framework, we calculated and plotted the cell volume of each sample vs time

214   (Fig. 4). What emerges clearly is that the volumes of the bioapatite cells in recent

215   (dead/living) and fossil materials are strongly variable, ranging from 521.7 to 535.6 Å^3

216   and 516.5 to 531.3 Å^3, respectively, indicating in general a reduction of the bioapatite cell

217   volumes of the fossil materials. However, distinction between recent and fossil material

218   becomes unclear when trying to state unequivocally the precise moment in which volume

219   reduction exactly starts. Based on rates of uptake and exchange, fossilization likely

220   occurs on timescales ranging from thousands to tens of thousands of years (Millard and

221   Hedges, 1996; Kohn and Law, 2006), although transformations of bone during the early

222   diagenetic period immediately following host death suggest changes may occur even

223   earlier (Keenan et al., 2015; Keenan, 2016).

224   Despite the major progress made towards evaluating composition, structure, and

225   mechanisms of preservation of bones, teeth and shells, there are still significant gaps in

226   our understanding of the process of fossilization and diagenesis of bioapatite material.

227   This study proves that bioapatite transforms after death of the organism. The large

228   variability of the material analyzed herein in terms of taxonomy, environmental and

229 geographical provenance has unraveled a separate fossilization/diagenetic overprinting

230 upon primary bioapatite crystal-chemistry that should be regarded unaffected by site-

231 specific geochemistry (Keenan, 2016) and, consequently, be regarded in terms of a global

232 trend.

233

234 **5. Conclusions**

235   This research presents a novel in-depth study of bioapatite in living, dead and the

236 fossil remains of apatite biomineralizing organisms, both vertebrates and invertebrates,

237 over a time-lapse spanning over 500 million years, using a multi-analytical (chemical,

238 microscopic and diffractometric) and interdisciplinary (crystallographic and

239 paleontologic) approach. Our data reveal that crystallographic cell parameters calculated

240 for fossils significantly differ from those derived for living material. In fact, fossil

241 organisms bear smaller cell parameters a and cell volumes. We discovered that the

242 bioapatite spatial arrangement within a common hexagonal crystal cell undergoes re-

243 modeling over time of the basal crystallographic cell frame with a general reduction of

244 the cell volume, mirroring chemical variations. These changes start at the death of the

245 organism and reach an overall stability only in the later stages of fossilization.

246

258

259   Author contributions

260   A.F., L.M. and D.M. conceived, designed and supervised the research. L.M.

261   performed microdiffraction experiments. A.F., M.S. and M.T.M. performed SEM/ESEM

262   studies. D.M. and M.S. carried out ICPM-LS investigation. A.F. wrote the paper with

263   contributions from all the authors. All authors gave final approval for publication.

264

265   References

266   Beckett S., Rogers K.D., Clement J.G., 2011. Inter- species variation in bone mineral

267   behavior upon heating. J. Forensic Sci. 56, 571–579. doi: 10.1111/j.1556-

268   4029.2010.01690.x

269   Benton M.J., Harper D.A.T., 2020. Introduction to Paleobiology and the Fossil Record.

270   John Wiley and Sons Ltd, United States, 642 pp.

271   Brigatti M.F., Malferrari D., Medici L., Ottolini L., Poppi L., 2004. Crystal Chemistry of

272   Apatites from the Tapira carbonatite complex, Brazil. Eur. J. Mineral. 16, 677–685.

273   doi: 10.1127/0935-1221/2004/0016-0677

274   Chakraborty S., Bag S., Pal S., Mukherjee, A.K., 2006. Structural and microstructural

275   characterization of bioapatites and synthetic hydroxyapatite using X-ray powder

276   diffraction and Fourier transform infrared techniques. J. Appl. Crystallogr. 39, 385–

277   390. doi: 10.1107/S0021889806010351

278   Combes C., Cazalbou S., Rey C., 2016. Apatite Biominerals. Minerals 6, 34. doi:

279   10.3390/min6020034

280   Emmons A.L., Mundorff A.Z., Keenan S.W., Davoren J., Andronowski J., Carter D.O.,

281   Debruyn J.M., 2020. Characterizing the postmortem human bone microbiome from

282   surface-decomposed remains. PLoS ONE, e0218636. doi:

283   10.1371/journal.pone.0218636

284   Ferretti A., Malferrari D., Medici L., Savioli M., 2017. Diagenesis does not invent

285   anything new: Precise replication of conodont structures by secondary apatite. Sci.

286   Rep. **7**, 1624–1632. doi: 10.1038/s41598-017-01694-4

287   Ferretti A., Malferrari D., Savioli M., Siepe T., Medici L., 2020. 'Conodont pearls' do not

288   belong to conodonts. Lethaia. doi: 10.1111/let.12403

289   Ferretti A., Messori A., Bergström, S.M., 2014. Composition and significance of the

290   Katian (Upper Ordovician) conodont fauna of the Vaux Limestone ('Calcaire des

291   Vaux') in Normandy, France. Estonian J. Earth Sci. 63, 214–219. doi:

292   10.3176/earth.2014.21

293   Georgiadis M., Müller R., Schneider P., 2016. Techniques to assess bone ultrastructure

294   organization: orientation and arrangement of mineralized collagen fibrils. J. R. Soc.

295   Interface 13, 20160088. doi: 10.1098/rsif.2016.0088

296   Gilinskaya L.G., Grigorieva T.N., Okuneva G.N., Vlasov Y.A., 2003. Investigation of

297   pathogenic mineralization on human heart valves. 1. Chemical and phase composition.

298   J. Struct. Chem. 44, 622–631. doi: 10.1023/B:JORY.0000017938.42883.9f

299   Holland T.J.B., Redfern S.A.T., 1997. Unit cell refinement from powder diffraction data:

300   the use of regression diagnostics. Mineral. Mag. 61, 65–77. doi:

301   10.1180/minmag.1997.061.404.07

302   Kallaste T., Nemliher J., 2005. Apatite varieties in extant and fossil vertebrate

303   mineralized tissues. J. Appl. Crystallogr. 38, 587–594. doi:

304   10.1107/S0021889805011404

305   Keenan S.H., 2016. From bone to fossil: A review of the diagenesis of bioapatite. Am.

306   Min. 101, 1943–1951. doi: 10.2138/am-2016-5737

307   Keenan S.H., Engel A.S., Roy A., Bovenkamp-Langlois G.L., 2015. Evaluating the

308   consequences of diagenesis and fossilization on bioapatite lattice structure and

309   composition. Chem. Geol. 413, 18–27. doi: 10.1016/j.chemgeo.2015.08.005

310   Kohn M.J., Law J.M., 2006. Stable isotope chemistry of fossil bone as a new

311   paleoclimate indicator. Geochim. Cosmochim. Acta 70, 931–946. doi:

312   10.1016/j.gca.2005.10.023

313   Lang L., Kirsimäe K., Vahur S., 2016. Diagenetic fate of bioapatite in linguliform

314   brachiopods: multiple apatite phases in shells of Cambrian lingulate brachiopod

315   *Ungula ingrica* (Eichwald). Lethaia 49, 13–27. doi: 10.1111/let.12127

316   Lonardelli I., Wenk H.-R., Lutterotti L., Goodwin M., 2005. Texture analysis from

317   synchrotron diffraction images with the Rietveld method: dinosaur tendon and salmon

318   scale. J. Synchrotron Rad. 12, 354–360. doi: 10.1107/S090904950500138X

319   Margariti E., Stathopoulou E.T., Sanakis Y., Kotopoulou E., Pavlakis P., Godelitsas A.,

320   2019. A geochemical approach to fossilization processes in Miocene vertebrate bones

321   from Sahabi, NE Libya. J. Afr. Earth Sci. 149, 1–18. doi:

322   10.1016/j.jafrearsci.2018.07.019

323   McClellan G.H., Lehr J.R., 1969. Crystal chemical investigation of natural apatites. Am.

324   Min. 54, 1374–1391.

325   Medici L., Malferrari D., Savioli M., Ferretti A., 2020. Mineralogy and crystallization

326   patterns in conodont bioapatite from first occurrence (Cambrian) to extinction (end-

327   Triassic). Palaeogeogr. Palaeoclimatol. Palaeoecol. 549, 109098. doi:

328   10.1016/j.palaeo.2019.02.024

329   Medici L., Savioli M., Ferretti A., Malferrari D., 2021. Zooming in REE and other trace

330   elements on conodonts: Does taxonomy guide diagenesis? J. Earth Sci. doi:

331   10.1007/s12583-020-1094-3

332   Meneghini C., Dalconi M.C., Nuzzo S., Mobilio S., Wenk R.H., 2003. Rietveld

333   refinement on X-ray diffraction patterns of bioapatite in human fetal bones. Biophys.

334   J. 84, 2021–2029. doi: 10.1016/S0006-3495(03)75010-3

335   Millard A.R., Hedges R E.M., 1996. A diffusion-adsorption model of uranium uptake by

336   archaeological bone. Geochim. Cosmochim. Acta 60, 2139–2152. doi: 10.1016/0016-

337   7037(96)00050-6

338   Nemliher J G., Baturin G.N., Kallaste T.E., Murdmaa I.O., 2004. Transformation of

339   hydroxyapatite of bone phosphate from the ocean bottom during fossilization. Lithol.

340   Miner. Resour. 39, 468–479. doi: 10.1023/B:LIMI.0000040736.62014.2d

341   Pan, Y.M., Fleet M.E., 2002. Compositions of the apatite-group minerals: substitution

342   mechanisms and controlling factors. Rev. Mineral. Geochem. 48, 13–49. doi:

343   10.2138/rmg.2002.48.2

344   Pasteris J.D., Wopenka B., Valsami-Jones E., 2008. Bone and tooth mineralization: why

345   apatite? Elements 4, 97–104. doi: 10.2113/GSELEMENTS.4.2.97

346   Piga G., Baró M.D., Golvano Escobal I., Gonçalves D., Makhoul C., Amarante A.,

347   Assumpció Malgosa A., Enzo S., Garroni S., 2016. A structural approach in the study

348   of bones: fossil and burnt bones at nanosize scale. Appl. Phys. A 122, 1031. doi:

349   10.1007/s00339-016-0562-1

350   Piga G., Santos-Cubedo A., Moya Solà S., Brunetti A., Malgosa A., Enzo S., 2009. An

351   X-ray diffraction (XRD) and X-ray fluorescence (XRF) investigation in human and

352   animal fossil bones from Holocene to Middle Triassic. J. Archaeol. Sci. 36, 1857–

353   1868. doi: 10.1016/j.jas.2009.04.013

354   Shohel M., McAdams N.E.B., Cramer B.D., Forbes T.Z., 2020. Ontogenetic variability in

355   crystallography and mosaicity of conodont apatite: implication for microstructure,

356   palaeothermometry and geochemistry. R. Soc. Open Sci. 7, 200322. doi:

357   10.1098/rsos.200322

358   Trueman C.N., Privat K., Field J., 2008. Why do crystallinity values fail to predict the

359   extent of diagenetic alteration of bone mineral? Palaeogeogr. Palaeoclimatol.

360   Palaeoecol. 266, 160–167. doi: 10.1016/j.palaeo.2008.03.038

361   Wei S.S., Tian Y.P., Li H., Guo L.H., 2007. In Situ Micro-XRD Structure Analysis of

362   Bioapatite in Human Ribs. Key Eng. Mater. 330-332, 11–14. doi:

363   10.4028/www.scientific.net/KEM.330-332.11

364 Wopenka B., Pasteris J.D., 2005. A mineralogical perspective on the apatite in bone.

365   Mater. Sci. Eng. C 25, 131–143. doi: 10.1016/j.msec.2005.01.008

366

CAPTION TO FIGURES

369   Fig. 1. Bioapatite at different hierarchical levels. SEM image of conodont element

370   *Icriodella* sp., displaying the overgrowth of bioapatite neo-crystals. Late Ordovician,

371   Normandy, France (after Ferretti et al., 2014). Scale bar corresponds to 100 μm. Round

372   inserts are details illustrating a single crystal of bioapatite (yellow; scale bars correspond

373   to 10 μm). At a lower hierarchical level, bioapatite ultrastructure reveals a network

374   formed of single crystallographic cells. Larger round insert: sketch of the bioapatite

375   hexagonal crystal cell framework (dotted lines) displaying cell parameters *a*, *b* and *c*

376   being *a=b*.

377

378   Fig. 2. Variability of bioapatite cell parameters within the main phyla of phosphatic taxa

379   analyzed in this paper. Binary plot of bioapatite crystallographic unit-cell parameters *c* vs

380   *a* for fossil, dead or alive material. Colours indicate different taxa, symbols refer to fossil

381   (F; circle), dead (D; triangle) and alive (A; star) material (see legend at the bottom).

382

383   Fig. 3. Variability of bioapatite cell parameters. Binary plot of bioapatite crystallographic

384   unit-cell parameters *c* vs *a* integrating data from this study (grey symbols) with those

385   from literature (Gilinskaya et al., 2003; Meneghini et al., 2003; Nemliher et al., 2004;

386   Kallaste and Nemliher, 2005; Lonardelli et al., 2005; Chakraborty et al., 2006; Wei et al.,

387   2007; Piga et al., 2009, 2016; Beckett et al., 2011; Lang et al., 2016: coloured symbols).

388   Data on conodonts are from Ferretti et al., 2020 and Medici et al., 2020. Symbols refer to

389   fossil (F; circle), dead (D; triangle) and alive (A; star) material (see legend at the bottom).

390   For major detail on literature data, see Table S2.

391

392   Fig. 4. Variability of bioapatite cell volume in time. Dashed vertical lines indicate the

393   boundary between Eras (below, a magnification addressed to the Cenozoic). For symbols,

394   refer to legends in Figs 2 and 3. Full symbols: this research; open symbols: data derived

395   from literature.

396

397   **TABLE S1.** Taxa analyzed in the present paper and from our past research (after Ferretti

398   et al., 2020 and Medici et al., 2020).

399

400   **TABLE S2.** Taxa analyzed from literature.
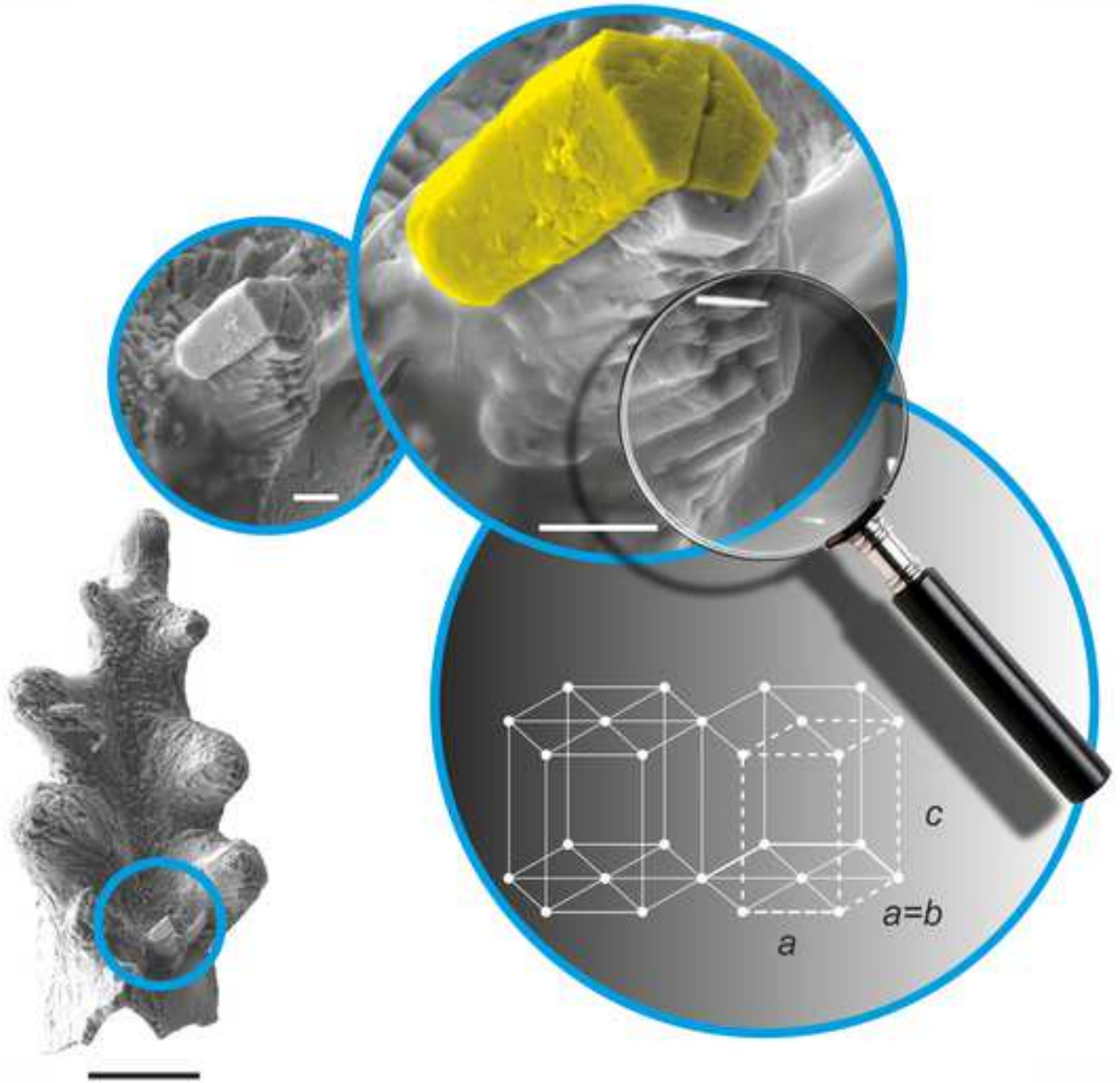
Figure 1

Figure 2   Click here to access/download;Figure;Figure 2.TIF ⬇
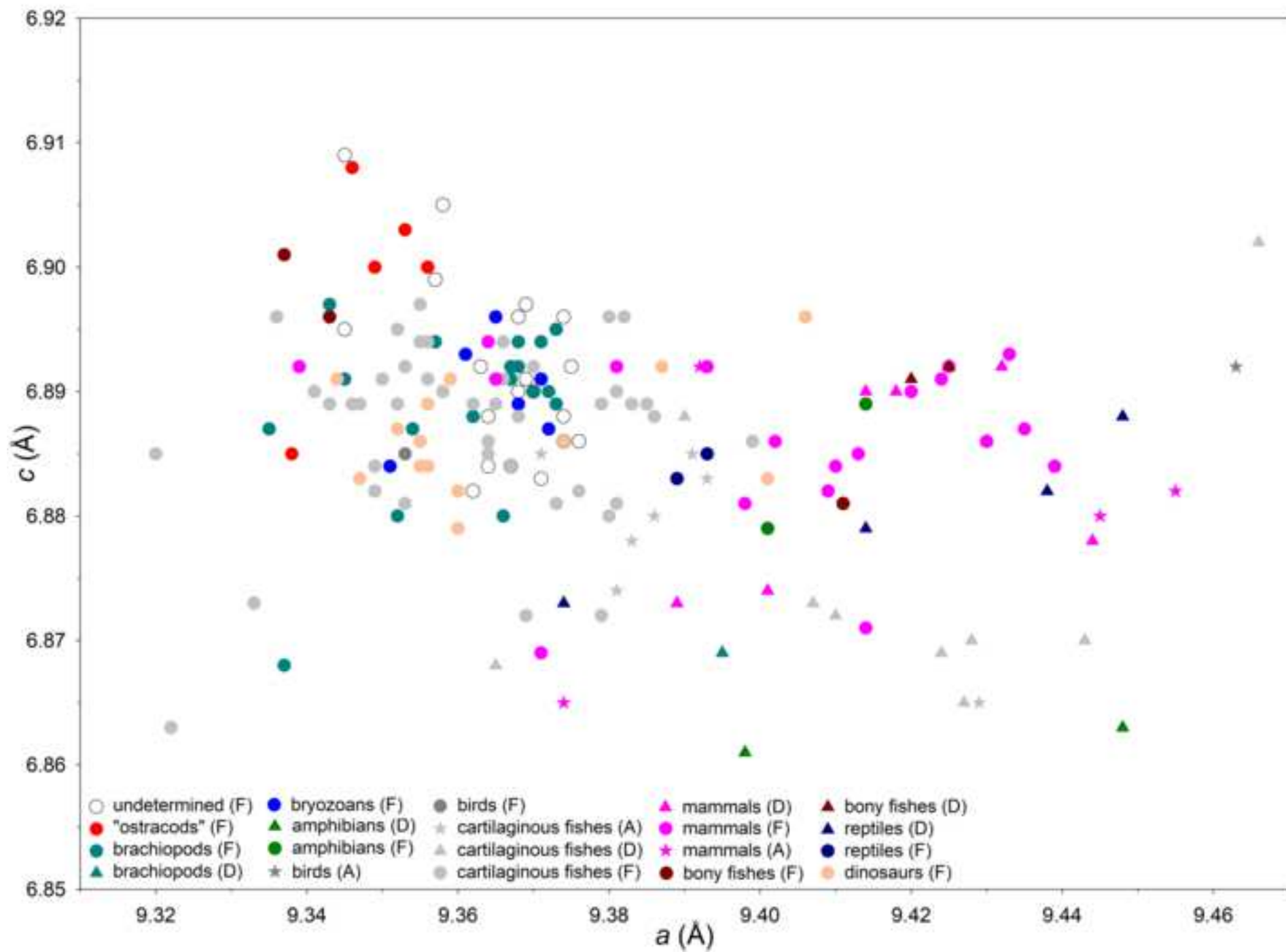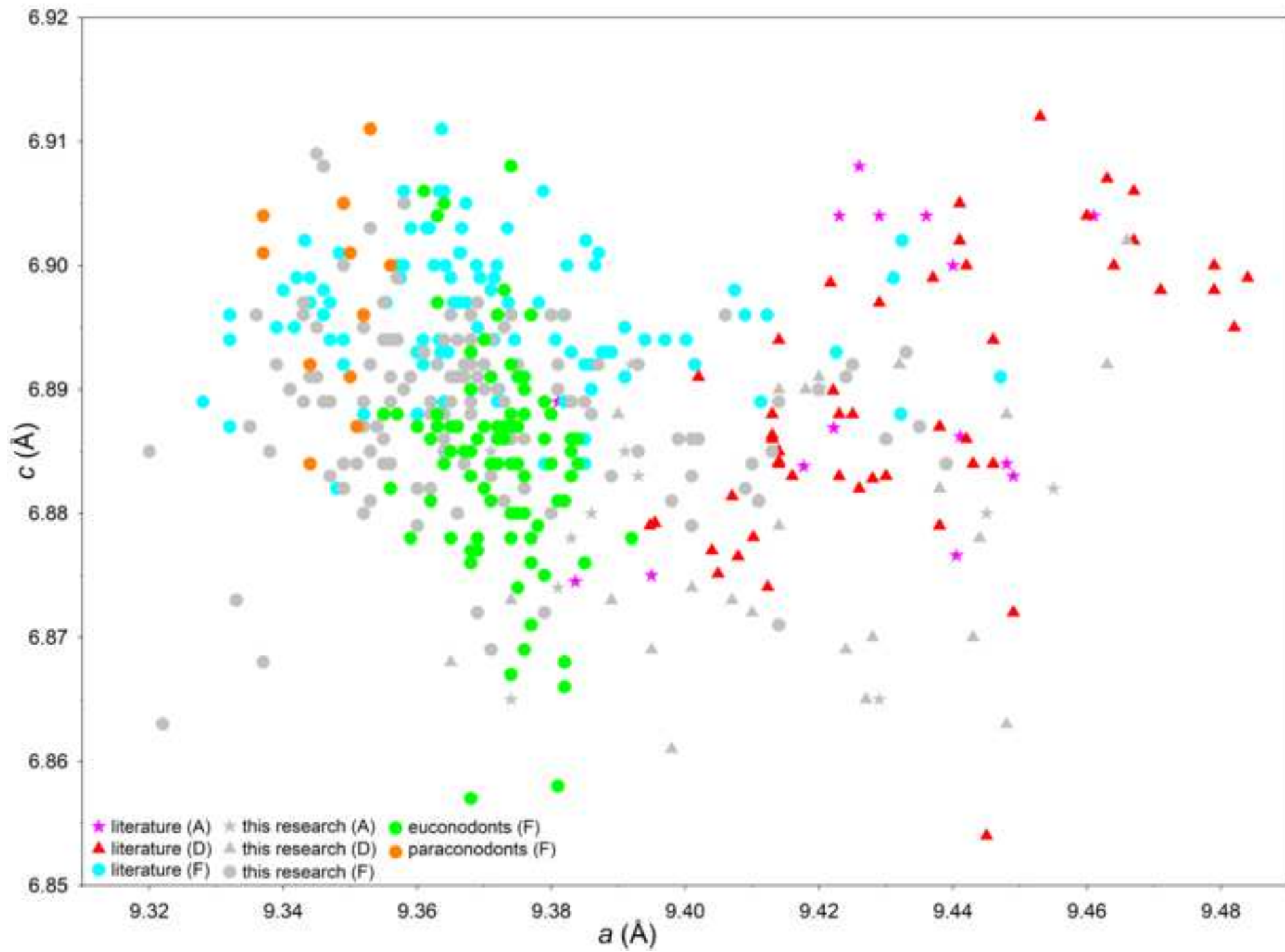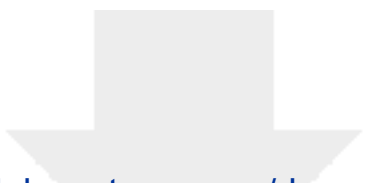
Figure 3

Figure 4

Click here to access/download;Figure;Figure 4.tif
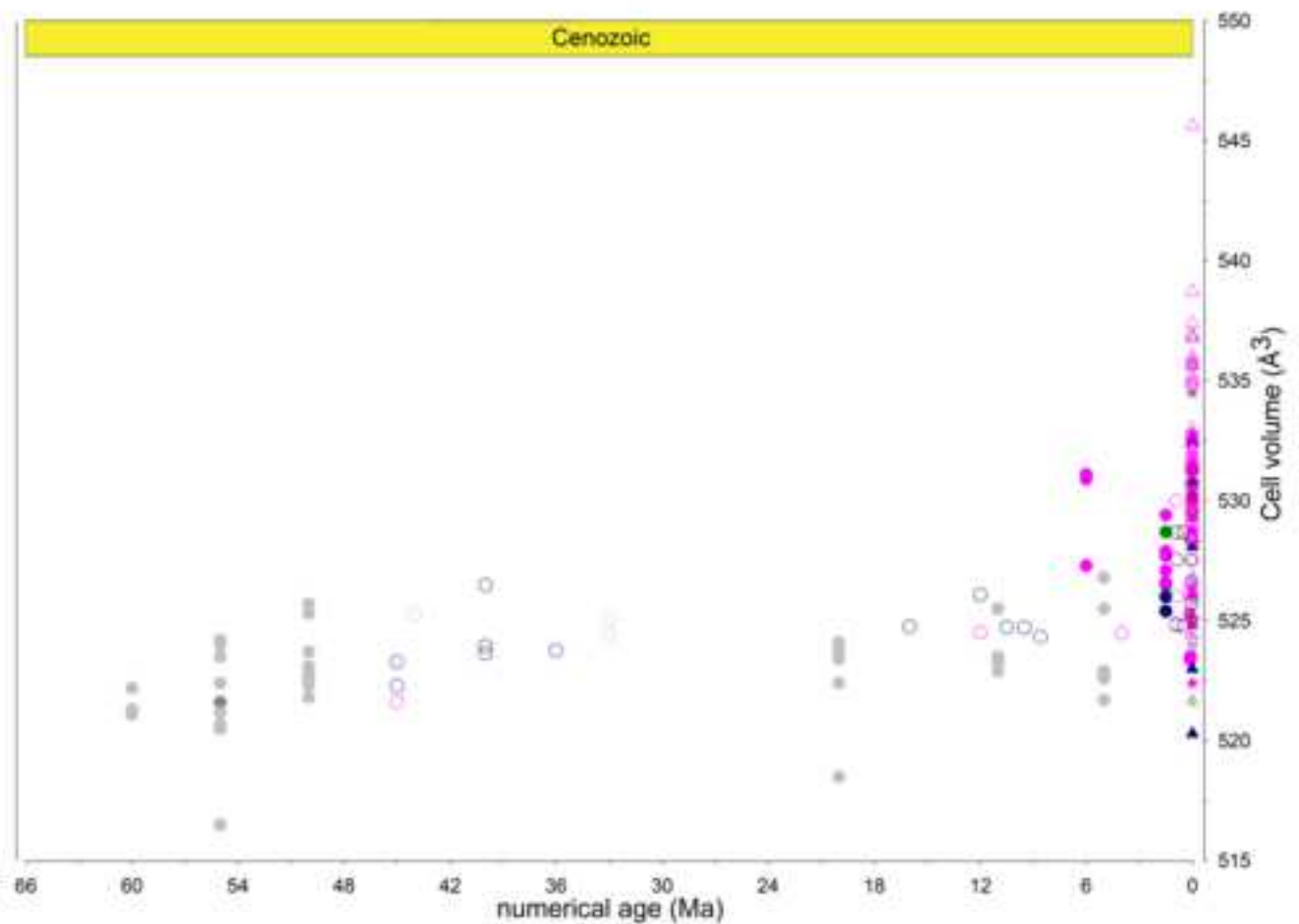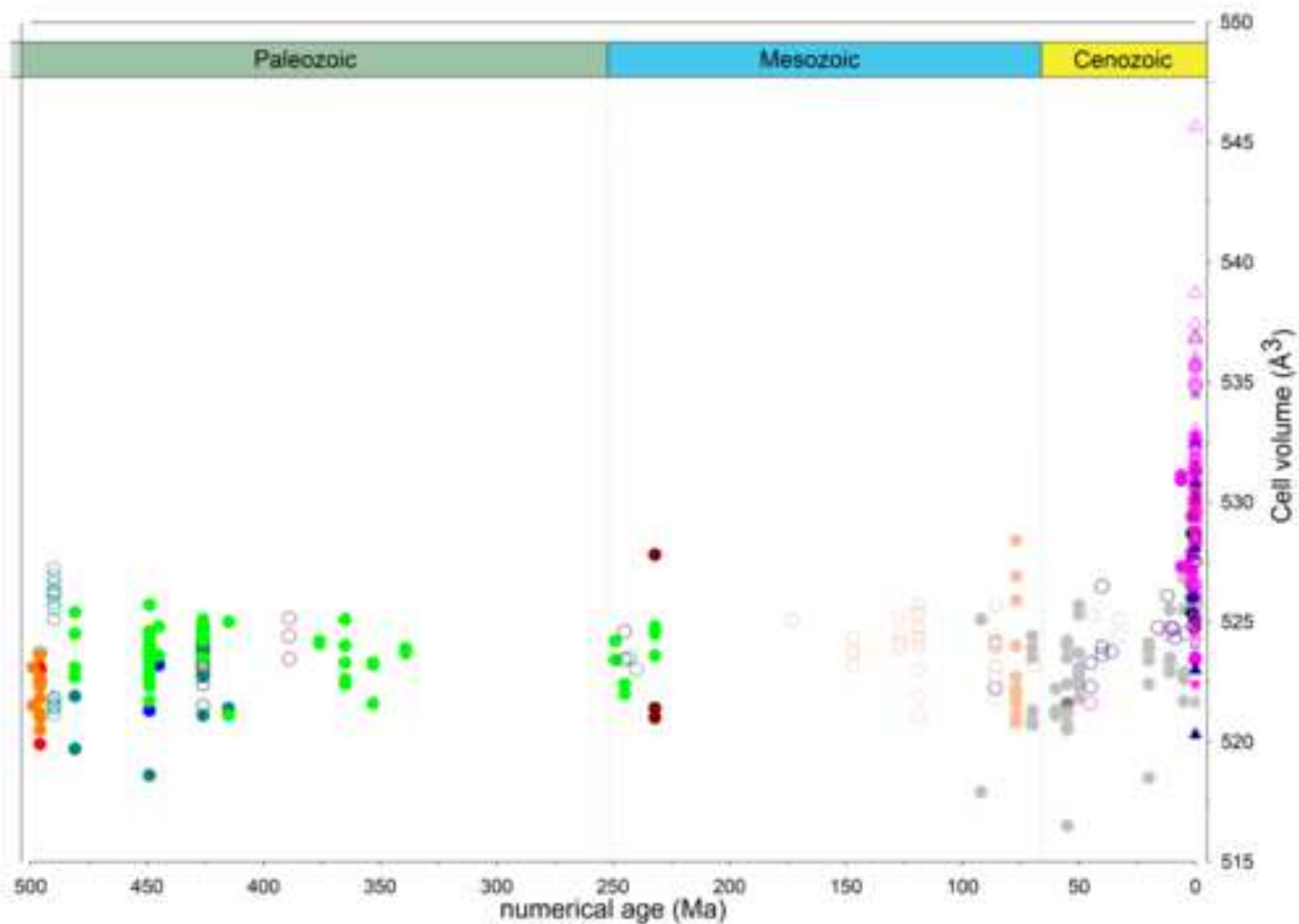
Declaration of interests

☒ The authors declare that they have no known competing financial interests or personal relationships that could have appeared to influence the work reported in this paper.

☐The authors declare the following financial interests/personal relationships which may be considered as potential competing interests:

Click here to access/download
Supplementary Material
4) SOM.docx

Tab. 1 SOM | Taxa analyzed in the present paper and from our past research[7-8].

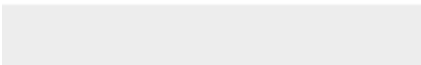| CODE	PHYLUM (Subphylum)/Class/Order	TAXONOMIC ASSIGNMENT	BONE (B), TEETH (T), SHELL (S), OTHER (O)	AGE	DEAD (D), FOSSIL (F), ALIVE (A)	a	c	CELL VOLUME (Å³)	NUMERICAL AGE (Ma)
A55	BRACHIOPODA (Linguliformea)	undetermined	S	Late Ordovician (Katian)	F	9.337	6.868	518.6	449
A8	BRACHIOPODA (Linguliformea)	undetermined	S	Early Ordovician (Tremadocian)	F	9.335	6.887	519.7	481
P15	BRACHIOPODA (Linguliformea)	undetermined	S	Silurian (Ludlow, latest Gorstian-early Ludfordian)	F	9.352	6.88	521.1	426
A4	BRACHIOPODA (Linguliformea)	undetermined	S	Early Devonian (Lochkovian)	F	9.345	6.891	521.2	415
A3	BRACHIOPODA (Linguliformea)	undetermined	S	Early Devonian (Lochkovian)	F	9.343	6.897	521.4	415
A7	BRACHIOPODA (Linguliformea)	undetermined	S	Early Ordovician (Tremadocian)	F	9.354	6.887	521.9	481
P19	BRACHIOPODA (Linguliformea)	undetermined	S	Silurian (Ludlow, latest Gorstian-early Ludfordian)	F	9.357	6.894	522.7	426
A73	BRACHIOPODA (Linguliformea)	undetermined	S	Late Ordovician (Katian)	F	9.366	6.880	522.7	449
A36	BRACHIOPODA (Linguliformea)	undetermined	S	Late Ordovician (Katian)	F	9.362	6.888	522.8	449
P43	BRACHIOPODA (Linguliformea)	undetermined	S	Silurian (Ludlow, latest Gorstian-early Ludfordian)	F	9.367	6.891	523.6	426
P51	BRACHIOPODA (Linguliformea)	undetermined	S	Silurian (Ludlow, latest Gorstian-early Ludfordian)	F	9.37	6.89	523.8	426
A25	BRACHIOPODA (Linguliformea)	undetermined	S	Late Ordovician (Katian)	F	9.367	6.892	523.8	449
A26	BRACHIOPODA (Linguliformea)	undetermined	S	Late Ordovician (Katian)	F	9.368	6.892	523.8	449
P52	BRACHIOPODA (Linguliformea)	undetermined	S	Silurian (Ludlow, latest Gorstian-early Ludfordian)	F	9.368	6.894	523.9	426
P16	BRACHIOPODA (Linguliformea)	undetermined	S	Silurian (Ludlow, latest Gorstian-early Ludfordian)	F	9.373	6.889	524.2	426
A64	BRACHIOPODA (Linguliformea)	undetermined	S	Late Ordovician (Katian)	F	9.372	6.890	524.2	449
P42	BRACHIOPODA (Linguliformea)	undetermined	S	Silurian (Ludlow, latest Gorstian-early Ludfordian)	F	9.371	6.894	524.4	426
P41	BRACHIOPODA (Linguliformea)	undetermined	S	Silurian (Ludlow, latest Gorstian-early Ludfordian)	F	9.373	6.895	524.6	426
B10_1	BRACHIOPODA (Linguliformea)/Lingulata//Lingulida	*Lingula anatina* Lamarck, 1801	S	Recent (living)	D	9.395	6.869	525.1	0.000001
A94	ARTHROPODA/Ostracoda	phosphatized undetermined specimen	O	Cambrian Furongian (Paibian)	F	9.338	6.885	519.9	496
A92	ARTHROPODA/Ostracoda	phosphatized undetermined specimen	O	Cambrian Furongian (Paibian)	F	9.349	6.900	522.3	496
A93	ARTHROPODA/Ostracoda	phosphatized undetermined specimen	O	Cambrian Furongian (Paibian)	F	9.346	6.908	522.6	496
A17	ARTHROPODA/Ostracoda	phosphatized undetermined specimen	O	Cambrian Furongian (Paibian)	F	9.353	6.903	523.0	496
A16	ARTHROPODA/Ostracoda	phosphatized undetermined specimen	O	Cambrian Furongian (Paibian)	F	9.356	6.900	523.1	496
A71	BRYOZOA	phosphatized undetermined specimen	O	Late Ordovician (Katian)	F	9.351	6.884	521.3	449
A24	BRYOZOA	phosphatized undetermined specimen	O	Late Ordovician	F	9.361	6.893	523.2	445
A58	BRYOZOA	phosphatized undetermined specimen	O	Late Ordovician (Katian)	F	9.368	6.889	523.5	449
A35	BRYOZOA	phosphatized undetermined specimen	O	Late Ordovician (Katian)	F	9.365	6.896	523.8	449
A65	BRYOZOA	phosphatized undetermined specimen	O	Late Ordovician (Katian)	F	9.372	6.887	523.9	449
A61	BRYOZOA	phosphatized undetermined specimen	O	Late Ordovician (Katian)	F	9.371	6.891	524.0	449
49	CHORDATA/Conodonta/Belodellida	*Hamarodus brevirameus* (Walliser, 1964) (Sc)	O	Late Ordovician (Katian)	F	9.365	6.887	523.1	449
68	CHORDATA/Conodonta/Belodellida	*Hamarodus brevirameus* (Walliser, 1964) (M)	O	Late Ordovician (Katian)	F	9.379	6.875	523.8	449
82	CHORDATA/Conodonta/Belodellida	*Hamarodus brevirameus* (Walliser, 1964) (M)	O	Late Ordovician (Katian)	F	9.376	6.880	523.8	449
P34	CHORDATA/Conodonta/Belodellida	*Dapsilodus obliquicostatus* (Branson & Mehl, 1933)	O	Silurian (Ludlow, latest Gorstian-early Ludfordian)	F	9.376	6.888	524.4	426
P35	CHORDATA/Conodonta/Belodellida	*Dapsilodus* sp.	O	Silurian (Ludlow, latest Gorstian-early Ludfordian)	F	9.376	6.89	524.5	426
P36	CHORDATA/Conodonta/Belodellida	*Dapsilodus* sp.	O	Silurian (Ludlow, latest Gorstian-early Ludfordian)	F	9.373	6.898	524.9	426
P29	CHORDATA/Conodonta/Belodellida	*Dapsilodus obliquicostatus* (Branson & Mehl, 1933)	O	Silurian (Ludlow, latest Gorstian-early Ludfordian)	F	9.383	6.886	525	426
A1	CHORDATA/Conodonta/Ozarkodinida	*Zieglerodina planilingua* (Murphy & Valenzuela-Ríos, 1999)	O	Early Devonian (Lochkovian)	F	9.368	6.857	521.1	415
A101	CHORDATA/Conodonta/Ozarkodinida	*Palmatolepis triangularis* Sannemann, 1955	O	Late Devonian (Famennian)	F	9.365	6.878	522.4	365
A81	CHORDATA/Conodonta/Ozarkodinida	*Branmehla werneri* (Ziegler, 1957)	O	Late Devonian (Famennian)	F	9.371	6.881	523.3	365
A42	CHORDATA/Conodonta/Ozarkodinida	*Carnepigondolella pseudodiebeli* (Kozur, 1972)	O	Late Triassic (Carnian)	F	9.372	6.884	523.6	232
A79	CHORDATA/Conodonta/Ozarkodinida	*Gnathodus* sp.	O	Carboniferous-Middle Mississippian (Visean)	F	9.370	6.887	523.7	339
A78	CHORDATA/Conodonta/Ozarkodinida	*Gnathodus* sp.	O	Carboniferous-Middle Mississippian (Visean)	F	9.374	6.884	523.9	339
A83	CHORDATA/Conodonta/Ozarkodinida	*Polygnathus decorosus* Stauffer, 1938	O	Late Devonian (Frasnian)	F	9.376	6.883	524.1	376
A82	CHORDATA/Conodonta/Ozarkodinida	*Palmatolepis* sp.	O	Late Devonian (Frasnian)	F	9.370	6.894	524.2	376
A44	CHORDATA/Conodonta/Ozarkodinida	*Carnepigondolella pseudodiebeli* (Kozur, 1972)	O	Late Triassic (Carnian)	F	9.382	6.881	524.5	232
P32	CHORDATA/Conodonta/Ozarkodinida	*Kockelella variabilis ichnusae* Serpagli & Corradini, 1998	O	Silurian (Ludlow, latest Gorstian-early Ludfordian)	F	9.38	6.884	524.5	426
P33	CHORDATA/Conodonta/Ozarkodinida	*Kockelella variabilis ichnusae* Serpagli & Corradini, 1998	O	Silurian (Ludlow, latest Gorstian-early Ludfordian)	F	9.376	6.891	524.6	426
A43	CHORDATA/Conodonta/Ozarkodinida	*Carnepigondolella pseudodiebeli* (Kozur, 1972)	O	Late Triassic (Carnian)	F	9.383	6.883	524.8	232
P31	CHORDATA/Conodonta/Ozarkodinida	*Kockelella* sp.	O	Silurian (Ludlow, latest Gorstian-early Ludfordian)	F	9.38	6.888	524.8	426
A2	CHORDATA/Conodonta/Ozarkodinida	*Lanea omoalpha* (Murphy & Valenzuela-Ríos, 1999)	O	Early Devonian (Lochkovian)	F	9.383	6.885	525.0	415
P28	CHORDATA/Conodonta/Ozarkodinida	*Kockelella* sp.	O	Silurian (Ludlow, latest Gorstian-early Ludfordian)	F	9.384	6.884	525	426
A102	CHORDATA/Conodonta/Ozarkodinida	*Palmatolepis subperlobata* Branson & Mehl, 1934	O	Late Devonian (Famennian)	F	9.384	6.886	525.1	365
56	CHORDATA/Conodonta/Panderodontida	*Panderodus* sp.	O	Late Ordovician (Katian)	F	9.374	6.867	522.6	449
A53	CHORDATA/Conodonta/Panderodontida	*Panderodus* sp.	O	Late Ordovician (Katian)	F	9.369	6.878	522.9	449
P30	CHORDATA/Conodonta/Panderodontida	*Panderodus* sp.	O	Silurian (Ludlow, latest Gorstian-early Ludfordian)	F	9.382	6.868	523.5	426
A23	CHORDATA/Conodonta/Panderodontida	*Panderodus* sp.	O	Late Ordovician	F	9.363	6.897	523.6	445
20	CHORDATA/Conodonta/Panderodontida	*Panderodus* sp.	O	Late Ordovician (Katian)	F	9.374	6.884	523.9	449
A104	CHORDATA/Conodonta/Panderodontida	*Belodina* sp.	O	Late Ordovician	F	9.374	6.887	524.1	449
P38	CHORDATA/Conodonta/Panderodontida	*Panderodus unicostatus* (Branson & Mehl, 1933)	O	Silurian (Ludlow, latest Gorstian-early Ludfordian)	F	9.374	6.888	524.2	426
P37	CHORDATA/Conodonta/Panderodontida	*Panderodus* sp.	O	Silurian (Ludlow, latest Gorstian-early Ludfordian)	F	9.376	6.888	524.3	426
A106	CHORDATA/Conodonta/Panderodontida	*Panderodus* sp.	O	Late Ordovician	F	9.379	6.886	524.6	449
P39	CHORDATA/Conodonta/Panderodontida	*Panderodus unicostatus* (Branson & Mehl, 1933)	O	Silurian (Ludlow, latest Gorstian-early Ludfordian)	F	9.377	6.896	525.1	426
A12	CHORDATA/Conodonta/Paraconodontida	*Westergaardodina* sp.	O	Cambrian-Furongian (Paibian)	F	9.344	6.884	520.5	496
A14	CHORDATA/Conodonta/Paraconodontida	*Furnishina* sp.	O	Cambrian-Furongian (Paibian)	F	9.337	6.901	521.0	496
A11	CHORDATA/Conodonta/Paraconodontida	*Westergaardodina* sp.	O	Cambrian-Furongian (Paibian)	F	9.344	6.892	521.1	496
A19	CHORDATA/Conodonta/Paraconodontida	*Furnishina alata* Szaniawski, 1971	O	Cambrian Miaolingian (Guzhangian)	F	9.351	6.887	521.5	499
A90	CHORDATA/Conodonta/Paraconodontida	*Westergaardodina* sp.	O	Cambrian-Furongian (Paibian)	F	9.350	6.891	521.8	496
A91	CHORDATA/Conodonta/Paraconodontida	*Westergaardodina* sp.	O	Cambrian-Furongian (Paibian)	F	9.352	6.896	522.3	496
A88	CHORDATA/Conodonta/Paraconodontida	*Furnishina* sp.	O	Cambrian-Furongian (Paibian)	F	9.350	6.901	522.5	496
A13	CHORDATA/Conodonta/Paraconodontida	*Furnishina* sp.	O	Cambrian-Furongian (Paibian)	F	9.349	6.905	522.7	496
A18	CHORDATA/Conodonta/Paraconodontida	*Furnishina alata* Szaniawski, 1971	O	Cambrian Miaolingian (Guzhangian)	F	9.356	6.900	523.1	499

A89	CHORDATA/Conodonta/Paraconodontida	*Furnishina* sp.	O	Cambrian-Furongian (Paibian)	F	9.353	6.911	523.6	496
A105	CHORDATA/Conodonta/Prioniodontida	*Plectodina* sp.	O	Late Ordovician	F	9.359	6.878	521.7	449
17	CHORDATA/Conodonta/Prioniodontida	*Amorphognathus* sp. (Sd)	O	Late Ordovician (Katian)	F	9.357	6.888	522.3	449
A107	CHORDATA/Conodonta/Prioniodontida	*Amorphognathus* sp. (Pb)	O	Late Ordovician (Katian)	F	9.360	6.887	522.6	449
46	CHORDATA/Conodonta/Prioniodontida	*Sagittodontina robusta* Knüpfer, 1967 (Sd)	O	Late Ordovician (Katian)	F	9.368	6.876	522.6	449
A49	CHORDATA/Conodonta/Prioniodontida	*Amorphognathus* sp. (Pa)	O	Late Ordovician (Katian)	F	9.364	6.884	522.7	449
A108	CHORDATA/Conodonta/Prioniodontida	*Amorphognathus* sp. (Pb)	O	Late Ordovician (Katian)	F	9.364	6.884	522.7	449
24	CHORDATA/Conodonta/Prioniodontida	*Sagittodontina robusta* Knüpfer, 1967 (Pa)	O	Late Ordovician (Katian)	F	9.369	6.877	522.7	449
A30	CHORDATA/Conodonta/Prioniodontida	*Amorphognathus* sp. (Pa)	O	Late Ordovician (Katian)	F	9.363	6.887	522.9	449
A37	CHORDATA/Conodonta/Prioniodontida	*Amorphognathus* sp. (Pb)	O	Late Ordovician (Katian)	F	9.363	6.887	522.9	449
A38	CHORDATA/Conodonta/Prioniodontida	*Amorphognathus* sp. (Pa)	O	Late Ordovician (Katian)	F	9.365	6.885	523.0	449
A29	CHORDATA/Conodonta/Prioniodontida	*Amorphognathus* sp. (Pb)	O	Late Ordovician (Katian)	F	9.363	6.888	523.0	449
A68	CHORDATA/Conodonta/Prioniodontida	*Amorphognathus* sp. (Pb)	O	Late Ordovician (Katian)	F	9.368	6.883	523.1	449
A50	CHORDATA/Conodonta/Prioniodontida	*Amorphognathus* sp. (Pa)	O	Late Ordovician (Katian)	F	9.367	6.885	523.2	449
62	CHORDATA/Conodonta/Prioniodontida	*Amorphognathus* sp. (Pb)	O	Late Ordovician (Katian)	F	9.366	6.887	523.2	449
A86	CHORDATA/Conodonta/Prioniodontida	*Pachycladina obliqua* Staesche, 1964	O	Early Triassic (Olenekian)	F	9.374	6.878	523.4	249
A51	CHORDATA/Conodonta/Prioniodontida	*Amorphognathus* sp. (Pa)	O	Late Ordovician (Katian)	F	9.371	6.884	523.5	449
A98	CHORDATA/Conodonta/Prioniodontida	*Amorphognathus* sp. (Pa)	O	Late Ordovician (Katian)	F	9.369	6.886	523.5	449
A31	CHORDATA/Conodonta/Prioniodontida	*Amorphognathus* sp. (Pa)	O	Late Ordovician (Katian)	F	9.368	6.890	523.6	449
A66	CHORDATA/Conodonta/Prioniodontida	*Amorphognathus* sp. (Pa)	O	Late Ordovician (Katian)	F	9.377	6.876	523.6	449
21	CHORDATA/Conodonta/Prioniodontida	*Icriodella* sp.	O	Late Ordovician (Katian)	F	9.374	6.880	523.6	449
41	CHORDATA/Conodonta/Prioniodontida	*Sagittodontina robusta* Knüpfer, 1967 (Pa)	O	Late Ordovician (Katian)	F	9.372	6.886	523.8	449
A72	CHORDATA/Conodonta/Prioniodontida	*Amorphognathus* sp. (Pb)	O	Late Ordovician (Katian)	F	9.372	6.887	523.9	449
A99	CHORDATA/Conodonta/Prioniodontida	*Amorphognathus* sp. (Pa)	O	Late Ordovician (Katian)	F	9.373	6.886	523.9	449
A103	CHORDATA/Conodonta/Prioniodontida	*Icriodus* sp.	O	Late Devonian (Famennian)	F	9.378	6.879	524.0	365
A52	CHORDATA/Conodonta/Prioniodontida	*Amorphognathus* sp. (Pb)	O	Late Ordovician (Katian)	F	9.371	6.891	524.1	449
A87	CHORDATA/Conodonta/Prioniodontida	*Pachycladina obliqua* Staesche, 1964	O	Early Triassic (Olenekian)	F	9.363	6.904	524.2	249
A27	CHORDATA/Conodonta/Prioniodontida	*Amorphognathus* sp. (Pb)	O	Late Ordovician (Katian)	F	9.375	6.887	524.2	449
A67	CHORDATA/Conodonta/Prioniodontida	*Amorphognathus* sp. (Pa)	O	Late Ordovician (Katian)	F	9.376	6.888	524.4	449
A41	CHORDATA/Conodonta/Prioniodontida	*Amorphognathus* sp. (Pb)	O	Late Ordovician (Katian)	F	9.364	6.905	524.4	449
A28	CHORDATA/Conodonta/Prioniodontida	*Amorphognathus* sp. (Pb)	O	Late Ordovician (Katian)	F	9.372	6.896	524.6	449
A22	CHORDATA/Conodonta/Prioniodontida	*Rhipidognathus symmetricus* Branson, Mehl & Branson, 1951	O	Late Ordovician	F	9.379	6.889	524.8	445
91	CHORDATA/Conodonta/Protopanderodontida	*Scabbardella altipes* (Henningsmoen, 1948)	O	Late Ordovician (Katian)	F	9.368	6.877	522.6	449
A6	CHORDATA/Conodonta/Protopanderodontida	*Paltodus deltifer deltifer* (Lindström, 1955)	O	Early Ordovician (Tremadocian)	F	9.381	6.858	522.7	481
A40	CHORDATA/Conodonta/Protopanderodontida	*Scabbardella altipes* (Henningsmoen, 1948)	O	Late Ordovician (Katian)	F	9.376	6.869	523.0	449
A5	CHORDATA/Conodonta/Protopanderodontida	*Paltodus deltifer deltifer* (Lindström, 1955)	O	Early Ordovician (Tremadocian)	F	9.375	6.874	523.1	481
A39	CHORDATA/Conodonta/Protopanderodontida	*Scabbardella altipes* (Henningsmoen, 1948)	O	Late Ordovician (Katian)	F	9.377	6.871	523.3	449
A69	CHORDATA/Conodonta/Protopanderodontida	*Scabbardella altipes* (Henningsmoen, 1948)	O	Late Ordovician (Katian)	F	9.368	6.885	523.3	449
A32	CHORDATA/Conodonta/Protopanderodontida	*Scabbardella altipes* (Henningsmoen, 1948)	O	Late Ordovician (Katian)	F	9.382	6.866	523.4	449
A75	CHORDATA/Conodonta/Protopanderodontida	*Scabbardella altipes* (Henningsmoen, 1948)	O	Late Ordovician (Katian)	F	9.377	6.878	523.7	449
59	CHORDATA/Conodonta/Protopanderodontida	*Scabbardella altipes* (Henningsmoen, 1948)	O	Late Ordovician (Katian)	F	9.375	6.880	523.7	449
A34	CHORDATA/Conodonta/Protopanderodontida	*Scabbardella altipes* (Henningsmoen, 1948)	O	Late Ordovician (Katian)	F	9.368	6.893	523.9	449
A70	CHORDATA/Conodonta/Protopanderodontida	*Scabbardella altipes* (Henningsmoen, 1948)	O	Late Ordovician (Katian)	F	9.373	6.887	524.0	449
45	CHORDATA/Conodonta/Protopanderodontida	*Scabbardella altipes* (Henningsmoen, 1948)	O	Late Ordovician (Katian)	F	9.375	6.884	524.0	449
A54	CHORDATA/Conodonta/Protopanderodontida	*Scabbardella altipes* (Henningsmoen, 1948)	O	Late Ordovician (Katian)	F	9.361	6.906	524.1	449
A33	CHORDATA/Conodonta/Protopanderodontida	*Scabbardella altipes* (Henningsmoen, 1948)	O	Late Ordovician (Katian)	F	9.374	6.892	524.5	449
A74	CHORDATA/Conodonta/Protopanderodontida	*Scabbardella altipes* (Henningsmoen, 1948)	O	Late Ordovician (Katian)	F	9.385	6.876	524.5	449
A20	CHORDATA/Conodonta/Protopanderodontida	*Paltodus deltifer pristinus* (Viira, 1970)	O	Early Ordovician (Tremadocian)	F	9.375	6.891	524.5	481
60	CHORDATA/Conodonta/Protopanderodontida	*Scabbardella altipes* (Henningsmoen, 1948)	O	Late Ordovician (Katian)	F	9.381	6.881	524.5	449
A21	CHORDATA/Conodonta/Protopanderodontida	*Paltodus deltifer pristinus* (Viira, 1970)	O	Early Ordovician (Tremadocian)	F	9.392	6.878	525.4	481
103	CHORDATA/Conodonta/Protopanderodontida	*Scabbardella altipes* (Henningsmoen, 1948)	O	Late Ordovician (Katian)	F	9.374	6.908	525.7	449
A15	CHORDATA/Conodonta/Unknown	undetermined	O	Cambrian-Furongian (Paibian)	F	9.337	6.904	521.2	496
A77	CHORDATA/Conodonta/Unknown	undetermined	O	Carboniferous- Early Mississippian (Tournaisian)	F	9.356	6.882	521.6	353
A84	CHORDATA/Conodonta/Unknown	undetermined	O	Middle Triassic (Anisian)	F	9.355	6.888	522.0	245
A85	CHORDATA/Conodonta/Unknown	undetermined	O	Middle Triassic (Anisian)	F	9.362	6.881	522.4	245
A80	CHORDATA/Conodonta/Unknown	undetermined	O	Late Devonian (Famennian)	F	9.362	6.886	522.6	365
A76	CHORDATA/Conodonta/Unknown	undetermined	O	Carboniferous- Early Mississippian (Tournaisian)	F	9.377	6.871	523.2	353
A100	CHORDATA/Conodonta/Unknown	undetermined	O	Carboniferous- Early Mississippian (Tournaisian)	F	9.370	6.882	523.3	353
B25	CHORDATA/Chondrichthyes	undetermined	T	early Eocene (Ypresian, NP10 Zone)	F	9.38	6.88	524.2	55
B7_2	CHORDATA/Chondrichthyes/Carcharhiniformes	*Carcharhinus leucas* (Müller & Henle, 1839)	T	Recent (living)	D	9.365	6.868	521.7	0.000001
B23_2	CHORDATA/Chondrichthyes/Carcharhiniformes	*Carcharias taurus* (Rafinesque, 1810)	T	Recent (living)	A	9.371	6.885	523.6	0.000001
B23L_A2_4	CHORDATA/Chondrichthyes/Carcharhiniformes	*Carcharias taurus* (Rafinesque, 1810)	T	Recent (living)	A	9.381	6.874	523.9	0.000001
B23_1	CHORDATA/Chondrichthyes/Carcharhiniformes	*Carcharias taurus* (Rafinesque, 1810)	T	Recent (living)	A	9.383	6.878	524.4	0.000001
B3L_A2_3	CHORDATA/Chondrichthyes/Carcharhiniformes	*Carcharias taurus* (Rafinesque, 1810)	T	Recent (living)	A	9.386	6.880	525.0	0.000001
B23_TQ_1	CHORDATA/Chondrichthyes/Carcharhiniformes	*Carcharias taurus* (Rafinesque, 1810)	T	Recent (living)	A	9.391	6.885	525.8	0.000001
B23_TQ_2	CHORDATA/Chondrichthyes/Carcharhiniformes	*Carcharias taurus* (Rafinesque, 1810)	T	Recent (living)	A	9.393	6.883	525.9	0.000001
B8	CHORDATA/Chondrichthyes/Carcharhiniformes	*Galeocerdo cuvier* (Péron & Lesueur, 1822)	T	Recent (living)	D	9.424	6.869	528.3	0.000001
B23L_A2_2	CHORDATA/Chondrichthyes/Carcharhiniformes	*Carcharias taurus* (Rafinesque, 1810)	T	Recent (living)	A	9.429	6.865	528.5	0.000001
B8_2	CHORDATA/Chondrichthyes/Carcharhiniformes	*Galeocerdo cuvier* (Péron & Lesueur, 1822)	T	Recent (living)	D	9.428	6.870	528.8	0.000001
B7_1	CHORDATA/Chondrichthyes/Carcharhiniformes	*Carcharhinus leucas* (Müller & Henle, 1839)	T	Recent (living)	D	9.443	6.870	530.5	0.000001
52_2	CHORDATA/Chondrichthyes/Hybodontiformes	*Ptychodus whipplei* Marcou, 1858	T	Late Cretaceous (Turonian)	F	9.32	6.885	517.9	92
52_1	CHORDATA/Chondrichthyes/Hybodontiformes	*Ptychodus whipplei* Marcou, 1858	T	Late Cretaceous (Turonian)	F	9.381	6.89	525.1	92
B14_1	CHORDATA/Chondrichthyes/Lamniformes	Odontaspididae	T	early Eocene (Ypresian, NP10 Zone)	F	9.322	6.863	516.5	55
B37	CHORDATA/Chondrichthyes/Lamniformes	*Cosmopolitodus hastalis* (Agassiz, 1843)	T	early Miocene (Aquitanian-Burdigalian)	F	9.333	6.873	518.5	20

B19_3	CHORDATA/Chondrichthyes/Lamniformes	Odontaspididae	T	early Eocene (Ypresian, NP10 Zone)	F	9.336	6.896	520.5	55
B19_2	CHORDATA/Chondrichthyes/Lamniformes	Odontaspididae	T	early Eocene (Ypresian, NP10 Zone)	F	9.341	6.89	520.7	55
B28L_A1_3	CHORDATA/Chondrichthyes/Lamniformes	*Squalicorax*	T	Late Cretaceous	F	9.343	6.889	520.7	70
B16	CHORDATA/Chondrichthyes/Lamniformes	*Squalicorax pristodontus* (Agassiz, 1843)	T	Late Cretaceous	F	9.349	6.882	520.9	70
B13_2	CHORDATA/Chondrichthyes/Lamniformes	*Palaeocarcharodon orientalis* (Sinzow, 1899)	T	Paleocene	F	9.349	6.884	521.1	60
B13_5	CHORDATA/Chondrichthyes/Lamniformes	*Palaeocarcharodon orientalis* (Sinzow, 1899)	T	Paleocene	F	9.344	6.891	521.1	60
B14_2	CHORDATA/Chondrichthyes/Lamniformes	Odontaspididae	T	early Eocene (Ypresian, NP10 Zone)	F	9.346	6.889	521.2	55
B13_1	CHORDATA/Chondrichthyes/Lamniformes	*Palaeocarcharodon orientalis* (Sinzow, 1899)	T	Paleocene	F	9.353	6.881	521.3	60
B5_2	CHORDATA/Chondrichthyes/Lamniformes	*Squalicorax* sp.	T	Late Cretaceous	F	9.347	6.889	521.3	70
B34L_B1_2	CHORDATA/Chondrichthyes/Lamniformes	*Carcharodon carcharias* (Linnaeus, 1758)	T	early Pliocene	F	9.350	6.891	521.7	5
B32_2	CHORDATA/Chondrichthyes/Lamniformes	*Otodus* sp.	T	Eocene	F	9.352	6.889	521.8	50
B13_3	CHORDATA/Chondrichthyes/Lamniformes	*Palaeocarcharodon orientalis* (Sinzow, 1899)	T	Paleocene	F	9.353	6.892	522.2	60
B36L_B2_2	CHORDATA/Chondrichthyes/Lamniformes	*Otodus* sp.	T	Eocene	F	9.352	6.895	522.3	50
B37L_B1_2	CHORDATA/Chondrichthyes/Lamniformes	*Cosmopolitodus hastalis* (Agassiz, 1843)	T	early Miocene (Aquitanian-Burdigalian)	F	9.356	6.891	522.4	20
B19_1	CHORDATA/Chondrichthyes/Lamniformes	Odontaspididae	T	early Eocene (Ypresian, NP10 Zone)	F	9.369	6.872	522.4	55
B36L_B2_1	CHORDATA/Chondrichthyes/Lamniformes	*Otodus* sp.	T	Eocene	F	9.355	6.894	522.5	50
B34L_B1_3	CHORDATA/Chondrichthyes/Lamniformes	*Carcharodon carcharias* (Linnaeus, 1758)	T	early Pliocene	F	9.356	6.894	522.6	5
B35L_A2_3	CHORDATA/Chondrichthyes/Lamniformes	*Otodus* sp.	T	Eocene	F	9.358	6.890	522.6	50
B34	CHORDATA/Chondrichthyes/Lamniformes	*Carcharodon carcharias* (Linnaeus, 1758)	T	early Pliocene	F	9.355	6.897	522.7	5
B35L_A2_1	CHORDATA/Chondrichthyes/Lamniformes	*Otodus* sp.	T	Eocene	F	9.359	6.891	522.7	50
B34L_A2_1	CHORDATA/Chondrichthyes/Lamniformes	*Carcharodon carcharias* (Linnaeus, 1758)	T	early Pliocene	F	9.364	6.886	522.9	5
B15_c_3	CHORDATA/Chondrichthyes/Lamniformes	*Carcharocles megalodon* Agassiz, 1843	T	Miocene	F	9.364	6.885	522.9	11
B35L_A2_2	CHORDATA/Chondrichthyes/Lamniformes	*Otodus* sp.	T	Eocene	F	9.362	6.889	522.9	50
B32_1	CHORDATA/Chondrichthyes/Lamniformes	*Otodus* sp.	T	Eocene	F	9.367	6.884	523.1	50
B15_c_4	CHORDATA/Chondrichthyes/Lamniformes	*Carcharocles megalodon* Agassiz, 1843	T	Miocene	F	9.365	6.889	523.3	11
B37L_B1_1	CHORDATA/Chondrichthyes/Lamniformes	*Cosmopolitodus hastalis* (Agassiz, 1843)	T	early Miocene (Aquitanian-Burdigalian)	F	9.366	6.891	523.4	20
B15_c_2	CHORDATA/Chondrichthyes/Lamniformes	*Carcharocles megalodon* Agassiz, 1843	T	Miocene	F	9.368	6.888	523.5	11
B14_4	CHORDATA/Chondrichthyes/Lamniformes	Odontaspididae	T	early Eocene (Ypresian, NP10 Zone)	F	9.373	6.881	523.5	55
B28L_A1_2	CHORDATA/Chondrichthyes/Lamniformes	*Squalicorax* sp.	T	Late Cretaceous	F	9.379	6.872	523.5	70
B36L_A1_1	CHORDATA/Chondrichthyes/Lamniformes	*Otodus* sp.	T	Eocene	F	9.366	6.894	523.7	50
B37L_A2_2	CHORDATA/Chondrichthyes/Lamniformes	*Cosmopolitodus hastalis* (Agassiz, 1843)	T	early Miocene (Aquitanian-Burdigalian)	F	9.379	6.889	523.8	20
B5_1	CHORDATA/Chondrichthyes/Lamniformes	*Squalicorax* sp.	T	Late Cretaceous	F	9.376	6.882	523.9	70
B14_3	CHORDATA/Chondrichthyes/Lamniformes	Odontaspididae	T	early Eocene (Ypresian, NP10 Zone)	F	9.376	6.882	524.0	55
B37L_A2_1	CHORDATA/Chondrichthyes/Lamniformes	*Cosmopolitodus hastalis* (Agassiz, 1843)	T	early Miocene (Aquitanian-Burdigalian)	F	9.370	6.892	524.1	20
B28L_A1_1	CHORDATA/Chondrichthyes/Lamniformes	*Squalicorax* sp.	T	Late Cretaceous	F	9.381	6.881	524.4	70
B35L_A2_4	CHORDATA/Chondrichthyes/Lamniformes	*Otodus* sp.	T	Eocene	F	9.383	6.889	525.3	50
B34L_A2_2	CHORDATA/Chondrichthyes/Lamniformes	*Carcharodon carcharias* (Linnaeus, 1758)	T	early Pliocene	F	9.386	6.888	525.5	5
B15_c_1	CHORDATA/Chondrichthyes/Lamniformes	*Carcharocles megalodon* Agassiz, 1843	T	Miocene	F	9.385	6.889	525.5	11
B15_c_5	CHORDATA/Chondrichthyes/Lamniformes	*Carcharocles megalodon* Agassiz, 1843	T	Miocene	F	9.380	6.896	525.5	11
B36L_B2_3	CHORDATA/Chondrichthyes/Lamniformes	*Otodus* sp.	T	Eocene	F	9.382	6.896	525.7	50
B2 Q1_3	CHORDATA/Chondrichthyes/Lamniformes	*Prionace glauca* (Linnaeus, 1758)	T	Recent (1989)	D	9.390	6.888	526.0	0.00003
B34L_B1_1	CHORDATA/Chondrichthyes/Lamniformes	*Carcharodon carcharias* (Linnaeus, 1758)	T	early Pliocene	F	9.399	6.886	526.8	5
B1_2	CHORDATA/Chondrichthyes/Pristiformes	*Pristis* sp.	T	Recent (1962)	D	9.410	6.872	526.9	0.000057
B1_1	CHORDATA/Chondrichthyes/Pristiformes	*Pristis* sp.	T	Recent (1962)	D	9.427	6.865	528.4	0.000057
B1_3	CHORDATA/Chondrichthyes/Pristiformes	*Pristis* sp.	T	Recent (1962)	D	9.466	6.902	535.6	0.000057
B9_1	CHORDATA/Chondrichthyes/Rajiformes	*Raja* sp.	O	Recent (living)	D	9.407	6.873	526.7	0.000001
A45	CHORDATA/Osteichthyes	undetermined	T	Late Triassic (Carnian)	F	9.337	6.901	521.0	232
A46	CHORDATA/Osteichthyes	undetermined	T	Late Triassic (Carnian)	F	9.343	6.896	521.4	232
A47	CHORDATA/Osteichthyes	undetermined	T	Late Triassic (Norian)	F	9.411	6.881	527.8	232
B3_1	CHORDATA/Osteichthyes/Perciformes	*Diplodus* cf. *sargus* (Linnaeus, 1758)	T	Recent (1957)	D	9.42	6.891	530.0	0.000062
B3_2	CHORDATA/Osteichthyes/Perciformes	*Diplodus* cf. *sargus* (Linnaeus, 1758)	T	Recent (1957)	D	9.425	6.892	530.2	0.000062
54_2	CHORDATA/"Amphibia"/Anura	*Hoplobatrachus rugulosus* (Wiegmann, 1834)	B	Recent	D	9.398	6.861	524.8	0.000001
B43_1	CHORDATA/"Amphibia"/Anura	*Bufotes* gr. *viridis* (Laurenti, 1768)	B	Early Pleistocene	F	9.401	6.879	526.5	1.5
B43_2	CHORDATA/"Amphibia"/Anura	*Bufotes* gr. *viridis* (Laurenti, 1768)	B	Early Pleistocene	F	9.414	6.889	528.7	1.5
54_1	CHORDATA/"Amphibia"/Anura	*Hoplobatrachus rugulosus* (Wiegmann, 1834)	B	Recent	D	9.448	6.863	530.5	0.000001
55_1	CHORDATA/Reptilia/Crocodylia	*Crocodylus niloticus* Laurenti, 1768	T	Recent	D	9.448	6.888	532.5	0.000001
B11_2	CHORDATA/Reptilia/Testudines	*Dermochelys coriacea* (Vandelli, 1761)	S	Recent	D	9.374	6.873	523.0	0.000012
B44_2	CHORDATA/Reptilia/Testudines	*Testudo hermanni* Gmelin, 1789	B	Early Pleistocene	F	9.389	6.883	525.4	1.5
B44_1	CHORDATA/Reptilia/Testudines	*Testudo hermanni* Gmelin, 1789	B	Early Pleistocene	F	9.393	6.885	526.0	1.5
B4_2	CHORDATA/Reptilia/Testudines	*Caretta caretta* Linnaeus, 1758	B	Recent	D	9.414	6.879	528.1	0.000001
B4_1	CHORDATA/Reptilia/Testudines	*Caretta caretta* Linnaeus, 1758	B	Recent	D	9.438	6.882	530.8	0.000001
DT5_1	CHORDATA/Sauropsida/Ornithischia	undetermined	T	Late Cretaceous (Campanian)	F	9.347	6.883	520.8	77
DT2_3	CHORDATA/Sauropsida/Ornithischia	undetermined	T	Late Cretaceous (Campanian)	F	9.344	6.891	521.1	77
DT1_2	CHORDATA/Sauropsida/Ornithischia	undetermined	T	Late Cretaceous (Campanian)	F	9.352	6.887	521.6	77
DT10_1	CHORDATA/Sauropsida/Ornithischia	undetermined	T	Late Cretaceous (Campanian)	F	9.356	6.884	521.8	77
DT8_1	CHORDATA/Sauropsida/Ornithischia	undetermined	T	Late Cretaceous (Campanian)	F	9.355	6.886	521.9	77
DT10_5_L2	CHORDATA/Sauropsida/Ornithischia	undetermined	T	Late Cretaceous (Campanian)	F	9.387	6.892	525.9	77
DT10_5_L1	CHORDATA/Sauropsida/Ornithischia	undetermined	T	Late Cretaceous (Campanian)	F	9.401	6.883	526.9	77
DT8_2_B	CHORDATA/Sauropsida/Saurischia	undetermined	T	Late Cretaceous (Campanian)	F	9.355	6.884	521.8	77
DT1_1	CHORDATA/Sauropsida/Saurischia	undetermined	T	Late Cretaceous (Campanian)	F	9.360	6.879	522.0	77
DT8_2_A	CHORDATA/Sauropsida/Saurischia	undetermined	T	Late Cretaceous (Campanian)	F	9.360	6.882	522.1	77
DT2_1	CHORDATA/Sauropsida/Saurischia	undetermined	T	Late Cretaceous (Campanian)	F	9.356	6.889	522.2	77
DT15_6	CHORDATA/Sauropsida/Saurischia	undetermined	T	Late Cretaceous (Campanian)	F	9.359	6.891	522.7	77
DT10_2_L2	CHORDATA/Sauropsida/Saurischia	undetermined	T	Late Cretaceous (Campanian)	F	9.374	6.886	524.0	77

ID	Taxonomy	Identification		Age					
DT10_2_L1	CHORDATA/Sauropsida/Saurischia	undetermined	T	Late Cretaceous (Campanian)	F	9.406	6.896	528.4	77
56_1	CHORDATA/Aves/Galliformes	*Gallus gallus domesticus* (Linnaeus, 1758)	B	Recent	D	9.463	6.892	534.5	0.000001
B63	CHORDATA/Aves/Odontopterygiformes	*Odontopteryx* sp.	B	Eocene	F	9.353	6.885	521.6	55
B42	CHORDATA/Mammalia/Artiodactyla	*Dama dama* (Linnaeus, 1758)	B	Late Pleistocene	F	9.365	6.891	523.4	0.12
B24_2	CHORDATA/Mammalia/Artiodactyla	*Ovis aries* Linnaeus, 1758	T	Recent (1998)	D	9.401	6.874	526.1	0.00003
B45_1	CHORDATA/Mammalia/Artiodactyla	*Dama eurygonos* (Azzaroli, 1947)	B	Early Pleistocene	F	9.409	6.882	527.7	1.5
B45_2	CHORDATA/Mammalia/Artiodactyla	*Dama eurygonos* (Azzaroli, 1947)	B	Early Pleistocene	F	9.410	6.884	527.9	1.5
B24_1	CHORDATA/Mammalia/Artiodactyla	*Ovis aries* Linnaeus, 1758	T	Recent (1998)	D	9.414	6.890	528.8	0.00003
B6_2	CHORDATA/Mammalia/Artiodactyla	*Bos taurus* Linnaeus, 1758	B	Recent	D	9.418	6.890	529.3	0.000001
B45	CHORDATA/Mammalia/Artiodactyla	*Dama eurygonos* (Azzaroli, 1947)	B	Early Pleistocene	F	9.420	6.890	529.4	1.5
B6_1	CHORDATA/Mammalia/Artiodactyla	*Bos taurus* Linnaeus, 1758	B	Recent	D	9.430	6.886	530.3	0.000001
B38.1	CHORDATA/Mammalia/Artiodactyla	*Sus scrofa domesticus* Linnaeus, 1758	T	Recent (2018)	D	9.444	6.878	531.3	0.000001
B47_2	CHORDATA/Mammalia/Carnivora	*Canis lupus* Linnaeus, 1758	B	Late Pleistocene	F	9.364	6.894	523.5	0.12
B47_1	CHORDATA/Mammalia/Carnivora	*Canis lupus* Linnaeus, 1758	B	Late Pleistocene	F	9.381	6.892	525.3	0.12
B46_1	CHORDATA/Mammalia/Carnivora	*Ursus etruscus* (Cuvier, 1823)	B	Early Pleistocene	F	9.393	6.892	526.6	1.5
B46_2	CHORDATA/Mammalia/Carnivora	*Ursus etruscus* (Cuvier, 1823)	B	Early Pleistocene	F	9.402	6.886	527.1	1.5
B17	CHORDATA/Mammalia/Primates	*Homo sapiens* (Linnaeus, 1758)	B	Recent (2017)	A	9.374	6.865	522.4	0.000002
B54	CHORDATA/Mammalia/Primates	*Homo sapiens* (Linnaeus, 1758)	B	Recent (2018)	D	9.389	6.873	524.8	0.000001
B21.5_B	CHORDATA/Mammalia/Primates	*Homo sapiens* (Linnaeus, 1758)	T	Recent (2018)	A	9.392	6.892	526.4	0.000001
B21.5_A	CHORDATA/Mammalia/Primates	*Homo sapiens* (Linnaeus, 1758)	T	Recent (2018)	A	9.439	6.884	531.2	0.000001
21_1_3	CHORDATA/Mammalia/Primates	*Homo sapiens* (Linnaeus, 1758)	T	Recent (2018)	A	9.445	6.880	531.4	0.000001
B21_1_I+2	CHORDATA/Mammalia/Primates	*Homo sapiens* (Linnaeus, 1758)	T	Recent (2018)	A	9.445	6.880	531.4	0.000001
AM11	CHORDATA/Mammalia/Primates	*Homo sapiens* (Linnaeus, 1758)	T	Recent (2018)	A	9.455	6.882	532.8	0.000001
B39_4	CHORDATA/Mammalia/Proboscidea	*Mammuthus* sp.	T	Pleistocene	F	9.371	6.869	522.3	unknown
B41_2	CHORDATA/Mammalia/Proboscidea	*"Mastodon" gigantorostris* (Klähn, 1922)	T	late Miocene	F	9.414	6.871	527.3	unknown
B39_3	CHORDATA/Mammalia/Proboscidea	*Mammuthus* sp.	T	Pleistocene	F	9.424	6.891	530.0	unknown
B40_1	CHORDATA/Mammalia/Proboscidea	*Elephas* sp.	T	Pliocene	F	9.430	6.886	530.2	unknown
B39	CHORDATA/Mammalia/Proboscidea	*Mammuthus* sp.	T	Pleistocene	F	9.425	6.892	530.2	unknown
B41_1	CHORDATA/Mammalia/Proboscidea	*"Mastodon" gigantorostris* (Klähn, 1922)	T	late Miocene	F	9.435	6.887	530.9	unknown
B41_3	CHORDATA/Mammalia/Proboscidea	*"Mastodon" gigantorostris* (Klähn, 1922)	T	late Miocene	F	9.439	6.884	531.1	unknown
B40_2	CHORDATA/Mammalia/Proboscidea	*Elephas* sp.	T	Pliocene	F	9.433	6.893	531.3	unknown
P10	?	undetermined skeletal element	O	Silurian (Ludlow, latest Gorstian-early Ludfordian)	F	9.345	6.895	521.5	426
P06	?	?Conodont pearl	O	Silurian (Ludlow, latest Gorstian-early Ludfordian)	F	9.362	6.882	522.4	426
A96	?	undetermined	O	Cambrian Furongian (Paibian)	F	9.345	6.909	522.5	496
P02	?	?Conodont pearl	O	Silurian (Ludlow, latest Gorstian-early Ludfordian)	F	9.364	6.884	522.8	426
A97	?	undetermined	O	Cambrian Furongian (Paibian)	F	9.357	6.899	523.0	496
P04	?	?Conodont pearl	O	Silurian (Ludlow, latest Gorstian-early Ludfordian)	F	9.364	6.888	523.1	426
P07	?	?Conodont pearl	O	Silurian (Ludlow, latest Gorstian-early Ludfordian)	F	9.367	6.884	523.1	426
P26	?	undetermined skeletal element	O	Silurian (Ludlow, latest Gorstian-early Ludfordian)	F	9.363	6.892	523.2	426
P27	?	undetermined skeletal element	O	Silurian (Ludlow, latest Gorstian-early Ludfordian)	F	9.363	6.892	523.2	426
P69	?	undetermined skeletal element	O	Silurian (Ludlow, latest Gorstian-early Ludfordian)	F	9.371	6.883	523.4	426
P25	?	undetermined skeletal element	O	Silurian (Ludlow, latest Gorstian-early Ludfordian)	F	9.368	6.89	523.7	426
A95	?	undetermined	O	Cambrian Furongian (Paibian)	F	9.358	6.905	523.7	496
P22	?	undetermined skeletal element	O	Silurian (Ludlow, latest Gorstian-early Ludfordian)	F	9.369	6.891	523.8	426
P23	?	undetermined skeletal element	O	Silurian (Ludlow, latest Gorstian-early Ludfordian)	F	9.369	6.891	523.8	426
P21	?	undetermined skeletal element	O	Silurian (Ludlow, latest Gorstian-early Ludfordian)	F	9.37	6.89	523.9	426
P03	?	?Conodont pearl	O	Silurian (Ludlow, latest Gorstian-early Ludfordian)	F	9.374	6.886	524	426
P20	?	undetermined skeletal element	O	Silurian (Ludlow, latest Gorstian-early Ludfordian)	F	9.368	6.896	524.1	426
P08	?	?Conodont pearl	O	Silurian (Ludlow, latest Gorstian-early Ludfordian)	F	9.374	6.888	524.2	426
P49	?	undetermined skeletal element	O	Silurian (Ludlow, latest Gorstian-early Ludfordian)	F	9.376	6.886	524.2	426
P24	?	undetermined skeletal element	O	Silurian (Ludlow, latest Gorstian-early Ludfordian)	F	9.369	6.897	524.3	426
P12	?	?Conodont pearl	O	Silurian (Ludlow, latest Gorstian-early Ludfordian)	F	9.375	6.892	524.6	426
P14	?	undetermined skeletal element	O	Silurian (Ludlow, latest Gorstian-early Ludfordian)	F	9.374	6.896	524.8	426

Tab. 2 SOM | Taxa analyzed from literature[20-30].

CODE	PHYLUM (Subphylum)/Class/Order	TAXONOMIC ASSIGNMENT	BONE (B), TEETH (T), SHELL (S), OTHER (O)	AGE	DEAD (D), FOSSIL (F), ALIVE (A)	a	c	CELL VOLUME (Å³)	NUMERICAL AGE (Ma)
55 L	BRACHIOPODA (Linguliformea)/Lingulata//Lingulida	*Ungula ingrica*	S	late Cambrian (Furongian)	F	9.34	6.898	521.1	490
53 L	BRACHIOPODA (Linguliformea)/Lingulata//Lingulida	*Ungula ingrica*	S	late Cambrian (Furongian)	F	9.342	6.899	521.4	490
57 L	BRACHIOPODA (Linguliformea)/Lingulata//Lingulida	*Ungula ingrica*	S	late Cambrian (Furongian)	F	9.342	6.899	521.4	490
52 L	BRACHIOPODA (Linguliformea)/Lingulata//Lingulida	*Ungula ingrica*	S	late Cambrian (Furongian)	F	9.344	6.897	521.5	490
54 L	BRACHIOPODA (Linguliformea)/Lingulata//Lingulida	*Ungula ingrica*	S	late Cambrian (Furongian)	F	9.344	6.897	521.5	490
51 L	BRACHIOPODA (Linguliformea)/Lingulata//Lingulida	*Ungula ingrica*	S	late Cambrian (Furongian)	F	9.346	6.896	521.7	490
59 L	BRACHIOPODA (Linguliformea)/Lingulata//Lingulida	*Ungula ingrica*	S	late Cambrian (Furongian)	F	9.344	6.899	521.7	490
60 L	BRACHIOPODA (Linguliformea)/Lingulata//Lingulida	*Ungula ingrica*	S	late Cambrian (Furongian)	F	9.344	6.899	521.7	490
56 L	BRACHIOPODA (Linguliformea)/Lingulata//Lingulida	*Ungula ingrica*	S	late Cambrian (Furongian)	F	9.346	6.898	521.8	490
58 L	BRACHIOPODA (Linguliformea)/Lingulata//Lingulida	*Ungula ingrica*	S	late Cambrian (Furongian)	F	9.347	6.897	521.8	490
63 L	BRACHIOPODA (Linguliformea)/Lingulata//Lingulida	*Ungula ingrica*	S	late Cambrian (Furongian)	F	9.377	6.896	525.1	490
68 L	BRACHIOPODA (Linguliformea)/Lingulata//Lingulida	*Ungula ingrica*	S	late Cambrian (Furongian)	F	9.383	6.893	525.6	490
70 L	BRACHIOPODA (Linguliformea)/Lingulata//Lingulida	*Ungula ingrica*	S	late Cambrian (Furongian)	F	9.386	6.892	525.8	490
69 L	BRACHIOPODA (Linguliformea)/Lingulata//Lingulida	*Ungula ingrica*	S	late Cambrian (Furongian)	F	9.388	6.893	526.1	490
64 L	BRACHIOPODA (Linguliformea)/Lingulata//Lingulida	*Ungula ingrica*	S	late Cambrian (Furongian)	F	9.389	6.893	526.2	490
61 L	BRACHIOPODA (Linguliformea)/Lingulata//Lingulida	*Ungula ingrica*	S	late Cambrian (Furongian)	F	9.391	6.891	526.3	490
66 L	BRACHIOPODA (Linguliformea)/Lingulata//Lingulida	*Ungula ingrica*	S	late Cambrian (Furongian)	F	9.391	6.895	526.6	490
62 L	BRACHIOPODA (Linguliformea)/Lingulata//Lingulida	*Ungula ingrica*	S	late Cambrian (Furongian)	F	9.394	6.894	526.9	490
67 L	BRACHIOPODA (Linguliformea)/Lingulata//Lingulida	*Ungula ingrica*	S	late Cambrian (Furongian)	F	9.394	6.894	526.9	490
65 L	BRACHIOPODA (Linguliformea)/Lingulata//Lingulida	*Ungula ingrica*	S	late Cambrian (Furongian)	F	9.397	6.894	527.2	490
96 L	BRACHIOPODA (Linguliformea)	undetermined	S	unknown	?	9.379	6.871	523.4	unknown
95 L	BRACHIOPODA (Linguliformea)	undetermined	S	unknown	?	9.38	6.873	523.7	unknown
94 L	BRACHIOPODA (Linguliformea)	undetermined	S	unknown	?	9.385	6.871	524.1	unknown
71 L	CHORDATA/Chondrichthyes	undetermined	T	Recent	A	9.395	6.875	525.5	0.000001
74 L	CHORDATA/Chondrichthyes	undetermined	T	Cenozoic	F	9.379	6.884	524.4	33
73 L	CHORDATA/Chondrichthyes	undetermined	T	Cenozoic	F	9.385	6.884	525.1	33
75 L	CHORDATA/Chondrichthyes	undetermined	T	Paleogene	F	9.385	6.886	525.3	44
4 L	CHORDATA/Chondrichthyes	undetermined	T	Jurassic	F	9.385	6.884	525.1	173
10 L	CHORDATA/Chondrichthyes/Lamniformes	*Isurus oxyrinchus*	T	Recent	D	9.404	6.877	526.7	0.000001
3 L	CHORDATA/Osteichthyes	Sarcopterygii gen. et sp. indet.	T	Devonian	F	9.369	6.886	523.5	389
81 L	CHORDATA/Osteichthyes	undetermined	B	unknown	F	9.328	6.889	519.1	unknown
79 L	CHORDATA/Osteichthyes	undetermined	B	unknown	F	9.348	6.882	520.8	unknown
80 L	CHORDATA/Osteichthyes	undetermined	B	unknown	F	9.349	6.892	521.7	unknown
83 L	CHORDATA/Osteichthyes	undetermined	B	unknown	?	9.352	6.889	521.8	unknown
78 L	CHORDATA/Osteichthyes	undetermined	B	unknown	F	9.355	6.886	521.9	unknown
11 L	CHORDATA/Osteichthyes/Coelacanthiformes	*Latimeria chalumnae*	O	Recent	D	9.438	6.879	530.7	0.000001
12 L	CHORDATA/Osteichthyes/Cypriniformes	*Abramis brama*	T	Recent	D	9.449	6.872	531.4	0.000001
72 L	CHORDATA/Osteichthyes/Gadiformes	undetermined	T	Recent	A	9.381	6.889	525.0	0.000001
1 L	CHORDATA/Osteichthyes/Porolepiformes	*Glyptolepis* sp.	T	Devonian	F	9.376	6.888	524.4	389
2 L	CHORDATA/Osteichthyes/Porolepiformes	*Glyptolepis* sp.	T	Devonian	F	9.382	6.889	525.1	389
107 L	CHORDATA/Osteichthyes/Salmoniformes	*Salmo salar*	O	Recent	D	9.445	6.854	529.5	0.000001
82 L	CHORDATA/Osteichthyes/Siluriformes	undetermined	B	unknown	?	9.367	6.885	523.2	unknown
145 L	CHORDATA/Amphibia	undetermined	B	Middle Triassic (Anisian-Ladinian)	F	9.360888	6.892	523.0	240
144 L	CHORDATA/Amphibia/Temnospondyli	*Eryosuchus* sp.	B	Middle Triassic (Anisian)	F	9.364593	6.893	523.5	243
192 L	CHORDATA/Reptilia	undetermined	B	Middle Pleistocene	F	9.363638	6.911	524.8	0.5
183 L	CHORDATA/Reptilia	undetermined	B	late Miocene	F	9.363277	6.906	524.3	8.6
181 L	CHORDATA/Reptilia	undetermined	B	late Miocene	F	9.37151	6.899	524.7	10.5
114 L	CHORDATA/Reptilia	undetermined	B	Eocene (Priabonian)	F	9.358	6.906	523.7	36
176 L	CHORDATA/Reptilia	undetermined	B	Eocene (Priabonian)	F	9.359058	6.903	523.6	40
172 L	CHORDATA/Reptilia	undetermined	B	Eocene (early Lutetian)	F	9.348341	6.901	522.3	45
171 L	CHORDATA/Reptilia	undetermined	B	Eocene (early Lutetian)	F	9.357964	6.900	523.3	45
111 L	CHORDATA/Reptilia	undetermined	B	Late Cretaceous	F	9.356	6.889	522.2	86
110 L	CHORDATA/Reptilia	"ziphodont"	T	Late Cretaceous	F	9.369	6.895	524.1	86
177 L	CHORDATA/Reptilia	undetermined	B	Eocene (early Lutetian) - early Miocene	F	9.363519	6.893	523.4	unknown
143 L	CHORDATA/Reptilia/Therapsida	Seymouriamorpha	B	Middle Triassic (Anisian)	F	9.363287	6.894	523.4	245
108 L	CHORDATA/Reptilia/Therapsida	Seymouriamorpha	B	Middle Triassic (Anisian)	F	9.371	6.898	524.6	245
170 L	CHORDATA/Sauropsida	undetermined	B	Late Cretaceous (Maastrichtian)	F	9.35698	6.900	523.2	69
165 L	CHORDATA/Sauropsida	undetermined	B	Late Cretaceous	F	9.343188	6.902	521.8	86
169 L	CHORDATA/Sauropsida	undetermined	B	Late Cretaceous	F	9.355347	6.897	522.8	86
168 L	CHORDATA/Sauropsida	undetermined	B	Late Cretaceous	F	9.357479	6.899	523.2	86
166 L	CHORDATA/Sauropsida	undetermined	B	Late Cretaceous	F	9.366168	6.897	524.0	86
167 L	CHORDATA/Sauropsida	undetermined	B	Late Cretaceous	F	9.364221	6.900	524.0	86
106 L	CHORDATA/Sauropsida	*Stygimoloch spinifer*	O	Late Cretaceous	F	9.386	6.89	525.7	86
160 L	CHORDATA/Sauropsida	undetermined	B	Early Cretaceous (Aptian)	F	9.341657	6.895	521.1	119
109 L	CHORDATA/Sauropsida	undetermined	B	Early Cretaceous (Aptian)	F	9.347	6.897	521.8	119
161 L	CHORDATA/Sauropsida	undetermined	B	Early Cretaceous (Aptian)	F	9.35994	6.893	523.0	119
155 L	CHORDATA/Sauropsida	Ornithopoda	B	Early Cretaceous (Aptian)	F	9.364989	6.899	524.0	119
162 L	CHORDATA/Sauropsida	undetermined	B	Early Cretaceous (Aptian)	F	9.366312	6.901	524.3	119
159 L	CHORDATA/Sauropsida	undetermined	B	Early Cretaceous (Aptian)	F	9.371423	6.894	524.3	119
158 L	CHORDATA/Sauropsida	undetermined	B	Early Cretaceous (Aptian)	F	9.37455	6.894	524.7	119
154 L	CHORDATA/Sauropsida	undetermined	B	Early Cretaceous (Aptian)	F	9.378136	6.897	525.3	119

ID	Taxon	Species		Age					
157 L	CHORDATA/Sauropsida	undetermined	B	Early Cretaceous (Aptian)	F	9.380623	6.894	525.4	119
156 L	CHORDATA/Sauropsida	undetermined	B	Early Cretaceous (Aptian)	F	9.381851	6.896	525.7	119
153 L	CHORDATA/Sauropsida	undetermined	B	Early Cretaceous (Barremian)	F	9.361382	6.903	523.9	127
150 L	CHORDATA/Sauropsida	undetermined	B	Early Cretaceous (Barremian)	F	9.367329	6.897	524.1	127
151 L	CHORDATA/Sauropsida	undetermined	B	Early Cretaceous (Barremian)	F	9.369366	6.899	524.5	127
152 L	CHORDATA/Sauropsida	undetermined	B	Early Cretaceous (Barremian)	F	9.373435	6.903	525.3	127
146 L	CHORDATA/Sauropsida	undetermined	B	Late Jurassic - Early Cretaceous	F	9.360872	6.894	523.2	147
149 L	CHORDATA/Sauropsida	undetermined	B	Late Jurassic - Early Cretaceous	F	9.35806	6.905	523.7	147
148 L	CHORDATA/Sauropsida	undetermined	B	Late Jurassic - Early Cretaceous	F	9.362523	6.900	523.8	147
147 L	CHORDATA/Sauropsida	undetermined	B	Late Jurassic - Early Cretaceous	F	9.36649	6.901	524.3	147
112 L	CHORDATA/Sauropsida/Ornithischia	undetermined	B	Late Cretaceous	F	9.364	6.889	523.1	86
164 L	CHORDATA/Sauropsida/Ornithischia	undetermined	B	Late Cretaceous	F	9.365453	6.897	523.9	86
163 L	CHORDATA/Sauropsida/Ornithischia	undetermined	B	Late Cretaceous	F	9.372176	6.890	524.1	86
113 L	CHORDATA/Sauropsida/Ornithischia	undetermined	B	Late Cretaceous	F	9.364	6.906	524.4	86
24 L	CHORDATA/Aves/Galliformes	Gallus gallus domesticus	B	Recent	D	9.423	6.883	529.3	0.000001
13 L	CHORDATA/Aves/Galliformes	Gallus gallus domesticus	B	Recent	D	9.482	6.895	536.9	0.000001
198 L	CHORDATA/Mammalia	undetermined	B	Late Pleistocene	F	9.387551	6.893	526.1	0.06
197 L	CHORDATA/Mammalia	undetermined	B	Late Pleistocene	F	9.385173	6.902	526.5	0.06
196 L	CHORDATA/Mammalia	undetermined	B	Late Pleistocene	F	9.387101	6.901	526.6	0.06
180 L	CHORDATA/Mammalia	undetermined	B	middle Miocene (13-11 Ma)	F	9.368866	6.900	524.5	12
173 L	CHORDATA/Mammalia	undetermined	B	Eocene (early Lutetian)	F	9.346995	6.894	521.6	45
86 L	CHORDATA/Mammalia	undetermined	B	unknown	?	9.362	6.901	523.8	unknown
85 L	CHORDATA/Mammalia	undetermined	B	unknown	?	9.39	6.906	527.3	unknown
84 L	CHORDATA/Mammalia	undetermined	B	unknown	?	9.396	6.904	527.9	unknown
91 L	CHORDATA/Mammalia/?Cetartiodactyla	undetermined	B	unknown	F	9.332	6.887	519.4	unknown
90 L	CHORDATA/Mammalia/?Cetartiodactyla	undetermined	B	unknown	F	9.332	6.894	519.9	unknown
92 L	CHORDATA/Mammalia/?Cetartiodactyla	undetermined	B	unknown	F	9.332	6.896	520.1	unknown
89 L	CHORDATA/Mammalia/?Cetartiodactyla	undetermined	B	unknown	F	9.339	6.895	520.8	unknown
93 L	CHORDATA/Mammalia/?Cetartiodactyla	undetermined	B	unknown	F	9.349	6.894	521.8	unknown
88 L	CHORDATA/Mammalia/?Cetartiodactyla	undetermined	B	unknown	F	9.36	6.888	522.6	unknown
87 L	CHORDATA/Mammalia/?Cetartiodactyla	undetermined	B	unknown	F	9.372	6.889	524.0	unknown
26 L	CHORDATA/Mammalia/Artiodactyla	Cervus elaphus	B	Recent	D	9.414	6.884	528.3	0.000001
25 L	CHORDATA/Mammalia/Artiodactyla	Bos taurus	B	Recent	D	9.414	6.8842	528.4	0.000001
29 L	CHORDATA/Mammalia/Artiodactyla	Capra aegagrus hircus	B	Recent	D	9.413	6.8863	528.4	0.000001
32 L	CHORDATA/Mammalia/Artiodactyla	Sus scrofa domesticus	B	Recent	D	9.414	6.885	528.4	0.000001
35 L	CHORDATA/Mammalia/Artiodactyla	Ovis aries	B	Recent	D	9.416	6.883	528.5	0.000001
130 L	CHORDATA/Mammalia/Artiodactyla	Capra aegagrus hircus	B	Recent	D	9.4221	6.8899	529.7	0.000001
18 L	CHORDATA/Mammalia/Artiodactyla	Capra aegagrus hircus	B	Recent	D	9.46	6.904	535.1	0.000001
14 L	CHORDATA/Mammalia/Artiodactyla	Bos taurus	B	Recent	D	9.464	6.9	535.2	0.000001
23 L	CHORDATA/Mammalia/Artiodactyla	Ovis aries	B	Recent	D	9.479	6.898	536.8	0.000001
15 L	CHORDATA/Mammalia/Artiodactyla	Cervus elaphus	B	Recent	D	9.479	6.9	536.9	0.000001
21 L	CHORDATA/Mammalia/Artiodactyla	Sus scrofa domesticus	B	Recent	D	9.484	6.899	537.4	0.000001
27 L	CHORDATA/Mammalia/Carnivora	Canis lupus familiaris	B	Recent	D	9.413	6.888	528.5	0.000001
16 L	CHORDATA/Mammalia/Carnivora	Canis lupus familiaris	B	Recent	D	9.467	6.902	535.7	0.000001
33 L	CHORDATA/Mammalia/Lagomorpha	Oryctolagus cuniculus	B	Recent	D	9.413	6.886	528.4	0.000001
131 L	CHORDATA/Mammalia/Lagomorpha	undetermined	B	Recent	D	9.4217	6.8986	530.3	0.000001
22 L	CHORDATA/Mammalia/Lagomorpha	Oryctolagus cuniculus	B	Recent	D	9.471	6.898	535.9	0.000001
201 L	CHORDATA/Mammalia/Lagomorpha	Prolagus sardus	B	Holocene	F	9.412232	6.896	529.1	0.007
188 L	CHORDATA/Mammalia/Perissodactyla	undetermined	B	Early Peistocene	F	9.422551	6.893	530.0	0.9
184 L	CHORDATA/Mammalia/Perissodactyla	Stephanorhinus etruscus	B	early Pliocene	F	9.366651	6.903	524.5	4
102 L	CHORDATA/Mammalia/Primates	Homo sapiens	B	Recent	A	9.3836	6.8745	524.2	0.000001
31 L	CHORDATA/Mammalia/Primates	Macaca mulatta	B	Recent	D	9.413	6.886	528.4	0.000001
129 L	CHORDATA/Mammalia/Primates	Homo sapiens	B	Recent	A	9.4177	6.8838	528.7	0.000001
30 L	CHORDATA/Mammalia/Primates	Homo sapiens	B	Recent	D	9.414	6.894	529.1	0.000001
45 L	CHORDATA/Mammalia/Primates	Homo sapiens	O	Recent	A	9.42	6.89	529.5	0.000001
46 L	CHORDATA/Mammalia/Primates	Homo sapiens	O	Recent	A	9.42	6.89	529.5	0.000001
47 L	CHORDATA/Mammalia/Primates	Homo sapiens	O	Recent	A	9.42	6.89	529.5	0.000001
48 L	CHORDATA/Mammalia/Primates	Homo sapiens	O	Recent	A	9.42	6.89	529.5	0.000001
49 L	CHORDATA/Mammalia/Primates	Homo sapiens	O	Recent	A	9.42	6.89	529.5	0.000001
132 L	CHORDATA/Mammalia/Primates	Homo sapiens	T	Recent	A	9.4222	6.8869	529.5	0.000001
118 L	CHORDATA/Mammalia/Primates	Homo sapiens	B	Recent	D	9.425	6.888	529.9	0.000001
36 L	CHORDATA/Mammalia/Primates	Homo sapiens	O	Recent	A	9.423	6.904	530.3	0.000001
38 L	CHORDATA/Mammalia/Primates	Homo sapiens	O	Recent	A	9.426	6.908	530.3	0.000001
40 L	CHORDATA/Mammalia/Primates	Homo sapiens	O	Recent	A	9.429	6.904	530.3	0.000001
104 L	CHORDATA/Mammalia/Primates	Homo sapiens	B	Recent	A	9.4405	6.8766	530.8	0.000001
123 L	CHORDATA/Mammalia/Primates	Homo sapiens	B	Recent	D	9.429	6.897	531.0	0.000001
119 L	CHORDATA/Mammalia/Primates	Homo sapiens	T	Recent	D	9.438	6.887	531.3	0.000001
37 L	CHORDATA/Mammalia/Primates	Homo sapiens	O	Recent	A	9.436	6.904	531.4	0.000001
103 L	CHORDATA/Mammalia/Primates	Homo sapiens	B	Recent	A	9.4411	6.8862	531.6	0.000001
128 L	CHORDATA/Mammalia/Primates	Homo sapiens	T	Recent	D	9.442	6.886	531.6	0.000001
121 L	CHORDATA/Mammalia/Primates	Homo sapiens	B	Recent	D	9.437	6.899	532.1	0.000001
9 L	CHORDATA/Mammalia/Primates	Homo sapiens	T	Recent	A	9.448	6.884	532.2	0.000001
8 L	CHORDATA/Mammalia/Primates	Homo sapiens	T	Recent	A	9.449	6.883	532.2	0.000001

39 L	CHORDATA/Mammalia/Primates	*Homo sapiens*	O	Recent	A	9.44	6.9	532.5	0.000001
120 L	CHORDATA/Mammalia/Primates	*Homo sapiens*	B	Recent	D	9.446	6.894	532.7	0.000001
122 L	CHORDATA/Mammalia/Primates	*Homo sapiens*	B	Recent	D	9.442	6.9	532.7	0.000001
19 L	CHORDATA/Mammalia/Primates	*Homo sapiens*	B	Recent	D	9.441	6.902	532.8	0.000001
124 L	CHORDATA/Mammalia/Primates	*Homo sapiens*	B	Recent	D	9.441	6.905	533.0	0.000001
41 L	CHORDATA/Mammalia/Primates	*Homo sapiens*	T	Recent	A	9.461	6.904	534.8	0.000001
126 L	CHORDATA/Mammalia/Primates	*Homo sapiens*	B	Recent	D	9.453	6.912	534.9	0.000001
20 L	CHORDATA/Mammalia/Primates	*Macaca mulatta*	B	Recent	D	9.467	6.906	536.0	0.000001
125 L	CHORDATA/Mammalia/Primates	*Homo sapiens*	B	Recent	D	9.473	6.932	538.7	0.000001
127 L	CHORDATA/Mammalia/Primates	*Homo sapiens*	B	Recent	D	9.511	6.965	545.6	0.000001
203 L	CHORDATA/Mammalia/Primates	*Rhesus sp.*	B	Holocene	D	9.432382	6.902	531.8	0.000013
7 L	CHORDATA/Mammalia/Primates	*Homo sapiens*	T	18th century	D	9.43	6.883	530.1	0.00027
6 L	CHORDATA/Mammalia/Primates	*Homo sapiens*	T	18th century	D	9.443	6.884	531.6	0.00027
5 L	CHORDATA/Mammalia/Primates	*Homo sapiens*	T	14th century	D	9.446	6.884	531.9	0.00067
117 L	CHORDATA/Mammalia/Primates	*Homo sapiens*	B	Holocene	D	9.426	6.882	529.5	0.0024
202 L	CHORDATA/Mammalia/Primates	*Homo sapiens*	B	Holocene	F	9.43115	6.899	531.4	0.0024
116 L	CHORDATA/Mammalia/Primates	*Homo sapiens*	B	Holocene	D	9.423	6.888	529.7	0.0027
115 L	CHORDATA/Mammalia/Primates	*Homo sapiens*	O	Holocene	D	9.431	6.899	531.4	0.0031
199 L	CHORDATA/Mammalia/Primates	*Homo sapiens*	B	Holocene	F	9.447094	6.891	532.6	0.005
200 L	CHORDATA/Mammalia/Primates	*Homo sapiens*	B	Holocene	F	9.432193	6.888	530.7	0.007
50 L	CHORDATA/Mammalia/Primates	undetermined	B	Holocene	?	9.39	6.9	526.9	unknown
28 L	CHORDATA/Mammalia/Proboscidea	*Elephas maximus*	B	Recent	D	9.402	6.891	527.5	0.000001
17 L	CHORDATA/Mammalia/Proboscidea	*Elephas maximus*	B	Recent	D	9.463	6.907	535.6	0.000001
186 L	CHORDATA/Mammalia/Proboscidea	*Archidiskodon meridionalis*	B	Early Pleistocene	F	9.373583	6.897	524.8	0.9
185 L	CHORDATA/Mammalia/Proboscidea	undetermined	B	Early Pleistocene	F	9.382342	6.900	526.0	0.9
34 L	CHORDATA/Mammalia/Rodentia	*Rattus norvegicus*	B	Recent	D	9.428	6.8828	529.8	0.000001
195 L	?	undetermined	B	Late Pleistocene	F	9.385019	6.892	525.7	0.06
194 L	?	undetermined	B	Late Pleistocene	F	9.401429	6.892	527.6	0.06
193 L	?	undetermined	B	Late Pleistocene	F	9.411315	6.889	528.4	0.06
191 L	?	undetermined	B	Middle Pleistocene	F	9.40894	6.896	528.7	0.5
187 L	?	undetermined	B	Early Peistocene	F	9.371902	6.900	524.9	0.9
190 L	?	undetermined	B	Early Peistocene	F	9.400154	6.894	527.6	0.9
189 L	?	undetermined	B	Early Peistocene	F	9.407398	6.898	528.7	0.9
182 L	?	undetermined	B	late Miocene	F	9.367259	6.905	524.7	9.5
179 L	?	undetermined	B	late Miocene	F	9.3788	6.906	526.1	12
178 L	?	undetermined	B	early Miocene	F	9.363638	6.911	524.8	16
175 L	?	undetermined	B	Eocene (Priabonian)	F	9.361828	6.903	524.0	40
174 L	?	undetermined	B	Eocene (Bartonian)	F	9.386533	6.900	526.5	40

Conclusions

During this PhD project "*Bioapatite in fossil and living organisms*" we have worked with living, dead and fossil bioapatite from samples of the major phyla that share the use of this mineral with the purpose to unravel the response of bioapatite to fossilization and diagenesis and, in case, to decipher how the re-arrangements of the crystal lattice occur in geological time.

In the first part of the research, considering that crystal lattice parameters depend on major element substitutions, we set up the method in order to obtain proper standards and analytical conditions for quantifying major elements on bioapatite samples (*Malferrari et al., 2019,* Annex-1). We proposed a method that involves the use of home-made matrix matched calibration standards for laser ablation inductively coupled plasma mass spectrometry (LA-ICPMS). We demonstrated that matrix-matched calibration is mandatory for obtaining a reliable chemical characterization even if factors such as matrix aggregation variability, diverse presence of volatile compounds, the fossilization footprint and the instrumental variability can represent further variability parameters.. We also directly tested the method on chaetae, mineralized structures of the fireworm *Hermodice carunculata* (*Righi et al., 2020*, Annex-2) and demonstrated that the chemical composition and ultrastructure of the chaetae differ from other annelids promoting a debate insight the Scientific Community.

The first group of organisms that we processed are conodonts. We combined classic technique in conodont observation, like optical and electronic microscopy, with the crystallographic approach based on X-ray microdiffraction, previously (and for the first time) introduced in conodont study by our research group (*Ferretti et al., 2017*). In *Medici et al., 2020* (Annex-3) we showed that cell parameters of the crystal unit cell calculated for paraconodonts significantly differ from those derived for euconodonts. Moreover, we detected no correlation between cell parameters and age, taxonomic assignment, geographic provenance and, for euconodonts, CAI (correlated with heating during fossilization). Other phosphatic/phosphatized material from the same residue, that we considered too, are characterized by cell parameters values that appear to be mainly correlated with the type of organisms. It is also conceivable that major elements content strongly depends not only on fossilization and diagenesis, but mostly on the primary bioapatite composition.

In order to completely characterize conodonts, in *Medici et al., 2021* (Annex-4) we detected the uptake of HFSE in conodont elements recovered from a single stratigraphic horizon in the Upper Ordovician of Normandy (France). Assuming that all the samples have undergone an identical diagenetic history, we have assessed whether conodont taxonomy (and morphology) impacts HFSE uptake and the crystallinity index. We found that a clear diagenetic signature is present in all the samples, with significant differences among taxa. These distinctions are also evidenced by the crystallinity index (that strongly depends on the method adopted for its calculation) values which showed positive correlations with some elements and diagenesis.

With the two latter researches we identified the so call "conodont signature": a specific range of cell parameters of the crystal unit cell of conodont bioapatite. So, we considered the "conodont pearls" (*Ferretti et al., 2020,* Annex-5) and analysed them and all the phosphate/phosphatized material from the same residue, including conodonts, in order to identify a possible affinity of

the microspherules with some of the considered taxa. Our study indicated that bioapatite crystallographic parameters *a* and *c* and cell volume of the "pearls" are not similar to those of conodont, but appear to be included within the variability of bioapatite crystallographic lattice configuration of brachiopods from the same residue.

The final step of our work is described in *Ferretti et al. (submitted*, Annex-6) where the resulting collection of this PhD study (fossil, dead and living samples) from all the major groups that share the use of bioapatite were analysed. We confirmed that bioapatite is not stable in time and we showed that alive, dead and fossil organisms keep a distinct geometric signature in terms of apatite lattice cell parameters mirroring atom re-arrangements within cell crystal lattice. Plotting cell volume of the samples *vs* time, we showed that there is a general reduction of cell volume in time. More in detail, this comparison revealed that bioapatite transforms after death and changes start at the death of the organisms and reach a final stability only in mature fossils.

Despite the incredible progress made towards evaluating composition, structure and mechanisms of preservation of bones, teeth and shells, the results here provided as well as the critical analyses of literature revealed that there are still significant gaps in understanding of the process of fossilization of bioapatite material. More in detail, we believe that differences in the fossilization process, which may be more or less markedly influenced by taxonomy, will certainly have to be investigated in greater detail in the future. Likewise, it must be well considered the possible interferences determined by the type of hard tissue (such as, for example, enamel and dentin in the teeth) which, as showed in this study and in the literature, can "react" very differently in time.

Bibliography

Armstrong, H. A., Pearson, D. G. & Griselin, M. (2001). Thermal effects on rare earth element and strontium isotope chemistry in single conodont elements. *Geochimica et Cosmochimica Acta*, *65*(3), 435-441.

Arnott, H. J. & Pautard, F. G. (1970). Calcification in plants. In *Biological calcification: Cellular and molecular aspects* (pp. 375-446). Springer, Boston, MA.

Arsenault, M. & Janvier, P. (1991). The anaspid-like craniates of the Escuminac Formation (Upper Devonian) from Miguasha (Quebec, Canada), with remarks on anaspid-petromyzontid relationships. *Early vertebrates and related problems of evolutionary biology*, 19-40.

Balzer, A., Gleixner, G., Grupe, G., Schmidt, H. L., Schramm, S. & Turban-Just, S. (1997). In vitro decomposition of bone collagen by soil bacteria: the implications for stable isotope analysis in archaeometry. *Archaeometry*, *39*(2), 415-429.

Barakat, N. A., Khalil, K. A., Sheikh, F. A., Omran, A. M., Gaihre, B., Khil, S. M. & Kim, H. Y. (2008). Physiochemical characterizations of hydroxyapatite extracted from bovine bones by three different methods: extraction of biologically desirable HAp. *Materials Science and Engineering: C*, *28*(8), 1381-1387.

Becker, G. L., Chen, C. H., Greenawalt, J. W. & Lehninger, A. L. (1974). Calcium phosphate granules in the hepatopancreas of the blue crab Callinectes sapidus. *The Journal of Cell Biology*, *61*(2), 316-326.

Beresford, W. A. (1981). *Chondroid bone, secondary cartilage, and metaplasia*. Urban & Schwarzenberg.

Bocherens, H., Tresset, A., Wiedemann, F., Giligny, F., Lafage, F., Lanchon, Y. & Mariotti, A. (1997). Diagenetic evolution of mammal bones in two French Neolithic sites. *BULLETIN-SOCIETE GEOLOGIQUE DE FRANCE*, *168*, 555-564.

Boskey, A. L. (2007). Mineralization of bones and teeth. *Elements*, *3*(6), 385-391.

Brand, U., Logan, A., Hiller, N. & Richardson, J. (2003). Geochemistry of modern brachiopods: applications and implications for oceanography and paleoceanography. *Chemical Geology*, *198*(3-4), 305-334.

Bright, C. A., Cruse, A. M., Lyons, T. W., MacLeod, K. G., Glascock, M. D. & Ethington, R. L. (2009). Seawater rare-earth element patterns preserved in apatite of Pennsylvanian conodonts?. *Geochimica et Cosmochimica Acta*, *73*(6), 1609-1624.

Burke, E. A. (2008). Tidying up mineral names: an IMA-CNMNC scheme for suffixes, hyphens and diacritical marks. *Mineralogical record*, *39*(2), 131.

Carbonara, P. & Follesa, M. C. (2019). Handbook on fish age determination: a Mediterranean experience. *General Fisheries Commission for the Mediterranean. Studies and Reviews*, (98), I-179.

Carter, J. G. & Clark, G. R. (1985). Classification and phylogenetic significance of molluscan shell microstructure. *Studies in Geology, Notes for a Short Course*, *13*, 50-71.

Chen, J., Algeo, T. J., Zhao, L., Chen, Z. Q., Cao, L., Zhang, L. & Li, Y. (2015). Diagenetic uptake of rare earth elements by bioapatite, with an example from Lower Triassic conodonts of South China. *Earth-science reviews*, *149*, 181-202.

Child, A. M. (1995). Microbial taphonomy of archaeological bone. *Studies in conservation*, *40*(1), 19-30.

Cole, A. G. & Hall, B. K. (2004). The nature and significance of invertebrate cartilages revisited: distribution and histology of cartilage and cartilage-like tissues within the Metazoa. *Zoology*, *107*(4), 261-273.

Collins, M. J., Nielsen–Marsh, C. M., Hiller, J., Smith, C. I., Roberts, J. P., Prigodich, R. V., Wess, T. J., Csapò, J., Millard, A. R. & Turner–Walker, G. (2002). The survival of organic matter in bone: a review. *Archaeometry*, *44*(3), 383-394.

Currey, J. D. (2002). The structure of bone tissue. *Bones: Structure and mechanics*, 3-26.

Currey, J. D. (2004). Tensile yield in compact bone is determined by strain, post-yield behaviour by mineral content. *Journal of biomechanics*, *37*(4), 549-556.

Currey, J. D., Brear, K. & Zioupos, P. (2004). Notch sensitivity of mammalian mineralized tissues in impact. *Proceedings of the Royal Society of London. Series B: Biological Sciences*, *271*(1538), 517-522.

Cusack, M. & Williams, A. (2007). Biochemistry and diversity of brachiopod shells. *Treatise on Invertebrate Paleontology*, *Part H. Geological Society of America*, 2373 -2395. ISBN 9780813731360

Cusack, M., Williams, A. & Buckman, J. O. (1999). Chemico-structural evolution of linguloid brachiopod shells. *Palaeontology*, *42*(5), 799-840.

Daculsi, G. & Kerebel, B. (1978). High-resolution electron microscope study of human enamel crystallites: size, shape, and growth. *Journal of ultrastructure research*, *65*(2), 163-172.

Davit-Beal, T., Allizard, F. & Sire, J. Y. (2007). Enameloid/enamel transition through successive tooth replacements in Pleurodeles waltl (Lissamphibia, Caudata). *Cell and tissue research*, *328*(1), 167-183.

De Beer, G. R. (1937). *The development on the vertebrate skull* (No. 566 DEB) Oxford: Oxford University Press.

Dean, B. & Bhushan, B. (2010). Shark-skin surfaces for fluid-drag reduction in turbulent flow: a review. *Philosophical Transactions of the Royal Society A: Mathematical, Physical and Engineering Sciences*, *368*(1929), 4775-4806.

Denison, R. H. (1978). *Placodermi* (Vol. 2). München [Germany].

Donoghue, P. C. & Sansom, I. J. (2002). Origin and early evolution of vertebrate skeletonization. *Microscopy research and technique*, *59*(5), 352-372.

Donoghue, P. C. & Smith, M. P. (2001). The anatomy of Turinia pagei (Powrie), and the phylogenetic status of the Thelodonti. *Earth and Environmental Science Transactions of The Royal Society of Edinburgh*, *92*(1), 15-37.

Donoghue, P. C., Forey, P. L. & Aldridge, R. J. (2000). Conodont affinity and chordate phylogeny. *Biological Reviews*, *75*(2), 191-251.

Elliott, J. C. (2002). Calcium phosphate biominerals. *Reviews in Mineralogy and Geochemistry*, *48*(1), 427-453.

Elliott, J. C. (2013). *Structure and chemistry of the apatites and other calcium orthophosphates*. Elsevier.

Elliott, J. C., Mackie, P. E. & Young, R. A. (1973). Monoclinic hydroxyapatite. *Science*, *180*(4090), 1055-1057.

Ferretti, A., Malferrari, D., Medici, L. & Savioli, M. (2017). Diagenesis does not invent anything new: Precise replication of conodont structures by secondary apatite. *Scientific reports*, *7*(1), 1-9.

Ferretti, A., Malferrari, D., Savioli, M., Siepe, T. & Medici, L. (2020) 'Conodont pearls' do not belong to conodonts. *Lethaia*. <u>Annex-5</u>

Ferretti, A., Medici, L., Savioli, M., Mascia, M.T., & Malferrari. D. Dead, Fossil or Alive. *Submitted*. <u>Annex-6</u>

Forey, P. & Janvier, P. (1994). Evolution of the early vertebrates. *American Scientist*, *82*(6), 554-566.

Forey, P. L. (1995). Agnathans recent and fossil, and the origin of jawed vertebrates. *Reviews in Fish Biology and Fisheries*, *5*(3), 267-303.

Fournie, J. & Chetail, M. (1984). Calcium dynamics in land gastropods. *American Zoologist*, *24*(4), 857-870.

Francillon-Vieillot, H., De Buffrénil, V., Castanet, J. D., Géraudie, J., Meunier, F. J., Sire, J. Y., Zylberberg, L. & De Ricqlès, A. (1990). Microstructure and mineralization of vertebrate skeletal tissues. *Skeletal biomineralization: patterns, processes and evolutionary trends*, *1*, 471-530.

Garant, P. R. (2003). *Oral cells and tissues*. Quintessence,. ISSN: 0867154292.

Girard, C. & Albarède, F. (1996). Trace elements in conodont phosphates from the Frasnian/Famennian boundary. *Palaeogeography, Palaeoclimatology, Palaeoecology*, *126*(1-2), 195-209.

Glimcher, M. J. (2006). Bone: nature of the calcium phosphate crystals and cellular, structural, and physical chemical mechanisms in their formation. *Reviews in mineralogy and geochemistry*, *64*(1), 223-282.

Goodwin, M. B., Grant, P. G., Bench, G. & Holroyd, P. A. (2007). Elemental composition and diagenetic alteration of dinosaur bone: Distinguishing micron-scale spatial and compositional heterogeneity using PIXE. *Palaeogeography, Palaeoclimatology, Palaeoecology*, *253*(3-4), 458-476.

Grandjean, P., Cappetta, H., Michard, A. & Albarede, F. (1987). The assessment of REE patterns and 143Nd/144Nd ratios in fish remains. *Earth and Planetary Science Letters*, *84*(2-3), 181-196.

Grandjean-Lécuyer, P., Feist, R. & Albarède, F. (1993). Rare earth elements in old biogenic apatites. *Geochimica et Cosmochimica Acta*, *57*(11), 2507-2514.

Greenlee, D. M. (1996). An electron microprobe evaluation of diagenetic alteration in archaeological bone.

Gross, K. A. & Berndt, C. C. (2002). Biomedical application of apatites. *Reviews in mineralogy and geochemistry*, *48*(1), 631-672.

Grupe, G. (1995). Preservation of collagen in bone from dry, sandy soil. *Journal of Archaeological Science*, *22*(2), 193-199.

Guillong, M., Hametner, K., Reusser, E., Wilson, S. A. & Günther, D. (2005). Preliminary characterisation of new glass reference materials (GSA-1G, GSC-1G, GSD-1G and GSE-1G) by laser ablation-inductively coupled plasma-mass spectrometry using 193 nm, 213 nm and 266 nm wavelengths. *Geostandards and Geoanalytical Research*, *29*(3), 315-331.

Hassan, A. A., Termine, J. D. & Haynes, C. V. (1977). Mineralogical studies on bone apatite and their implications for radiocarbon dating. *Radiocarbon*, *19*(3), 364-374.

Hedges, R. E. (2002). Bone diagenesis: an overview of processes. *Archaeometry*, *44*(3), 319-328.

Hench, L. L. (1993). *An introduction to bioceramics* (Vol. 1). World scientific.

Herold, R. C., Graver, H. T. & Christner, P. (1980). Immunohistochemical localization of amelogenins in enameloid of lower vertebrate teeth. *Science*, *207*(4437), 1357-1358.

Herwartz, D., Tütken, T., Jochum, K. P. & Sander, P. M. (2013). Rare earth element systematics of fossil bone revealed by LA-ICPMS analysis. *Geochimica et Cosmochimica Acta*, *103*, 161-183.

Herwartz, D., Tütken, T., Münker, C., Jochum, K. P., Stoll, B. & Sander, P. M. (2011). Timescales and mechanisms of REE and Hf uptake in fossil bones. *Geochimica et Cosmochimica Acta*, *75*(1), 82-105.

Hinz, E. A. & Kohn, M. J. (2010). The effect of tissue structure and soil chemistry on trace element uptake in fossils. *Geochimica et Cosmochimica Acta*, *74*(11), 3213-3231.

Holser, W. T. (1997). Evaluation of the application of rare-earth elements to paleoceanography. *Palaeogeography, Palaeoclimatology, Palaeoecology*, *132*(1-4), 309-323.

Howard, B., Mitchell, P. C., Ritchie, A., Simkiss, K. & Taylor, M. (1981). The composition of intracellular granules from the metal-accumulating cells of the common garden snail (Helix aspersa). *Biochemical Journal*, *194*(2), 507-511.

Hughes, J. M. & Rakovan, J. (2002). The crystal structure of apatite, Ca5 (PO4) 3 (F, OH, Cl). *Reviews in Mineralogy and Geochemistry*, *48*(1), 1-12.

Huysseune, A. & Sire, J. Y. (1998). Evolution of patterns and processes in teeth and tooth-related tissues in non-mammalian vertebrates. *European journal of oral sciences*, *106*(S1), 437-481.

Imbeni, V., Kruzic, J. J., Marshall, G. W., Marshall, S. J. & Ritchie, R. O. (2005). The dentin–enamel junction and the fracture of human teeth. *Nature materials*, *4*(3), 229-232.

Jans, M. M. (2008). Microbial bioerosion of bone–a review. In *Current developments in bioerosion* (pp. 397-413). Springer, Berlin, Heidelberg.

Jans, M. M. E., Nielsen-Marsh, C. M., Smith, C. I., Collins, M. J. & Kars, H. (2004). Characterisation of microbial attack on archaeological bone. *Journal of Archaeological Science*, *31*(1), 87-95.

Janus, A. M., Faryna, M., Haberko, K., Rakowska, A. & Panz, T. (2008). Chemical and microstructural characterization of natural hydroxyapatite derived from pig bones. *Microchimica Acta*, *161*(3-4), 349-353.

Janvier, P. (1990). La structure de l'exosquelette des Galeaspida (Vertebrata). *CR Acad Sci Paris*, *310*, 655-659.

Joschek, S., Nies, B., Krotz, R. & Göpferich, A. (2000). Chemical and physicochemical characterization of porous hydroxyapatite ceramics made of natural bone. *Biomaterials*, *21*(16), 1645-1658.

Keenan, S. W. (2014). Gastrointestinal microbial diversity and diagenetic alteration of bone from the American alligator (Alligator mississippiensis). PhD diss., University of Tennessee, 2014.

Keenan, S. W. (2016). From bone to fossil: A review of the diagenesis of bioapatite. *American Mineralogist*, *101*(9), 1943-1951.

Keenan, S. W., Engel, A. S., Roy, A. & Bovenkamp-Langlois, G. L. (2015). Evaluating the consequences of diagenesis and fossilization on bioapatite lattice structure and composition. *Chemical Geology*, *413*, 18-27.

Kim, S. H., Shin, J. W., Park, S. A., Kim, Y. K., Park, M. S., Mok, J. M., Yang, W. I. & Lee, J. W. (2004). Chemical, structural properties, and osteoconductive effectiveness of bone block derived from porcine cancellous bone. *Journal of Biomedical Materials Research Part B: Applied Biomaterials: An Official Journal of The Society for Biomaterials, The Japanese Society for*

Biomaterials, and The Australian Society for Biomaterials and the Korean Society for Biomaterials, *68*(1), 69-74.

Kirkham, J., Zhang, J., Brookes, S. J., Shore, R. C., Wood, S. R., Smith, D. A., Wallwork, M. L., Ryu, O. H. & Robinson, C. (2000). Evidence for charge domains on developing enamel crystal surfaces. *Journal of dental research*, *79*(12), 1943-1947.

Kocsis, L., Trueman, C. N. & Palmer, M. R. (2010). Protracted diagenetic alteration of REE contents in fossil bioapatites: direct evidence from Lu–Hf isotope systematics. *Geochimica et Cosmochimica Acta*, *74*(21), 6077-6092.

Kolmas, J., Szwaja, M. & Kolodziejski, W. (2012). Solid-state NMR and IR characterization of commercial xenogeneic biomaterials used as bone substitutes. *Journal of pharmaceutical and biomedical analysis*, *61*, 136-141.

Kuhn, L. T., Grynpas, M. D., Rey, C. C., Wu, Y., Ackerman, J. L. & Glimcher, M. J. (2008). A comparison of the physical and chemical differences between cancellous and cortical bovine bone mineral at two ages. *Calcified tissue international*, *83*(2), 146-154.

Lambert, G., Lambert, C. C. & Lowenstam, H. A. (1990). Skeletal Biomineralization: Patterns, Processes and Evolutionary Trends, ed JG Carter.

Langille, R. M. & Hall, B. K. (1993). Pattern formation and the neural crest. *The skull*, *1*, 77-111.

Lee–Thorp, J. (2002). Two decades of progress towards understanding fossilization processes and isotopic signals in calcified tissue minerals. *Archaeometry*, *44*(3), 435-446.

LeGeros, R. Z. (1991). Calcium phosphates in oral biology and medicine. *Monographs in oral sciences*, *15*, 109-111.

LeGeros, R. Z. (1999). Calcium phosphates in demineralization/remineralization processes. *Journal of Clinical Dentistry*, *10*(2), 65-73.

LeGeros, R. Z. (2008). Calcium phosphate-based osteoinductive materials. *Chemical reviews*, *108*(11), 4742-4753.

LeGeros, R. Z., & LeGeros, J. P. (1984). Phosphate minerals in human tissues. In *Phosphate minerals* (pp. 351-385). Springer, Berlin, Heidelberg.

Leikina, E., Mertts, M. V., Kuznetsova, N., & Leikin, S. (2002). Type I collagen is thermally unstable at body temperature. *Proceedings of the National Academy of Sciences*, *99*(3), 1314-1318.

Liao, J., Sun, X., Li, D., Sa, R., Lu, Y., Lin, Z., Xu, L., Zhan, R., Pan, Y. & Xu, H. (2019). New insights into nanostructure and geochemistry of bioapatite in REE-rich deep-sea sediments: LA-ICP-MS, TEM, and Z-contrast imaging studies. *Chemical Geology*, *512*, 58-68.

Lin, C. P., Douglas, W. H. & Erlandsen, S. L. (1993). Scanning electron microscopy of type I collagen at the dentin-enamel junction of human teeth. *Journal of Histochemistry & Cytochemistry*, *41*(3), 381-388.

Liu, Q., Huang, S., Matinlinna, J. P., Chen, Z. & Pan, H. (2013). Insight into biological apatite: physiochemical properties and preparation approaches. *BioMed research international*, *2013*.

Liu, Y., Hu, Z., Gao, S., Günther, D., Xu, J., Gao, C. & Chen, H. (2008). In situ analysis of major and trace elements of anhydrous minerals by LA-ICP-MS without applying an internal standard. *Chemical Geology*, *257*(1-2), 34-43.

Lowenstam, H. A. & Rossman, G. R. (1975). Amorphous, hydrous, ferric phosphatic dermal granules in Molpadia (Holothuroidea): physical and chemical characterization and ecologic implications of the bioinorganic fraction. *Chemical geology*, *15*(1), 15-51.

Lowenstam, H. A. & Weiner, S. (1985). Transformation of amorphous calcium phosphate to crystalline dahillite in the radular teeth of chitons. *Science*, *227*(4682), 51-53.

Lowenstam, H. A. (1967). Lepidocrocite, an apatite mineral, and magnetite in teeth of chitons (Polyplacophora). *Science*, *156*(3780), 1373-1375.

Mackie, G. O. & Marx, R. M. (1988). Phosphatic spicules in the nematocyst batteries of Nanomia cara (Hydrozoa, Siphonophora). *Zoomorphology*, *108*(2), 85-91.

Malferrari, D., Ferretti, A., Mascia, M. T., Savioli, M. & Medici, L. (2019). How Much Can We Trust Major Element Quantification in Bioapatite Investigation?. *ACS omega*, *4*(18), 17814-17822. Annex-1

Mann, S. (2001). *Biomineralization: principles and concepts in bioinorganic materials chemistry* (Vol. 5). Oxford University Press on Demand.

Marinelli, W. & Strenger, A. (1954). *Vergleichende Anatomie und Morphologie der Wirbeltiere*. F. Deuticke.

McConnell, D. (2012). *Apatite: its crystal chemistry, mineralogy, utilization, and geologic and biologic occurrences* (Vol. 5). Springer Science & Business Media.

Medici L., Savioli M., Ferretti A. & Malferrari D. (2021). Zooming in REE and other trace elements on conodonts: Does taxonomy guide diagenesis? *Journal of Earth Science*, 1-11. Annex-4

Medici, L., Malferrari, D., Savioli, M. & Ferretti, A. (2020). Mineralogy and crystallization patterns in conodont bioapatite from first occurrence (Cambrian) to extinction (end-Triassic). *Palaeogeography, Palaeoclimatology, Palaeoecology*, *549*, 109098. Annex-3

Meunier, F. J. (1987). Os cellulaire, os acellulaire et tissus dérivés chez les ostéichthyiens: les phénomènes de l'acellularisation et de la perte de minéralisation. *L'Année biologique*, *26*(4), 201-233.

Min, Z. & Janvier, P. (1998). The histological structure of the endoskeleton in galeaspids (Galeaspida, Vertebrata). *Journal of Vertebrate Paleontology*, *18*(3), 650-654.

Moss, M. L. (1961). Studies of the acellular bone of teleost fish. *Cells Tissues Organs*, *46*(4), 343-362.

Moss, M. L. (1963). The biology of acellular teleost bone. *Annals of the New York Academy of Sciences*, *109*, 337-350.

Moss, M. L. (1964). Development of cellular dentin and lepidosteal tubules in the bowfin, Amia calva. *Cells Tissues Organs*, *58*(4), 333-354.

Moss, M. L. (1965). STUDIES OF THE ACELLULAR BONE OF TELEOST FISH. V. *Cells Tissues Organs*, *60*(2), 262-276.

Moss, M. L. (1970). Enamel and bone in shark teeth: with a note on fibrous enamel in fishes. *Cells Tissues Organs*, *77*(2), 161-187.

Murdock, D. J., Dong, X. P., Repetski, J. E., Marone, F., Stampanoni, M. & Donoghue, P. C. (2013). The origin of conodonts and of vertebrate mineralized skeletons. *Nature*, *502*(7472), 546-549.

Nemliher, J. G., Baturin, G. N., Kallaste, T. E. & Murdmaa, I. O. (2004). Transformation of hydroxyapatite of bone phosphate from the ocean bottom during fossilization. *Lithology and Mineral Resources*, *39*(5), 468-479.

Nielsen-Marsh, C. (1997). *Studies in archaeological bone diagenesis* (Doctoral dissertation, University of Oxford).

Nielsen-Marsh, C. M. & Hedges, R. E. (2000). Patterns of diagenesis in bone I: the effects of site environments. *Journal of Archaeological Science*, *27*(12), 1139-1150.

Nomura, S., Hiltner, A., Lando, J. B. & Baer, E. (1977). Interaction of water with native collagen. *Biopolymers: Original Research on Biomolecules*, *16*(2), 231-246.

Nyman, J. S., Roy, A., Shen, X., Acuna, R. L., Tyler, J. H. & Wang, X. (2006). The influence of water removal on the strength and toughness of cortical bone. *Journal of biomechanics*, *39*(5), 931-938.

Oakley, K. P. (1934). Phosphatic calculi in Silurian polyzoa. *Proceedings of the Royal Society of London. Series B-Biological Sciences*, *116*(798), 296-314.

Ørvig, T. (1973). Acanthodian dentition and its bearing on the relationships of the group. *Palaeontographica, Abteilung A*, *143*(1-6), 119-150.

Ørvig, T. (1977). A survey of odontodes ('dermal teeth') from developmental, structural, functional, and phyletic points of view. *Problems in vertebrate evolution*.

Ørvig, T. (1980). Histologic Studies of Ostracoderms, Placoderms and Fossil Elasmobranchs: 3. Structure and growth of the gnathalia of certain arthrodires '. *Zoologica Scripta*, *9*(1-4), 141-159.

Pan, Y. & Fleet, M. E. (2002). Compositions of the apatite-group minerals: substitution mechanisms and controlling factors. *Reviews in Mineralogy and Geochemistry*, *48*(1), 13-49.

Pasero, M., Kampf, A. R., Ferraris, C., Pekov, I. V., Rakovan, J. & White, T. J. (2010). Nomenclature of the apatite supergroup minerals. *European Journal of Mineralogy*, *22*(2), 163-179.
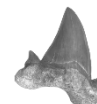
Pasteris, J. D., Wopenka, B. & Valsami-Jones, E. (2008). Bone and tooth mineralization: why apatite?. *Elements*, *4*(2), 97-104.

Pasteris, J. D., Wopenka, B. & Valsami-Jones, E. (2008). Bone and tooth mineralization: why apatite?. *Elements*, *4*(2), 97-104.

Pautard, F. G. (1959). Hydroxyapatite as a developmental feature of Spirostomum ambiguum. *Biochimica et biophysica acta*, *35*, 33-46.

Pautard, F. G. E. (1981). Calcium phosphate microspheres in biology. *Progress in Crystal Growth and Characterization*, *4*(1-2), 89-98.

Person, A., Bocherens, H., Saliège, J. F., Paris, F., Zeitoun, V. & Gérard, M. (1995). Early diagenetic evolution of bone phosphate: an X-ray diffractometry analysis. *Journal of Archaeological Science*, *22*(2), 211-221.

Peters, F., Schwarz, K. & Epple, M. (2000). The structure of bone studied with synchrotron X-ray diffraction, X-ray absorption spectroscopy and thermal analysis. *Thermochimica Acta*, *361*(1-2), 131-138.

Pfretzschner, H. U. (2004). Fossilization of Haversian bone in aquatic environments. *Comptes Rendus Palevol*, *3*(6-7), 605-616.

Picard, S., Lécuyer, C., Barrat, J. A., Garcia, J. P., Dromart, G. & Sheppard, S. M. (2002). Rare earth element contents of Jurassic fish and reptile teeth and their potential relation to seawater composition (Anglo-Paris Basin, France and England). *Chemical Geology*, *186*(1-2), 1-16.

Piccoli, P. M. & Candela, P. A. (2002). Apatite in igneous systems. *Reviews in Mineralogy and Geochemistry*, *48*(1), 255-292.

Pietsch, C. & Bottjer, D. J. (2010). Comparison of changes in ocean chemistry in the early triassic with trends in diversity and ecology. *Journal of Earth Science*, *21*(1), 147-150.

Pietzner, H., Vahl, J., Werner, H. & Ziegler, W. (1968). The chemical composition and micromorphology of conodonts. *Palaeontographica, Abteilung A: Palaeozoologie—Stratigraphie*, *128*(4-6), 115-148.

Piga, G., Solinas, G., Thompson, T. J. U., Brunetti, A., Malgosa, A. & Enzo, S. (2013). Is X-ray diffraction able to distinguish between animal and human bones?. *Journal of archaeological science*, *40*(1), 778-785.

Piga, G., Thompson, T. J., Malgosa, A. & Enzo, S. (2009). The potential of X-ray diffraction in the analysis of burned remains from forensic contexts. *Journal of Forensic Sciences*, *54*(3), 534-539.

Pike, A., Nielsen-Marsh, C. M. & Hedges, R. E. M. (2001). Modelling bone dissolution under different hydrological regimes. *Archaeological Sciences '97*. pp. 127-132 .

Poole, D. F. G. (1967). Phylogeny of tooth tissues: enameloid and enamel in recent vertebrates with a note on the history of cementum. *Structural and chemical organization of teeth*. 111-149.

Posner, A. S., Perloff, A. & Diorio, A. F. (1958). Refinement of the hydroxyapatite structure. *Acta Crystallographica*, *11*(4), 308-309.

Reynard, B., Lécuyer, C. & Grandjean, P. (1999). Crystal-chemical controls on rare-earth element concentrations in fossil biogenic apatites and implications for paleoenvironmental reconstructions. *Chemical Geology*, *155*(3-4), 233-241.

Rho, J. Y., Kuhn-Spearing, L. & Zioupos, P. (1998). Mechanical properties and the hierarchical structure of bone. *Medical engineering & physics*, *20*(2), 92-102.

Richter, M. & Smith, M. (1995). A microstructural study of the ganoine tissue of selected lower vertebrates. *Zoological Journal of the Linnean Society*, *114*(2), 173-212.

Righi, S., Savioli, M., Prevedelli, D., Simonini, R. & Malferrari, D. (2020). Unravelling the ultrastructure and mineralogical composition of fireworm stinging bristles. *Zoology*, *144*, 125851. <u>Annex-2</u>

Ritchie, A. (1968). New evidence on *Jamoytius kerwoodi* White, an important ostracoderm from the Silurian of Lanarkshire, Scotland. *Palaeontology*, *11*(1), 21-39.

Robinson, C., Kirkham, J. & Shore, R. C. (Eds.). (2017). *Dental enamel formation to destruction*. CRC press. ISBN 1351366076, 9781351366076.

Robinson, C., Kirkham, J., Brookes, S. J., Bonass, W. A. & Shore, R. C. (2003). The chemistry of enamel development. *International Journal of Developmental Biology*, *39*(1), 145-152.

Rogers, K. D. & Zioupos, P. (1999). The bone tissue of the rostrum of a Mesoplodon densirostris whale: A mammalian biomineral demonstrating extreme texture. *Journal of Materials Science Letters*, *18*(8), 651-654.

Romer, A. S. (1933). Eurypterid influence on vertebrate history. *Science*, *78*(2015), 114-117.

Romer, A. S. (1942). Cartilage an embryonic adaptation. *The American Naturalist*, *76*(765), 394-404.

Romer, A. S. (1963). The "ancient history" of bone. *Annals of the New York Academy of Sciences*, *109*(1), 168-176.

Romer, A. S. (1964). Bone in early vertebrates. *Bone biodynamics*, *14*, 13.

Romer, A. S. (1967). Major steps in vertebrate evolution. *Science*, *158*(3809), 1629-1637.

Rosenberg, H. (1966). The isolation and identification of "volutin" granules from Tetrahymena. *Experimental cell research*, *41*(2), 397-410.

Sander, P. M. (2000). Prismless enamel in amniotes: terminology, function, and evolution. *Development, function and evolution of teeth*, 92-106.

Sansom, I. J., Smith, M. M. & Smith, M. P. (1996). Scales of thelodont and shark-like fishes from the Ordovician of Colorado. *Nature*, *379*(6566), 628-630.

Sansom, I. J., Smith, M. M. & Smith, M. P. (2001). The Ordovician radiation of vertebrates. *SYSTEMATICS ASSOCIATION SPECIAL VOLUME*, *61*, 156-171.

Schaeffer, B. (1977). The dermal skeleton in fishes. *Problems in vertebrate evolution*.

Shimada, K., Sato, I. & Moriyama, H. (1992). Morphology of the tooth of the American Alligator (Alligator mississippiensis): the fine structure and elemental analysis of the cementum. *Journal of morphology*, *211*(3), 319-329.

Shu, D. G., Luo, H. L., Morris, S. C., Zhang, X. L., Hu, S. X., Chen, L., Han, J., Zhu, M. & Chen, L. Z. (1999). Lower Cambrian vertebrates from south China. *Nature*, *402*(6757), 42-46.

Sillen, A. (1989). Diagenesis of the inorganic phase of cortical bone. In *The chemistry of prehistoric human bone* (pp. 211-229). Cambridge University Press Cambridge.

Silverman, H., Steffens, W. L. & Dietz, T. H. (1983). Calcium concretions in the gills of a freshwater mussel serve as a calcium reservoir during periods of hypoxia. *Journal of Experimental Zoology*, *227*(2), 177-189.

Silverman, H., Steffens, W. L. & Dietz, T. H. (1985). Calcium from extracellular concretions in the gills of freshwater unionid mussels is mobilized during reproduction. *Journal of Experimental Zoology*, *236*(2), 137-147.

Simkiss, K. & Mason, A. Z. (1983). Metal ions: metabolic and toxic effects. In *The mollusca* (pp. 101-164). Academic Press.

Simkiss, K. & Mason, A. Z. (1984). Cellular responses of molluscan tissues to environmental metals. *Marine Environmental Research*, *14*(1-4), 103-118.

Simkiss, K. (1976). Intracellular and extracellular routes in biomineralization. In *Symp Soc Exp Biol* (Vol. 30, pp. 423-444).

Sire, J. Y. & Huysseune, A. N. N. (2003). Formation of dermal skeletal and dental tissues in fish: a comparative and evolutionary approach. *Biological Reviews*, *78*(2), 219-249.

Sire, J. Y. & Kawasaki, K. (2012). Origin and evolution of bone and dentin and of acidic secretory calcium-binding phosphoproteins. *Phosphorylated extracellular matrix proteins of bone and dentin. Sharjah, UAE: Bentham Science. p*, 3-60.

Skinner, H. C. W. (2005). Biominerals. *Mineralogical Magazine*, *69*(5), 621-641.

Skinner, H. C. W., Albright, J. A. & Brand, R. A. (1987). Bone: mineralization. *The Scientific Basics of Orthopaedics*, 199-211.

Song, H., Wignall, P. B., Song, H., Dai, X. & Chu, D. (2019). Seawater temperature and dissolved oxygen over the past 500 million years. *Journal of Earth Science*, *30*(2), 236-243.

Sponheimer, M. & Lee-Thorp, J. A. (1999). Alteration of enamel carbonate environments during fossilization. *Journal of Archaeological Science*, *26*(2), 143-150.

Stensiö, E. A. (1927). The Downtonian and Devonian vertebrates of Spitsbergen. I, Family Cephalaspidae.

Stensiö, E. A. (1939). *A new anaspid from the Upper Devonian of Scaumenac Bay in Canada, with remarks on the other anaspids*. Almqvist & Wiksell boktryckeri-a.-b.

Stricker, S. A. & Cloney, R. A. (1981). The stylet apparatus of the nemertean Paranemertes peregrina: Its ultrastructure and role in prey capture. *Zoomorphology*, *97*(3), 205-223.

Stricker, S. A. & Weiner, S. (1985). Amorphous calcium phosphate in the stylets produced by a marine worm (Nemertea). *Experientia*, *41*(12), 1557-1559.

Suarez, C. A., Macpherson, G. L., González, L. A. & Grandstaff, D. E. (2010). Heterogeneous rare earth element (REE) patterns and concentrations in a fossil bone: implications for the use of REE in vertebrate taphonomy and fossilization history. *Geochimica et Cosmochimica Acta*, *74*(10), 2970-2988.

Toyoda, K. & Tokonami, M. (1990). Diffusion of rare-earth elements in fish teeth from deep-sea sediments. *Nature*, *345*(6276), 607-609.

Trotter, J. A. & Eggins, S. M. (2006). Chemical systematics of conodont apatite determined by laser ablation ICPMS. *Chemical Geology*, *233*(3-4), 196-216.

Trotter, J. A., Barnes, C. R. & McCracken, A. D. (2016). Rare earth elements in conodont apatite: Seawater or pore-water signatures?. *Palaeogeography, Palaeoclimatology, Palaeoecology*, *462*, 92-100.

Trueman, C. N. & Benton, M. J. (1997). A geochemical method to trace the taphonomic history of reworked bones in sedimentary settings. *Geology*, *25*(3), 263-266.

Trueman, C. N. & Tuross, N. (2002). Trace elements in recent and fossil bone apatite. *Reviews in mineralogy and geochemistry*, *48*(1), 489-521.

Trueman, C. N. (1999). Rare earth element geochemistry and taphonomy of terrestrial vertebrate assemblages. *Palaios*, *14*(6), 555-568.

Trueman, C. N., Palmer, M. R., Field, J., Privat, K., Ludgate, N., Chavagnac, V., Eberth, D. A., Cifelli, R. & Rogers, R. R. (2008a). Comparing rates of recrystallisation and the potential for preservation of biomolecules from the distribution of trace elements in fossil bones. *Comptes Rendus Palevol*, *7*(2-3), 145-158.

Trueman, C. N., Privat, K. & Field, J. (2008b). Why do crystallinity values fail to predict the extent of diagenetic alteration of bone mineral?. *Palaeogeography, Palaeoclimatology, Palaeoecology*, *266*(3-4), 160-167.

Tuross, N., Behrensmeyer, A. K., Eanes, E. D., Fisher, L. W. & Hare, P. E. (1989). Molecular preservation and crystallographic alterations in a weathering sequence of wildebeest bones. *Applied Geochemistry*, *4*(3), 261-270.

Van der Brugghen, W. & Janvier, P. (1993). Denticles in thelodonts. *Nature*, *364*(6433), 107-107.

Von Brand, T. (2013). *Biochemistry of parasites*. Elsevier. ISBN 1483269051, 9781483269054.

Waller, T. R. (1983). Dahllite in the periostracum of Lithophaga nigra (Mollusca: Bivalvia) and its taxonomic and functional implications. *American Malacological Bulletin*, *1*, 101.

Wang, P., Li, C., Gong, H., Jiang, X., Wang, H. & Li, K. (2010). Effects of synthesis conditions on the morphology of hydroxyapatite nanoparticles produced by wet chemical process. Powder Technology, 203(2), 315-321.

Watabe, N. (1989). Calcium phosphate structures in invertebrates and protozoans. *Skeletal Biomineralization: patterns, processes and evolutionary trends*, *5*, 35-44.

Watabe, N., Meenakshi, V. R., Blackwelder, P. L., Kurtz, E. M. & Dunkelberger, D. G. (1976). Calcareous spherules in the gastropod, Pomacea paludosa. *The Belle W. Baruch Library in Marine Science*, (5).

Watanabe, K. (2004). Collagenolytic proteases from bacteria. *Applied microbiology and biotechnology*, *63*(5), 520-526.

Weiner, S., & Traub, W. (1992). Bone structure: from angstroms to microns. *The FASEB journal*, *6*(3), 879-885.

Weiner, S., & Wagner, H. D. (1998). The material bone: structure-mechanical function relations. *Annual review of materials science*, *28*(1), 271-298.

Weiner, S., Goldberg, P. & Bar-Yosef, O. (1993). Bone preservation in Kebara Cave, Israel using on-site Fourier transform infrared spectrometry. *Journal of Archaeological Science*, *20*(6), 613-627.

Wen, X., Lei, Y. P., Zhou, Y. L., Okamoto, C. T., Snead, M. L. & Paine, M. L. (2005). Structural organization and cellular localization of tuftelin-interacting protein 11 (TFIP11). *Cellular and Molecular Life Sciences CMLS*, *62*(9), 1038-1046.

White, S. N., Luo, W., Paine, M. L., Fong, H., Sarikaya, M. & Snead, M. L. (2001). Biological organization of hydroxyapatite crystallites into a fibrous continuum toughens and controls anisotropy in human enamel. *Journal of dental research*, *80*(1), 321-326.

Williams, A. & Cusack, M. (1999). Evolution of a rhythmic lamination in the organophosphatic shells of brachiopods. *Journal of Structural Biology*, *126*(3), 227-240.

Williams, A. & Cusack, M. (2007). Chemico-structural diversity of the Brachiopod shell. *Geological Society of America*. ISBN: 9780813731360

Wilson, R. M., Elliott, J. C. & Dowker, S. E. P. (1999). Rietveld refinement of the crystallographic structure of human dental enamel apatites. *American mineralogist*, *84*(9), 1406-1414.

Wopenka, B. & Pasteris, J. D. (2005). A mineralogical perspective on the apatite in bone. *Materials Science and Engineering: C, 25*(2), 131-143.

Wright, J., Seymour, R. S. & Shaw, H. F. (1984). REE and Nd isotopes in conodont apatite: variations with geological age and depositional environment. In *Conodont Biofacies and Provincialism* (Vol. 196, pp. 325-340). Geological Society of America Special Paper.

Zhang, L., Algeo, T. J., Cao, L., Zhao, L., Chen, Z. Q. & Li, Z. (2016). Diagenetic uptake of rare earth elements by conodont apatite. *Palaeogeography, Palaeoclimatology, Palaeoecology*, *458*, 176-197.

Zhao, L., Chen, Z. Q., Algeo, T. J., Chen, J., Chen, Y., Tong, J., Gao, S., Zhou, L., Hu, Z. & Liu, Y. (2013). Rare-earth element patterns in conodont albid crowns: evidence for massive inputs of volcanic ash during the latest Permian biocrisis?. *Global and Planetary Change*, *105*, 135-151.

Žigaitė, Ž., Qvarnström, M., Bancroft, A., Pérez-Huerta, A., Blom, H. & Ahlberg, P. E. (2020). Trace and rare earth element compositions of Silurian conodonts from the Vesiku Bone Bed: Histological and palaeoenvironmental implications. *Palaeogeography, Palaeoclimatology, Palaeoecology*, *549*, 109449.

Zylberberg, L., Bonaventure, J., Cohen-Solal, L., Hartmann, D. J. & Bereiterhahn, J. (1992). Organization and characterization of fibrillar collagens in fish scales in situ and in vitro. *Journal of Cell Science*, *103*(1), 273-285.

Acknowledgements

Thanks also to…

Grazie di cuore ai miei genitori e a entrambi i miei nonni che in questi anni mi hanno sostenuta e supportata.
Grazie ad Andrea e alle amiche di sempre, Luisa, Chiara e Gilda, per il prezioso e costante sostegno morale.
Grazie a Lidia con la quale ho avuto il piacere di condividere questo percorso.

Sample Tables

Samples

B1: *Pristis* sp., tooth, recent (1962)
B2 *Prionace glauca* (Linnaeus, 1758), tooth, recent (1989)
B3: *Diplodus* cf. *sargus* (Linnaeus, 1758), tooth, recent(1957)
B4: *Caretta caretta* Linnaeus, 1758, bone, recent
B5, B28: *Squalicorax* sp., tooth, Late Cretaceous
B6: *Bos taurus* Linnaeus, 1758, bone, recent
B7: *Carcharhinus leucas* (Müller & Henle, 1839), tooth, recent (living)
B8, B51: *Galeocerdo cuvier* (Péron & Lesueur, 1822), tooth, recent (living)
B9: *Raja* sp., bone, recent
B10: *Lingula anatina* Lamarck, 1801, shell, recent (living)
B11: *Dermochelys coriacea* (Vandelli, 1761), bone, recent
B13: *Palaeocarcharodon orientalis* (Sinzow, 1899), tooth, Paleocene
B14, B19: Odontaspididae, tooth, early Eocene (Ypresian, NP10 Zone)
B15: *Carcharocles megalodon* Agassiz, 1843, tooth, Miocene
B16: *Squalicorax pristodontus* (Agassiz, 1843), tooth, Late Cretaceous
B17: *Homo sapiens* (Linnaeus, 1758), bone, recent (2017)
B18: undetermined, tooth, fossil (unknown)
B20: undetermined, tooth, fossil (unknown)
B21.1, B22.1: *Homo sapiens* (Linnaeus, 1758), tooth, recent
B23.1, B23.2: *Carcharias taurus* (Rafinesque, 1810), tooth, recent (living)
B24: *Ovis aries* Linnaeus, 1758, tooth, recent (1998)
B25: undetermined, tooth, early Eocene (Ypresian, NP10 Zone)
B26, B27, B29, B30, B31, B32, B33, B35, B36: *Otodus* sp., tooth, Eocene
B34: *Carcharodon carcharias* (Linnaeus, 1758), tooth, early Pliocene
B37: *Cosmopolitodus hastalis* (Agassiz, 1843), tooth, early Miocene (Aquitanian-Burdigalian)
B38.5, B38.6: *Sus scrofa domesticus* Linnaeus, 1758, teeth and bones, recent (2018)
B39: *Mammuthus* sp., tooth, Pleistocene
B40: *Elephas* sp., tooth, Pliocene
B41: *"Mastodon" gigantorostris* (Klähn, 1922), tooth, late Miocene
B42: *Dama dama* (Linnaeus, 1758), bone, late Pleistocene
B43: *Bufotes gr. viridis* (Laurenti, 1768), bone, Early Pleistocene
B44: *Testudo hermanni* Gmelin, 1789, bone, Early Pleistocene
B45: *Dama eurygonos* (Azzaroli, 1947), bone, Early Pleistocene
B46: *Ursus etruscus* (Cuvier, 1823), bone, Early Pleistocene
B47: *Canis lupus* Linnaeus, 1758, bone, Early Pleistocene
B48: *Sus scrofa* Linnaeus, 1758, bone, Pleistocene
B49: undetermined (Bovidae), bone, Pleistocene
B50: *Elephas maximus* Linnaeus, 1758, bone, recent
B52: *Ursus spelaeus* Rosenmüller, 1794, tooth, Pleistocene
B53: *Martes foina* (Erxleben, 1777), bone, recent (2014)
B55: *Scyliorhinus canicula* (Linnaeus, 1758), tooth, recent (2019)

B1   B2   B3   B4   B5

B6   B7   B8   B9

B10   B11   B13

B14   B15   B16   B17

1cm

B18

B19

B20

B21.1

B22.1

B23.1

B23.2

B24

B25

B26

B27

B28

B29

B30

B31

B32

1cm

B33

B34

B35

B36

B37

B38.5

B38.5

1cm

B38.6
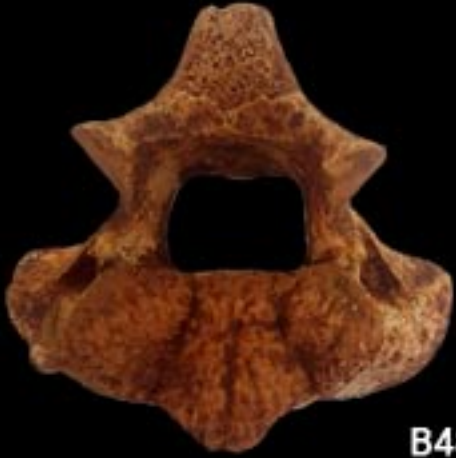
B38.6

B38.6

B38.6

B39

B40

B41

B42

B43

B44

1cm

B45

B46

B47

B48

B49

B50

B51

B52

B52

B53

B55

1cm

B55

1cm